

MAR 20 1961

# ARS JOURNAL

A PUBLICATION OF THE AMERICAN ROCKET SOCIETY

VOLUME 31 NUMBER 2

FEBRUARY 1961

BIND  
 1  
 2  
 3  
 4  
 5  
 6  
 7  
 8  
 9  
 10  
 11  
 12  
 13  
 14  
 15  
 16  
 17  
 18  
 19  
 20  
 21  
 22  
 23  
 24  
 25  
 26  
 27  
 28  
 29  
 30  
 31  
 32  
 33  
 34  
 35  
 36  
 37  
 38  
 39  
 40  
 41  
 42  
 43  
 44  
 45  
 46  
 47  
 48  
 49  
 50  
 51  
 52  
 53  
 54  
 55  
 56  
 57  
 58  
 59  
 60  
 61  
 62  
 63  
 64  
 65  
 66  
 67  
 68  
 69  
 70  
 71  
 72  
 73  
 74  
 75  
 76  
 77  
 78  
 79  
 80  
 81  
 82  
 83  
 84  
 85  
 86  
 87  
 88  
 89  
 90  
 91  
 92  
 93  
 94  
 95  
 96  
 97  
 98  
 99  
 100  
 101  
 102  
 103  
 104  
 105  
 106  
 107  
 108  
 109  
 110  
 111  
 112  
 113  
 114  
 115  
 116  
 117  
 118  
 119  
 120  
 121  
 122  
 123  
 124  
 125  
 126  
 127  
 128  
 129  
 130  
 131  
 132  
 133  
 134  
 135  
 136  
 137  
 138  
 139  
 140  
 141  
 142  
 143  
 144  
 145  
 146  
 147  
 148  
 149  
 150  
 151  
 152  
 153  
 154  
 155  
 156  
 157  
 158  
 159  
 160  
 161  
 162  
 163  
 164  
 165  
 166  
 167  
 168  
 169  
 170  
 171  
 172  
 173  
 174  
 175  
 176  
 177  
 178  
 179  
 180  
 181  
 182  
 183  
 184  
 185  
 186  
 187  
 188  
 189  
 190  
 191  
 192  
 193  
 194  
 195  
 196  
 197  
 198  
 199  
 200  
 201  
 202  
 203  
 204  
 205  
 206  
 207  
 208  
 209  
 210  
 211  
 212  
 213  
 214  
 215  
 216  
 217  
 218  
 219  
 220  
 221  
 222  
 223  
 224  
 225  
 226  
 227  
 228  
 229  
 230  
 231  
 232  
 233  
 234  
 235  
 236  
 237  
 238  
 239  
 240  
 241  
 242  
 243  
 244  
 245  
 246  
 247  
 248  
 249  
 250  
 251  
 252  
 253  
 254  
 255  
 256  
 257  
 258  
 259  
 260  
 261  
 262  
 263  
 264  
 265  
 266  
 267  
 268  
 269  
 270  
 271  
 272  
 273  
 274  
 275  
 276  
 277  
 278  
 279  
 280  
 281  
 282  
 283  
 284  
 285  
 286  
 287  
 288  
 289  
 290  
 291  
 292  
 293  
 294  
 295  
 296  
 297  
 298  
 299  
 300  
 301  
 302  
 303  
 304  
 305  
 306  
 307  
 308  
 309  
 310  
 311  
 312  
 313  
 314  
 315  
 316  
 317  
 318  
 319  
 320  
 321  
 322  
 323  
 324  
 325  
 326  
 327  
 328  
 329  
 330  
 331  
 332  
 333  
 334  
 335  
 336  
 337  
 338  
 339  
 340  
 341  
 342  
 343  
 344  
 345  
 346  
 347  
 348  
 349  
 350  
 351  
 352  
 353  
 354  
 355  
 356  
 357  
 358  
 359  
 360  
 361  
 362  
 363  
 364  
 365  
 366  
 367  
 368  
 369  
 370  
 371  
 372  
 373  
 374  
 375  
 376  
 377  
 378  
 379  
 380  
 381  
 382  
 383  
 384  
 385  
 386  
 387  
 388  
 389  
 390  
 391  
 392  
 393  
 394  
 395  
 396  
 397  
 398  
 399  
 400  
 401  
 402  
 403  
 404  
 405  
 406  
 407  
 408  
 409  
 410  
 411  
 412  
 413  
 414  
 415  
 416  
 417  
 418  
 419  
 420  
 421  
 422  
 423  
 424  
 425  
 426  
 427  
 428  
 429  
 430  
 431  
 432  
 433  
 434  
 435  
 436  
 437  
 438  
 439  
 440  
 441  
 442  
 443  
 444  
 445  
 446  
 447  
 448  
 449  
 450  
 451  
 452  
 453  
 454  
 455  
 456  
 457  
 458  
 459  
 460  
 461  
 462  
 463  
 464  
 465  
 466  
 467  
 468  
 469  
 470  
 471  
 472  
 473  
 474  
 475  
 476  
 477  
 478  
 479  
 480  
 481  
 482  
 483  
 484  
 485  
 486  
 487  
 488  
 489  
 490  
 491  
 492  
 493  
 494  
 495  
 496  
 497  
 498  
 499  
 500  
 501  
 502  
 503  
 504  
 505  
 506  
 507  
 508  
 509  
 510  
 511  
 512  
 513  
 514  
 515  
 516  
 517  
 518  
 519  
 520  
 521  
 522  
 523  
 524  
 525  
 526  
 527  
 528  
 529  
 530  
 531  
 532  
 533  
 534  
 535  
 536  
 537  
 538  
 539  
 540  
 541  
 542  
 543  
 544  
 545  
 546  
 547  
 548  
 549  
 550  
 551  
 552  
 553  
 554  
 555  
 556  
 557  
 558  
 559  
 560  
 561  
 562  
 563  
 564  
 565  
 566  
 567  
 568  
 569  
 570  
 571  
 572  
 573  
 574  
 575  
 576  
 577  
 578  
 579  
 580  
 581  
 582  
 583  
 584  
 585  
 586  
 587  
 588  
 589  
 590  
 591  
 592  
 593  
 594  
 595  
 596  
 597  
 598  
 599  
 600  
 601  
 602  
 603  
 604  
 605  
 606  
 607  
 608  
 609  
 610  
 611  
 612  
 613  
 614  
 615  
 616  
 617  
 618  
 619  
 620  
 621  
 622  
 623  
 624  
 625  
 626  
 627  
 628  
 629  
 630  
 631  
 632  
 633  
 634  
 635  
 636  
 637  
 638  
 639  
 640  
 641  
 642  
 643  
 644  
 645  
 646  
 647  
 648  
 649  
 650  
 651  
 652  
 653  
 654  
 655  
 656  
 657  
 658  
 659  
 660  
 661  
 662  
 663  
 664  
 665  
 666  
 667  
 668  
 669  
 670  
 671  
 672  
 673  
 674  
 675  
 676  
 677  
 678  
 679  
 680  
 681  
 682  
 683  
 684  
 685  
 686  
 687  
 688  
 689  
 690  
 691  
 692  
 693  
 694  
 695  
 696  
 697  
 698  
 699  
 700  
 701  
 702  
 703  
 704  
 705  
 706  
 707  
 708  
 709  
 710  
 711  
 712  
 713  
 714  
 715  
 716  
 717  
 718  
 719  
 720  
 721  
 722  
 723  
 724  
 725  
 726  
 727  
 728  
 729  
 730  
 731  
 732  
 733  
 734  
 735  
 736  
 737  
 738  
 739  
 740  
 741  
 742  
 743  
 744  
 745  
 746  
 747  
 748  
 749  
 750  
 751  
 752  
 753  
 754  
 755  
 756  
 757  
 758  
 759  
 760  
 761  
 762  
 763  
 764  
 765  
 766  
 767  
 768  
 769  
 770  
 771  
 772  
 773  
 774  
 775  
 776  
 777  
 778  
 779  
 780  
 781  
 782  
 783  
 784  
 785  
 786  
 787  
 788  
 789  
 790  
 791  
 792  
 793  
 794  
 795  
 796  
 797  
 798  
 799  
 800  
 801  
 802  
 803  
 804  
 805  
 806  
 807  
 808  
 809  
 810  
 811  
 812  
 813  
 814  
 815  
 816  
 817  
 818  
 819  
 820  
 821  
 822  
 823  
 824  
 825  
 826  
 827  
 828  
 829  
 830  
 831  
 832  
 833  
 834  
 835  
 836  
 837  
 838  
 839  
 840  
 841  
 842  
 843  
 844  
 845  
 846  
 847  
 848  
 849  
 850  
 851  
 852  
 853  
 854  
 855  
 856  
 857  
 858  
 859  
 860  
 861  
 862  
 863  
 864  
 865  
 866  
 867  
 868  
 869  
 870  
 871  
 872  
 873  
 874  
 875  
 876  
 877  
 878  
 879  
 880  
 881  
 882  
 883  
 884  
 885  
 886  
 887  
 888  
 889  
 890  
 891  
 892  
 893  
 894  
 895  
 896  
 897  
 898  
 899  
 900  
 901  
 902  
 903  
 904  
 905  
 906  
 907  
 908  
 909  
 910  
 911  
 912  
 913  
 914  
 915  
 916  
 917  
 918  
 919  
 920  
 921  
 922  
 923  
 924  
 925  
 926  
 927  
 928  
 929  
 930  
 931  
 932  
 933  
 934  
 935  
 936  
 937  
 938  
 939  
 940  
 941  
 942  
 943  
 944  
 945  
 946  
 947  
 948  
 949  
 950  
 951  
 952  
 953  
 954  
 955  
 956  
 957  
 958  
 959  
 960  
 961  
 962  
 963  
 964  
 965  
 966  
 967  
 968  
 969  
 970  
 971  
 972  
 973  
 974  
 975  
 976  
 977  
 978  
 979  
 980  
 981  
 982  
 983  
 984  
 985  
 986  
 987  
 988  
 989  
 990  
 991  
 992  
 993  
 994  
 995  
 996  
 997  
 998  
 999  
 1000  
 1001  
 1002  
 1003  
 1004  
 1005  
 1006  
 1007  
 1008  
 1009  
 1010  
 1011  
 1012  
 1013  
 1014  
 1015  
 1016  
 1017  
 1018  
 1019  
 1020  
 1021  
 1022  
 1023  
 1024  
 1025  
 1026  
 1027  
 1028  
 1029  
 1030  
 1031  
 1032  
 1033  
 1034  
 1035  
 1036  
 1037  
 1038  
 1039  
 1040  
 1041  
 1042  
 1043  
 1044  
 1045  
 1046  
 1047  
 1048  
 1049  
 1050  
 1051  
 1052  
 1053  
 1054  
 1055  
 1056  
 1057  
 1058  
 1059  
 1060  
 1061  
 1062  
 1063  
 1064  
 1065  
 1066  
 1067  
 1068  
 1069  
 1070  
 1071  
 1072  
 1073  
 1074  
 1075  
 1076  
 1077  
 1078  
 1079  
 1080  
 1081  
 1082  
 1083  
 1084  
 1085  
 1086  
 1087  
 1088  
 1089  
 1090  
 1091  
 1092  
 1093  
 1094  
 1095  
 1096  
 1097  
 1098  
 1099  
 1100  
 1101  
 1102  
 1103  
 1104  
 1105  
 1106  
 1107  
 1108  
 1109  
 1110  
 1111  
 1112  
 1113  
 1114  
 1115  
 1116  
 1117  
 1118  
 1119  
 1120  
 1121  
 1122  
 1123  
 1124  
 1125  
 1126  
 1127  
 1128  
 1129  
 1130  
 1131  
 1132  
 1133  
 1134  
 1135  
 1136  
 1137  
 1138  
 1139  
 1140  
 1141  
 1142  
 1143  
 1144  
 1145  
 1146  
 1147  
 1148  
 1149  
 1150  
 1151  
 1152  
 1153  
 1154  
 1155  
 1156  
 1157  
 1158  
 1159  
 1160  
 1161  
 1162  
 1163  
 1164  
 1165  
 1166  
 1167  
 1168  
 1169  
 1170  
 1171  
 1172  
 1173  
 1174  
 1175  
 1176  
 1177  
 1178  
 1179  
 1180  
 1181  
 1182  
 1183  
 1184  
 1185  
 1186  
 1187  
 1188  
 1189  
 1190  
 1191  
 1192  
 1193  
 1194  
 1195  
 1196  
 1197  
 1198  
 1199  
 1200  
 1201  
 1202  
 1203  
 1204  
 1205  
 1206  
 1207  
 1208  
 1209  
 1210  
 1211  
 1212  
 1213  
 1214  
 1215  
 1216  
 1217  
 1218  
 1219  
 1220  
 1221  
 1222  
 1223  
 1224  
 1225  
 1226  
 1227  
 1228  
 1229  
 1230  
 1231  
 1232  
 1233  
 1234  
 1235  
 1236  
 1237  
 1238  
 1239  
 1240  
 1241  
 1242  
 1243  
 1244  
 1245  
 1246  
 1247  
 1248  
 1249  
 1250  
 1251  
 1252  
 1253  
 1254  
 1255  
 1256  
 1257  
 1258  
 1259  
 1260  
 1261  
 1262  
 1263  
 1264  
 1265  
 1266  
 1267  
 1268  
 1269  
 1270  
 1271  
 1272  
 1273  
 1274  
 1275  
 1276  
 1277  
 1278  
 1279  
 1280  
 1281  
 1282  
 1283  
 1284  
 1285  
 1286  
 1287  
 1288  
 1289  
 1290  
 1291  
 1292  
 1293  
 1294  
 1295  
 1296  
 1297  
 1298  
 1299  
 1300  
 1301  
 1302  
 1303  
 1304  
 1305  
 1306  
 1307  
 1308  
 1309  
 1310  
 1311  
 1312  
 1313  
 1314  
 1315  
 1316  
 1317  
 1318  
 1319  
 1320  
 1321  
 1322  
 1323  
 1324  
 1325  
 1326  
 1327  
 1328  
 1329  
 1330  
 1331  
 1332  
 1333  
 1334  
 1335  
 1336  
 1337  
 1338  
 1339  
 1340  
 1341  
 1342  
 1343  
 1344  
 1345  
 1346  
 1347  
 1348  
 1349  
 1350  
 1351  
 1352  
 1353  
 1354  
 1355  
 1356  
 1357  
 1358  
 1359  
 1360  
 1361  
 1362  
 1363  
 1364  
 1365  
 1366  
 1367  
 1368  
 1369  
 1370  
 1371  
 1372  
 1373  
 1374  
 1375  
 1376  
 1377  
 1378  
 1379  
 1380  
 1381  
 1382  
 1383  
 1384  
 1385  
 1386  
 1387  
 1388  
 1389  
 1390  
 1391  
 1392  
 1393  
 1394  
 1395  
 1396  
 1397  
 1398  
 1399  
 1400  
 1401  
 1402  
 1403  
 1404  
 1405  
 1406  
 1407  
 1408  
 1409  
 1410  
 1411  
 1412  
 1413  
 1414  
 1415  
 1416  
 1417  
 1418  
 1419  
 1420  
 1421  
 1422  
 1423  
 1424  
 1425  
 1426  
 1427  
 1428  
 1429  
 1430  
 1431  
 1432  
 1433  
 1434  
 1435  
 1436  
 1437  
 1438  
 1439  
 1440  
 1441  
 1442  
 1443  
 1444  
 1445  
 1446  
 1447  
 1448  
 1449  
 1450  
 1451  
 1452  
 1453  
 1454  
 1455  
 1456  
 1457  
 1458  
 1459  
 1460  
 1461  
 1462  
 1463  
 1464  
 1465



# **AEROSPACE CORPORATION**

*present genuine challenge to scientists  
and engineers of demonstrated competence*

*"To preserve our free institutions, it is absolutely essential that the United States find the most effective means of advancing the science and technology of space and also of applying them to military space systems. This is the mission of Aerospace Corporation."*

**IVAN A. GETTING**  
PRESIDENT  
AEROSPACE CORPORATION

In accomplishing its mission, this non-profit public service organization performs the unique role of space systems architect. Aerospace Corporation provides scientific and technical leadership to the science/industry team responsible for developing complete space and ballistic missile systems on behalf of the United States Air Force.

Specific responsibilities of the new corporation include advanced systems analysis, research and experimentation, initial systems engineering, and general technical supervision of new systems through their critical phases.

The broad charter of Aerospace Corporation offers its scientists and engineers more than the usual scope for creative expression and significant achievement, within a stimulating atmosphere of dedication to the public interest.

Aerospace Corporation scientists and engineers are already engaged in a wide variety of specific systems projects and forward research programs, under the leadership of scientist/administrators including corporation president Dr. Ivan A. Getting, senior vice president Allen F. Donovan, and vice presidents Edward J. Barlow, William W. Drake, Jr., Jack H. Irving, and Chalmers W. Sherwin.

Aerospace Corporation is currently seeking scientists and engineers capable of meeting genuine challenge and with proven ability in the fields of:

- Space booster project engineering
- Spacecraft design and analysis
- Aerothermodynamics
- Solid rocket research
- Nuclear rocket propulsion
- Ion and plasma propulsion
- Chemical propulsion
- Large scale weapons operations research
- Weapon system reliability planning
- Vehicle control systems

Those qualified and experienced in these and related fields are urged to direct their resumes to:

Mr. James M. Benning, Room 103  
P.O. Box 95081, Los Angeles 45, Calif.



**AEROSPACE CORPORATION**

*A new and vital force*

*engaged in accelerating the advancement of space science and technology*

# ARS JOURNAL

A PUBLICATION OF THE AMERICAN ROCKET SOCIETY

**EDITOR** Martin Summerfield  
**ASSOCIATE TECHNICAL EDITOR** Irvin Glassman  
**MANAGING EDITOR** Barbara Nowak  
**ART EDITOR** John Culin

## ASSOCIATE EDITORS

Igor Jurkevich, G. E. Space Sciences Laboratory, Russian Supplement;  
 George F. McLaughlin, Patents; Charles J. Mundo Jr., Raytheon Co.,  
 Guidance; Bernard H. Paiewonsky, Aeronautical Research Associates  
 of Princeton, Flight Mechanics; M. H. Smith, Princeton University,  
 Technical Literature Digest

## ASSISTANT EDITORS

Maureen O'Mara, Carol Rubenstein, Estelle Viertel

## DIRECTOR OF MARKETING

Owen A. Kean

## ADVERTISING PRODUCTION MANAGER

Walter Brunke

## ADVERTISING REPRESENTATIVES

### New York

D. C. Emery and Associates  
 400 Madison Ave., New York, N. Y.  
 Telephone: Plaza 9-7460

### Chicago

Jim Summers and Associates  
 35 E. Wacker Dr., Chicago, Ill.  
 Telephone: Andover 3-1154

### Atlanta

Joe H. Howell  
 1776 Peachtree Bldg., Atlanta 9, Ga.  
 Telephone: 873-2136

### Los Angeles

James C. Galloway and Co.  
 6535 Wilshire Blvd., Los Angeles, Calif.  
 Telephone: Olive 3-3223

### Detroit

R. F. Pickrell and Associates  
 318 Stephenson Bldg., Detroit, Mich.  
 Telephone: Trinity 1-0790

### London

B. C. Nichols  
 151 Fleet St.  
 London E. C. 4, England

## American Rocket Society

500 Fifth Avenue, New York 36, N. Y.

Founded 1930

## OFFICERS

President  
 Vice-President  
 Executive Secretary  
 Treasurer  
 General Counsel  
 Director of Publications

Harold W. Ritchey  
 William H. Pickering  
 James J. Harford  
 Robert M. Lawrence  
 Andrew G. Haley  
 Irwin Hersey

## BOARD OF DIRECTORS

Terms expiring on dates indicated

Ali B. Cambel	1962	Samuel Herrick	1963
Richard B. Canright	1962	Arthur Kantrowitz	1963
William J. Cecka Jr.	1963	A. K. Oppenheim	1961
J. R. Dempsey	1961	Simon Ramo	1963
Herbert Friedman	1962	David G. Simons	1961
George Gerard	1961	John L. Sloop	1961
Robert A. Gross	1962	Martin Summerfield	1962
		A. M. Zarem	1963

## TECHNICAL COMMITTEE CHAIRMEN

William H. Avery, Ramjets	Martin Goldsmith, Liquid Rockets
R. M. L. Baker Jr., Astrodynamics	Andrew G. Haley, Space Law and Sociology
G. Daniel Brewer, Solid Rockets	John H. Huth, Power Systems
Robert W. Bussard, Nuclear Propulsion	Eugene B. Konecni, Human Factors and Bioastronautics
Bernhardt L. Dorman, Test, Operations and Support	Frank W. Lehan, Communications and Instrumentation
William M. Duke, Missiles and Space Vehicles	Peter L. Nichols Jr., Propellants and Combustion
William H. Dorrance, Hypersonics	Milton M. Slawsky, Magnetohydrodynamics
James S. Farrior, Guidance and Navigation	Herman E. Sheets, Underwater Propulsion
Herbert Friedman, Physics of the Atmosphere and Space	Ernst Stuhlinger, Electric Propulsion
George Gerard, Structures and Materials	

## Scope of ARS JOURNAL

This Journal is devoted to the advancement of astronautics through the dissemination of original papers disclosing new scientific knowledge and basic applications of such knowledge. The sciences of astronautics are understood here to embrace selected aspects of jet and rocket propulsion, spaceflight mechanics, high speed aerodynamics, flight guidance, space communications, atmospheric and outer space physics, materials and structures, human engineering, overall system analysis, and possibly certain other scientific areas. The selection of papers to be printed will be governed by the pertinence of the topic to the field of astronautics, by the current or probable future significance of the research, and by the importance of distributing the information to the members of the Society and to the profession at large.

## Information for Authors

Manuscripts must be as brief as the proper presentation of the ideas will allow. Exclusion of dispensable material and conciseness of expression will influence the Editors' acceptance of a manuscript. In terms of standard-size double-spaced typed pages, a typical maximum length is 22 pages of text (including equations), 1 page of references, 1 page of abstract and 12 illustrations. Fewer illustrations permit more text, and vice versa. Greater length will be acceptable only in exceptional cases.

Short manuscripts, not more than one quarter of the maximum length stated for full articles, may qualify for publication as Technical Notes or Technical Comments. They may be devoted to new developments requiring prompt disclosure or to comments on previously published papers. Such manuscripts are published within a few months of the date of receipt.

Sponsored manuscripts are published occasionally as an ARS service to the industry. A manuscript that does not qualify for publication, according to the above-stated requirements as to subject, scope or length, but which nevertheless deserves widespread distribution among jet propulsion engineers, may be printed as an extra part of the Journal or as a special supplement, if the author or his sponsor will reimburse the Society for actual publication costs. Estimates are available on request. Acknowledgment of such financial sponsorship appears as a footnote on the first page of the article. Publication is prompt since such papers are not in the ordinary backlog.

Manuscripts must be double spaced on one side of paper only with wide margins to allow for instructions to printer. Include a 100 to 200 word abstract. State the authors' positions and affiliations in a footnote on the first page. Equations and symbols may be handwritten or typewritten; clarity for the printer is essential. Greek letters and unusual symbols should be identified in the margin. If handwritten, distinguish between capital and lower case letters, and indicate subscripts and superscripts. References are to be grouped at the end of the manuscript and are to be given as follows. For journal articles: Authors first, then title, journal, volume, year, page numbers; for books: Authors first, then title, publisher, city, edition and page or chapter numbers. Line drawings must be clear and sharp to make clear engravings. Use black ink on white paper or tracing cloth. Lettering should be large enough to be legible after reduction. Photographs should be glossy prints, not matte or semi-matte. Each illustration must have a legend; legends should be listed in order on a separate sheet.

Manuscripts must be accompanied by written assurance as to security clearance in the event the subject matter lies in a classified area or if the paper originates under government sponsorship. Full responsibility rests with the author.

Preprints of papers presented at ARS meetings are automatically considered for publication.

Submit manuscripts in duplicate (original plus first carbon, with two sets of illustrations) to the Managing Editor, ARS JOURNAL, 500 Fifth Avenue, New York 36, N. Y.

ARS JOURNAL is published monthly by the American Rocket Society, Inc. and the American Interplanetary Society at 20th & Northampton Sts., Easton, Pa., U. S. A. Editorial offices: 500 Fifth Ave., New York 36, N. Y. Price: \$18.00 per year, \$3.00 per single copy. Second-class postage paid at Easton, Pa., with additional entry at New York, N. Y. This publication is authorized to be mailed at the special rates of postage prescribed by Section 132.122. Notice of change of address should be sent to the Secretary, ARS, at least 30 days prior to publication. Opinions expressed herein are the authors' and do not necessarily reflect the views of the Editors or of the Society. © Copyright 1961 by the American Rocket Society, Inc.

# Recent Advances in Nonequilibrium Dissociating Gasdynamics<sup>1</sup>

TING Y. LI

Rensselaer Polytechnic Institute  
Troy, N. Y.

**THE PURPOSE** of this paper is to review some recent advances in the study of gasdynamic problems including effects of chemical reactions. To provide a background for the study the general concepts shall be outlined briefly. The discussions of the recent developments are restricted to inviscid flow problems only, neglecting viscosity, heat conduction and diffusion. Particular attention is directed to recent advances in analyses of nonequilibrium dissociating gas flows. In the hypersonic flight regime, high stagnation enthalpies sufficient to cause dissociation are realized. When the time to reach equilibrium is comparable with the time it takes for a fluid particle to pass through the flow, then there exist regions of the flow field where nonequilibrium states are encountered. A brief survey of both the linear and the nonlinear methods of treatment of these nonequilibrium flows, including some new developments that have not appeared elsewhere, will be presented.

## Basic Concepts

The formulation of gasdynamic problems including chemical reactions depends on general concepts from three essential areas:

- 1 Thermodynamics of reacting mixtures.
- 2 Gasdynamics of reacting mixtures.
- 3 Chemical kinetics of reacting mixtures.

Useful concepts from these areas which are essential for the subject matter treated here shall be outlined briefly.

## Fundamental Thermodynamic Equation

The present study deals with the flow of a gaseous mixture which consists, generally, of  $N$  component gases among which chemical reactions may take place. The thermodynamic state of such a gaseous mixture is completely specified by  $2N + 5$  variables. Of these variables only  $N + 2$  are independent variables. There are  $N + 3$  relations between the  $2N + 5$  variables. A fundamental thermodynamic equation (1)<sup>2</sup> is any equation from which these  $N + 3$  relations can be de-

duced. For instance, let  $h$ ,  $p$  and  $s$  denote specific enthalpy, pressure and specific entropy of the mixture, respectively, and let  $c_i$  denote the mass fraction of the  $i$  species ( $i = 1, \dots, N$ ), then the functional relation

$$h = h(p, s, c_i) \quad [1]$$

is a fundamental thermodynamic equation. From Equation [1],  $N + 2$  relations are deduced

$$T = (\partial h / \partial s)_{p, c_i} \quad [2]$$

$$1/\rho = (\partial h / \partial p)_{s, c_i} \quad [3]$$

$$\mu_i = (\partial h / \partial c_i)_{s, p, c_j} \quad [4]$$

where

$T, \rho$  = temperature and density of the mixture, respectively

$\mu_i$  = specific chemical potential of  $i$  species

The suffixes in Equations [2-4] denote which of the variables are held constant. Suffix  $c_i$  implies that all the values of  $c_i$  are held constant, suffix  $c_j$  that all the values of  $c_j$  except that of  $c_i$  itself are held constant.  $h, p, s, c_i, T, \rho$  and  $\mu_i$  are  $5 + 2N$  variables which completely determine the thermodynamic state of the gaseous system. A general thermodynamic change in the system satisfies the relation

$$Tds = dh - \frac{1}{\rho} dp - \sum_{i=1}^N \mu_i dc_i \quad [5]$$

from which one can deduce the relations in Equations [2-4].

## Gasdynamic Equations

Kinetic theory provides a microscopic formulation of gasdynamics. The microscopic state of a system is specified by molecular distribution functions, one for each species in the system. The equations which govern these distribution functions have the form of nonlinear integro-differential equations. These equations can be interpreted as the microscopic equations of motion. This paper is concerned with gas flows in which the characteristic length is much larger than the length of free path of the molecules. For such flows a microscopically formulated problem can be translated into an equivalent system of differential equations governing the macroscopic flow variables. These differential equations

Received Dec. 29, 1960.

<sup>1</sup> This research was supported by the United States Air Force through the Air Force Office of Scientific Research of the Air Research Development Command, under contract no. AF 18(600)-1591.

<sup>2</sup> Numbers in parentheses indicate References at end of paper.

Dr. Li is Professor of Aeronautical Engineering and Director of Hypersonic Research, Rensselaer Polytechnic Institute. He received his B.S. degree from the National Central University, China, in 1940, and his Ph.D. from the California Institute of Technology in 1950. Before joining the faculty of Rensselaer, he was a senior research engineer, engaged in hypersonic research, at the California Institute of Technology until 1955. Dr. Li has served as a consultant on hypersonic aerodynamics for several research laboratories including General Electric, Convair and Rand. He is presently a member of the ARS Hypersonics Committee.



form the continuum equations of motion which are designated here as the gasdynamic equations. The gasdynamic equations for a binary mixture have been given by Chapman and Cowling (2). The gasdynamic equations for a multimixture have been given by Hirschfelder, Curtiss and Bird (3). To the Navier-Stokes approximation, a nonlinear coupled system of gasdynamic equations obtainable from the kinetic theory method is given in detail in (3) to which the interested reader is referred.

In the present paper, attention is given to recent developments in inviscid flows of reacting mixtures, neglecting viscosity, heat conduction and diffusion. The equations of motion can be therefore simplified as follows:

Continuity equation of  $i$  species

$$\rho(Dc_i/Dt) = \sigma_i \quad [6]$$

where  $D/Dt = \partial/\partial t + \mathbf{u} \cdot \nabla$ .  $\mathbf{u}$  denotes the macroscopic velocity vector of the mixture.  $\sigma_i$  denotes the chemical source function of  $i$  species, i.e., the mass rate of production of species  $i$  per unit volume by chemical reactions. By definition,  $\sum_{i=1}^N c_i = 1$ .

Continuity equation for the mixture

$$\partial \rho / \partial t + \nabla \cdot (\rho \mathbf{u}) = 0 \quad [7]$$

Momentum equation for the mixture

$$\rho(D\mathbf{u}/Dt) + \nabla p = 0 \quad [8]$$

Energy equation for the mixture

$$\rho(Dh/Dt) = Dp/Dt \quad [9]$$

Define the stagnation enthalpy as

$$H = h + (1/2)\mathbf{u} \cdot \mathbf{u} \quad [10]$$

Then the energy equation can also be written as

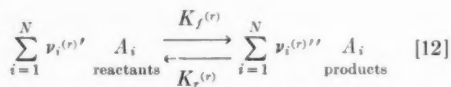
$$\rho(DH/Dt) = \partial p / \partial t \quad [11]$$

From Equation [11], an important conclusion is obtained: In steady inviscid flow of a reacting gas mixture, the stagnation enthalpy  $H$  remains invariant along a streamline.

A suitable expression of  $\sigma_i$  shall be obtained by using concepts of chemical kinetics in the following section. At this point it may be pointed out that the dynamic and thermodynamic state of the gaseous system can be determined completely from the calculation of  $\rho, c_i, \mathbf{u}, p, h, s, T, \mu_i$  satisfying the system of Equations [1-4], [6-9] under specific boundary and initial conditions for a given problem.

#### Determination of Chemical Source Function (4-8)

Suppose that the mixture consists of  $N_a$  separate atomic species ( $A_1, A_2, \dots, A_{N_a}$ ) plus  $N_m$  separate molecular species ( $A_{N_a+1}, A_{N_a+2}, \dots, A_{N_a+N_m}$ ). The molecules are formed from combinations among the  $N_a$  different species of atoms. The total number of chemical species are  $N = N_a + N_m$ , and the total number of possible independent chemical reactions is  $N_m$ . For the  $r$ th chemical reaction one may write the chemical equation



where  $\nu_i^{(r)'}$  and  $\nu_i^{(r)''}$  are stoichiometric coefficients of reactants and products, respectively. Stoichiometric coefficients give the number of moles reacting.  $K_f^{(r)}$  and  $K_r^{(r)}$  are the forward and reverse specific reaction rate constants, respectively, for the  $r$ th reaction. The net rate of progress in the

forward direction of the  $r$ th reaction is then expressible as

$$R^{(r)} = K_f^{(r)} \prod_{i=1}^N [A_i]^{\nu_i^{(r)'}} - K_r^{(r)} \prod_{i=1}^N [A_i]^{\nu_i^{(r)'}} \quad [13]$$

where

$$\begin{aligned} [A_i] &= \rho c_i / M_i = \text{molar concentration of the } i \text{ species} \\ M_i &= \text{molecular weight of } A_i \end{aligned} \quad [14]$$

Since the  $r$ th reaction yields  $\nu_i^{(r)''} - \nu_i^{(r)'}$  moles of  $A_i$ , the corresponding mass rate production of  $A_i$  is

$$\sigma_i^{(r)} = M_i (\nu_i^{(r)''} - \nu_i^{(r)'}) R^{(r)} \quad [15]$$

It follows that the net mass rate of production of  $A_i$  in all  $N_m$  reactions is

$$\sigma_i = \sum_{r=1}^{N_m} \sigma_i^{(r)} \quad [16a]$$

Combining Equations [13-16a], one obtains

$$\sigma_i = \sum_{r=1}^{N_m} \frac{\rho M_i}{\tau^{(r)}} [\nu_i^{(r)''} - \nu_i^{(r)'}] \left[ K^{(r)} \prod_{i=1}^N c_i^{\nu_i^{(r)'}} - \prod_{i=1}^N c_i^{\nu_i^{(r)'}} \right] \quad [16b]$$

where

$$K^{(r)} = \frac{K_f^{(r)}}{K_r^{(r)}} \prod_{i=1}^N \left( \frac{\rho}{M_i} \right)^{\nu_i^{(r)''} - \nu_i^{(r)'}} \quad [17]$$

$$\tau^{(r)} = \rho \left/ \left[ K_r^{(r)} \prod_{i=1}^N \left( \frac{\rho}{M_i} \right)^{\nu_i^{(r)'}} \right] \right. \quad [18]$$

$\tau^{(r)}$  has the dimension of time and is the characteristic reaction time for the  $r$ th reaction. It may also be noted that  $K^{(r)}$  is nondimensional and that if the  $r$ th reaction is at equilibrium, then, from Equation [16b]

$$K_e^{(r)} = \prod_{i=1}^N (c_i)^{\nu_i^{(r)''} - \nu_i^{(r)'}}$$

and, from Equation [17]

$$K_e^{(r)} = \frac{K_f^{(r)}}{K_r^{(r)}} \prod_{i=1}^N \left( \frac{\rho_e}{M_i} \right)^{\nu_i^{(r)''} - \nu_i^{(r)'}}$$

and thus one obtains

$$K_{e_e}^{(r)} = \frac{K_f^{(r)}}{K_r^{(r)}} = \prod_{i=1}^N [A_{i_e}]^{\nu_i^{(r)''} - \nu_i^{(r)'}} \quad [19]$$

Equation [19] is the condition of chemical equilibrium of the  $r$ th reaction and  $K_{e_e}^{(r)}$  is the corresponding equilibrium constant.  $K_{e_e}^{(r)}$  is a known function of temperature obtainable from statistical thermodynamic principles (9).

#### General Theorems

In this section, some general results which are helpful for the understanding of inviscid flow of a reacting mixture will be outlined. In many problems, the energy equation can be substituted by the equation of variation of entropy, discussed in the following. General theorems of vorticity and circulation are also discussed. The equations of steady motion of a dissociating diatomic gas are obtained to illustrate the important coupling among the flow variables and the chemical reaction rate. The discussions in the section on a simple dissociating gas also pave the way for developments in the latter part of this paper, which deal with recent results in the flow of a dissociating diatomic gas.

## Entropy Production in the Flow of a Reacting Gaseous Mixture

Chemical reactions are spontaneous irreversible thermodynamic processes which lead to entropy production in the flow field. This entropy variation along a fluid element can be calculated from Equation [5], thus, one has

$$T \frac{Ds}{Dt} = \frac{Dh}{Dt} - \frac{1}{\rho} \frac{Dp}{Dt} - \sum_{i=1}^N \mu_i \frac{Dc_i}{Dt} \quad [20]$$

whence, by Equations [6 and 9], one obtains

$$\rho T \frac{Ds}{Dt} = - \sum_{i=1}^N \mu_i \sigma_i \quad [21]$$

The expression for  $\sigma_i$  as given in Equation [16b] can be substituted in Equation [21] to yield (8)

$$\frac{Ds}{Dt} = -R \sum_{r=1}^{N_m} \frac{1}{\tau^{(r)}} \left[ K^{(r)} \prod_{i=1}^N c_i^{\nu_i^{(r)'}} - \prod_{i=1}^N c_i^{\nu_i^{(r)'}} \right] \times \ln \prod_{i=1}^N \left( \frac{x_i}{x_{i_e}} \right)^{\nu_i^{(r)'}} - \nu_i^{(r)'} \quad [22]$$

where

$R$  = universal gas constant

$x_i$  =  $c_i(\bar{M}/M_i)$  = mole fraction of species  $i$

$\bar{M}$  = average molecular weight of the mixture

$x_{i_e}$  = equilibrium mole fraction of species  $i$

For  $\tau^{(r)} \rightarrow 0$ , i.e., the ideal case of equilibrium flow, one obtains

$$\left[ K^{(r)} \prod_{i=1}^N c_i^{\nu_i^{(r)'}} - \prod_{i=1}^N c_i^{\nu_i^{(r)'}} \right] \rightarrow 0$$

$$x_i/x_{i_e} \rightarrow 1$$

$$(Ds/Dt)_e \rightarrow 0$$

For  $\tau^{(r)} \rightarrow \infty$ , i.e., the case of frozen flow, one obtains  $(Ds/Dt)_f \rightarrow 0$ . Therefore, in the flow of a reacting gaseous mixture there is a variation of entropy along the fluid element owing to the spontaneous chemical reaction. This variation of entropy vanishes only in the cases of equilibrium and frozen flows.

In nonequilibrium flows, it is convenient to represent equilibrium quantities with subscript  $e$  and nonequilibrium quantities with primes (10-13). If the translational, rotational and vibrational energies are assumed at equilibrium, as has been assumed in the present study, the specific internal energy of the mixture is expressible as

$$e = e_e + e' \quad [23]$$

where

$$e' = - \sum_{i=1}^N c_i e_i^\circ \quad [24]$$

$e_i^\circ$  represents the heat evolved in the formation of species  $i$  per unit mass. One can also write

$$h = h_e + h' = (e_e + p/\rho) + h' = e + p/\rho$$

Then  $h' = e'$ . The entropy change  $ds$  can be written as

$$ds = ds_e + ds' \quad [25]$$

where

$$ds_e = dh_e/T - (1/\rho T) dp \quad [26]$$

$$ds' = dh'/T' = de'/T' \quad [27]$$

In Equation [27],  $T'$  represents the characteristic temperature of the nonequilibrium state. Combining Equations

[24-26], one obtains

$$T ds = dh - \frac{1}{\rho} dp - \left( \frac{T}{T'} - 1 \right) \sum_{i=1}^N e_i^\circ dc_i \quad [28]$$

Comparing this result with Equation [5], one has

$$\mu_i = (T/T' - 1) e_i^\circ \quad [29]$$

Consequently, one obtains from Equation [21]

$$\rho T \frac{Ds}{Dt} = \left( 1 - \frac{T}{T'} \right) \sum_{i=1}^N e_i^\circ \sigma_i \quad [30]$$

Equation [30] gives another variant of  $Ds/Dt$ . In this form, for equilibrium flow,  $T' \rightarrow T$ ,  $(Ds/Dt)_e \rightarrow 0$ ; for frozen flow,  $\sigma_i \rightarrow 0$ ,  $(Ds/Dt)_f \rightarrow 0$ .

This result shows clearly that entropy variation is coupled with the chemical relaxation processes along the fluid element.

## Variation of Vorticity and Circulation in Reacting Gas Flow

For steady homenergetic flow, Equations [8 and 11] can be combined to yield

$$-\mathbf{u} \times \boldsymbol{\zeta} = \nabla h - (1/\rho) \nabla p \quad [31]$$

where  $\boldsymbol{\zeta} = \nabla \times \mathbf{u}$  is the flow vorticity. In a reacting nonequilibrium flow, the entropy production owing to chemical reactions must be accounted for in the calculation of the vorticity variation. From Equation [28], one has

$$\nabla h - \frac{1}{\rho} \nabla p = T \nabla s + \left( \frac{T}{T'} - 1 \right) \sum_{i=1}^N e_i^\circ \nabla c_i$$

It follows that

$$-\mathbf{u} \times \boldsymbol{\zeta} = T \nabla s - \left( 1 - \frac{T}{T'} \right) \sum_{i=1}^N e_i^\circ \nabla c_i \quad [32]$$

It is concluded therefore that a steady homenergetic irrotational flow is homentropic only for equilibrium flow or for frozen flow. In the general case of nonequilibrium flow a steady homenergetic irrotational flow is not homentropic. Equation [32] is a generalization of Crocco's theorem for inert gas flow. The classical circulation theorem (of Bjerknes) can be extended to account for nonequilibrium flow effects. Let

$$\Gamma = \oint_C \mathbf{u} \cdot d\mathbf{l} \quad [33]$$

where  $\Gamma$  is the circulation around a closed contour  $C$  formed of the line element  $d\mathbf{l}$ . Then one obtains

$$D\Gamma/Dt = \iint_A [\nabla T \times \nabla s - \nabla(T/T') \times \nabla e'] \cdot d\mathbf{A} \quad [34]$$

where  $A$  is the simply connected surface whose boundary is  $C$ . For equilibrium flow or for frozen flow, Equation [34] becomes the classical circulation theorem. In the general case of nonequilibrium flow,  $D\Gamma/Dt$  is not equal to zero in a region of constant entropy or constant temperature. Equations [32 and 34] show clearly that vorticity and circulation are also coupled with the chemical relaxation processes in the flow field.

## Steady Inviscid Motion of a Simple Dissociating Gas

A simple dissociating gas is defined as the reacting gas mixture resulting from the dissociation of a pure diatomic gas:  $A_2 \rightleftharpoons 2A$ . In a simple dissociating gas, the translational, rotational and vibrational energies are assumed at equilibrium, vibrational energies being those pertaining to the simple harmonic oscillator model. It is further assumed that the ranges of density and temperature are restricted to such values that electronic excitation and ionization can be disre-

garded. Then, for a simple dissociating gas one obtains (13)

$$h = \left[ \frac{7}{2} + \frac{3}{2} \alpha + (1 - \alpha)f(\theta) \right] \frac{p/\rho}{1 + \alpha} + \alpha d \quad [35a]$$

$$p/\rho = (1 + \alpha)R_2T \quad [36a]$$

where

$$\begin{aligned} f(\theta) &= \theta/[\epsilon^\theta - 1] \\ \theta &= h^*v/kT \\ \alpha &= \text{degree of dissociation} \\ R_2 &= \text{gas constant for } A_2 \\ d &= \text{dissociation energy per unit mass} \\ h^*, k &= \text{Planck's and Boltzmann's constants, respectively} \\ \nu &= \text{vibrational frequency} \end{aligned}$$

In the case of a simple dissociating gas, Equation [6] can be written as (14)

$$D\alpha/Dt = \frac{1}{\tau} [K(1 - \alpha) - \alpha^2] \quad [37a]$$

where the right-hand side term has been obtained from Equation [16b] and

$$K = (M_2/4\rho)(K_f/K_s) \quad [38]$$

$$\tau = M_2^2/[4\rho^2K_s(1 + \alpha)] \quad [39]$$

which may be obtained from Equations [17 and 18]. For the case of steady inviscid flows, Equations [7, 8 and 11] can be combined to yield

$$\left[ \frac{1 - \rho(\partial h/\partial p)_{p,\alpha}}{\rho(\partial h/\partial p)_{p,\alpha}} \right] (\mathbf{u} \cdot \nabla) \left( \frac{1}{2} \mathbf{u} \cdot \mathbf{u} \right) - \nabla \cdot \mathbf{u} + \frac{(\partial h/\partial \alpha)_{p,\rho}}{\rho(\partial h/\partial p)_{p,\alpha}} \mathbf{u} \cdot \nabla \alpha = 0 \quad [40a]$$

Using Equation [5], one obtains

$$a_f^2 = \left( \frac{\partial p}{\partial \rho} \right)_{s,\alpha} = - \frac{(\partial h/\partial p)_{p,\alpha}}{(\partial h/\partial p)_{p,\alpha} - 1/\rho} \quad [41]$$

$a_f$  is defined as the frozen speed of sound of the mixture (15). Thus, the coefficient of the first term in Equation [40a] is expressible as  $1/a_f^2$ . The coefficient of the third term in Equation [40a] is a function of thermodynamic variables only and is expressible as (14)

$$-\lambda = \frac{(\partial h/\partial \alpha)_{p,\rho}}{\rho(\partial h/\partial p)_{p,\alpha}} = - \frac{1}{\rho} \left( \frac{\partial p}{\partial \alpha} \right)_{p,T} - \rho \beta_f \frac{1}{c_{pf}} \left( \frac{\partial h}{\partial \alpha} \right)_{p,T} \quad [42]$$

where

$$c_{pf} = (\partial h/\partial T)_{p,\alpha} = \text{specific heat at constant pressure and frozen composition}$$

$$\beta_f = -(1/\rho^2)(\partial \rho/\partial T)_{p,\alpha} = \text{volume expansion coefficient at constant pressure and frozen composition}$$

To illustrate, Equations [37a and 40a] are expanded in Cartesian coordinates  $(x, y, z)$ , for steady flow, to obtain

$$\begin{aligned} (u^2 - a_f^2) \frac{\partial u}{\partial x} + (v^2 - a_f^2) \frac{\partial v}{\partial y} + (w^2 - a_f^2) \frac{\partial w}{\partial z} + \\ uw \left( \frac{\partial u}{\partial y} + \frac{\partial v}{\partial x} \right) + uv \left( \frac{\partial u}{\partial z} + \frac{\partial w}{\partial x} \right) + vw \left( \frac{\partial v}{\partial z} + \frac{\partial w}{\partial y} \right) - \\ a_f^2 \lambda \left( u \frac{\partial \alpha}{\partial x} + v \frac{\partial \alpha}{\partial y} + w \frac{\partial \alpha}{\partial z} \right) = 0 \quad [40b] \end{aligned}$$

$$u \frac{\partial \alpha}{\partial x} + v \frac{\partial \alpha}{\partial y} + w \frac{\partial \alpha}{\partial z} = \frac{1}{\tau} [K(1 - \alpha) - \alpha^2] \quad [37b]$$

where  $(u, v, w)$  denote the Cartesian velocity components. Obviously, these equations are nonlinear and very involved

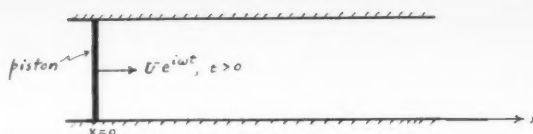


Fig. 1 Propagation of small disturbances produced by harmonic motion of a piston

and can be treated by simple mathematical methods only when suitable simplifications are introduced. Some of these developments are outlined in the following sections. Equations [40b and 37b] demonstrate very clearly the interdependence of  $\mathbf{u}$  and  $\alpha$ . From the results in the foregoing sections, one can say that in the study of nonequilibrium flow the main difficulty is in analyzing the nonlinear coupling between the flow field and the chemical reaction. The main simplification of frozen flow or equilibrium flow is the disappearance (or degeneration) of these coupling effects. In these simplified flows Equation [37b] becomes reducible to an algebraic equation:

For frozen flow

$$\alpha = \alpha_0 = \text{constant} \quad [37c]$$

For equilibrium flow

$$K_s = \alpha_s^2/(1 - \alpha_s) \quad [37d]$$

and Equation [40b] becomes

$$\begin{aligned} (u^2 - a_i^2) \frac{\partial u}{\partial x} + (v^2 - a_i^2) \frac{\partial v}{\partial y} + (w^2 - a_i^2) \frac{\partial w}{\partial z} + \\ uw \left( \frac{\partial u}{\partial y} + \frac{\partial v}{\partial x} \right) + uv \left( \frac{\partial u}{\partial z} + \frac{\partial w}{\partial x} \right) + vw \left( \frac{\partial v}{\partial z} + \frac{\partial w}{\partial y} \right) = 0 \quad [43] \end{aligned}$$

where  $a_i$  is equal to  $a_f$  for frozen flow, and  $a_i$  is equal to  $a_s$  for equilibrium flow. Equation [43] has the familiar form of the classical gasdynamic equation and is amenable to well-known methods of treatment (16,17). The extension of these methods of treatment for solution of nonequilibrium flow problems is the subject matter of current interest.

## Some Linear Results of Inviscid Flows of a Simple Dissociating Gas

Within the same limitations as in classical linear theories (16,17) linear results of nonequilibrium flow problems can be obtained. In linearized theories the entropy variation owing to chemical reaction along the fluid path can be shown to be a higher order effect and is neglected (14,15,18). Mathematically, the solution is greatly simplified because the governing equations are linearized. These recent linear results shall be reviewed briefly.

### Sound Propagation in a Simple Dissociating Gas

The most useful linear result is the calculation of the velocity of sound propagation in a simple dissociating gas. Consider the propagation of weak waves generated by a piston moving in an infinitely long tube (Fig. 1), dealing only with plane waves. The medium is assumed to be a simple dissociating gas initially ( $t = 0$ ) at rest and in a uniform undisturbed state of chemical equilibrium. For  $t > 0$ , the piston is given a small harmonic motion about  $x = 0$ . The disturbances caused by the piston are assumed small, and the governing equations are linearized to obtain the acoustic equation (8)

$$\left( \frac{1}{a_{\infty}^2} \frac{\partial^2 u'}{\partial t^2} - \frac{\partial^2 u'}{\partial x^2} \right) + \tau_{\infty}' \frac{\partial}{\partial t} \left[ \frac{1}{a_{\infty}^2} \frac{\partial^2 u'}{\partial t^2} - \frac{\partial^2 u'}{\partial x^2} \right] = 0 \quad [44]$$

where

$$\tau_{\infty}' = [(1 - \alpha_{\infty}^2)/2\alpha_{\infty}]\tau_{\infty} \quad [45]$$

$$\frac{1}{a_{\infty}^2} = \frac{1}{a_{f\infty}^2} + \rho_{\infty}\lambda_{\infty}\left(\frac{\partial\alpha_{\infty}}{\partial p}\right)_{\infty} \quad [46]$$

In Equation [44],  $u'$  denotes the perturbation velocity which is assumed small, and squares and products of small perturbation quantities have been neglected.  $a_{f\infty}$  is calculated from Equation [41] and represents the frozen speed of sound pertaining to the undisturbed state.  $a_{\infty}$  denotes the equilibrium speed of sound pertaining to the undisturbed state and is calculated from Equation [46] in which  $\lambda_{\infty}$  is the thermodynamic function defined in Equation [42] and evaluated at the undisturbed conditions.  $\tau_{\infty}'$  is related to  $\tau_{\infty}$  which represents the chemical relaxation time of the undisturbed state and is determined from Equation [39]. To Equation [44], the following boundary conditions must be applied:

$$\begin{aligned} t > 0 & \quad x = 0 & \quad u' = Ue^{i\omega t} \\ t > 0 & \quad x \rightarrow \infty & \quad u' = 0 \end{aligned} \quad [47]$$

where

$U$  = maximum velocity of the piston  
 $\omega$  = frequency of the piston's motion

In order for the linear theory to be applicable, the magnitude of  $U$  must be very small. Solution of Equation [44] under the conditions of Equation [47] is expressible as (8)

$$u' = U \exp [-(\omega m/a_{f\infty}) \sin \theta \cdot x] \times \exp \{i\omega [t - (m/a_{f\infty}) \cos \theta \cdot x]\} \quad [48]$$

where

$$m = \left[ \frac{(a_{f\infty}/a_{\infty})^4 + (\omega\tau_{\infty}')^2}{1 + (\omega\tau_{\infty}')^2} \right]^{1/4} \quad [49]$$

$$\theta = \frac{1}{2} \tan^{-1} \left\{ \frac{[(a_{f\infty}/a_{\infty})^2 - 1]\omega\tau_{\infty}'}{[(a_{f\infty}/a_{\infty})^2 + (\omega\tau_{\infty}')^2]} \right\} \quad [50]$$

From Equation [48], it is concluded that the disturbances are propagated at the following speed

$$a = a_{f\infty}/(m \cos \theta) \quad [51]$$

and that the amplitude of the disturbance is decaying with increasing  $x$  as

$$U \exp [-(\omega m/a_{f\infty}) \sin \theta \cdot x] \quad [52]$$

The dependence of  $a$ , as defined in Equation [51], on frequency represents the phenomena of sound dispersion. The amplitude decaying, as shown in Equation [52], represents sound absorption owing to chemical reaction occurring in the gas. This interesting example shows that chemical reaction could be an important factor contributing to sound absorption and dispersion. The present results also lead to the following conclusions:

1 For  $\omega \rightarrow 0$ , very low frequency wave does not decay with distance  $x$  and propagates with speed  $a_{\infty}$ .

2 For  $\omega \rightarrow \infty$ , very high frequency wave does decay with increasing  $x$  and propagates with speed  $a_{f\infty}$ .

3  $\omega\tau_{\infty}'$  is an important nondimensional parameter which can be interpreted as the ratio of chemical relaxation time and characteristic vibrational time.  $\omega\tau_{\infty}' \rightarrow 0$  for equilibrium flow and  $\omega\tau_{\infty}' \rightarrow \infty$  for frozen flow.

4 In equilibrium and frozen flows, the small disturbances (of finite frequency  $\omega$ ) are not attenuated and are propagated at speeds  $a_{\infty}$  and  $a_{f\infty}$ , respectively.

5 In nonequilibrium flow, the chemical reaction contributes to sound absorption and dispersion and  $a_{\infty} \leq a \leq a_{f\infty}$  according to  $0 \leq \omega\tau_{\infty}' \leq \infty$ .

## Linear Theory of Steady Flow of a Simple Dissociating Gas

For small disturbances to a free stream in chemical equilibrium, Equations [40b and 37b] may be linearized and combined to obtain (15)

$$\begin{aligned} \frac{1}{\chi} \frac{\partial}{\partial \xi} \left[ (1 - M_{f\infty}^2) \frac{\partial u'}{\partial \xi} + \frac{\partial v'}{\partial \eta} + \frac{\partial w'}{\partial \zeta} \right] + \\ (1 - M_{\infty}^2) \frac{\partial u'}{\partial \xi} + \frac{\partial v'}{\partial \eta} + \frac{\partial w'}{\partial \zeta} = 0 \end{aligned} \quad [53a]$$

where

$$\begin{aligned} M_{f\infty} &= u_{\infty}/a_{f\infty} \\ M_{\infty} &= u_{\infty}/a_{\infty} \\ \xi &= x/L \\ \eta &= y/L \\ \zeta &= z/L \\ \chi &= L/\tau_{\infty}u_{\infty} \\ L &= \text{suitable characteristic length} \\ \chi &= \text{nondimensional ratio of the characteristic flow time } L/u_{\infty} \text{ and chemical relaxation time } \tau_{\infty} \end{aligned}$$

In Equation [53a],  $u'$ ,  $v'$  and  $w'$  are nondimensional perturbation velocities defined as

$$u' = (u/u_{\infty}) - 1 \quad v' = v/u_{\infty} \quad w' = w/u_{\infty} \quad [54]$$

$M_{f\infty}$  and  $M_{\infty}$  are frozen and equilibrium Mach numbers, respectively. In linear theory, the entropy variation along a streamline is neglected. Consequently, the flow is irrotational, and a nondimensional velocity potential  $\phi(\xi, \eta, \zeta)$  can be introduced such that

$$u' = \partial\phi/\partial\xi \quad v' = \partial\phi/\partial\eta \quad w' = \partial\phi/\partial\zeta \quad [55]$$

Thus, from Equation [53a] the potential equation of nonequilibrium flow is obtained (15)

$$\begin{aligned} \frac{1}{\chi} \frac{\partial}{\partial \xi} \left[ (1 - M_{f\infty}^2) \frac{\partial^2 \phi}{\partial \xi^2} + \frac{\partial^2 \phi}{\partial \eta^2} + \frac{\partial^2 \phi}{\partial \zeta^2} \right] + \\ (1 - M_{\infty}^2) \frac{\partial^2 \phi}{\partial \xi^2} + \frac{\partial^2 \phi}{\partial \eta^2} + \frac{\partial^2 \phi}{\partial \zeta^2} = 0 \end{aligned} \quad [53b]$$

This equation is the governing differential equation for nonequilibrium flows that are a small departure from a uniform parallel stream.

Some good progress has been made in the study of two-dimensional linearized nonequilibrium flows. Vincenti (15) and Moore and Gibson (18) presented solutions for disturbance fields produced by a wavy wall in subsonic and supersonic nonequilibrium flows. These results illustrate some interesting nonequilibrium flow effects, such as the occurrence of pressure drag at subsonic speeds.

Another interesting linear solution is Clarke's (14), who considered the linearized planar flow past a sharp corner in a supersonic stream of an ideal dissociating gas (19,20).<sup>3</sup> Clarke found that the zone of influence of the corner is bounded upstream by the frozen Mach line (Figs. 2). In contrast to the inert gas Prandtl-Meyer flow around a corner, the pressure is not constant on the wall downstream of the corner, but varies continuously in a relaxation zone. The wall pressure  $p_{wf}$  immediately after the dissociating flow turns around the corner is determined by the formula

$$p_{wf} = p_{\infty} - (\rho_{\infty}u_{\infty}^2/\sqrt{M_{f\infty}^2 - 1})\theta \quad [56a]$$

<sup>3</sup> Lighthill's ideal dissociating gas (19) can be regarded as a simple dissociating gas for which  $f(\theta) = 1/2$  in Equation [35a]. The equilibrium law of dissociation for the ideal dissociating gas is expressible in a very simple formula

$$\frac{\alpha_{\infty}^2}{1 - \alpha_{\infty}} = \frac{\rho_d}{\rho} e^{-d/R_d T}$$

where  $\rho_d$  is a constant characteristic density for dissociation.



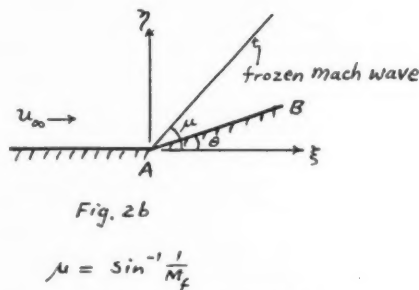
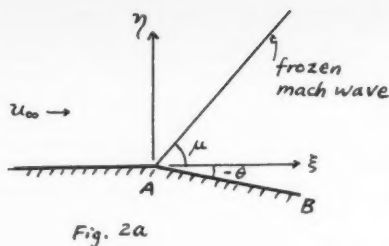


Fig. 2 Supersonic flow around a sharp corner

where  $\theta$  denotes the small angle through which the flow is turned at the corner. This result is to be expected, since the chemical reaction does not have time to develop at the corner and  $p_w$  must have the value pertaining to frozen flow. But as the flow proceeds, the chemical reaction tends to occur spontaneously. If the flow continues long enough without change in direction, the chemical reaction will continue until chemical equilibrium is established. Therefore at the end of the relaxation zone, it is expected that the wall pressure  $p_{we}$  will be given as

$$p_{we} = p_\infty - (\rho_\infty u_\infty^2 / \sqrt{M_{f_\infty}^2 - 1}) \theta \quad [57a]$$

Clarke gives a formula<sup>4</sup> for  $p_w$  which shows the continuous variation from  $p_{wf}$  to  $p_{we}$ . As shown in the preceding section,  $a_{f_\infty}$  is greater than  $a_{e_\infty}$ , therefore, we have  $p_{wf}$  is less than  $p_{we}$ . Hence, the boundary layer downstream of the convex corner in the relaxation zone on the wall is operating against an adverse pressure gradient which would tend to promote separation.

Clarke's solution should be applicable to flow in a concave corner of small angle (Fig. 2b). In this case, immediately downstream of the corner one obtains

$$p_{wf} = p_\infty + (\rho_\infty u_\infty^2 / \sqrt{M_{f_\infty}^2 - 1}) \theta \quad [56b]$$

and at the end of the relaxation zone, one obtains

$$p_{we} = p_\infty + (\rho_\infty u_\infty^2 / \sqrt{M_{e_\infty}^2 - 1}) \theta \quad [57b]$$

In the case of concave corner,  $p_{wf}$  is greater than  $p_{we}$ . Observe also that in the case of expansive flow past a convex

<sup>4</sup> The formula is of the form

$$p_w = p_\infty \mp (\rho_\infty u_\infty^2 / \sqrt{M_{f_\infty}^2 - 1}) \Gamma(\xi; \chi) \theta$$

where the top (minus) and the bottom (plus) signs apply, respectively, to the convex (Fig. 2a) and the concave (Fig. 2b) corners, and for a finite value of  $\chi$ , we have

$$\text{for } \xi \rightarrow 0, \quad \Gamma(0; \chi) \rightarrow 1$$

$$\text{for } \xi \rightarrow \infty, \quad \Gamma(\infty; \chi) \rightarrow \sqrt{M_{f_\infty}^2 - 1} / \sqrt{M_{e_\infty}^2 - 1} < 1$$

Clearly,  $\Gamma(\xi; \chi)$  represents the modification factor owing to nonequilibrium flow effects, and  $\chi$  is the nondimensional ratio introduced in Equation [53a].

corner there is recombination, which decreases the degree of dissociation from  $\alpha_\infty$ . In the case of compressive flow in a concave corner, the degree of dissociation tends to increase above  $\alpha_\infty$  on the wall downstream of the corner. It would be of some interest to apply these linear results to the calculation of the total lift on a flat plate airfoil at a small angle of attack (Fig. 3a). Equations [56a and 57a] can be used to determine the values of  $p_{wf}$  and  $p_{we}$  on the suction side of the airfoil; Equations [56b and 57b] can be used to obtain the corresponding values on the pressure side. Qualitatively, the suction and the pressure acting on the airfoil can be illustrated as in Fig. 3b. One obtains thus

$$\begin{aligned} 4\alpha / \sqrt{M_{f_\infty}^2 - 1} &= c_{Lf} > c_{L_{\text{nonequilibrium}}} > c_{Le} = 4\alpha / \sqrt{M_{e_\infty}^2 - 1} \\ 4\alpha^2 / \sqrt{M_{f_\infty}^2 - 1} &= c_{Df} > c_{D_{\text{nonequilibrium}}} > c_{De} = 4\alpha^2 / \sqrt{M_{e_\infty}^2 - 1} \end{aligned} \quad [58]$$

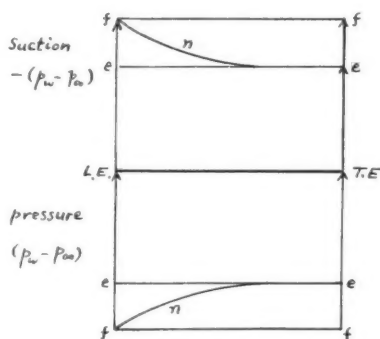
where  $\alpha$  is a small angle of attack. The location of the aerodynamic center of the airfoil is also affected by the nonequilibrium flow effects.

### Some Nonlinear Results of Inviscid Flows of a Simple Dissociating Gas

The results discussed in the foregoing section are restricted to small perturbation problems that are linearized. However, nonlinearity is a basic feature of hypersonic flows. Therefore, some nonlinear methods and solutions must be considered.

#### Method of Characteristics

For  $M_f > 1$ , Equation [40b] is a hyperbolic-type equation. The method of characteristics is suitable for its mathematical treatment. Many authors (11,21-26), using different ap-



ff : frozen flow  
 $\eta$  : nonequilibrium flow  
 ee : equilibrium flow

Figs. 3 Flat plate airfoil at an angle of attack

proaches, have discussed the method of characteristics for problems having two independent variables (one of which may be the time variable). We shall restrict ourselves to steady planar or axisymmetric flows. In these flows of a simple dissociating gas, it has been possible to show that the streamline is a three-fold characteristic and that the two frozen Mach lines are each a single-fold characteristic. Along the streamlines, there are three compatibility conditions among the flow variables. Thus along the streamline  $d\mathbf{l}$ , one has

$$ds = -(\sigma/\rho Tq)(\mu_1 - \mu_2)d\mathbf{l} \quad [59]$$

$$d\alpha = (\sigma/\rho q)d\mathbf{l} \quad [60]$$

$$qdq + (1/\rho)dp = 0 \quad [61]$$

where  $q = \sqrt{\mathbf{u} \cdot \mathbf{u}}$  is the velocity magnitude. Obviously, Equations [59 and 60] are obtainable directly from Equations [21 and 6], respectively. Equation [61] is simply the differential form of the condition of constancy of the stagnation enthalpy. Along the two frozen Mach lines  $d\mathbf{l}_\pm$ , there exists, respectively, the compatibility conditions

$$\frac{\sqrt{M_f^2 - 1}}{\rho q^2} dp \pm d\theta + \delta \frac{\sin \theta}{M_f} \frac{1}{y} d\mathbf{l}_\pm + \frac{1}{M_f} \frac{\sigma}{\rho q} d\mathbf{l}_\pm = 0 \quad [62]$$

where

$$\Sigma = -\frac{1}{\rho T} \left( \frac{\partial \rho}{\partial s} \right)_{p,\alpha} \left[ \mu_2 - \mu_1 + T \left( \frac{\partial s}{\partial \alpha} \right)_{p,\rho} \right] \quad [63]$$

and

- $M_f$  = local frozen Mach number
- $\delta$  = 0 and 1, respectively, for planar and axisymmetric flows
- $\sigma$  = chemical source function for atomic species
- $\mu_1, \mu_2$  = specific chemical potentials for atomic and molecular species, respectively
- $\theta$  = flow inclination to the  $x$ -axis

The characteristic directions  $d\mathbf{l}, d\mathbf{l}_\pm$  are illustrated in Fig. 4.

These results can be compared with classical results for inert gas flow. The new interesting features are:

- 1  $M_f$  replaces the usual Mach number  $M$ .
- 2 Equations [59 and 60] are new compatibility conditions on streamlines
- 3 The last term in Equation [62] represents the effects of entropy variation resulting from chemical reaction.

The characteristic equations can be integrated numerically by means of Massau's step-by-step method (27). In (25), this method has been applied to the investigation of the supersonic expansive flow at a convex corner. For small expansion angles, the method of characteristics calculations yield results in good agreement with the linear results discussed previously (14).

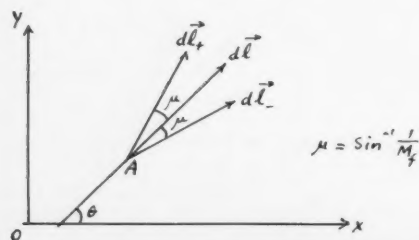


Fig. 4 Characteristic directions at A

## Nonlinear Results of Steady Flow of a Dissociating Gas

Recent advances in nonlinear treatment of inviscid dissociating gas flows took place mainly in two problem areas<sup>5</sup>: Quasi one-dimensional steady flow in a hypersonic wind tunnel nozzle (28-33), and dissociating gas flow past a blunt body (20,34). In a recent review article by the present writer (13), these recent advances have been discussed mainly on the basis of the works of Li (32) and Lick (34). These results are mentioned here only very briefly. In a nonlinear theory, it is desirable to adopt the simplest thermodynamic model in order to simplify the calculations. Lighthill's ideal dissociating gas has been used by many authors. Therefore, more attention shall be paid to these developments here.

For quasi one-dimensional steady flow in a hypersonic wind tunnel nozzle of a given geometry, the important nondimensional parameter is

$$\chi_1 = K_r(p/RT)^2/(u/A)(dA/dx) \quad [64]$$

where  $A(x)$  represents the given nozzle geometry along the  $x$ -axis in the direction of flow. (Other symbols have been defined previously.) For adiabatic expansion through the nozzle, in regions where  $\chi_1 \rightarrow 0$  frozen flow will prevail, and in regions where  $\chi_1 \rightarrow \infty$  equilibrium flow will prevail. This same parameter is important in an analysis using the streamtube method (35). Some useful qualitative information about a flow problem may be obtained from knowledge of the variation of  $\chi_1$ . For instance, in an accelerating flow region with falling pressure,  $\chi_1$  tends to decrease along the streamtube, and deviation from equilibrium flow would tend to appear. Bray (28) and others have shown that once an appreciable deviation from chemical equilibrium has occurred in a hypersonic nozzle, a return to equilibrium is unlikely to take place within the nozzle. Experimental evidence in partial support of these conclusions has been reported in the literature (36-38). Bray also considered what effects the nonequilibrium phenomena will have on quantities measured in the hypersonic wind tunnel test section. His estimates showed that the flow behind a normal shock wave is only changed slightly by freezing in the nozzle, that the heat transfer rate and drag of a blunt body are reduced by only about 25 per cent even if complete freezing occurs in the test section, and that the shock wave shape is sensitive to departures from equilibrium. A nozzle shape which would minimize the departure from equilibrium flow was also obtained (28,29).

For the calculation of the dissociating gas flow past a blunt body, Freeman (20) dealt with the direct problem, namely, the ideal dissociating gas (19) flow past a sphere. His scheme of calculations was based on a successive approximation method (39), assuming  $M_\infty \rightarrow \infty$  and  $\epsilon \ll 1$ . ( $\epsilon$  here denotes the ratio of the free stream density and the density in the shock layer.) As the zeroth approximation, let  $M_\infty \rightarrow \infty$ ,  $\epsilon \rightarrow 0$ ; then one obtains the Newtonian plus centrifugal pressure law which, in the case of hypersonic flow past a sphere, gives

$$p(x, \psi_A) = \rho_\infty u_\infty^2 \frac{\sin 3x/R + \sin^3 x_A/R}{3 \sin x/R} \quad [65]$$

where  $p(x, \psi_A)$  denotes the pressure at a point  $(x, \psi_A)$  lying on the streamline  $\psi_A$  in the shock layer (Fig. 5). To examine the effect of dissociation on the streamline patterns, first obtain the equation for streamline  $\psi_A$  as (20)

$$\frac{y}{R} = \int_0^{x_A/R} \epsilon \left[ \frac{\cos x_A/R}{\sin x/R} + 0(\epsilon) \right] d \left( \frac{x_A}{R} \right) \quad [66]$$

The body oriented coordinate system where  $x$  denotes the distance measured along the body surface from the stagnation point and  $y$  denotes the normal distance from the body surface

<sup>5</sup> Advances in the study of relaxation processes and reaction rates behind shock fronts in air and component gases have been reviewed in (45).

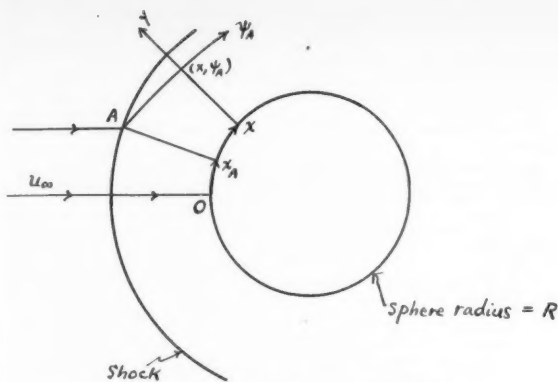


Fig. 5 Shock layer around a sphere

(Fig. 5) is used here. As  $\epsilon \rightarrow 0$ ,  $y \rightarrow 0$ , this means then that the shock wave coincides with the body surface. Generally, Equation [66] shows that the  $\psi_A$  streamline equation is

$$\frac{y}{R} = f\left(\frac{x}{R}, \frac{x_A}{R}; \epsilon\right)$$

To use Equation [66] for computations one must find the density variation  $\epsilon(x, \psi_A)$  along the streamline  $\psi_A$ . These calculations are simplified by adopting the ideal dissociating gas as a model, because the equations of state can then be written as (19)

$$h = (4 + \alpha)[(p/\rho)/(1 + \alpha)] + \alpha d \quad [35b]$$

$$p/\rho = (1 + \alpha)R_2T \quad [36b]$$

The chemical relaxation equation for an ideal dissociating gas is (20)

$$D\alpha/Dt = C\rho T^{-s} [(1 - \alpha)e^{-d/R_2T} - (\rho/\rho_d)\alpha^2] \quad [67]$$

where  $C \sim K_r T^s$ .  $C$  and  $s$  are assumed constants, and  $\rho_d$  is the constant characteristic density for dissociation (as mentioned previously). For the ideal dissociating gas,  $\epsilon$  in Equation [66] can be expressed as (20)

$$\epsilon = \frac{3}{2} \frac{(1 + \alpha) \{1 - (\alpha d)/[\frac{1}{2}u_\infty^2 \cos^2 x_A/R]\}}{(4 + \alpha)} \times \frac{(\cos^2 x_A/R) (\sin x/R)}{(\sin 3x/R + \sin^3 x_A/R)} \quad [68a]$$

Equation [67] becomes expressible as

$$\left(\frac{\partial \alpha}{\partial x/R}\right)_{\psi_A} = \left(\frac{\rho_\infty C R}{u_\infty}\right) \frac{1}{(\sin x_A/R)} \frac{1}{\epsilon} \times \left[ (1 - \alpha) \exp\left(\frac{4 + \alpha}{\alpha - \frac{1}{2} \frac{u_\infty^2 \cos^2 x_A/R}{d}}\right) - \frac{\rho_\infty}{\rho_d} \frac{\alpha^2}{\epsilon} \right] \quad [69a]$$

where  $s$  has been assumed zero.  $\epsilon$  has been given in Equation [68a]. This example again provides an illustration of the interdependence of the flow variables and the chemical reaction. Equation [69a] now must be integrated numerically to obtain  $\alpha(x, x_A)$  which can then be substituted into Equation [66] to obtain the streamline shape. In Equation [69a], the parameter

$$\chi_2 = \rho_\infty C R / u_\infty \quad [70]$$

is a nondimensional ratio of the characteristic flow time and the chemical relaxation time. For  $\chi_2 \rightarrow \infty$ , chemical equilibrium flow prevails; then Equation [69a] is replaced by the algebraic condition

$$\frac{\alpha_e^2}{1 - \alpha_e} = \epsilon \frac{\rho_d}{\rho_\infty} \exp\left\{\frac{4 + \alpha_e}{\alpha_e - (1/2)[u_\infty^2 \cos^2(x_A/R)/d]}\right\} \quad [69b]$$

For  $\chi_2 \rightarrow 0$ , frozen flow prevails; then Equation [69a] is replaced by

$$\alpha = \alpha_A \quad [69c]$$

where  $\alpha_A$  denotes the degree of dissociation at point A where  $\psi_A$  enters the shock layer. In Freeman's analysis (20) the gas is assumed undissociated at A (Fig. 5), i.e.,  $\alpha_A = 0$ . In the case of frozen flow, therefore, combining Equations [66, 68a and 69c], one obtains

$$\frac{y_f}{R} = \frac{3}{8} \int_0^{x_A/R} \frac{\cos^3 x_A/R}{(\sin 3x/R + \sin^3 x_A/R)} d\left(\frac{x_A}{R}\right) \quad [71]$$

In the case of an inert gas flow past a sphere, Freeman (39) obtained

$$\frac{y}{R} = 3\epsilon_A \int_0^{x_A/R} \frac{\cos^3 x_A/R}{(\sin 3x/R + \sin^3 x_A/R)} d\left(\frac{x_A}{R}\right) \quad [72]$$

where  $\epsilon_A = \rho_\infty/\rho_A = 1/7$  for Lighthill's ideal dissociating gas (19). The disagreement between Equations [71 and 72] shows that the adoption of  $\epsilon$  as given in Equation [68a] would lead to some inaccuracy in the results of the streamline pattern. It is difficult to obtain a rigorous higher approximation solution; however, on physical ground, we may proceed in the following manner. Dissociation takes place along  $\psi_A$  at a finite rate which would cause two effects: An increase in entropy, and a decrease in temperature. Assuming that the entropy effect is a higher order effect, we would have  $p/\rho^\gamma \approx p_A/\rho_A^\gamma$  along  $\psi_A$ , where  $\gamma$  can be regarded as an average adiabatic exponent. In our zeroth approximation,  $\epsilon \rightarrow 0$ ,  $\gamma \rightarrow 1$ , therefore,  $p/\rho \approx p_A/\rho_A$ . By Equation [36b] this implies  $T \approx T_A/(1 + \alpha)$ , which shows that as  $\alpha$  increases along  $\psi_A$ ,  $T$  decreases from the value of  $T_A$ . This thus constitutes a reasonable physical model which permits the representation of  $\epsilon$  as

$$\epsilon = \frac{(1 + \alpha) \{1 - (\alpha d)/[\frac{1}{2}u_\infty^2 \cos^2 x_A/R]\}}{2(4 + \alpha) - (1 + \alpha) \{1 - (\alpha d)/[\frac{1}{2}u_\infty^2 \cos^2 x_A/R]\}} \times \frac{3 (\cos^2 x_A/R) (\sin x/R)}{(\sin 3x/R + \sin^3 x_A/R)} \quad [68b]$$

Equation [68b] can be used instead of Equation [68a]. Then, in the case of frozen flow, the  $y_f/R$  expression would agree with Equation [72]. Obviously, since  $\epsilon \ll 1$ , Equations [68a and 68b] should have a common range of applicability when

$$(1 + \alpha) \left[ 1 - \frac{\alpha d}{(1/2)u_\infty^2 \cos^2 x_A/R} \right] \ll 2(4 + \alpha)$$

Therefore, in the present problem, results computed by Freeman (20) using Equation [68a] should give the correct trend. A rigorous higher approximation theory would decide the accuracy or inaccuracy of the physical model leading to Equation [68b].

The other significant results in the calculations of the dissociating gas flow past a blunt body are Lick's (34). These results were obtained from an inverse problem, using high speed computers in the numerical calculations. They have been reviewed in (13).

From these recent results on nonequilibrium flows past a blunt body, it is concluded:

1 Along the stagnation streamline, the flow decelerates and  $\chi_2$  tends to increase (toward infinity) as the stagnation point is approached. Thus at the stagnation point, the flow usually tends to the chemical equilibrium state, except in the ideal case of frozen flow.

2 As the flow accelerates away from the stagnation point along the body surface,  $\chi_2$  tends to decrease and deviation from equilibrium flow would tend to appear. Recently, Bloom and Steiger (40) also investigated the dissociating gas flow past blunt bodies. These authors assumed equilibrium flow in the subsonic region and found frozen flow in the supersonic expansion region.

3 The main complications in the calculations arise from the coupling between the fluid dynamic equations and chemical relaxation equation. In the case of frozen or equilibrium flow, the chemical relaxation equation can be replaced by algebraic relations, and the nonlinear coupling becomes amenable to much simpler treatment. This fact is amply demonstrated in our discussions of Freeman's results.

4 The effects of finite dissociation are to cause entropy increase and temperature decrease in the nose region. The shock layer gas is, then, of lower density in a frozen flow than that in an equilibrium flow. As deviations from equilibrium flow increases, the shock detachment distance tends to increase, and the shock wave shape tends to become more non-parallel to the body surface. Experimental evidence seems to support these predictions (41).

## Concluding Remarks

The basic nonlinear features of hypersonic flows make it almost necessary to resort to nonlinear methods of treatment. However, much can be gained for an understanding of the problem by an exploratory investigation using linearization. In the present survey, some interesting effects resulting from chemical nonequilibrium based on linear theories have been observed. Much remains to be done to carry out further developments in linear calculations of nonequilibrium dissociating gas flows. For instance, the calculations of inviscid dissociating gas flows past slender bodies are being carried out.

Methods of nonlinear treatments should be pursued with greater efforts in wider problem areas than those methods presently available. These are difficult undertakings, because the nonlinear gasdynamic problems are difficult even without nonequilibrium effects. It seems quite desirable here to follow Lighthill's suggestions to adopt the simplest thermodynamic model in order to simplify the calculations. However, the availability of high speed computers would perhaps permit adoption of more realistic gas models in numerical computations. The serious shortcoming of numerical methods is the lack of analytic formulas correlating the flow variables.

In order to obtain dependable results, either by analytical or by numerical schemes, one must correctly estimate the chemical reaction rates. At this point, the recent comprehensive experimental studies of oxygen dissociation rates as reported in (42 and 43) are noted. Further studies of chemical relaxation in reacting gaseous mixtures must be carried out. These studies would be most important for further advances in solving the problems of the nonequilibrium flows. It is encouraging to note that many studies are being directed to the complicated chemistry of high temperature air. These efforts have yielded such interesting results as reported in (44 and 45).

It may be stated that there are certain fundamental elements of nonequilibrium flows that are reasonably well understood. This is merely an attempt to review briefly these elements in inviscid flow problems. For recent advances in the study of chemically reacting laminar boundary layers, the reader is referred to a paper by Lees (46).

## References

- 1 Wilson, A. H., "Thermodynamics and Statistical Mechanics," Cambridge University Press, London, 1957, chap. 3, pp. 32-63.
- 2 Chapman, S. and Cowling, T. G., "The Mathematical Theory of Non-Uniform Gases," Cambridge Univ. Press, London, 1952, 2nd ed., chaps. 7 and 8, pp. 107-150.
- 3 Hirschfelder, J. O., Curtiss, C. F. and Bird, R. B., "Molecular Theory of Gases and Liquids," John Wiley & Sons, Inc., N. Y., 1954, chap. 7, pp. 441-513.
- 4 Hinshelwood, C. N., "The Kinetics of Chemical Change," Oxford Univ. Press, London, 1941.
- 5 Hinshelwood, C. N., "The Structure of Physical Chemistry," Oxford Univ. Press, London, 1951, pp. 351-432.
- 6 Glasstone, S., Laidler, K. and Eyring, H., "The Theory of Rate Processes," McGraw-Hill Book Co., N. Y., 1941.
- 7 Penner, S. S., "Chemical Reactions in Flow Systems," AGARDograph No. 7, Butterworths Scientific Publications, London, 1955.
- 8 Clarke, J. F., "The Flow of Chemically Reacting Gas Mixtures," Rep. no. 117, College of Aeronautics, Cranfield, England, Nov. 1958.
- 9 Fowler, R. H. and Guggenheim, E. A., "Statistical Thermodynamics," Cambridge Univ. Press, London, 1956, 4th impression, pp. 165-167.
- 10 Denbigh, K. G., "The Thermodynamics of the Steady State," Methuen & Co., Ltd., London, 1951.
- 11 Wood, W. W. and Kirkwood, J. G., "Hydrodynamics of a Reacting and Relaxing Fluid," *J. Appl. Phys.*, vol. 28, no. 4, April 1957, pp. 395-398.
- 12 Sedney, R., "Some Aspects of Nonequilibrium Flows," Ballistic Research Laboratories, Aberdeen Proving Ground, Md., BRL Rep. no. 1099, March 1960.
- 13 Li, T. Y., "Recent Advances in Nonequilibrium Flow in Gas Dynamics," Rensselaer Polytechnic Institute, Troy, N. Y., AFOSR TN60-597, RPI TR AE6001, May 1960.
- 14 Clarke, J. F., "The Linearized Flow of a Dissociating Gas," *J. Fluid Mech.*, vol. 7, Part 4, April 1960, pp. 577-595.
- 15 Vincenti, W. G., "Nonequilibrium Flow over a Wavy Wall," *J. Fluid Mech.*, vol. 6, Part 4, Nov. 1959, pp. 481-496.
- 16 Liepmann, H. W. and Roshko, A., "Elements of Gas Dynamics," John Wiley & Sons, Inc., N. Y., 1957.
- 17 Oswatitsch, K., "Gas Dynamics," English version by G. Kuerti, Academic Press, Inc., N. Y., 1956.
- 18 Moore, F. K. and Gibson, W. E., "Propagation of Weak Disturbances in a Gas Subject to Relaxation Effects," *J. Aero/Space Sci.*, vol. 27, no. 2, Feb. 1960, pp. 117-128.
- 19 Lighthill, M. J., "Dynamics of a Dissociating Gas, Part I. Equilibrium Flow," *J. Fluid Mech.*, vol. 2, Part 1, Jan. 1957, pp. 1-32.
- 20 Freeman, N. C., "Nonequilibrium Flow of an Ideal Dissociating Gas," *J. Fluid Mech.*, vol. 4, Part 4, Aug. 1958, pp. 407-425.
- 21 Chu, B. T., "Wave Propagation and the Method of Characteristics in Reacting Gas Mixtures with Applications to Hypersonic Flow," Brown University, Providence, R. I., WADC TN 57-213, AD 118,350, May 1957.
- 22 Wood, W. W. and Kirkwood, J. G., "Characteristic Equations for Reactive Flow," *J. Chem. Phys.*, vol. 27, no. 2, Aug. 1957, p. 596.
- 23 Resler, E. L., Jr., "Characteristics and Sound Speed in Nonisentropic Gas with Nonequilibrium Thermodynamic States," *J. Aeron. Sci.*, vol. 24, no. 11, Nov. 1957, pp. 785-791.
- 24 Broer, L. J. F., "Characteristics of Equations of Motion of a Reacting Gas," *J. Fluid Mech.*, vol. 4, Part 3, July 1958, p. 276.
- 25 Lick, W., "Inviscid Flow Around a Blunt Body of a Reacting Mixture of Gases, Part A. General Analysis," Rensselaer Polytechnic Institute, Troy, N. Y., AFOSR TN 58-522, AD 158 335, RPI TR AE5810, May 1958.
- 26 Cleaver, J. W., "Two-Dimensional Flow of an Ideal Dissociating Gas," Rep. no. 123, College of Aeronautics, Cranfield, England, Dec. 1959.
- 27 Howarth, L., Ed., "Modern Developments in Fluid Dynamics, High Speed Flow," Oxford Univ. Press, London, 1953, vol. 1, chap. 3, pp. 71-104 (by Meyer, R. E.).
- 28 Bray, K. N. C., "Atomic Recombination in a Hypersonic Wind Tunnel Nozzle," *J. Fluid Mech.*, vol. 6, Part 1, July 1959, pp. 1-32.
- 29 Hall, J. G. and Russo, A. L., "Studies of Chemical Nonequilibrium in Hypersonic Nozzle Flows," Cornell Aeron. Lab. Rep. no. AD 1118-A-6, Nov. 1959; see also Hall, J. G., "Dissociation Nonequilibrium in Hypersonic Nozzle Flow," AICHE preprint 7, May 1959.
- 30 Wegener, P. P., "Supersonic Nozzle Flow of a Reacting Gas Mixture," *Phys. Fluids*, vol. 2, no. 3, May-June 1959, pp. 264-275.
- 31 Rudin, M., "Criteria for Thermodynamic Equilibrium in Gas Flow," *Phys. Fluids*, vol. 1, no. 5, Sept.-Oct. 1958, pp. 384-392.
- 32 Li, T. Y., "Nonequilibrium Flow in Gas Dynamics," ARS preprint no. 852-59, June 1959; also Rensselaer Polytechnic Institute, Troy, N. Y., AFOSR TN 59-389, AD 213 893, RPI TR AE5901, May 1959.
- 33 Heims, S. P., "Effects of Chemical Dissociation and Molecular Vibrations on Steady One-Dimensional Flow," NASA TN D-87, August 1959.
- 34 Lick, W., "Inviscid Flow Around a Blunt Body of a Reacting Mixture of Gases, Part B. Numerical Solutions," Rensselaer Polytechnic Institute, Troy, N. Y., AFOSR TN 58-1124, AD 207 833, RPI TR AE5814, Dec. 1958; also, *J. Fluid Mech.*, vol. 7, Part 1, Jan. 1960, pp. 128-144.
- 35 Heims, S. P., "Effect of Oxygen Recombination on One-Dimensional Flow at High Mach Numbers," NACA TN 4144, Jan. 1958.
- 36 Wegener, P. P., "Experiments on Departure From Chemical Equilibrium in a Supersonic Flow," ARS JOURNAL, vol. 30, no. 4, April 1960, pp. 322-329.
- 37 Nagamatsu, H. T., Geiger, R. E. and Sheer, R. E., Jr., "Real Gas Effects in Flow over Blunt Bodies at Hypersonic Speeds," *J. Aero/Space Sci.*, vol. 27, no. 4, April 1960, pp. 241-251.
- 38 Nagamatsu, H. T., Workman, J. B. and Sheer, R. E., Jr., "Hypersonic Nozzle Expansion with Air Atom Recombination Present," Rep. no. 60-RL-2332C, General Electric Research Laboratory, Schenectady, N. Y., Jan. 1960.
- 39 Freeman, N. C., "On the Theory of Hypersonic Flow Past Plane and Axially Symmetric Bluff Bodies," *J. Fluid Mech.*, vol. 1, Part 4, Oct. 1956, pp. 366-387.
- 40 Bloom, M. H. and Steiger, M. H., "Inviscid Flow with Nonequilibrium Molecular Dissociation for Pressure Distributions Encountered in Hypersonic Flight," IAS preprint no. 60-26, Jan. 1960.
- 41 Eckerman, J., "The Measurement of the Rate of Dissociation of Oxygen at High Temperatures," PhD. Dissertation, Catholic University, Wash., D. C., 1958.
- 42 Byron, S. B., "Interferometric Measurement of the Rate of Dissociation of Oxygen Heated by Strong Shock Waves," *J. Chem. Phys.*, vol. 30, no. 6, June 1959, pp. 1380-1392.
- 43 Matthews, D. L., "Interferometric Measurement in the Shock Tube of the Dissociation Rate of Oxygen," *Phys. Fluids*, vol. 2, no. 2, March-April 1959, p. 170.
- 44 Zimman, W. G., "Recent Advances in Chemical Kinetics of Homogeneous Reaction in Dissociated Air," ARS JOURNAL, vol. 30, no. 3, March 1960, pp. 233-237.
- 45 Wray, K., Teare, J. D., Kivel, B. and Hammerling, P., "Relaxation Processes and Reaction Rates Behind Shock Fronts in Air and Component Gases," Avco-Everett Research Laboratory, Everett, Mass., Rep. AFBMD-TR-60-26, Avco Res. Rep. no. 83, Dec. 1959.
- 46 Lees, L., "Convective Heat Transfer with Mass Addition and Chemical Reactions," 3rd AGARD Combustion and Propulsion Panel Colloquium, Palermo, Sicily, March 17-21, 1958, Pergamon Press, N. Y., pp. 451-499.



# Satellite Networks for Continuous Zonal Coverage

R. DAVID LÜDERS<sup>1</sup>

Aerospace Corp.  
El Segundo, Calif.

Solutions are obtained to the problem of providing continuous surveillance of latitudinally bounded zones of the globe by means of a particular family of satellite networks. Each network of the family considered consists of satellites equally divided among, and uniformly distributed around, circular orbits of common altitude; the orbit planes are equally inclined with respect to the Equator and symmetrically arranged about the polar axis. Relations are obtained between the number and distribution of satellites used, the characteristics of the network in which they are arranged, and the extent of the continuous zonal coverage they accomplish. These relations are then employed to select from the family of networks considered those which minimize the number of satellites required as a function of altitude for a variety of coverage problems. Results obtained for several representative cases are given graphically.

IT MAY well be desirable in the near future to establish orbital systems which afford continuous coverage of either all or a limited portion of the globe. A large variety of missions requiring such systems are described in the literature (1,2,3).<sup>2</sup> An important consideration in the feasibility of such systems will be the number of satellites and the orbital altitudes required to accomplish the desired coverage missions. Recently Vargo (4) presented a solution to the problem of obtaining uninterrupted coverage of the entire globe by means of a particular network configuration. The present analysis treats a family of networks which provide continuous coverage of latitudinally bounded zones on Earth. Using relations obtained between network characteristics and the resultant coverage, one can select those networks which require the fewest satellites as a function of altitude for a variety of coverage problems.

## Assumptions

The networks considered in this analysis consist of satellites equally divided among, and uniformly distributed around, circular orbits of common altitude; the orbit planes are equally inclined with respect to the Equator and are symmetrically arranged about the polar axis. Each satellite carries a sensor which observes the segment of the globe subtended by the scanned solid cone whose axis is continually aligned with the local vertical. The globe is assumed spherical, and no differential perturbations are assumed to act (i.e., no perturbations which would alter the relative orientation of satellites in any orbit plane or the angular spacing between orbit planes). Results obtained by King-Hele (5) show that for identically inclined, equal circular orbits, perturbations resulting from Earth oblateness will not, in fact, produce a change in the interorbit spacing; one can compensate for the radial excursions executed by the satellites (and the non-spherical shape of Earth) by overdesigning the network.

Received May 9, 1960.

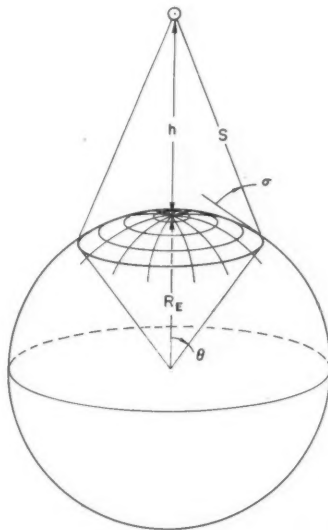
<sup>1</sup> Member of the Technical Staff, Systems Research and Planning Division. This study was performed while the writer was a member of the technical staff of Space Technology Laboratories, Inc., Los Angeles, Calif.

<sup>2</sup> Numbers in parentheses indicate References at end of paper.

## Analytical Development

### General Principles

A satellite at altitude  $h$  can view a spherical segment whose size  $\theta$  (measured by the great circle arc from the satellite sub-point to the small circle bounding the observed segment) depends upon  $\sigma$  the minimum angle of visibility consistent with the sensor capability and mission objectives. Fig. 1 illustrates



- $R_E$  RADIUS OF EARTH
- $h$  SATELLITE ALTITUDE
- $\theta$  OBSERVED HALF-ARC
- $\sigma$  MINIMUM ANGLE OF VISIBILITY
- $S$  MAXIMUM SLANT RANGE

Fig. 1 Area observed by a single satellite

the instantaneous coverage afforded by a single satellite. From the figure and the law of sines, it follows that

$$h = R_E [\cos \sigma / \cos (\theta + \sigma) - 1] \tag{1}$$

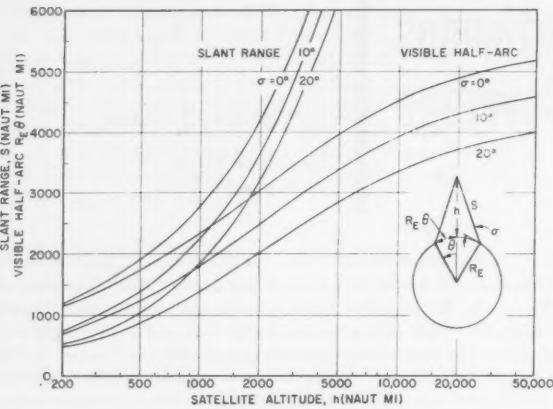


Fig. 2 Slant range and visible half-arc vs. satellite altitude and minimum viewing angle

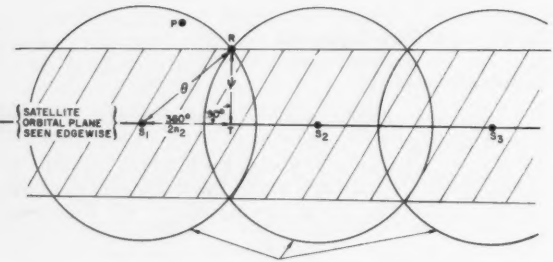
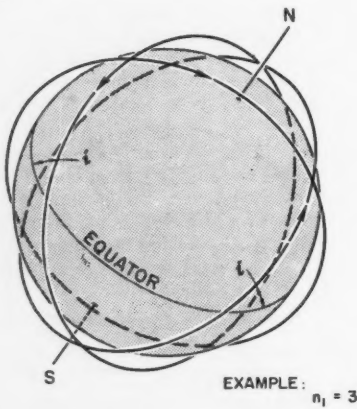


Fig. 3 Spherical segments visible from  $S_1$ ,  $S_2$  and  $S_3$ , respectively



- NETWORK CHARACTERISTICS:**
1. THE  $n_1$  ORBITS ARE CIRCLES OF COMMON SIZE.
  2.  $n_2$  SATELLITES (NOT SHOWN HERE) ARE EVENLY SPACED IN EACH ORBIT.
  3. THE ORBIT PLANES ARE EQUALLY INCLINED TO THE EQUATOR.
  4. THE NODAL AXES OF THE  $n_1$  ORBIT PLANES ARE UNIFORMLY SPACED AROUND THE EQUATOR.

Fig. 4 Typical satellite network

where  $R_E$  is the radius of the Earth or other central body. Fig. 2 shows the relation between slant range  $S$ , observed half-arc  $\theta$ , satellite altitude  $h$  and minimum viewing angle  $\sigma$ .

The spherical segments observed by the satellites in a common orbit plane will combine to observe a swath of angular half-width  $\psi$  on the globe. Fig. 3 illustrates the relation between great circle arcs  $\theta$  and  $\psi$  and  $n_2$  the number of satellites in each orbit plane. Although a point such as  $P$  will be uncovered periodically as the satellites advance in orbit, the shaded swath will *always* be observed from the orbit plane. By spherical trigonometry applied to triangle  $RS_1T$

$$\cos \theta = \cos \psi \cos \pi/n_2 \tag{2}$$

The angle  $\psi$  will be found to depend upon  $n_1$ , the number of orbit planes used, their inclination, and the location and extent of the area to be continuously observed.

Since  $N$  denotes the total number of satellites used in a network, it follows by definition that

$$N = n_1 n_2 \tag{3}$$

where  $n_1$  and  $n_2$  are integers.

The general network consists of  $n_1$  orbit planes which are equally inclined with respect to the Equator and whose nodal axes are uniformly spaced around the equatorial circle. Fig. 4 shows a typical satellite network of the type treated here, and Fig. 5 gives views of such inclined systems seen from above the pole. Note that as the orbit inclination with respect to the equator tends to 90 deg, the inclined network becomes polar. If  $n_1$  is odd, the resulting polar network will consist of  $n_1$  distinct orbit planes. However, if  $n_1$  is even, the polar network obtained will consist of only  $n_1/2$  distinct planes; each "double plane" will contain two chains of  $n_2$  satellites moving in opposition. This fact will be important later in the discussion.

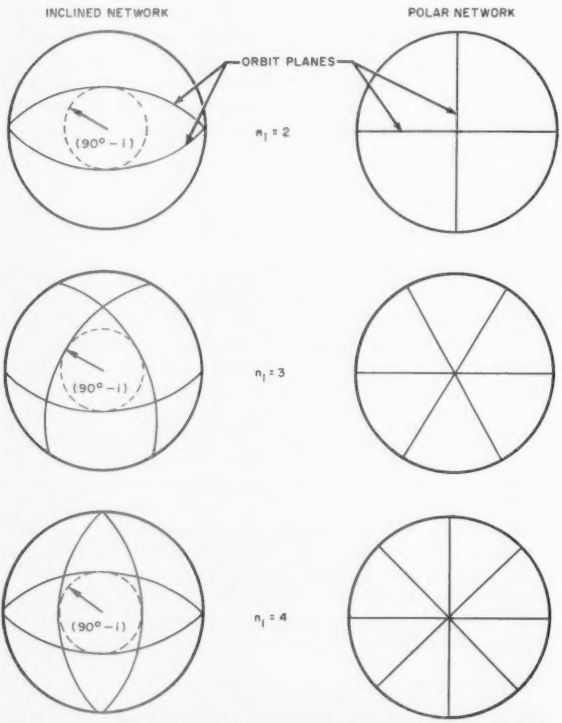


Fig. 5 Comparison of satellite networks viewed from above the pole

## Method

Fig. 6 indicates the manner in which the swaths observed by satellites in adjacent orbit planes will merge to provide continuous coverage of a latitude belt in each hemisphere.

The zones viewed from the northeastbound satellites in orbit planes 1 and 2 will intersect at point  $S$  which will thus be the southernmost<sup>3</sup> point viewed simultaneously from those planes. The southeastbound satellites in orbit planes  $(n_1 - p)$  and  $[n_1 - (p + 1)]$  will view swaths which intersect at point  $T$ . (This "plane index"  $p$  is chosen as the least integer such that  $T$  falls to the west of  $S$ .) Let point  $V$  at latitude  $\lambda$  be the southernmost point on the rotating Earth, continuously observed by the satellite network. Then  $V$  will be determined by the intersection of the northern boundaries of the unobserved areas terminating at points  $S$  and  $T$ ; by symmetry,  $V$  will fall directly below point  $B$ , the intersection of planes 1 and  $(n_1 - p)$ . The northernmost point  $N$  continuously observed by the network will be determined by the intersection of the northern boundaries of the swaths viewed from planes 1 and 2. Its latitude will be denoted by  $\mu$ .

Combining Equations [1, 2 and 3] to eliminate  $\theta$ , and applying spherical trigonometric relations to the geometry in Fig. 6 yields the following system of relations

$$h = R_E (\cos \sigma / \cos \{\arccos [\cos (\pi n_1 / N) \cos \psi] + \sigma\} - 1) \quad [4]$$

$$\lambda = \arctan \left\{ \tan i \cos \left[ \left( \frac{p+1}{n_1} \right) \pi \right] - \arcsin \left( \frac{\sin \psi}{\sqrt{1 - \sin^2 i \sin^2 \{[(p+1)/n_1]\pi\}}} \right) \right\} \quad [5]$$

where

$$\psi = \arcsin [\sin \mu \cos i - \cos (\pi/n_1) \cos \mu \sin i] \quad [6]$$

and where  $p$  is the least integer such that

$$p \geq \frac{n_1}{2} - 2 - \frac{n_1}{\pi} \arctan \left[ \frac{\cos i}{\sin \psi} \sqrt{\frac{\cos^2 \psi}{1 - \sin^2 i \sin^2 (\pi/n_1)} - 1} \right] \quad [7]$$

In the foregoing relations,  $0 \text{ deg} < \psi < 90 \text{ deg}$ . The extremes of required coverage will be specified in the range  $0 \text{ deg} \leq \lambda < \mu \leq 90 \text{ deg}$ , but a resulting negative value of  $\lambda$  or a value of  $\mu$  in excess of  $90 \text{ deg}$  will indicate, respectively, coverage south of the Equator by satellites in the northern hemisphere or coverage beyond the poles. (This will be mentioned again later in the discussion.) Note that in relation [7], in order that the quantity under the radical be positive  $\psi$  must not exceed  $\arccos \sqrt{1 - \sin^2 i \sin^2 (\pi/n_1)}$ ; this insures that the swaths observed from adjacent ascending orbits will have a discrete intersection. If  $\psi$  exceeds that value, the swaths will overlap everywhere (indeed, providing coverage to  $\lambda = 0 \text{ deg}$ , but making  $S$  an undefined point).

Relations [4-7] may be combined in principle to eliminate  $p$  and  $\psi$ ; then relations of the following form result

$$f_1(n_1, i, \lambda, \mu) = 0 \quad [8]$$

$$f_2(h, N/n_1, n_1, i, \mu, \sigma) = 0 \quad [9]$$

For a given coverage requirement and sensor resolution capability, the quantities  $\lambda$ ,  $\mu$  and  $\sigma$  will be known. Then from Equation [8] one may obtain values of  $i$  satisfying the coverage requirements for a series of integral values of  $n_1$ . These  $(n_1, i)$  pairs when substituted in Equation [9] yield curves of  $N$  vs.  $h$  for constant  $n_1$  and  $i$ . The envelope to the  $n_1$  family of curves thus obtained is the locus of the optimum

<sup>3</sup> Future remarks, applicable to either hemisphere, will be made in terms of only the northern hemisphere.

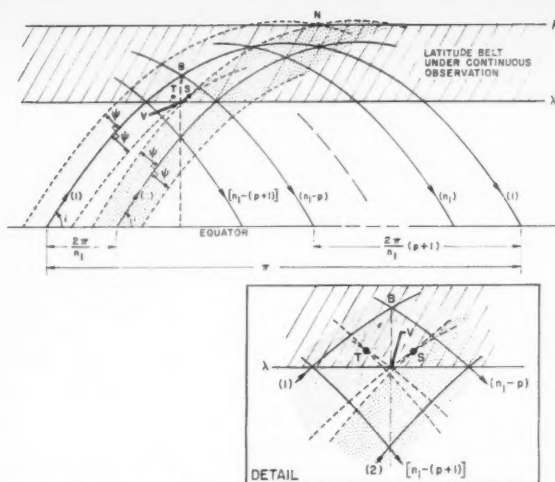


Fig. 6 Mercator projection of general coverage geometry

networks. An "optimum" network is defined here as one which accomplishes the specified coverage mission utilizing the minimum number of satellites at a given system altitude. Strictly speaking the envelope obtained is the theoretical optimum curve since both  $n_1$  and  $n_2$  will not, in general, assume integral values along it. The theoretical optimum curve will be useful primarily as a standard for comparison of practical networks (i.e., ones consisting of whole numbers of orbit planes containing whole numbers of satellites).

## Applications

The specified coverage will always be such that  $0 \text{ deg} \leq \lambda < \mu \leq 90 \text{ deg}$  and  $0 \text{ deg} \leq i \leq 90 \text{ deg}$ . However, if particular values are assigned to one or more of these quantities, certain special networks may be examined. Two of these, the polar and equatorial networks, are discussed in some detail in the following. The third case is concerned with the more common network where  $0 \text{ deg} < i < 90 \text{ deg}$ .

### Case A: The Polar Network

For an orbit inclination of  $90 \text{ deg}$ , the network is polar. (The particular case  $n_1 = 4$ ,  $n_2 = 3$  is shown in Fig. 7.) Relations [5-7] then simplify to the following forms

$$p \geq (n_1/2 - 2) \quad [10]$$

$$\psi = \arcsin (\cos \lambda \cos \{[(p+1)/n_1]\pi\}) \quad [11]$$

$$\mu = \arccos [-\sin \psi / \cos (\pi/n_1)] \quad [12]$$

Equation [12] indicates that  $\mu$  will exceed  $90 \text{ deg}$  for  $\psi > 0 \text{ deg}$ . The quantity  $p$  in inequality [10] may best be examined by considering its behavior for even and odd  $n_1$  values. For odd  $n_1$ ,  $p$  is equal to  $(n_1 - 3)/2$ ; then

$$\cos \{[(p+1)/n_1]\pi\} = \sin (\pi/2n_1) \quad [13a]$$

so Equation [11] becomes

$$\psi = \arcsin (\cos \lambda \sin [\pi/2n_1]) \quad [14a]$$

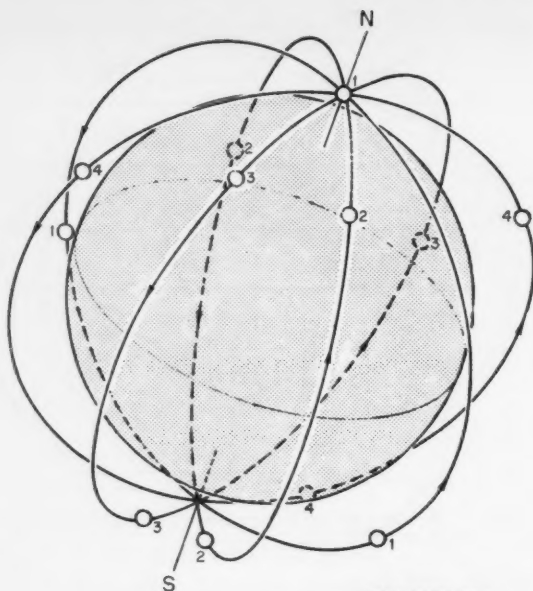
However, if  $n_1$  is even,  $p$  is equal to  $(n_1 - 4)/2$ ; then

$$\cos \{[(p+1)/n_1]\pi\} = \sin (\pi/n_1) \quad [13b]$$

in which case Equation [11] becomes

$$\psi = \arcsin (\cos \lambda \sin [\pi/n_1]) \quad [14b]$$

The discrepancy between Equations [14a and 14b] was anticipated earlier in the discussion, when it was realized that,



EXAMPLE:

$$n_1 = 4$$

$$n_2 = 3$$

#### ASSUMPTIONS

1. ALL ORBITS ARE CIRCLES OF COMMON SIZE.
2. THE PLANES ARE EVENLY FANNED ABOUT THEIR COMMON AXIS, NS.
3. THE SATELLITES ARE EVENLY SPACED IN ORBIT.

Fig. 7 Diagram of the polar satellite network

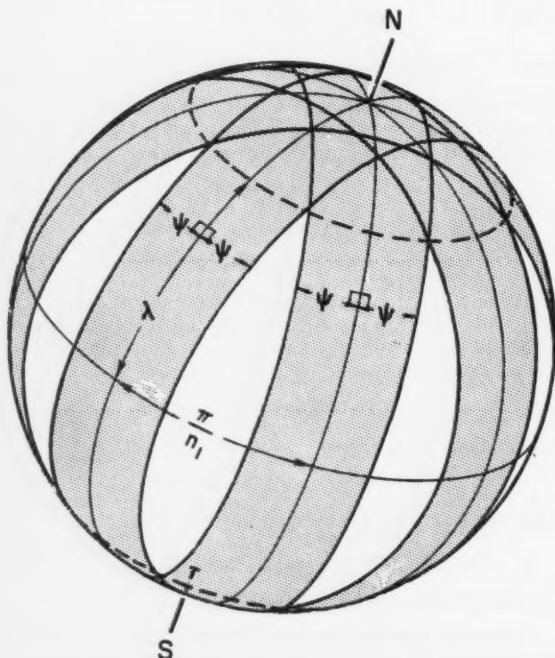


Fig. 8 Coverage geometry for a polar satellite network

for instance, a four-plane inclined network degenerated at  $i = 90$  deg to a double two-plane polar network. However, meaningful results may be obtained for a polar network containing any (even or odd) number of distinct orbit planes. To find  $\psi$  required for a two-plane polar network, one could set  $n_1$  equal to 4 in Equation [14b] to obtain  $\psi$  and substitute that value of  $\psi$  and  $n_1$  in Equation [4] to obtain  $N$ , the number of satellites actually required in a double two-plane network. But only half that number of satellites is required in a polar network consisting of two distinct orbit planes. Essentially then, whether  $n_1$  is odd or even, Equation [14a] can be applied to determine  $\psi$ . Consequently, Equation [11] becomes

$$\psi = \arcsin [\cos \lambda \sin (\pi / 2 n_1)] \quad [15]$$

Fig. 8 illustrates the manner in which coverage of the polar caps down to latitude  $\lambda$  is effected by overlapping zones of coverage swept out by the satellites in neighboring orbit planes.

Equations [4 and 15] were solved to obtain  $N$ , the total number of satellites required, as a function of system altitude  $h$  and the number of orbit planes  $n_1$  for the case of complete, global coverage ( $\lambda = 0$  deg) with ideal sensors (i.e.,  $\sigma = 0$  deg). The results are displayed in Fig. 9. The rather sharp heels appearing in the curves of constant  $n_1$  indicate that it is undesirable (if satellite altitude is to be minimized) to pack an excessively large number of satellites into each plane. Instead it is better to increase  $n_1$ , the number of orbit planes, and to decrease  $n_2$  the satellite density per plane, in order to reduce the system altitude at some  $N$  level. For example, 36 satellites may be arranged as follows to provide complete global coverage:

Orbit planes	Satellites/plane	Required altitude
$n_1 = 2$	$n_2 = 18$	1500 nautical miles
3	12	672
4	9	522
6	6	672
9	4	1500

Then, from a minimum altitude standpoint, a network of  $4 \times 9$  is most desirable for complete global coverage if a polar network consisting of 36 satellites is to be employed.

Fig. 10 presents the envelope to the  $n_1$  family of curves shown in Fig. 9. The requirement that both  $n_1$  and  $n_2$  be integers results in the step-like practical optimum curve. The variations in step size and frequency result from the irregular occurrence of  $N$  values which may be factored in an optimum or near-optimum fashion. For example, as was seen previously, the minimum altitude of a 36-satellite polar network which provides complete global coverage is 522 nautical miles. In order to reduce the network altitude further,  $N$  must be increased to at least 40 ( $h = 475$  nautical miles), since the best

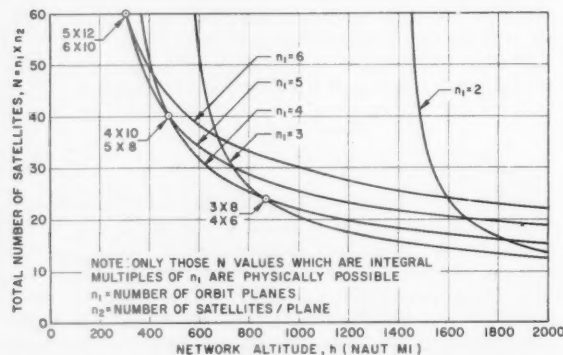


Fig. 9 Number and distribution of satellites in a polar network providing complete global coverage ( $\lambda = 0$  deg,  $\sigma = 0$  deg)



38- and 39-satellite networks require altitudes of 1492 and 651 nautical miles, respectively. Note that when  $N$  is twice the square of an integer ( $2n_1^2$ ), the theoretical optimum may actually be attained.

The theoretical optimum curves for  $\sigma = 10$  and 20 deg demonstrate the strong dependence of  $N$  on  $\sigma$ . The practical optimum curves for each of these  $\sigma$  values may be obtained by a point-by-point transformation of the practical optimum curve for  $\sigma = 0$  deg by means of the curves in Fig. 2.

The theoretical optimum satellite utilization curves for several nonzero values of  $\lambda$  were obtained in a similar manner and are presented in Fig. 11. Note that sizable reductions in system requirements may be effected by modification of the coverage requirement. For example, a system of 24 satellites providing complete global coverage requires an altitude of 859 nautical miles; but if  $\lambda = 30$  deg, the altitude need be only 691 nautical miles.

Equations [3, 4 and 15] indicate the following dependence of system altitude upon the number of orbit planes in a polar network

$$h = R_E \left\{ \frac{\cos \sigma}{\cos(\arccos \{\cos(\pi/n_2) \cos[\arcsin(\cos \lambda \sin \pi/2n_1)]\} + \sigma)} - 1 \right\} \quad [16]$$

Minimization of  $h$  with respect to  $n_1$ , holding  $N$ ,  $\sigma$  and  $\lambda$  constant, results in the expression

$$\frac{4n_1}{n_2} \frac{\tan \pi/n_2}{\cos^2 \lambda \sin \pi/n_1} \left( 1 - \cos^2 \lambda \sin^2 \frac{\pi}{2n_1} \right) - 1 = 0 \quad [17]$$

For the special case of complete global coverage mentioned earlier,  $\lambda$  is equal to zero deg and Equation [17] takes the form

$$2n_1 \tan \pi/n_2 = n_2 \tan \pi/2n_1 \quad [18]$$

whose solution is simply

$$n_2 = 2n_1 \quad [19]$$

In practice, an integral value of  $N$  will not generally be twice the square of an integer ( $2n_1^2$ ) permitting such a theoretical optimum distribution. A convenient rule of thumb for selecting the practical network which minimizes system altitude is to choose the pair of integer factors of  $N$  which minimizes quantity  $q$  defined by

$$q = |n_2 - 2n_1| \quad [20]$$

It is clear from the manner in which  $n_1$  and  $n_2$  are involved in Equation [16] why the  $(3 \times 10)$  and the  $(5 \times 6)$  polar networks mentioned earlier require identical altitudes to provide complete global coverage.

More generally, it appears that the minimum-altitude polar network of  $N$  satellites providing coverage down to latitude  $\lambda$  is the one for which  $q_\lambda$  assumes its minimum value, where

$$q_\lambda = |n_2 - 2n_1/\cos \lambda| \quad [21]$$

#### Case B: The Equatorial Network

In this case  $i$  is equal to zero deg, and a single orbit plane is used to avoid redundancy. From Equation [5] it is clear that

$$\psi = \mu \quad [22]$$

That is, the zone from  $-\mu$  to  $+\mu$  will be continuously observed by the equatorial chain of satellites. Then from Equations [4 and 22] it follows that

$$h = R_E \{ \cos \sigma / \cos [\arccos(\cos \pi/N \cos \mu) + \sigma] - 1 \} \quad [23]$$

Equation [23] was solved to obtain curves of  $N$  vs.  $\mu$  and  $h$  for a network consisting of a single equatorial orbit plane. The results are displayed in Fig. 13 together with the system requirements for multiplane inclined networks examined in case C. Discussion of the results is deferred until that time.

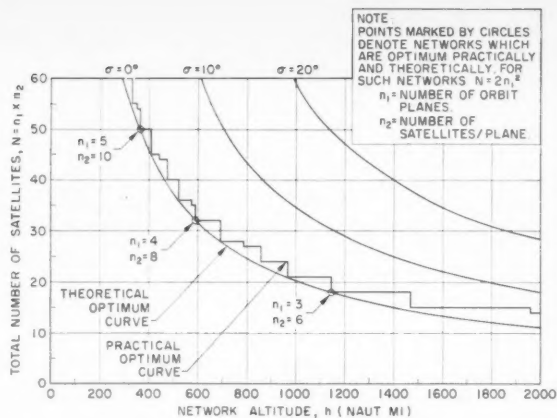


Fig. 10 Theoretical and practical optimum satellite utilization in a polar network providing complete global coverage ( $\lambda = 0$  deg)

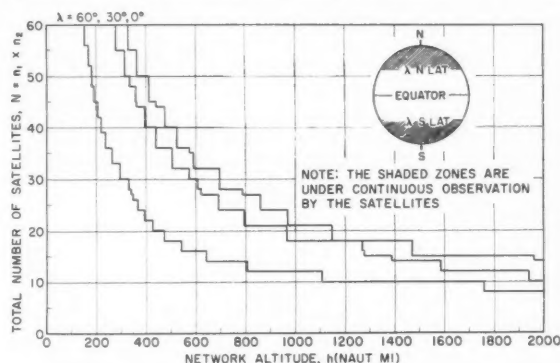


Fig. 11 Comparison of polar satellite networks providing coverage from the poles to minimum latitude  $\lambda$ . ( $\sigma = 0$  deg)

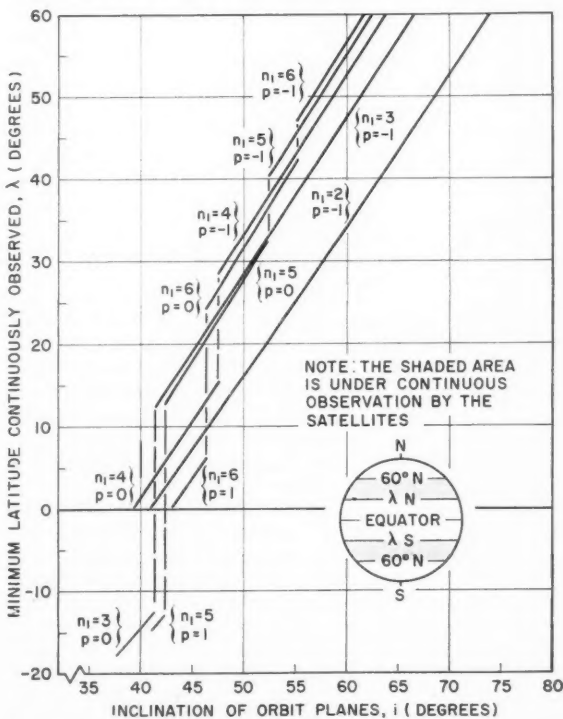


Fig. 12 Minimum latitude continuously observed as a function of inclination and number of orbit planes in network ( $\mu = 60$  deg)

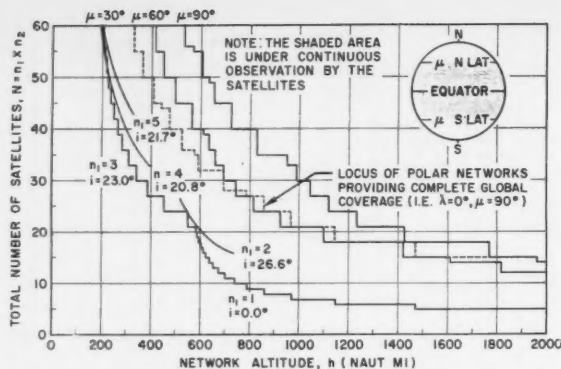


Fig. 13 Comparison of inclined and polar satellite networks providing coverage from the Equator to maximum latitude  $\mu$ . ( $\sigma = 0$  deg)

### Case C: The General Network

In the most common case, the orbit inclination will not necessarily be zero or 90 deg, nor will  $\lambda$  or  $\mu$  assume its extreme value of zero or 90 deg. For example, suppose coverage is required from a minimum latitude  $\lambda$  to a maximum latitude  $\mu$  of 60 deg. Substitution of values of  $\mu$ ,  $n_1$  and  $i$  in relations [5-7] yields  $\lambda$  as a function of those parameters as shown in Fig. 12.

Because of the role of the integer  $p$  in Equation [5],  $\lambda$  is a piecewise continuous function of  $i$  for  $n_1 > 2$ . The physical explanation for the discontinuous nature of  $\lambda$  is as follows. As the orbit inclination  $i$  decreases,  $\psi$  must increase so as to maintain coverage up to latitude  $\mu$ . Then, when the northernmost mesh (below latitude  $i$ ) becomes covered, point V (the southernmost continuously observed point) will suddenly appear in the next mesh to the south. As  $\psi$  increases further,  $\lambda$  will decrease continuously until that mesh is covered—and so on. For odd values of  $n_1$ ,  $\lambda$  will assume negative values until  $\psi$  reaches the value  $\arccos \sqrt{1 - \sin^2 i \sin^2 (\pi/n_1)}$ , when the swaths covered from adjacent ascending satellite orbits overlap everywhere. Then  $\lambda$  becomes undefined with coverage extending from  $-\mu$  to  $+\mu$ .

It is clear from Fig. 12 that the appropriate inclinations of networks providing coverage from  $\lambda = 0$  deg to  $\mu = 60$  deg are

$i = 40.9$ deg	for	$n_1 = 2$
41.4 deg		3
39.2 deg		4
42.4 deg		5

Substitution of these  $(n_1, i)$  pairs in Equations [4 and 6] yields  $N$  as a function of  $h$  and  $n_1$  for  $\lambda = 0$  deg and  $\mu = 60$  deg. Similarly, curves may be obtained for other values of  $\lambda$  and  $\mu$ . Fig. 13 shows the results appropriate to networks providing coverage from the Equator to latitude  $\mu$  in each hemisphere. The  $N$  vs.  $h$  curve for the polar network was included in the figure as a basis for comparison of the two kinds of networks for various coverage requirements.

Fig. 12 indicates that, in order to cover the latitude belt from  $-\mu$  to  $+\mu$ , a network consisting of an even number of orbit planes must observe all points down to latitude  $\lambda = 0$  deg. However, a network in which  $n_1$  is odd need not observe all points down to the Equator in order to cover the zone from  $-\mu$  to  $+\mu$ ; that is, for  $n_1$  odd, the most remote point to be observed will be north of the Equator. Note that in Fig. 13 for  $\mu = 30$  deg, networks for which  $n_1$  is odd are superior to those for which  $n_1$  is even; above a system altitude of 582 nautical miles, a single equatorial orbit plane should be used to provide the required coverage, but immediately below that altitude a three-plane network is preferred.

It appears from Fig. 13 that at low system altitudes a polar network providing complete global coverage requires fewer satellites than does an inclined network providing coverage of a wide equatorial zone. The altitude at which the polar and the inclined networks require equal numbers of satellites increases with  $\mu$ . For  $\mu = 90$  deg, the inclined and polar networks require equal numbers at an altitude of 1960 nautical miles, above which the inclined network consists of two orbit planes. Since each of the planes is inclined at 45 deg with respect to the equatorial plane, the polar and inclined networks are geometrically identical for a 90-deg rotation of the axis common to the orbit planes.

### Conclusions

A method was developed to determine the minimum number of satellites required to provide continuous coverage of a latitudinally bounded zone by means of a particular kind of satellite network.

Several representative cases of coverage requirements were examined with the following results:

1 The polar network is preferable to the inclined network in providing complete global coverage. Ideally, the distribution of satellites in it is such that the number of satellites in each orbit plane is twice the number of orbit planes.

2 The number and inclination of the orbit planes in the optimum inclined network designed to satisfy a particular coverage requirement vary discontinuously with system altitude.

3 To determine the properties of the optimum satellite network satisfying a certain coverage requirement, it is generally necessary to compare the  $N$  vs.  $h$  performance curves obtained separately for the polar, equatorial and inclined networks. From such performance curves, preferred orbital inclinations and distributions can be chosen for satellite networks at pre-assigned altitudes.

### Acknowledgment

The writer wishes to acknowledge the support of Douglas Aircraft Co., Santa Monica, Calif., where the early stages of the study were done. Appreciation is also extended to Dr. A. B. Greenberg and Mr. U. E. Lapins, both now with Aerospace Corp., for their many helpful suggestions and criticisms.

### Nomenclature

$h$	= altitude of each satellite in the network
$i$	= inclination of each orbit plane to the Equator
$n_1$	= number of orbit planes in the network
$n_2$	= number of satellites in each orbit plane
$N$	= total number of satellites in the network
$R_E$	= radius of Earth (= 3440 nautical miles) or other central body
$S$	= slant range (Fig. 2)
$\theta$	= central angle subtended by the observed great circle half-arc (Fig. 1)
$\lambda$	= minimum latitude to be observed continuously
$\mu$	= maximum latitude to be observed continuously
$\sigma$	= minimum angle of visibility (Fig. 1)
$\psi$	= great circle arc half-width of observed swath

### References

- 1 Clarke, A. C., "The Making of a Moon," Harper and Brothers, N. Y., 1958, revised ed., chaps. 8 and 15.
- 2 Select Committee on Astronautics and Space Exploration, "The Next Ten Years in Space 1959-1969," 86th Congress, 1st Session, House Document No. 115; U.S. Government Printing Office, Wash., D. C., 1959, pp. 10-13.
- 3 Pierce, J. R. and Kompfner, R., "Transoceanic Communication by Means of Satellites," Proc. IRE, vol. 47, March 1959, pp. 372-380.
- 4 Vargo, L. G., "Orbital Patterns for Satellite Systems," AAS preprint 60-48, Sixth National Annual Meeting, Jan. 18-21, 1960, N. Y.
- 5 King-Hele, D. G., "The Effect of the Earth's Oblateness on the Orbit of a Near Satellite," Proc. Royal Society of London, Series A, vol. 247, Oct. 1958, pp. 49-72.

# Shock Wave and Flow Field Development in Hypersonic Re-Entry<sup>1</sup>

RONALD F. PROBSTEIN<sup>2</sup>

Brown University  
Providence, R. I.

A study is made of when and how a shock wave and continuum-type flow field develop in the nose region of a highly cooled blunt body re-entering the atmosphere at hypersonic speed and in a free molecular flow regime. The various types of flow regimes encountered down to low altitude conditions are delineated, and the nature of the flow field and behavior of some of the aerodynamic characteristics are discussed. It is shown that for a highly cooled body, free molecule flow conditions occur at a higher altitude than previously indicated. Based on available evidence, it is suggested that kinetic theory solutions, which are essentially modified free molecule results, along with the Navier-Stokes equations with no surface slip, serve to define all of the flow regimes except for a narrow transitional layer regime which has a height of less than one factor of 10 in free stream density change. It is also suggested that the appearance of a definable shock wave occurs very rapidly in terms of density change near the beginning of the transitional layer regime, and that its location, as in continuum flow, is governed principally by the body geometry, whereas its thickness is determined by a local mean free path.

IN THIS paper a picture will be presented of when and how a shock wave and continuum-type flow field develop in the nose region of a blunt body which re-enters the atmosphere at hypersonic speed and at an altitude sufficiently high that the flow may at first be considered free molecular. For such a re-entering vehicle, the various types of flow regimes encountered down to low altitude conditions shall be delineated, and for each regime the nature of the flow field as well as the behavior of some of the more important aerodynamic characteristics shall be indicated. The basis of a theoretical treatment for calculating the flow characteristics in each regime, with the exception of a narrow transitional layer regime, will be outlined. Here, by narrow is meant less than one factor of 10 in free stream density change. In the higher altitude regions, the kinetic theory of gases will be used as the basis of the analysis, whereas in the lower altitude regions continuum theory will be applied and the full Navier-Stokes equations including the linear Fourier heat conduction law will be used.

Our considerations will, in general, be restricted to the stagnation region of a body which is roughly spherical in character. In addition, the gas shall be considered a neutral perfect one. When applying the kinetic theory, the gas is taken to be monatomic, although any conclusions from such an analysis probably will also hold for gases of more complicated structure, provided relaxation phenomena in the transfer of energy to or from a vibrational degree of freedom, or to or from energy of dissociation, are not too important. In this same context, relaxation phenomenon shall not be considered

when using continuum theory and appropriate "average" equilibrium values for defining the state of the gas shall be used. Finally, although the importance of knowing the re-emission process at the surface in a rarefied gas flow is recognized, for lack of more detailed information at present, average accommodation coefficients which measure the extent to which the mean energy and momentum of the molecules are accommodated to the surface shall be used, in common with other works on the subject. It is clear that not all of the restrictions mentioned are essential and their removal would only increase the technical complexity of the calculation.

On the basis of these assumptions, it will be shown that for a highly cooled body the onset of free molecule conditions occurs at a higher altitude than suggested in many classical works on this subject, e.g., Tsien (1)<sup>3</sup> and Schaaf and Chambre (2). More important, however, it appears that kinetic theory solutions which result in slightly modified free molecule results ("first collision" type theories) along with solutions of the Navier-Stokes equations with no slip at the surface (at least for a cold body) serve to define all of the flow regimes except for a narrow transitional layer regime which has a height of less than one factor of 10 in free stream density change. (The available evidence for this will be presented later.) Connected with this feature is the fact that the appearance of a definable shock wave occurs very rapidly (in terms of density increase) near the beginning of the transitional layer regime. From these considerations, it seems likely that for engineering purposes it may be possible to calculate the flow field behavior and aerodynamic characteristics in the nose region of a blunt vehicle re-entering the atmosphere at hypersonic speed.

## Free Molecule Regime

Above about 90- to 100-miles altitude, when a vehicle re-enters the atmosphere, the vehicle can be shown to be in what is usually termed the free molecule flow regime. The characteristic of this regime is that the gas is sufficiently rarefied so

Presented at the ARS Semi-Annual Meeting, Los Angeles, Calif., May 9-12, 1960.

<sup>1</sup> The present study has been supported by the Fluid Dynamics Research Branch of the Aeronautical Research Laboratory, Wright Air Development Division, USAF, under Contract no. AF 33(616)-5442. The author wishes to thank Prof. Michal Lunc and Mr. Jan Lubonski of the Polish Academy of Sciences and Brown University for their many suggestions and for the assistance given through long weeks of discussion. The author would also like to thank Prof. Lester Lees of the California Institute of Technology for helpful suggestions.

<sup>2</sup> Professor of Engineering.

<sup>3</sup> Numbers in parentheses indicate References at end of paper.



that the mean free path is everywhere much greater than a characteristic body dimension, so that collisions between the molecules and the boundary dominate over collisions between the molecules themselves.

In order to define a free molecule flow in terms of mean free path, we must first properly define what we mean by mean free path. The mean free path, it is to be recalled, is the mean distance (in a statistical sense) traveled by a molecule between successive collisions in a given time. Unlike the collision frequency, which is the average number of collisions undergone by each molecule per unit time, the mean free path is dependent upon the choice of coordinate system. In addition, the mean free path is inversely proportional to the density, so that it will vary from point to point in the flow field except when the density is uniform. Therefore, when using the mean free path as a characteristic length in a field of nonuniform density, one must exercise extreme caution.

In this paper the body shall be considered moving through a gas with a macroscopic velocity  $U$ , which is large (not infinitely so) in comparison with the mean random velocity of the molecules in the free stream. In addition, the body shall also be considered highly cooled, so that  $U$  is also large in comparison with the mean velocity of the molecules which are emitted diffusely from the surface. Such a flow has been termed hyperthermal by Schamberg (3).

For a rarefied gas flow, one may think of the gas as composed of essentially two types of molecules, the incident molecules and those molecules emitted from the body surface. To illustrate the mean free path computation, let us calculate for rigid elastic spherical molecules the mean free path of the emitted molecules, denoted by the subscript  $e$ , with respect to the incident molecules, denoted by the subscript  $i$ . With a coordinate system fixed in the body, the average number of collisions per unit time of an  $e$  molecule passing through a cloud of  $i$  molecules will be equal to the density of  $i$  molecules per unit volume  $n_i$ , multiplied by their speed relative to the  $e$  molecule times the effective mutual collision cross section  $\pi\sigma^2$ . Within the hyperthermal assumption, the relative speed will be approximately  $U$ , so that the collision frequency is given by  $\nu_{ei} = Un_i\pi\sigma^2$ . The mean free path will then be the mean speed of the  $e$  molecule  $\bar{c}_e$  divided by the collision frequency. With  $\lambda$  denoting the mean free path in this coordinate system, this gives

$$\lambda_{ei} = \bar{c}_e / n_i U \pi \sigma^2 \quad [1]$$

where

$$\begin{aligned} \bar{c}_e &= (8kT_e/\pi m)^{1/2} \\ k &= \text{Boltzmann constant} \\ m &= \text{mass of one molecule} \end{aligned}$$

The corresponding mean free path can also be calculated relative to a coordinate system fixed in the gas. Since the collision frequency is invariant with coordinate transformation, it will remain unchanged, but the average velocity of the  $e$  molecule will now be approximately equal to the velocity of the body  $U$ . With  $\lambda'$  denoting the mean free path in this coordinate system, we then have

$$\lambda'_{ei} = 1/n_i \pi \sigma^2 \quad [2]$$

These calculations can also be carried out for the other three possible mean free paths  $ii$ ,  $ie$  and  $ee$ . The results are given in Table 1.

The appearance of the  $\sqrt{2}$  factor in  $\lambda'_{ii}$  and  $\lambda_{ee}$  is a result of the usual more exact mean free path calculation for a uniform gas at rest [see, e.g., Chapman and Cowling (4)], where it is not necessary to introduce the approximation of hyperthermal flow as in our derivation. It is to be noted that when  $n_i = n_\infty$  that  $\lambda'_{ii}$  is the conventional mean free path found in a table of atmospheric properties. In the remainder of the paper, this mean free path shall be referred to as  $\lambda_\infty$ , that is

$$\lambda'_{ii} = \lambda_\infty \quad \text{for} \quad n_i = n_\infty \quad [3]$$

**Table 1 Mean free paths for highly cooled body and hypersonic speed**

Coordinate system fixed in gas	Coordinate system fixed in body
$\lambda'_{ii} = 1/\sqrt{2} n_i \pi \sigma^2$	$\lambda_{ii} = U/n_i \bar{c}_i \pi \sigma^2$
$\lambda'_{ei} = 1/n_i \pi \sigma^2$	$\lambda_{ei} = \bar{c}_e/n_i U \pi \sigma^2$
$\lambda'_{ie} = \bar{c}_i/n_e U \pi \sigma^2$	$\lambda_{ie} = 1/n_e \pi \sigma^2$
$\lambda'_{ee} = U/n_e \bar{c}_e \pi \sigma^2$	$\lambda_{ee} = 1/\sqrt{2} n_e \pi \sigma^2$

From the preceding considerations, it is clear that the criterion for free molecule flow, that the mean free path  $\lambda_\infty$  be large compared to a characteristic body dimension, as used for example in (1), is irrelevant. On the other hand, bearing in mind that both the densities  $n_i$  and  $n_e$  depend on distance from the body (except in a free molecule flow where  $n_i$  is constant and equal to  $n_\infty$ ), it must be asked which is the smallest mean free path in the flow field, and then require that this quantity must be large in comparison with the appropriate characteristic flow length. Since, in general, the body will be treated as at rest with the gas flowing past it, the appropriate mean free path will be considered relative to a frame of reference fixed in the body.

For a hypersonic free molecule flow with a cold body, the following relation holds on the surface

$$n_\infty U = (1/4) n_b \bar{c}_b \quad [4]$$

[See, e.g., Hayes and Probstein (5).] However, it would be incorrect to conclude from this relation that  $\lambda_{ei}$ ,  $\lambda_{ie}$  and  $\lambda_{ee}$  were all of the same order, since, as will be shown later, near the surface of the body the density of  $e$  molecules drop off very rapidly even in a free molecule flow (at least for a sphere); whereas for sufficiently rarefied flow conditions  $n_i$  remains roughly constant and equal to  $n_\infty$ . We may conclude then that the "critical" mean free path is  $\lambda_{ei}$ , which is the mean free path of the emitted molecules with respect to the incident molecules.

From the relations given in Table 1

$$\lambda_{ei} = \sqrt{2}(\bar{c}_e/U)\lambda'_{ei} \quad [5]$$

Now if  $n_i = n_\infty$  and the emitted molecules have a mean density corresponding to the surface temperature ( $T_s = T_b$ ), we shall denote  $\lambda_{ei}$  by  $\lambda_\sigma$ , that is

$$\lambda_{ei} = \lambda_\sigma \quad \text{for} \quad n_i = n_\infty \quad [6]$$

In this case, we then write

$$\lambda_\sigma = (4/\sqrt{\pi\gamma})(T_b/T_\infty)^{1/2}(\lambda_\infty/M_\infty) \quad [7]$$

It would appear from the foregoing that the more appropriate requirement for a free molecule flow is that the mean free path  $\lambda_\sigma$  be large in comparison with a characteristic flow length. This length is chosen to be the radius of a sphere  $R_b$ , since this is the principal geometrical configuration to be considered. From Equation [7], the criterion for free molecule flow will then be

$$\lambda_\sigma/R_b \gg (\sqrt{\pi\gamma}/4)(T_\infty/T_b)^{1/2}M_\infty \quad [8]$$

In Fig. 1 this free molecule "limit" is shown for a sphere of radius  $R_b = 1$  ft and for a surface temperature equal to the free stream temperature. This limit has been calculated assuming that by "large in comparison with one" is meant 10. With  $\gamma = 1.4$ , the limit is then

$$\lambda_\sigma(\text{ft}) = 5.24M_\infty \quad [9]$$

For a given Mach number  $\lambda_\infty$  is known, and the corresponding altitude, free stream density and free stream speed of sound are determined from the ICAO standard atmosphere tables of

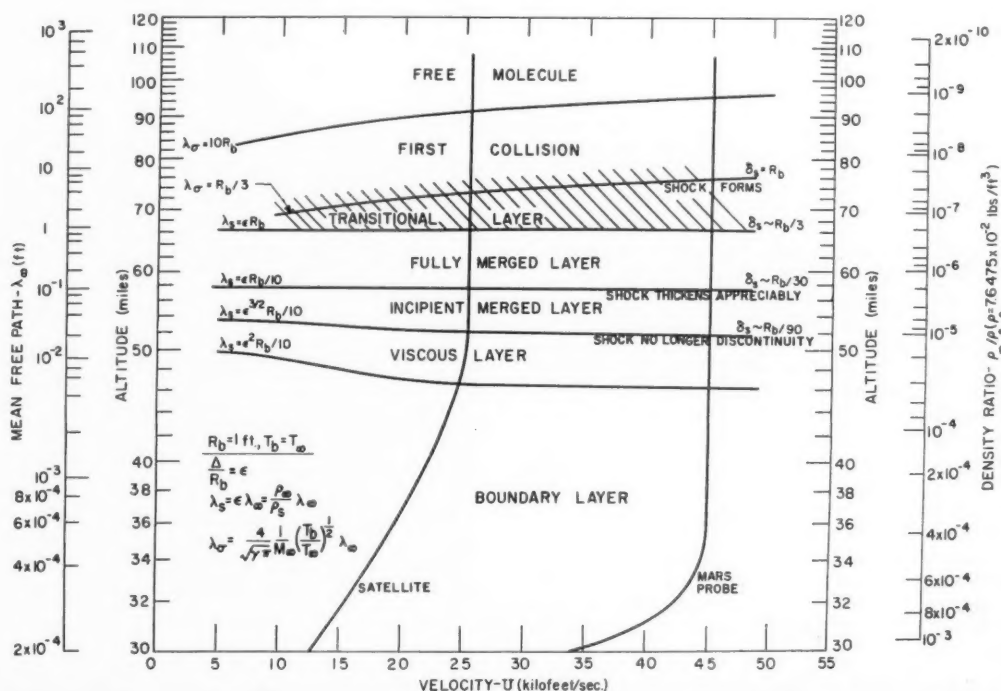


The calculation of any free molecule flow depends of course upon the surface interaction model which is chosen. Here and in what follows, fully diffuse reflection with the molecules completely accommodated to the surface conditions is assumed. That is, it is assumed that the molecules are emitted with a Maxwellian distribution of thermal velocities corresponding to the surface temperature, and in a random direc-

For a hypersonic flow where the macroscopic velocity  $U$  is large in comparison with both the mean random velocity of the free stream molecules and the emitted particles, the number of incident molecules per unit area per second striking the surface, the surface pressure, the surface shear and heat transfer rate per unit area per second on a convex body can be shown to be given, respectively, by [see, e.g., (8)]

$$\dot{q} = \frac{1}{2}\rho_{\infty}U^3 \cos \theta \quad [10d]$$

Also of interest here is the character of the flow field for such a free molecule flow. To illustrate the behavior of one flow field parameter, we shall calculate the density variation along the axis in front of a sphere. According to the free molecule concept, the number of molecules per unit volume will be the sum of the incident molecules  $n_i$  and the emitted molecules  $n_e$ . As mentioned previously, for a free molecule flow the density of incident particles  $n_i$  is equal to  $n_\infty$  and is constant every-



FEBRUARY 1961

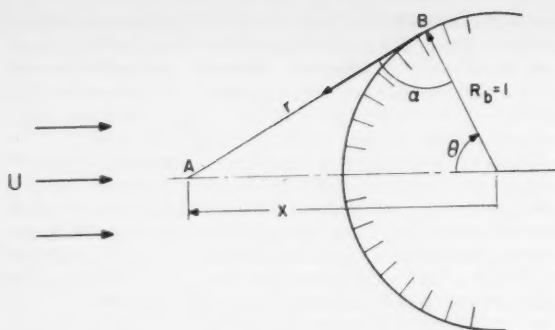


Fig. 2 Geometry for calculation of emitted molecular density distribution along axis of a sphere in free molecule flow

where in the flow field. At the surface of the body  $n_s \equiv n_b$  and is related to  $n_\infty$  by Equation [4].

We may readily derive an expression for the density along the axis as a function of distance in front of the sphere by referring to Fig. 2. It is to be recalled that the molecules leaving the sphere will travel in straight lines, and their directions according to the cosine law will be proportional to  $\cos \alpha$ . Furthermore, the number striking the surface as given by Equation [10a] must equal the number emitted. In addition, from Equation [4] it can be seen that the emitted flux per unit solid angle subtended by the sphere must be proportional to  $n_b \epsilon_b / 4$ . The contribution to the density of emitted molecules at a point on the axis from an element of the sphere surface will, therefore, be

$$dn_e(x) = (4n_\infty U / \epsilon_b) \cos \alpha \cos \theta (\sin \theta / r^2) dr \quad [11]$$

Here the radial distance along the line of emission  $r$  has been made dimensionless with respect to a unit body radius. To find the total number of emitted molecules at any point  $x$ , we must integrate Equation [11] over all ray angles  $\theta$ , from  $\theta = 0$  to  $\theta = \cos^{-1} 1/x$ ; here  $x$  has also been made dimensionless with respect to a unit body radius  $R_b$ . We may then write the following integral for  $n_e(x)$

$$n_e(x) = \frac{4n_\infty U}{\epsilon_b} \int_0^{\cos^{-1} 1/x} \frac{(x \cos \theta - 1) \cos \theta \sin \theta}{(x^2 - 2x \cos \theta + 1)^{3/2}} d\theta \quad [12]$$

As may be deduced from Fig. 2, we have used the fact that  $\cos \alpha = (x^2 - 1 - r^2) / 2r$ , where  $r^2 = x^2 - 2x \cos \theta + 1$ . Expression [12] can be integrated with the following result

$$n_e(x) = (4/3)(n_\infty U / \epsilon_b x^2) [(2x^3 + 1) - (2x^2 + 1)(x^2 - 1)^{1/2}] \quad [13]$$

with  $x$  taking on values from 1 to  $\infty$ . Again, the total density at any point  $x$  will be given by the sum  $n_\infty + n_e$ .

The behavior of Equation [13] is rather interesting, since it shows, among other things, that the density falls off smoothly but rapidly from the body, with the density of the emitted molecules approaching zero at infinity. From Equation [13] it can be shown that at a distance of about one sphere radius, the density has dropped to about 10 per cent of its value at the body. The geometrical decay factor in this relation can be very closely represented by  $1 - \sqrt{1 - (1/x^2)}$ , which is simply the solid angle subtended by the sphere. In agreement with Equation [13], this solid angle factor decays as  $x^{-2}$  for large  $x$ . Nowhere along the stagnation line are any inflection points present to indicate the appearance of even a weak discontinuity. However at the surface, a singularity in the density gradient is present. This is seen by differentiating Equation [13] and taking the limit as  $x \rightarrow 1$ , which leads to the condition that

$$\lim_{x \rightarrow 1} \frac{dn_e}{dx} \rightarrow \frac{-\text{constant}}{\sqrt{2(x-1)}} \rightarrow -\infty$$

The cusp-like singularity found is associated with the molecules of glancing incidence and is a direct result of the geometry of the problem. It will be present for all convex (and concave) configurations and can be avoided only in the case of a plate normal to the stream.

It is likely, though not as yet definitively established, that this singularity is only associated with free molecule flow and will disappear for all finite mean free paths. We may therefore say that, in this sense, free molecule flow is a singular solution valid only for a mean free path which is everywhere infinite. The appearance of this infinite density gradient at the surface should not affect the mean surface characteristics, such as pressure, shear and heat transfer. It seems likely, however, that a clear idea as to the nature of this free molecular singularity would contribute to a better understanding of near free molecule type solutions.

### Near Free Molecule Regime

A variety of methods employing kinetic theory treatments have been developed in an effort to calculate the aerodynamic characteristics and flow field for a body flying in near free molecular conditions. For a discussion and analysis of the various methods, the reader is referred to the paper of Willis (9). Because of the highly nonlinear nature of the problem, many of the methods have met with only limited success. The most successful of them have been the so-called first collision schemes, where only a certain class of intermolecular collisions are considered, principally the collisions between a molecule coming from the body without a prior collision and an incident molecule. An example of such a treatment may be found in Willis' work (9).

In Willis' method, the Boltzmann integro-differential equation is formally integrated into a pure integral equation. The distribution function is then solved for by an iterative scheme starting with the free molecule solution and neglecting certain classes of collisions. In addition, the collision integrals are simplified by employing a modified Krook (10) model appropriate to the nonlinear problem. Willis carried out a first iterate solution for the case of rarefied flow past a sphere. His results for the drag and heat transfer for pseudo-hard sphere molecules may be expressed as

$$C_D / C_{DFM} = 1 - (R_b / \lambda_\sigma) [0.835 + 6.4(\epsilon_b / U)] \quad [14]$$

$$q / q_{FM} = 1 - (R_b / \lambda_\sigma) [0.53 + 3.2(\epsilon_b / U)] \quad [15]$$

Here the results are written in terms of the notation used in this paper. Willis points out that these analytic expressions are only valid for  $U / \epsilon_b > 2$  (approximately). In agreement with other works, both the drag and heat transfer are seen to decrease below the free molecule value with decreasing mean free path. We may expect such first collision type results as given here to hold down to values of  $R_b / \lambda_\sigma$  of about  $\frac{1}{2}$  or  $\frac{1}{3}$ . Indeed, it is clear from Equations [14 and 15] that for large enough values of  $R_b / \lambda_\sigma$ , the drag and heat transfer become negative.

Unfortunately the flow field itself was not calculated to this degree of approximation. However, along the stagnation line we can estimate the density behavior which corresponds roughly to the first collision regime by the following simple iterative scheme. Let us consider first the density of the incident molecules which, according to the free molecule solution, will remain unchanged everywhere in the flow field. A first-order correction to this constant density may be made by recognizing that, for a non free molecular flow, the probability of an  $i$  molecule surviving unhit to a given distance without a collision with an emitted  $e$  molecule will be

$$\exp \left[ - \int \frac{R_b}{\lambda_{ie}} dx \right] \quad [16]$$

Now the mean free path  $\lambda_{ie}$  is given in Table 1 and is equal to  $(n_i \pi \sigma^2)^{-1}$ , where the reader is reminded that  $n_e$  is a func-

tion of  $x$ . A first correction to  $n_i$  can be obtained by using the value of  $n_e(x)$  corresponding to free molecule flow. From Equations [16 and 13] this gives

$$n_i^{(1)}(x) = n_\infty \exp \left\{ -\frac{4}{3} \frac{R_b}{\lambda_\sigma} \times \int_\infty^x \left[ \frac{(2x^3 + 1)}{x^2} - \frac{(2x^2 + 1)(x^2 - 1)^{1/2}}{x^2} \right] dx \right\} \quad [17]$$

It is of interest to the classical aerodynamicist to note that the integral expression is of the form  $\int f dx$ , which is exactly the Howarth-Dorodnitsyn variable used in boundary layer theory. It would seem that this variable again plays the same "stretching" role as it does in classical fluid mechanics. The integration of Equation [17] can be readily carried out, and the result is

$$n_i^{(1)}(x) = n_\infty \exp \left\{ \frac{4}{3} (R_b/\lambda_\sigma) [1/x + 3/2 - x^2 + (x^2 - 1)^{3/2}/x] \right\} \quad [18]$$

By a similar argument we can now correct the free molecule expression for  $n_e^{(0)}(x)$  and obtain  $n_e^{(1)}(x)$ . Such a correction would give a faster decay in the density of molecules emitted from the body. The new decay curve would be a smooth function lying between that of Equation [13] and Equation [13] multiplied by  $\exp [-R_b/\lambda_\sigma]$ . However, for purposes of the present discussion, this additional calculation does not seem warranted.

The important point to be observed is that to this first approximation the total density, which is the sum of the densities given by Equations [18 and 13], is a smoothly decaying function for which there is no indication of the appearance of a shock-like structure in the flow field. Modifying  $n_e^{(0)}(x)$  as indicated to obtain  $n_e^{(1)}(x)$  would not seem to alter this behavior. However, there is a boundary layer type of structure near the surface of the body which is manifested in this approximation and which can be distinguished even in the free molecule solution.

Our results lead us to question whether, in the stagnation region, the conjecture of Grad (11) that a shock-like structure manifests itself in a near free molecule condition is valid. His reasoning was based partly on the idea that the significant characteristic length would be a distance from the body of the order of the mean free path  $\lambda_i$ , which was taken constant and equal to  $\lambda_\sigma$ . At this point in the flow, it was assumed that collisions to form a shock-like structure would occur, since the emitted stream would encounter the incident stream here and both would be altered. However, as we have shown, one must interpret this length with great care, since it cannot be taken constant in a field of nonuniform density. Indeed, we recognize that the collision frequency will have its maximum value at the surface of the body and not in the flow field.

Based on the results given previously, we put forward the alternative hypothesis that for  $\lambda_\sigma > R_b$  (approximately), first collision solutions can be used to define the flow field structure and aerodynamic characteristics. Furthermore, the flow field, at least in the region of the stagnation line ahead of a sphere, has a smooth uniform behavior with no appearance of a shock-like structure.

In order to answer the question as to when and where the shock wave forms, we make the following assumptions. First, that its location will be governed principally by the geometry of the problem (e.g., by the fact that the body is a sphere of radius  $R_b$ ). As we shall show, this is a reasonable assumption which is true in continuum flow, and which, as we shall also show, holds in a near continuum flow. Second, we will assume that when there is a shock-like structure, its thickness will be of the order of several mean free paths behind the shock. In our notation this appropriate mean free path would be  $\lambda_\sigma$ . This latter assumption is a fairly well-verified result of kinetic theory [see, e.g., Grad (12)]. In other words, the location of the shock will be governed principally by the geometry and will not be too significantly altered by the mean free path, al-

though its appearance in the flow and its thickness will be determined by the mean free path.

According to one of our assumptions, the shock thickness is given approximately by the relation

$$\delta_s = 3 \lambda_\sigma \quad [19]$$

Now when can we say we have what might be called a shock wave? Here, we shall arbitrarily define a shock-like structure as being present when flow changes brought about by a finite  $\delta_s$  occur over a distance in the flow field of the order of the radius of the sphere. Hence, a shock-like structure occurs for

$$\delta_s = R_b \quad [20]$$

Combining Equations [19 and 20] we see that a shock will begin to form when

$$\lambda_\sigma = R_b/3 \quad [21]$$

But from our previous results, this is just somewhat below the limit of validity of first collision theory. In other words, there must be a highly nonlinear "cascading" effect in the flow field when  $\lambda_\sigma$  gets to be of the order of  $R_b$  or somewhat less. That is, when the density of the emitted molecules reaches a critical value at a point in the field which is less than, or of the order of, one radius ahead of the sphere, the collision frequency between the incident and emitted molecules increases very fast locally.

As Prof. Lunc has pointed out to the author, a shock wave represents a strong entropy increase, and with this increase must be associated a large increase in the randomization of the molecules. Therefore, the picture of the incident molecules interacting only in a perturbed sense with the emitted molecules must be destroyed when a shock forms, and the first collision type of picture breaks down. Although the present picture is self-consistent, we emphasize again that it is only conjectural, and that it will require much more detailed analysis for its proof than has been given.

In Fig. 1 is drawn the curve corresponding to Equation [20]. This curve must roughly represent the point at which a shock-like structure has formed, and must lie somewhat below the limit of the first collision types of theories. What we shall attempt to show in the succeeding sections is that, within a very narrow transitional layer in terms of density change (or change in mean free path), a definite shock is introduced into the flow field at a position governed by the body geometry. Beyond this transitional regime, the continuum Navier-Stokes equations apply and can be used to describe the flow field and aerodynamic characteristics from there on.

## Continuum Flow Regimes

When considering the nose region of a blunt axisymmetric body such as a sphere, there are essentially two fundamental classes of problems in the continuum region (13-15): A viscous layer class and a merged layer class, the latter corresponding to a larger degree of rarefaction. For the viscous layer class there is a thin shock wave, but the shock layer region between the shock and the body is fully viscous, although the viscous stresses and conductive heat transfer are small at the shock boundary. Here, the use of the Navier-Stokes equations with outer boundary conditions given by the Hugoniot relations is justified. For the merged layer class, the shock wave is no longer thin, and the Navier-Stokes equations can be used to give a solution which includes the shock structure and has free stream conditions as outer boundary conditions. A schematic picture of these two classes of problems is shown in Fig. 3.

In such an analysis, a main point is the degree of rarefaction to which one may justifiably apply the Navier-Stokes equations. To assess this limit, we assume that the local mean free path must everywhere be small compared to the characteristic length of interest for the Navier-Stokes equations (continuum



theory) to be valid. Therefore, in the nose region of a blunt body the basic criterion for continuum flow is taken to be that the mean free path behind the shock<sup>4</sup>  $\lambda$ , be small compared to the shock layer thickness  $\Delta$  (see Fig. 3). That is,

$$\lambda_s/\Delta \ll 1 \quad [22]$$

Here, we recognize that the shock wave itself may not be too sharply defined.

As noted previously, in a continuum flow past a sphere the shock detachment distance is dependent primarily on the geometry. This distance is given approximately by the relation

$$\Delta/R_b = \epsilon \equiv \rho_\infty/\rho_s \quad [23]$$

with  $\epsilon$  the density ratio across the shock.

Now in (13-15) it was shown that for Reynolds numbers lower than those for which boundary layer theory is valid, the various regimes could be classified as follows in the direction of decreasing Reynolds numbers: A vorticity interaction regime where the vorticity in the inviscid part of the shock layer is sufficiently high so that, although boundary layer concepts can be used, the boundary conditions must be modified; a viscous layer regime where the shock layer is fully viscous but the shock wave is still discontinuous; an incipient merged layer regime where the Navier-Stokes equations are still applicable and the shock wave is thin but not discontinuous; and a fully merged layer regime where the

<sup>4</sup> Here  $\lambda_s$  is defined in the same coordinate system as  $\lambda_\infty$ , and as with  $\lambda_\infty$ , we drop the prime notation.

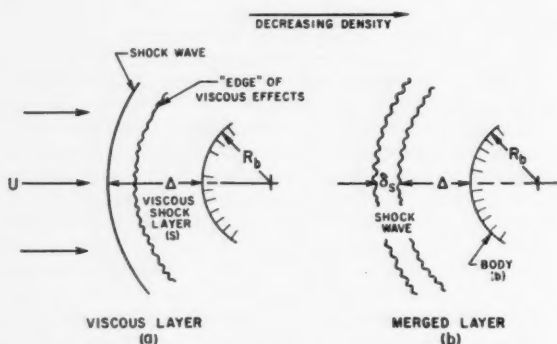


Fig. 3 Sketch of stagnation region flow field in Navier-Stokes regimes

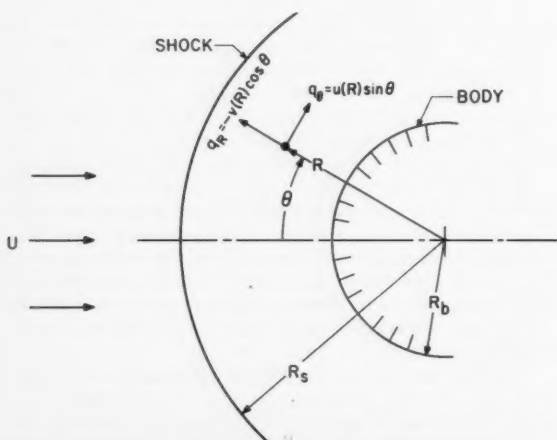


Fig. 4 Coordinate system for sphere in Navier-Stokes analysis

shock layer is in an almost continuum state and the shock wave is beginning to have a thickness approaching that of the body radius but is still smaller than it.

It was further shown in (13-15) that including the incipient merged layer regime, condition [22] was met and the Navier-Stokes equations could be justifiably used. Based on available evidence, it was also suggested that the Navier-Stokes equations could be used for mean aerodynamic characteristics in the fully merged layer regime as well. Furthermore, it was shown in (14) that, up to and including the fully merged layer regime, slip and temperature jump will not be important in affecting the mean flow variables if the body is highly cooled, although as phenomena they could be present in the more rarefied part of the Navier-Stokes continuum regions.

Limits for the various regimes were estimated using hypersonic approximations and the condition that across the shock wave

$$\rho_\infty \lambda_\infty = \rho_s \lambda_s \quad [24]$$

As noted in footnote 4,  $\lambda_s$  is, of course, defined in the same coordinate system as  $\lambda_\infty$ . This relation assumes that the viscosity is proportional to the square root of the absolute temperature, and corresponds to the rigid sphere kinetic model adopted previously. The limits obtained were:

Vorticity interaction regime (modified boundary layer)

$$\lambda_s/R_b \ll \epsilon^2 \quad [25]$$

Viscous layer regime

$$\lambda_s/R_b \ll \epsilon^{3/2} \quad [26]$$

Incipient merged layer regime

$$\lambda_s/R_b \ll \epsilon \quad [27]$$

Fully merged layer regime

$$\lambda_s/R_b < \epsilon \quad [28]$$

Corresponding to each of these regimes we may also estimate the thickness of the shock wave in the stagnation region using the one-dimensional Navier-Stokes shock structure result. With the hypersonic approximations, the viscosity  $\mu \propto T^{1/2}$  and the Prandtl number  $Pr = \frac{3}{4}$ , the expression for the shock thickness may be written (15)

$$\delta_s = (U - v_s)/(dv/dR)_{max} \quad [29a]$$

where

$$(dv/dR)_{max} = (3/4)[Re/(1 + \epsilon)](U/R_b)[1 - 2\sqrt{\epsilon}] \quad [29b]$$

where

- $s$  = values of the quantities behind the shock wave
- $v$  = normal velocity component positive in the direction of negative  $R$  (see Fig. 4)
- $Re$  = Reynolds number

$$Re = \rho_\infty U R_b / \mu_s \quad [30]$$

Here, the viscosity  $\mu_s$  is based on temperature conditions behind the shock. The limiting value of the density ratio  $\epsilon$  for a strong shock wave is used here and is given by

$$\epsilon = (\gamma_s - 1)/(\gamma_s + 1) \quad [31]$$

with  $\gamma_s$  the isentropic exponent behind the shock wave. Using the relations

$$\begin{aligned} \mu_s/\mu_\infty &= (T_s/T_\infty)^{1/2} = [\epsilon/(1 - \epsilon)]^{1/2} M_\infty \\ \mu &= (1/2)\rho\epsilon\lambda \end{aligned}$$

we may rewrite the shock thickness relation as

$$\delta_s/R_b = \frac{4}{3} \sqrt{\frac{2}{\pi\gamma}} \frac{1}{\epsilon(1 - 2\sqrt{\epsilon})} \left( \frac{\epsilon}{1 - \epsilon} \right)^{1/2} \frac{\lambda_s}{R_b} \quad [32]$$



In deriving this equation,  $v_\infty/U$  has been replaced by  $\epsilon$ , and  $\epsilon^2$  dropped in comparison with one. Note that  $\gamma$  refers to the free stream isentropic exponent. When using Equation [32] the appropriate value of  $\epsilon$  must be inserted, since as shown in (15), beginning with the incipient merged layer and with decreasing density (i.e., increasing altitude) the effective  $\epsilon$  for a highly cooled body drops below its high Reynolds number value.

In Fig. 1 are indicated the limits of the various regimes as given by Equations [25 to 28]. In drawing the limits for the beginning of the viscous layer regime and incipient merged layer regime, a value of  $\epsilon$  which varies from about  $\frac{1}{10}$  at 5000 fps to about  $\frac{1}{20}$  at 45,000 fps has been used. On each of these curves, is given an estimate of the shock thickness as computed from Equation [32]. We note only that an average value of  $\epsilon$  of about  $\frac{1}{15}$  was used for computing the shock thickness for the beginning of the incipient merged layer regime, whereas a value of  $\frac{1}{20}$  was used for the beginning and end of the fully merged layer regime. This is consistent with the decrease in  $\epsilon$  indicated by the calculations for a highly cooled body in (15).

For reference purposes we have shown in Fig. 1 a typical trajectory for a satellite and Mars probe re-entry. The most important feature indicated in this figure is that, except for a narrow transitional layer regime, the flow field in the nose region of a blunt body can be handled either by the Navier-Stokes equations with no slip in the higher density regimes, or by a free molecule or first collision type approach in the lower density regimes. Furthermore, it can be seen that the Navier-Stokes shock thickness estimates are consistent with the previous estimates for the altitude where what we call a definable shock will form. However, we always bear in mind that what we are calling a shock is somewhat arbitrarily defined, since, of course, in reality the field is a continuous one. Nevertheless, these results offer further support to the idea that the development of the shock wave must be cascading in nature.

The conjecture made previously that the location of the shock will be governed principally by the geometry with its location given approximately by Equation [23] is also consistent with our picture. It is to be noted, as stated in (15), that with a thin shock and high cooling, the shock wave will move in somewhat toward the body with decreasing Reynolds number. Of course, with a still further decrease in Reynolds number the shock will tend to thicken at the same time. This movement of what is essentially the back of the shock toward the body has been confirmed by the calculations of Ho and Probstein (16) and Herring (17) in the region corresponding

to the viscous layer regime, and by the constant density incipient merged layer calculations of (15) where the shock can no longer be considered discontinuous.

Until recently only constant density calculations were available for the Navier-Stokes region; in (16), however, variable density stagnation point solutions have been obtained for the viscous layer region. This was done using the Navier-Stokes equations in ordinary differential form with the Hugoniot shock conditions as outer boundary conditions. The reduction of the Navier-Stokes equations to ordinary differential equations was carried out by assuming essentially a locally spherically symmetric solution of a type first given in (13). It consists of assuming, in the neighborhood of the stagnation point, a solution for the various flow quantities (see Fig. 4) of the form

$$\rho = \rho_0(R) \quad [33a]$$

$$q_\theta = u(R) \sin \theta \quad [33b]$$

$$q_R = -v(R) \cos \theta \quad [33c]$$

$$\mu = \mu_0(R) \cos \theta \quad [33d]$$

$$p = p_0(R) \cos^2 \theta + p_2(R) \sin^2 \theta \quad [33e]$$

$$h = h_0(R) \cos^2 \theta \quad [33f]$$

Substitution of these assumed forms into the Navier-Stokes equations reduces them to a system of ordinary simultaneous differential equations which can be integrated numerically.

In Figs. 5 and 6 are shown, respectively, the shear and heat transfer results in the stagnation region of a sphere for a wall cooling ratio of  $h_b/\frac{1}{2}U^2 = 0.05$  and density ratio  $\epsilon = 0.1$ . Also shown for reference in these figures are the free molecule results given by Equations [10c and 10d], as well as the corresponding boundary layer and vorticity interaction results for compressible flow. The boundary layer shear and heat transfer results on a sphere are given by

$$\frac{\tau Re}{\tau_{FM}} = \sqrt{\frac{2Re}{\epsilon}} \left[ \frac{R_b}{U} \left( \frac{du_\delta}{dx} \right)_{stag} \right]^{1/2} \left( \frac{\rho_b \mu_b}{\rho_s \mu_s} \right)^{1/2} f''_b \quad [34]$$

$$\frac{q Re}{q_{FM}} = \frac{1}{Pr} \sqrt{\frac{2Re}{\epsilon}} \left[ \frac{R_b}{U} \left( \frac{du_\delta}{dx} \right)_{stag} \right]^{1/2} \left( \frac{\rho_b \mu_b}{\rho_s \mu_s} \right)^{1/2} g'_b \quad [35]$$

Here  $(R_b/U)(du_\delta/dx)_{stag}$  is the dimensionless inviscid stagnation point velocity gradient which was taken equal to  $(1 - \epsilon)\sqrt{(8/3)\epsilon}$  corresponding to the inviscid constant density solution (18). The quantities  $f''_b$  and  $g'_b$  are the non-dimensional shear and heat transfer quantities defined by

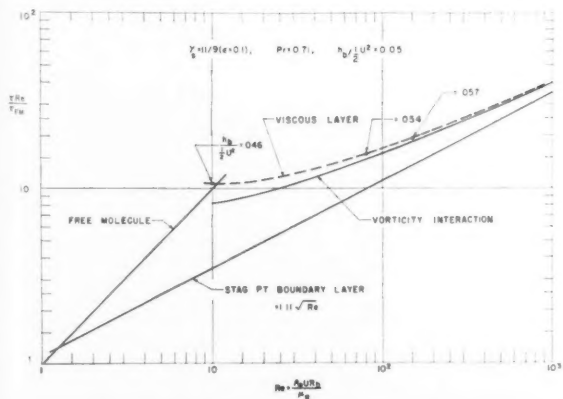


Fig. 5 Surface shear stress in stagnation region of a sphere from Navier-Stokes calculation

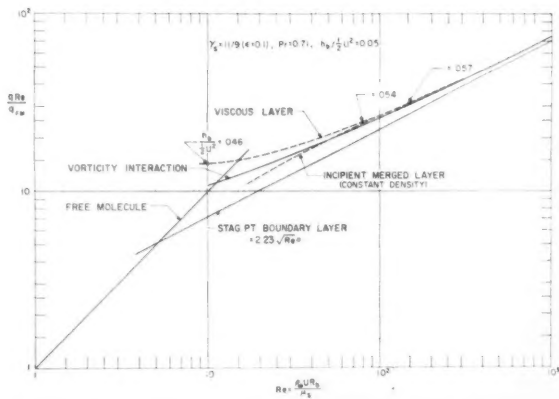


Fig. 6 Stagnation point heat transfer rate on a sphere from Navier-Stokes calculation

Fay and Riddell (19). Fay and Riddell give the following correlation for  $g'_b$

$$g'_b = 0.473 \left( \frac{\rho_s \mu_s}{\rho_b \mu_b} \right)^{0.4} \left( \frac{h_s - h_b}{U^2/2} \right) \quad (Pr = 0.71) \quad [36]$$

The corresponding correlation for  $f''_b$  was derived from unpublished calculations of Fay and Riddell which were given to the author by N. H. Kemp of the Avco Research Laboratory. The result is

$$f''_b = 0.727 (\rho_s \mu_s / \rho_b \mu_b)^{0.447} \quad (Pr = 0.71) \quad [37]$$

The vorticity interaction curves were obtained from calculations of the present author (20) and may be written in the form

$$f''_b / (f''_b)_{BL} = 1 + 0.49 \Omega \quad [38]$$

$$g'_b / (g'_b)_{BL} = 1 + 0.19 \Omega \quad [39]$$

Here the subscript  $BL$  stands for the boundary layer values given by Equations [36 and 37], and  $\Omega$  is the vorticity interaction parameter given by

$$\Omega = \frac{1}{\sqrt{2\epsilon}[(8/3)\epsilon]^{1/4}} \left( \frac{\rho_b}{\rho_s} \right) \sqrt{\frac{\mu_b}{\rho_b U R_b}} \frac{1 - (8/3)\epsilon}{(1 + \epsilon)^{1/2}} \quad [40]$$

In Fig. 6 the constant density incipient merged layer results of (15) have been interpolated, since the corresponding compressible calculations have not, as yet, been performed. On this scale the first collision results which are not shown would be valid up to a Reynolds number of about  $\frac{1}{2}$ ; whereas a fully merged layer calculation should carry down to about a Reynolds number of 5. Clearly then, this leaves only a narrow transitional layer regime not covered by either the presently existing rarefied or continuum theories.

In order to give some idea of the behavior of the flow field quantities we have shown in Fig. 7 profiles of the stagnation

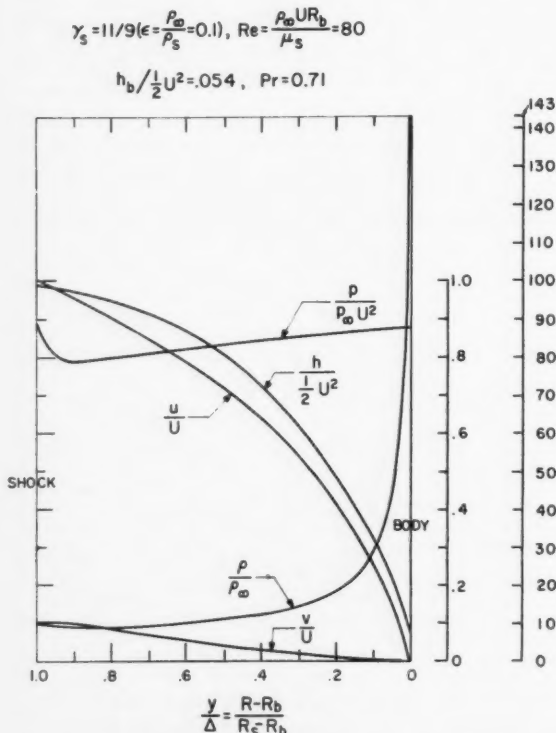


Fig. 7 Viscous layer profiles in stagnation region of a sphere ( $\Delta/R_b = 0.066$ )

point  $R$  dependent flow functions defined by Equations [33]. In the figure, the subscript zero on the flow functions has been dropped. These curves are drawn for a Reynolds number  $Re = 80$  and were calculated for the same conditions as were the shear and heat transfer results shown previously. The stand-off distance  $\Delta/R_b$  was calculated to be 0.066. We may expect that these profiles will not be significantly altered for a somewhat thickened shock, other than for the addition of the usual type of viscous shock profiles at the boundary where the discontinuous shock wave is shown.

## Transitional Layer Regime

At the present time, the only solution of a nonlinear problem providing a complete transition from the free molecule flow condition to the Navier-Stokes solution is that of Lees and Liu (21) on nonlinear plane Couette flow. In their solution they use the Maxwell integral equation of transfer and assume a form for the distribution function which contains a number of unknown parameters. By satisfying mass, momentum and energy conservation requirements and certain higher moments, they are able to reduce the problem to the solution of ordinary differential equations. This procedure is analogous in many respects to the classical integral methods in fluid mechanics such as the Kármán-Pohlhausen method for boundary layer flows. Hopefully this new method may offer a significant advance in obtaining solutions to rarefied gas problems, as well as in obtaining solutions which pass continuously through the transition regime to the usual continuum results.

In Fig. 8 we have shown the velocity profiles obtained by Lees and Liu for plane Couette flow between a hot and cold wall at a Mach number of 3 (the speed of sound in this definition is based on the temperature of the cold surface). In spite of the fact that the cooling ratio is not too large ( $T_b/T_0 = \frac{1}{4}$ ), the results are quite significant. They show that slip at the lower surface does not become significant until  $\lambda_b/d = \frac{1}{50}$ , where  $\lambda_b$  is the mean free path based on the cold wall temperature and  $d$  is the plate spacing. The mean free path  $\lambda_b$  can be expressed in terms of a mean free path  $\lambda^*$ , which more closely corresponds to the mean free path behind the shock  $\lambda_s$ . This mean free path  $\lambda^*$  is based on the "mean kinetic temperature" between the upper and lower plates and is given by (21)

$$\frac{\lambda^*}{d} = \frac{\lambda_b}{d} \left( \frac{T_M}{T_b} \right) = \frac{\lambda_b}{d} \left\{ \frac{1}{2} \left[ 1 + \frac{T_0}{T_b} + \frac{(\gamma - 1)}{6} Pr \left( \frac{U^2}{\gamma R T_b} \right) \right] \right\} \quad [41]$$

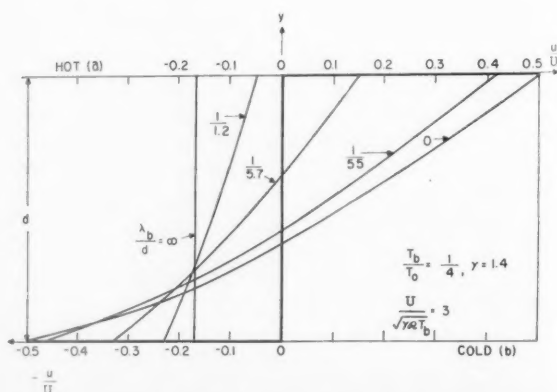


Fig. 8 Velocity profiles for plane Couette flow (Lees and Liu)

Thus in this case slip at the lower surface is not significant for  $\lambda^*/d < \frac{1}{20}$ , which is in agreement with the estimates shown in Fig. 1. More important, however, is that one can see from this figure that the transitional layer regime begins very suddenly, and within a decade in mean free path the slip at the lower surface almost corresponds to the free molecule value. Again this is in agreement with the picture given previously for the height of the transitional layer in terms of density change. Furthermore, the transition is seen to occur at about the mean free path values given by our previous estimates.

In Fig. 9 is shown the corresponding drag coefficient curve as a function of  $d/\lambda_s$ . Here again, in agreement with the estimates of Fig. 1 we see that the whole transitional region occupies a range in terms of  $d/\lambda^*$  from about 1 to 10, or a factor of 10 in density.

Although not directly related to the blunt body problem discussed in this paper, these results nevertheless do tend to give support to the picture of the flow field development as put forward, namely, that for a highly cooled body flying at hypersonic speed outside of a narrow transitional layer, whose height is of the order or less than one factor of 10 in density, it is possible to calculate the highly rarefied regime using free molecule and first collision type solutions and to calculate the less rarefied regimes using the Navier-Stokes equations without slip.

Of course, from a fundamental point of view, solutions of the transitional layer regime are quite significant, although from the point of view of the aerodynamicist it is questionable whether such complete solutions will be needed in order to define the rarefied gasdynamics problem.

## Nomenclature

$c$	= isentropic speed of sound, $(\gamma kT/m)^{1/2}$
$\bar{c}$	= mean molecular velocity, $(8kT/\pi m)^{1/2}$
$C_D$	= drag coefficient, $\text{drag}/\frac{1}{2}\rho_\infty U^2$
$d$	= plate separation distance for Couette flow
$f''_0$	= dimensionless boundary layer surface shear constant
$g'_{1/2}$	= dimensionless boundary layer surface heat transfer constant
$h$	= specific enthalpy
$k$	= Boltzmann constant
$m$	= mass of a molecule
$M_\infty$	= free stream Mach number, $U/c_\infty$
$n$	= number of molecules per unit volume of gas
$n_\infty$	= number of incident molecules per unit volume of gas in free stream
$n_b$	= number of emitted molecules per unit volume of gas at surface of body when completely accommodated
$n_e$	= number of emitted molecules per unit volume of gas, equal to $n_b$ at body surface
$n_i$	= number of incident molecules per unit volume of gas, equal to $n_\infty$ in free stream
$N$	= total number of molecules per unit area per second striking surface
$p$	= pressure
$Pr$	= Prandtl number
$q_R, q_\theta$	= radial and tangential velocity component
$\dot{q}$	= stagnation point surface heat transfer rate
$R$	= radial polar coordinate
$R_b$	= radius of sphere or radius of curvature of body
$\mathcal{R}$	= gas constant
$Re$	= Reynolds number, $\rho_\infty UR_b/\mu_s$
$T$	= absolute temperature
$T_0$	= temperature of body or temperature of cold plate in Couette flow
$T_h$	= temperature of hot plate in Couette flow
$v$	= tangential velocity divided by $\sin \theta$
$(du_\theta/dx)_{\text{stag}}$	= inviscid stagnation point velocity gradient
$U$	= macroscopic free stream velocity
$v$	= radial velocity divided by $-\cos \theta$
$x$	= distance from center of sphere along axis divided by $R_b$

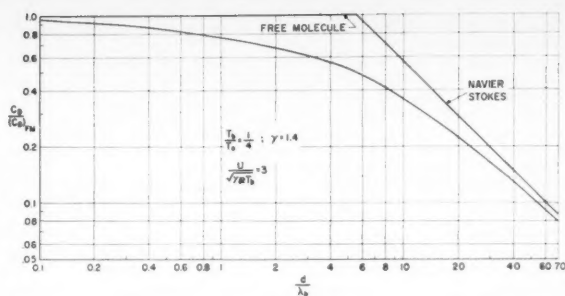


Fig. 9 Drag coefficient for plane Couette flow (Lees and Liu)

$\alpha$	= angle between normal to body surface and direction of emission
$\gamma$	= isentropic exponent, free stream value without subscript
$\Delta$	= detachment or standoff distance of shock wave from stagnation point
$\delta_s$	= shock wave thickness
$\epsilon$	= density ratio across shock, $\rho_\infty/\rho_s$
$\theta$	= polar angle, also angle between outward normal to surface and free stream velocity vector
$\lambda$	= mean free path, coordinate system fixed in body
$\lambda'$	= mean free path, coordinate system fixed in gas
$\lambda_\sigma$	= mean free path at body, coordinates fixed in body with $n_i = n_\infty, \bar{c}_b/n_\infty U \pi \sigma^2$
$\lambda$	= free stream mean free path, coordinates fixed in gas, $1/\sqrt{2} n_\infty \pi \sigma^2$
$\lambda_b$	= mean free path at wall in Couette flow, $1/\sqrt{2} n_b \pi \sigma^2$
$\lambda_s$	= mean free path behind shock, $1/\sqrt{2} n_s \pi \sigma^2$
$\lambda^*$	= mean free path in Couette flow based on mean kinetic temperature, Equation [41]
$\mu$	= viscosity coefficient
$\nu$	= molecular collision frequency, number per second
$\rho$	= mass density, $mn$
$\sigma$	= effective molecular diameter
$\tau$	= shear stress at body
$\Omega$	= vorticity interaction parameter, Equation [40]

## Subscripts

$b$	= conditions at body surface
$BL$	= boundary layer value
$e$	= emitted molecules
$ee$	= emitted relative to emitted molecules
$ei$	= emitted relative to incident molecules
$FM$	= free molecule value
$i$	= incident molecules
$ii$	= incident relative to incident molecules
$ie$	= incident relative to emitted molecules
$s$	= conditions behind (downstream of) shock wave
$\infty$	= conditions in free stream
$0$	= $R$ dependent quantities in separated Navier-Stokes equations

## References

- 1 Tsien, H. S., "Superaerodynamics, Mechanics of Rarefied Gases," *J. Aerom. Sci.*, vol. 13, 1946 pp. 653-664.
- 2 Schaaf, S. A. and Chambre, P. L., "Flow of Rarefied Gases," in "Fundamentals of Gas Dynamics," H. W. Emmons, Ed., Sect. H. (Vol. III of "High Speed Aerodynamics and Jet Propulsion"), Princeton Univ. Press, Princeton, 1958, pp. 687-739.
- 3 Schamberg, R., "Analytic Representation of Surface Interaction for Free-Molecule Flow with Application to Drag of Various Bodies," in Symposium on the Aerodynamics of the Upper Atmosphere, Rep. no. R-339, Rand Corp., Santa Monica, Calif., June 1959, pp. 12-1 to 12-41.
- 4 Chapman, S. and Cowling, T. C., "The Mathematical Theory of Non-Uniform Gases," Cambridge Univ. Press, Cambridge, 1958, p. 91.
- 5 Hayes, W. D. and Probstein, R. F., "Hypersonic Flow Theory," Academic Press, N. Y., 1959, p. 401.
- 6 Minzner, R. A., Ripley, W. S. and Condon, T. P., "U. S. Extension

to the ICAO Standard Atmosphere," U. S. Govt. Printing Office, Wash., D. C., 1958.

7 Schaaf, S. A., "Aerodynamics of Satellites," in Symposium on the Aerodynamics of the Upper Atmosphere, Rep. no. R-339, Rand Corp., Santa Monica, Calif., June 1959, pp. 1-1 to 1-13.

8 Hayes, W. D. and Probstein, R. F., *ibid.*, pp. 404, 405.

9 Willis, D. R., "A Study of Near Free Molecule Flow," in Symposium on the Aerodynamics of the Upper Atmosphere, Rep. no. R-339, Rand Corp., Santa Monica, Calif., June 1959, pp. 13-1 to 13-31.

10 Bhatnager, P. L., Gross, E. P. and Krook, M., "A Model for Collision Processes in Gases. I. Small Amplitude Processes in Charged and Neutral One-Component Systems," *Phys. Rev.*, vol. 94, 1954, pp. 511-525.

11 Grad, H., "Equations of Flow in a Rarefied Atmosphere," in Symposium on the Aerodynamics of the Upper Atmosphere, Rep. no. R-339, Rand Corp., Santa Monica, Calif., June 1959, pp. 11-1 to 11-37.

12 Grad, H., "Principles of the Kinetic Theory of Gases," in "Thermodynamics of Gases," Flügge, S. Ed., Sect. 33 (vol. XII of "Handbuch der Physik"), Springer, Berlin, 1958, p. 288.

13 Probstein, R. F., "Continuum Theory and Rarefied Hypersonic Aerodynamics," WADC Tech. Note no. 58-145, Div. of Engng., Brown University, Providence, R. I., July 1958; also "Rarefied Gas Dynamics," F. M.

Devienne, Ed., Pergamon Press, London, 1960, pp. 416-431.

14 Hayes, W. D. and Probstein, R. F., *ibid.*, pp. 375-395.

15 Probstein, R. F. and Kemp, N. H., "Viscous Aerodynamic Characteristics in Hypersonic Rarefied Gas Flow," *J. Aero/Space Sci.*, vol. 27, 1960, pp. 174-192, 218; see also Addendum and Errata, vol. 27, 1960, pp. 554, 555.

16 Ho, H. T. and Probstein, R. F., "The Compressible Viscous Layer in Rarefied Hypersonic Flow," ARL Tech Note no. 60-132, Div. of Engng., Brown University, Providence, R. I., Aug. 1960. (To appear in "Proc. Second Int. Symposium on Rarefied Gas Dynamics," L. Talbot, Ed., Academic Press, N. Y.)

17 Herring, T. K., "The Boundary Layer Near the Stagnation Point in Hypersonic Flow Past a Sphere," *J. Fluid Mech.*, vol. 7, 1960, pp. 257-272.

18 Hayes, W. D. and Probstein, R. F., *ibid.*, p. 161.

19 Fay, J. A. and Riddell, F. R., "Theory of Stagnation Point Heat Transfer in Dissociated Air," *J. Aero/Space Sci.*, vol. 25, 1958, pp. 73-85, 121.

20 Hayes, W. D. and Probstein, R. F., *ibid.*, p. 372.

21 Lees, L. and Liu, C. Y., "Kinetic Theory Description of Plane Compressible Couette Flow," Guggenheim Aeron. Lab., Hypersonic Memo no. 58, CIT, Pasadena, Calif., Sept. 1960. (To appear in "Proc. Second Int. Symposium on Rarefied Gas Dynamics," L. Talbot, Ed., Academic Press, N. Y.)

## Aerodynamic Characteristics of Wedges in Low Density Supersonic Flow

S. A. SCHAAF,<sup>1</sup>  
E. S. MOULIC,<sup>2</sup>  
M. T. CHAHINE<sup>3</sup>  
and G. J. MASLACH<sup>4</sup>

University of California  
Berkeley, Calif.

Experimental measurements of the lift, drag and pitching moment coefficients of wedge shaped airfoils are presented. The experiments were carried out for 5- and 30-deg half-angle sharp leading edge wedges at Mach numbers of 4 and 6 and with Reynolds numbers in the range of 1500 to 8900. The results exhibited strong viscous effects, particularly for the slender wedges, and were in reasonably good agreement with a simplified form of "weak interaction" boundary layer theory for a perfect gas. An extension of this theory indicates the probable importance of heat transfer effects on viscous aerodynamic characteristics.

IT IS the purpose of this paper to present some experimental and theoretical results dealing with the aerodynamic characteristics of wedge shaped two-dimensional "airfoils" in low density supersonic flow. The tests were carried out in the Berkeley low density supersonic wind tunnel (1)<sup>a</sup> at Mach numbers of 4 and 6, and at Reynolds numbers in the range 1500 to 8900. The experiments thus fall within the slip flow regime of gasdynamics as originally defined by Tsien (2), but, in accordance with considerable recent discussion (3-5), do not exhibit any marked noncontinuum effects. They do, however, exhibit quite large viscous effects arising from the thick laminar boundary layers associated with the low Reynolds numbers of the tests.

The boundary layer has two important aerodynamic effects for the present range of conditions: First, it produces a skin

friction along the surface, and second, through the displacement effect, disturbs the surface pressure from its inviscid value. (The boundary layer can also be expected to influence the base pressure. However, at the Mach numbers of these tests and for this geometry, this is of secondary importance in affecting the gross aerodynamic characteristics of lift, drag and pitching moment.) These boundary layer effects are influenced in a rather complicated way by Mach number, geometry and heat transfer conditions, in addition to their primary dependence on Reynolds number. Accordingly, variation in Mach number and geometry—utilizing slender 5-deg half-angle wedges on the one hand, and blunt 30-deg half-angle wedges on the other—was considered an important part of the investigations. Experiments incorporating variations in the heat transfer conditions will be made following alterations in the wind tunnel, but were not possible for the present program. However, some idealized calculations of the effect of heat transfer on the aerodynamic characteristics are presented which serve to indicate the expected trend of these effects, and also to emphasize their importance and the consequent need for more work along these lines.

Presented at the ARS Semi-Annual Meeting, Los Angeles, Calif., May 9-12, 1960.

<sup>1</sup> Professor and Chairman, Department of Mechanical Engineering.

<sup>2</sup> Assistant Research Engineer.

<sup>3</sup> Graduate Research Engineer.

<sup>4</sup> Professor of Aeronautical Engineering.

<sup>a</sup> Numbers in parentheses indicate References at end of paper.



For many applications, the leading edges of the configurations would be blunt, introducing an additional source of disturbance (6) primarily to the pressure distribution along the surface, but also to the structure of the boundary layer. To simplify the problem as much as possible and isolate the true viscous effects, the present tests were confined to the case of essentially infinitely sharp leading edges.

## Experimental Method

All data were obtained in the number 4 low density wind tunnel of the University of California Aeronautical Sciences Laboratory. The wind tunnel and associated instrumentation are described in Appendix D of (1). Axially symmetric nozzles producing nominal Mach numbers of 4 and 6 were used to produce continuous flow conditions for these tests. The wind tunnel employs an ambient stagnation temperature.

The axial and normal components of the aerodynamic force on the wedge shaped models were measured with a null-type beam balance incorporating a crossed-strip flexure pivot. A linear variable differential transformer was used to sense the null position of the beam, and the force on the model was computed from a moment summation about the pivot center. The extension of a precision steel quartz spring was used to oppose the moment created by the aerodynamic force. Fig. 1 presents a schematic drawing of the balance system. The angle of attack of the model relative to the flow direction was achieved by rotating the entire balance about the centerline of the model sting. The pitching moments were measured with a similar balance system, but for this case the model was positioned on the pivot axis rather than at a known distance from it, as in the case of the one-component balance. Fig. 2 presents a schematic drawing of the moment balance and shows how it differed from the one-component balance. The angle of attack mechanism allowed the model to be rotated with respect to the balance beam; the null weights compensated for any static unbalance in the model; the flexure pivot at the outer end of the model sting provided a nearly frictionless support for this end of the sting.

The two models were 5-deg ( $\pm 5'$ ) and 30-deg ( $\pm 3'$ ) half-angle wedges. The width was 0.750 in. for both models, and the slant length along one flat surface was 1.211 and 0.865 in. for the 5- and 30-deg half-angle wedges, respectively. There was no afterbody attached to the wedge. The internal, cross stream sting was centered 0.612 in. behind the vertex of the 30-deg half-angle model and 1.091 in. behind the vertex of the 5-deg half-angle model.

The two-dimensionality of the flow about the models was improved by fitting dummy models or end pieces to both ends of the element connected to the balance beam. Thus the model configuration approached the ideal of a central slice from an infinite wedge. The dummy end pieces extended approximately two model widths on each side of the central element. The end pieces were kept in alignment with the central element by a stiff support rod which passed through a clearance hole in the central element; the sting for the central element passed through a clearance hole in one of the end pieces. The possibility of flow through the gaps between the end pieces and central element causing forces on the sting was minimized by making the gaps only a few thousandths of an inch wide, and by fixing a small tubular sting shield to one end piece and allowing the other end of it to protrude into a recess in the central element.

Careful analysis of the various steps in the experimental techniques indicate that all sources of error, excluding those in the actual force measurement and in model or model mounting eccentricities, amounted to 2 or 3 per cent for these tests. These errors were mainly attributable to uncertainties in the dynamic pressure. The percentage error in the force or moment measurements decreased as the magnitude of the force increased, because the least count of both balances was fixed during a particular test. For reasonably large forces,

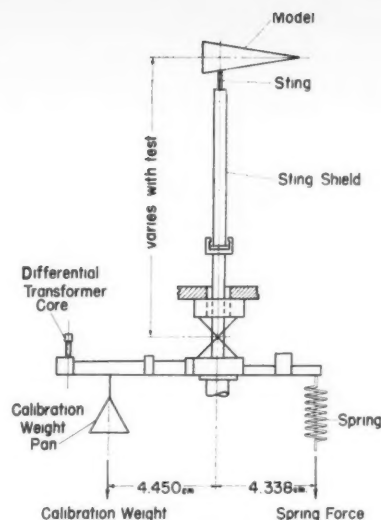


Fig. 1 Force measurement schematic

it could be reduced to 1 per cent or less; however, when either normal force or pitching moment were measured on a symmetrical body, the relative uncertainty in the force measurements was appreciable near zero angle of attack. In addition, there was another important source of error in the pitching moment measurements owing to eccentricity of the model about the pivot axis of the balance beam, which resulted in an additional moment component caused by the axial component of the resultant force on the model. This source of error could be reduced to a value approximately equal to the uncertainty in the force measurement by painstaking preparation of the apparatus before the tests. The final errors in the pitching moment were approximately twice the errors in the normal and axial force measurements.

An additional possible source of error in the force and moment measurements was the spurious force resulting from misalignment between the central element of the model and the two end pieces. This was explored experimentally by intentionally misaligning the model and measuring the change in force or moment. The effect was very small, since misalignment errors approximately 10 times larger than those present during the tests caused only a half per cent change in the force. Consequently, such errors were entirely negligible

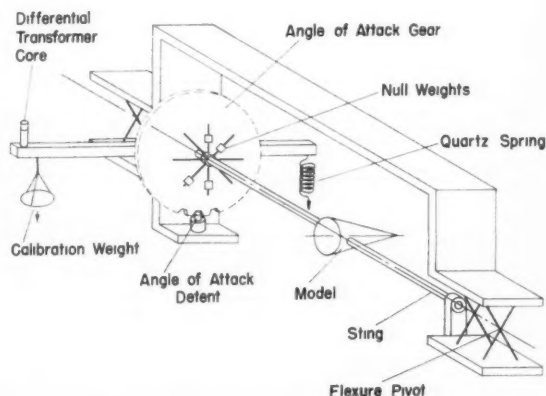


Fig. 2 Moment measurement schematic

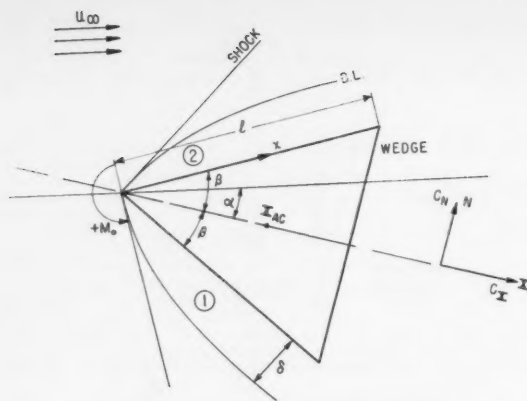


Fig. 3 Wedge airfoil at angle of attack

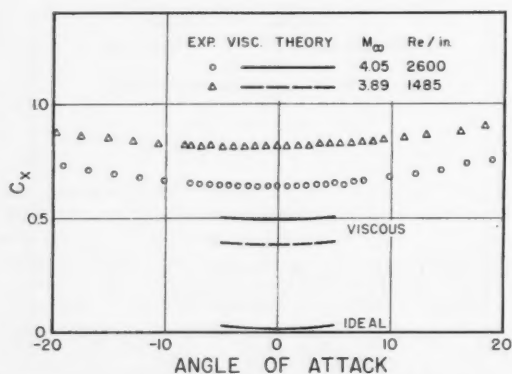


Fig. 4 5-deg half-angle wedge, axial force coefficient, Mach 4

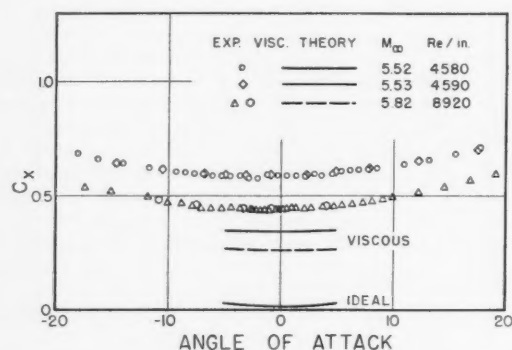


Fig. 5 5-deg half-angle wedge, axial force coefficient, Mach 5.7

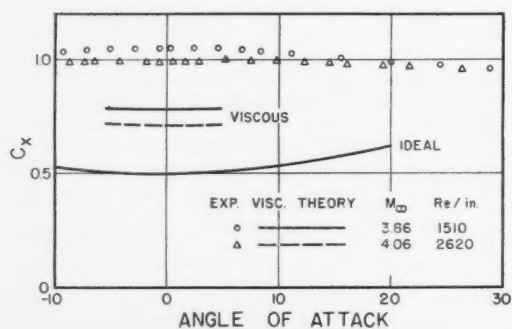


Fig. 6 30-deg half-angle wedge, axial force coefficient, Mach 4

during the tests. A further possible source of error was forces on the ends of the central element resulting from air flow through the gaps between the element and the end pieces. Gross forces were determined with the gaps adjusted to 0.011, 0.0057 and 0.0021 in., and the results showed that the forces were 0.6 to 1.7 per cent higher for the 0.011 gaps than the 0.0021 gaps, but that the force obtained when the gaps were 0.0057 in. was only 0.3 per cent different from the small gap conditions. These conclusions were based on tests encompassing the entire angle of attack range. Since the gaps for all tests reported were  $0.00175 \pm 0.00025$  in., the errors from this source were considered negligible.

Owing to the variable percentage error in the normal force and pitching measurements, the errors in the coefficients are presented as

$$\pm \% C_{N,M_0} = K_1 / |C_{N,M_0}| + K_2$$

where

$K_1$  = uncertainty in the force measurement expressed in coefficient form and multiplied by 100 to obtain percentages

$K_2$  = total percentage error in the coefficient from all other sources, including dynamic pressure, spring calibration, linear dimensions of the balance and linear dimensions of the model

Values for  $K_1$  and  $K_2$  are

$$K_1 = \frac{C_N}{\beta = 5^\circ, 30^\circ} = 1, \quad \frac{C_{M_0}}{\beta = 5^\circ} = 15, \quad \frac{C_{M_0}}{\beta = 30^\circ} = 2$$

$$K_2 = 2 \text{ for } M = 4$$

$$K_2 = 3 \text{ for } M = 5.7$$

Use of the foregoing expression shows that the final normal force coefficients have an overall  $\pm 5$  per cent error at angles of attack of 3 and 7 deg for the 5- and 30-deg half-angle models, respectively. The moment coefficients have an overall  $\pm 10$  per cent error at 5- and 7-deg angles of attack for the 5- and 30-deg half-angle models, respectively.

The errors in the axial force coefficient are based on the magnitude of the coefficient at zero angle of attack and are  $\pm 3$  per cent for both models in the Mach 4 flows, and  $\pm 3.5$  and  $\pm 4$  per cent for the 5- and 30-deg half-angle models, respectively, in the Mach 5.7 flows. The maximum errors in the angle of attack are  $\pm 0.1$  deg for the axial and normal force tests and  $\pm 0.25$  deg for the moment tests. The estimated error in Mach number is  $\pm 1$  and  $\pm 1.5$  per cent, and in Reynolds number is  $\pm 4$  and  $\pm 5$  per cent for Mach 4 and 5.7, respectively.

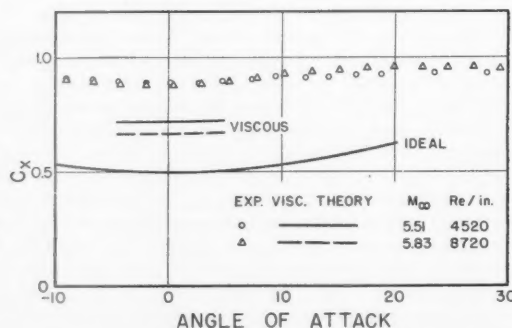


Fig. 7 30-deg half-angle wedge, axial force coefficient, Mach 5.7

## Results

The sign conventions used for the various force components are indicated in Fig. 3. The flow parameters were computed by the methods described in (1), Appendix D, and the Reynolds number computations were based on the viscosity data of Bromley and Wilke (7).

The experimental axial force coefficients for both models in the neighborhood of zero angle of attack are presented in Figs. 4 through 7.

The experimental normal force coefficient for both models near zero angle of attack is presented in Figs. 8 through 11.

The experimental pitching moment coefficients in the neighborhood of zero angle of attack are presented in Figs. 12 through 15.

## Theory

We consider a wedge (see Fig. 3) of semivertex angle  $\beta$  at an angle of attack  $\alpha$  to the incident hypersonic flow, with the length of either of its surfaces equal to  $l$ . A form of the "weak interaction" theory is used to obtain the pressure  $P$  and shear  $\tau$  distributions. The wedge is treated as a two-dimensional figure. It is assumed that ideal oblique attached shocks originate at the leading edge for both the lower and upper surfaces. Subscripts 1 and 2 refer to conditions immediately behind these shocks, but outside the boundary layer on the lower and upper surfaces, respectively. The flow behind the shock is that of an ideal flow parallel to the wedge surfaces under conditions imposed by the shock wave as a function of  $M_\infty$ ,  $\alpha$  and  $\beta$ . Therefore each surface is treated separately as a flat plate, in a flow regime defined by conditions 1 and 2. It is then assumed that laminar boundary layers form on the upper and lower surfaces, giving rise to skin friction  $\tau$  and boundary layer displacement thickness  $\delta^*$  given by (8)

$$\tau_1 = \frac{0.332 \rho_1 u_1^2}{\sqrt{u_1 x_1 / \nu_1}} \times \left[ 0.45 + 0.55 \frac{T_{P_1}}{T_1} + 0.09(\gamma - 1) M_1^2 P r^{1/2} \right]^{(n-1)/2} \\ = (B_1 q_\infty / \sqrt{Re_h}) \sqrt{l/x_1} \quad [1]$$

and

$$\delta_1^* = \frac{x}{0.332 \sqrt{u_1 x_1 / \nu_1}} \left[ 0.45 + 0.55 \frac{T_{P_1}}{T_1} + 0.09(\gamma - 1) M_1^2 P r^{1/2} \right]^{(n-1)/2} \times \\ \left[ \left( \frac{T_{P_1}}{T_1} - P r \frac{\gamma - 1}{4} M_1^2 \right) \frac{\pi}{2} - 1 - P r^{1/2} \left( \frac{T_{P_1}}{T_1} - 1 - P r^{1/2} \frac{\gamma - 1}{2} M_1^2 \right) \right] = \frac{A_1 \sqrt{x_1 l}}{\sqrt{Re_h}} \quad [2]$$

These expressions are semi-empirical, but have been confirmed by experiment over quite a range of Mach, Reynolds and temperature conditions. They are, however, limited to the case of an ideal gas in thermodynamic equilibrium. The only variations in gas properties which can be accounted for are those describable in terms of different mean values selected for the constants  $Pr$ ,  $\gamma$  and  $n$ , and do not hold for conditions where the gas will dissociate, or condense or exhibit other nonideal properties.

For calculating the pressure distribution on the wedge surface it is assumed that the effective surface is at the position of the boundary layer displacement thickness. It would perhaps be logical to use a shock expansion or tangent wedge or other gasdynamic method to calculate the pressures corresponding to this curved surface. However, this would lead to a very lengthy calculation which would, in any case, not necessarily be more accurate than that carried out here—namely, simple Newtonian flow. The emphasis of the present study is to get some insight into the viscous effects

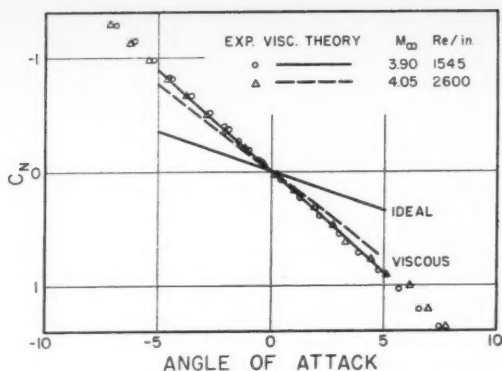


Fig. 8 5-deg half-angle wedge, normal force coefficient, Mach 4

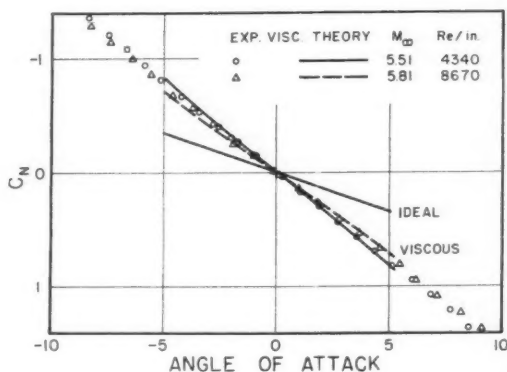


Fig. 9 5-deg half-angle wedge, normal force coefficient, Mach 5.7

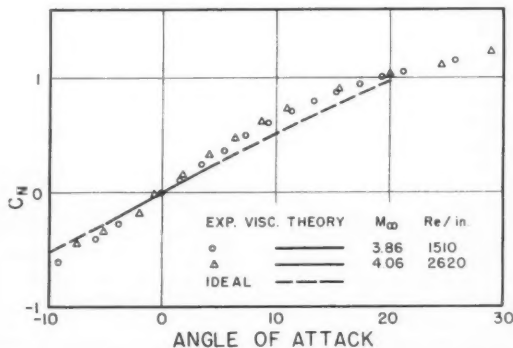


Fig. 10 30-deg half-angle wedge, normal force coefficient, Mach 4

and their dependence on heat transfer, Mach number, Reynolds number and geometry. We therefore calculate both the inviscid and the viscous pressure distributions by means of Newtonian theory. Logical consistency is thus preserved, and the results should give a good indication of the viscous corrections to ideal flow. We thus write

$$P_1(x_1) = 2q_\infty [\sin^2(\alpha + \beta) + \tan^{-1}(d\delta_1^*/dx_1)] = 2q_\infty \left[ \frac{2\sqrt{x_1}}{\sqrt{A_1^2/Re_1 + 4x_1}} \sin(\alpha + \beta) + \frac{A_1/\sqrt{Re_1}}{\sqrt{A_1^2/Re_1 + 4x_1}} \cos(\alpha + \beta) \right]^2 \quad [3]$$

The total axial and normal forces  $F_X$  and  $F_N$  are obtained by integrating, respectively, the axial and normal component of Equations [1 and 2] along the upper and lower surfaces. The moment about the vertex  $M_0$  is obtained by integrating in the same domain the product of forces on the wedge by their corresponding moment arms. Base pressure is ignored. By using the oblique shock relation, conditions in regions 1 and 2 can be replaced by conditions in the free stream (subscript  $\infty$ ). The results are then reduced to the usual coefficient form with the base area  $A$  as a reference

$$C_X = F_X/q_\infty 2l \sin \beta$$

$$C_N = F_N/q_\infty 2l \sin \beta$$

and using the height of the base as a reference the moment coefficient reduces to

$$C_{M_0} = M_0/q_\infty (2l \sin \beta)^2$$

Since the difference between a coefficient and its ideal (inviscid, Newtonian) value contains the free stream Reynolds number to the inverse square root as the dominant term, consider the expressions

$$C_N = \cotan \beta [\sin^2(\beta + \alpha) - \sin^2(\beta - \alpha)] + (1/\sqrt{Re_{t_1}}) \{ \cotan \beta [A_1 \sin 2(\beta + \alpha) - \sqrt{Re_1/Re_2} A_2 \sin 2(\beta - \alpha)] + \sqrt{Re_1/Re_2} B_2 - B_1 \} \quad [4]$$

$$C_X = \sin^2(\beta + \alpha) + \sin^2(\beta - \alpha) + (1/\sqrt{Re_{t_1}}) \{ A_1 \sin 2(\beta + \alpha) + \sqrt{Re_1/Re_2} A_2 \sin 2(\beta - \alpha) + \cotan \beta (\sqrt{Re_1/Re_2} B_2 + B_1) \} \quad [5]$$

$$C_{M_0} = \frac{\sin^2(\beta + \alpha) - \sin^2(\beta - \alpha)}{4 \sin^2 \beta} + \frac{1}{6 \sin^2 \beta \sqrt{Re_{t_1}}} \left[ A_1 \sin 2(\beta + \alpha) - \sqrt{\frac{Re_1}{Re_2}} A_2 \sin 2(\beta - \alpha) \right] \quad [6]$$

where  $A_1$  and  $B_1$  are defined by Equations [1 and 2], and only the terms of  $O(1/\sqrt{Re})$  have been retained.

Equations [4, 5, and 6] present in a concise form the aerodynamic forces on a given wedge as a function of the angle of attack  $\alpha$ , the surface temperature  $T_P$  and the free stream conditions. These equations were used to compute the theoretical variations of the axial and normal forces as well as the moment with respect to the angle of attack  $\alpha$ . The free stream conditions ( $M_\infty$ ,  $Re_\infty$ , ...) were fixed by the wind tunnel conditions during the various runs. The results of these computations are shown in Figs. 4 through 15 in connection with the experimental data.

In order to explore the effect of heat transfer, Equations [4, 5 and 6] are presented only in the limit of vanishing  $\alpha$  and large  $Re_\infty$ , as follows. At  $\alpha = 0$ , Equation [4] becomes identically zero, but the derivative of this equation remains different from zero. We thus consider the expressions

$$\frac{\partial}{\partial \alpha} (C_N - C_{N_{Newt}})_{\alpha=0} \sqrt{Re_{t_\infty}} = \left( \sqrt{\frac{Re_\infty}{Re_1}} \right)_{\alpha=0} \left\{ 2 \cotan \beta \left[ \left( \frac{\partial}{\partial \alpha} A_1 - \frac{A_1}{2} \frac{\partial}{\partial \alpha} \sqrt{\frac{Re_1}{Re_2}} \right) \sin 2\beta + 2A_1 \cos 2\beta \right] + B_1 \frac{\partial}{\partial \alpha} \sqrt{\frac{Re_1}{Re_2}} - 2 \frac{\partial}{\partial \alpha} B_1 \right\}$$

with

$$\left( \frac{\partial}{\partial \alpha} C_{N_{Newt}} \right)_{\alpha=0} = 4 \cos^2 \beta \quad [7]$$

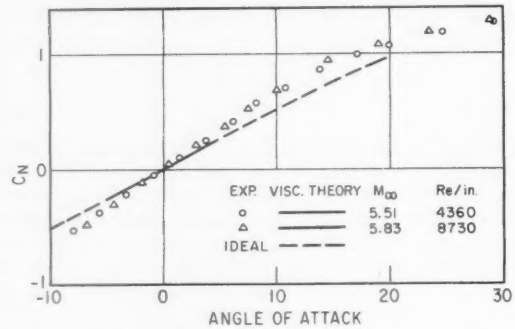


Fig. 11 30-deg half-angle wedge, normal force coefficient, Mach 5.7

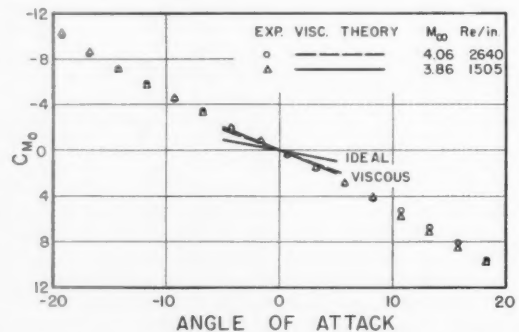


Fig. 12 5-deg half-angle wedge, pitching moment coefficient about vertex, Mach 4



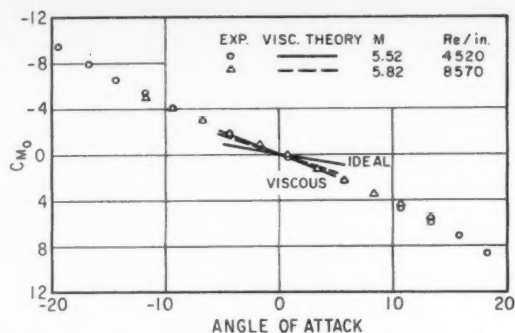


Fig. 13 5-deg half-angle wedge, pitching moment coefficient about vertex, Mach 5.7

Similarly, at  $\alpha = 0$ , Equation [5] becomes

$$[C_X - C_{X_{Newt}}]_{\alpha=0} \sqrt{Re_{l_\infty}} = (2 A_1 \sin 2\beta + 2 B_1 \cotan \beta) (\sqrt{Re_{l_\infty}}/Re_1)_{\alpha=0}$$

with

$$(C_{X_{Newt}})_{\alpha=0} = 2 \sin^2 \beta \quad [8]$$

and finally

$$\frac{\partial}{\partial \alpha} (C_{M_0} - C_{M_{0Newt}})_{\alpha=0} \sqrt{Re_{l_\infty}} = \frac{(\sqrt{Re_{l_\infty}}/Re_1)_{\alpha=0}}{3 \sin^2 \beta} \times \left[ \left( \frac{\partial}{\partial \alpha} A_1 - \frac{A_1}{2} \frac{\partial}{\partial \alpha} \sqrt{\frac{Re_1}{Re_2}} \right) \sin 2\beta + 2 A_1 \cos 2\beta \right]_{\alpha=0} \quad [9]$$

with

$$(\partial/\partial \alpha)(C_{M_{0Newt}})_{\alpha=0} = \cotan \beta$$

In the second of these equations (Eq. [8]),  $\alpha$  has already been put equal to zero. In the first (Eq. [7]) and the third (Eq. [9]), only the limit  $\alpha \rightarrow 0$  has been presented. In the final results  $(\partial/\partial \alpha)A_1$  and  $(\partial/\partial \alpha)B_1$  were calculated numerically because of the complexity of their dependence on  $\alpha$ . Equations [7, 8 and 9] are plotted on Figs. 16, 17 and 18. The results are discussed in the next section.

## Discussion and Conclusions

The generally acceptable agreement between the simple theory sketched in the foregoing and experimental results will be noted on Figs. 4 through 15. The agreement in the case of the normal forces and the pitching moment is probably better than should be expected, whereas the theoretical prediction of the axial forces is somewhat poorer. The difference between ideal inviscid Newtonian predictions and ideal inviscid gasdynamic predictions are within about this range, however, so that theory appears to predict the final viscous effect in a reasonably valid fashion, as is certainly to be expected.

Inspection of the results confirms the prediction that viscous effects are of major importance in determining the aerodynamic characteristics in the range of flow conditions of these tests. This is particularly true of the slender configuration and only to a lesser extent for the blunt configuration. Thus viscous effects will begin to be of importance at higher altitudes for blunt configurations as compared with slender configurations.

The reasonably good agreement between experiment and theory for the adiabatic wind tunnel case suggests that a tentative estimate of the effect on the aerodynamic characteristics of different heat transfer conditions may be made

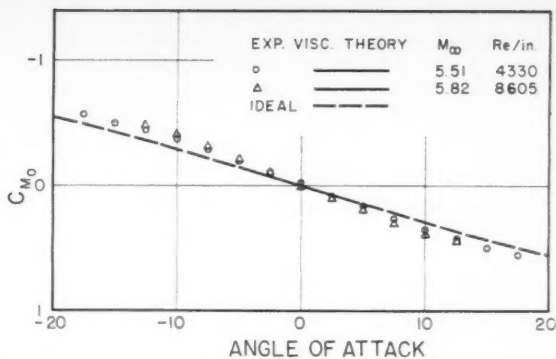


Fig. 14 30-deg half-angle wedge, pitching moment coefficient about vertex, Mach 5.7

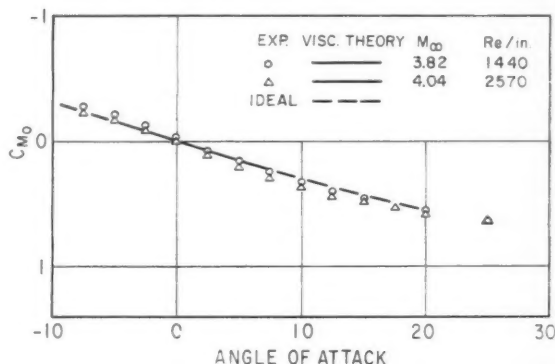


Fig. 15 30-deg half-angle wedge, pitching moment coefficient about vertex, Mach 4

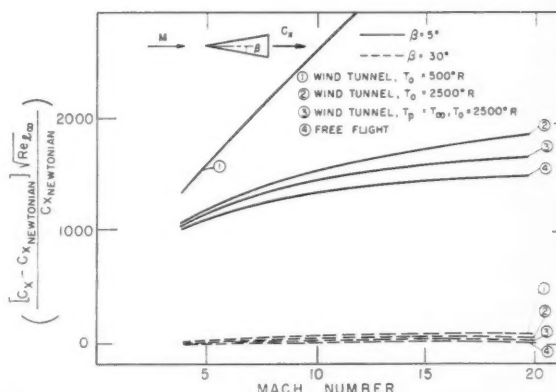


Fig. 16 Viscous effect on the axial forces of a wedge at zero angle of attack

on the basis of the same theory. This can be done with any assurance of accuracy only for a very slight extension of the parameters involved because of real gas effects. These real gas effects would involve dissociation, ionization and probably nonequilibrium phenomena for the free flight case and condensation for the wind tunnel case. Nominal results, however, utilizing expressions [7, 8 and 9] have been computed and presented in Figs. 16, 17 and 18 for the adiabatic wind tunnel heat transfer conditions and three other heat

transfer conditions which are more or less typical of free flight conditions, and of two intermediate heat transfer conditions corresponding to a low density wind tunnel utilizing 2500 R stagnation air and either adiabatic or cooled models, as follows:

1 Unheated wind tunnel

$$T_0 = T_P = 500 \text{ R} \quad Pr = 0.75 \quad n = 1$$

2 Moderately heated tunnel with adiabatic models

$$T_0 = T_P = 2500 \text{ R} \quad Pr = 0.75 \quad n = 0.67$$

3 Moderately heated tunnel with cooled models

$$T_0 = 2500 \text{ R} \quad T_P = T_0/[1 + M^2(\gamma - 1)/2] \\ Pr = 0.75 \quad n = 0.67$$

4 Free flight

$$T_P = 500 \text{ R} \quad T_0 = T_P[1 + M^2(\gamma - 1)/2] \\ Pr = 0.75 \quad n = 0.5$$

The results serve to indicate several expectations. First, it seems clear that aerodynamic characteristics, particularly for the slender configuration, will be quite seriously affected by heat transfer conditions. Duplication of geometry, Mach number and Reynolds number does not imply duplication of aerodynamic characteristics if heat transfer condition

are different. A second conclusion which seems apparent is that the viscous effects are considerably larger for adiabatic wind tunnel results than for corresponding heat transfer cases, such as free flight. A third and interesting possibility seems to be offered by the close agreement between results for the last two cases, namely, that only moderate heating of a low density wind tunnel accompanied by proper cooling of the models so as to reproduce correct temperature ratios may very well prove to be adequate for insuring proper scaling, at least for aerodynamic characteristics. This is of course a highly tentative conclusion pending a proper evaluation of the real gas effects.

## Nomenclature

- $\alpha$  = free stream angle of attack (Fig. 3)
- $\beta$  = wedge semi-angle (Fig. 3)
- $\delta^*$  = boundary layer displacement thickness (2)
- $\nu$  = kinematic viscosity
- $\tau$  = shear stress
- $A$  = base area, after wedge base
- $A_1$  = dimensionless quantity (see Eq. [2])
- $B_1$  = dimensionless quantity (see Eq. [1])
- $C_N$  = dimensionless normal force coefficient
- $C_X$  = dimensionless axial force coefficient
- $C_{M_0}$  = dimensionless moment coefficient with respect to the vertex
- $F_N$  = overall normal force (Fig. 3)
- $F_X$  = overall axial force (Fig. 3)
- $H$  = height of wedge base
- $K$  = uncertainty in the force measurement
- $l$  = length of wedge side (Fig. 3)
- $M$  = Mach number
- $M_0$  = moment with respect to the vertex, positive in the counterclockwise direction
- $n$  = temperature viscosity exponent ( $\mu \sim T^n$ )
- $0$  = order of magnitude
- $P$  = local pressure force
- $Pr$  = Prandtl number
- $q$  = dynamic pressure =  $\frac{1}{2}\rho u^2$
- $Re$  = Reynolds number,  $ul/\nu$
- $T$  = temperature
- $\rho$  = gas density
- $T_p$  = surface temperature
- $u$  = velocity
- $x$  = distance measured from the vertex along the wedge side surfaces (Fig. 3)

## Subscripts

- $0$  = stagnation condition when applied to temperature and vertex when applied to the moment notation
- $1$  = conditions pertaining to the lower surface outside the boundary layer and behind the shock
- $2$  = same as 1, but for the upper surface
- $\infty$  = free stream conditions
- $w$  = condition at the wall (surface of the wedge)
- Newt = Newtonian—inviscid, ideal flow

## References

- 1 Maalach, G. J. and Sherman, F. S., "Design and Testing of an Axisymmetric Hypersonic Nozzle for a Low Density Wind Tunnel," WADC-TR-341, Aug. 1956.
- 2 Tsien, H. S., "Superaerodynamics, Mechanics of Rarefied Gases," *J. Aeron. Sci.*, vol. 13, no. 12, Dec. 1946, pp. 643-664.
- 3 Adams, M. C. and Probst, R. F., "On the Validity of Continuum Theory for Satellite and Hypersonic Flight Problems at High Altitudes," *JET PROPULSION*, vol. 28, no. 1, 1958, p. 86.
- 4 Herman, R., "Hypersonic Flow Regimes at the Re-Entry of Satellite Vehicles," Proc. 6th Tech. Conference of Rosemount Aeronautical Laboratories, Univ. of Minn., Rep. no. 165, Oct. 1959.
- 5 Schaaf, S. A., "Recent Progress in Rarefied Gasdynamics," *ARS JOURNAL*, vol. 30, no. 5, May 1960, pp. 443-447.
- 6 Lees, L. and Kubota, T., "Inviscid Hypersonic Flow Over Blunt-Nosed Slender Bodies," *J. Aeron. Sci.*, vol. 24, no. 3, March 1957.
- 7 Bromley, L. A. and Wilke, C. R., "Viscosity Behavior of Gases," *Ind. Engng. Chem.*, vol. 43, July 1951, p. 1641.
- 8 Monaghan, R. J., "An Approximate Solution of the Compressible Laminar Boundary Layer on a Flat Plate," British Air Ministry, R and M no. 2760, Nov. 1949.

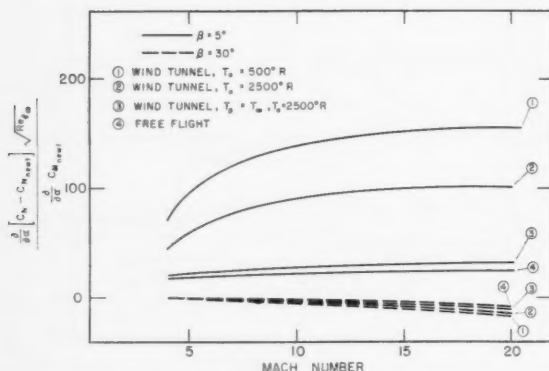


Fig. 17 Viscous effect of the normal forces of a wedge at zero angle of attack

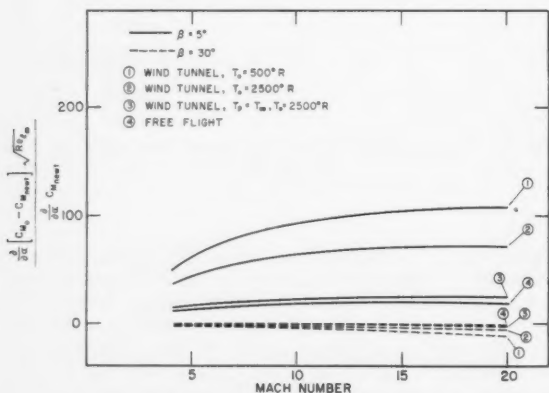


Fig. 18 Viscous effect on the moment coefficient of a wedge at zero angle of attack

# Researches in Interplanetary Transfer

JOHN V. BREAKWELL,<sup>1</sup>  
ROLLIN W. GILLESPIE<sup>2</sup>  
and STANLEY ROSS<sup>3</sup>

Lockheed Missiles and Space Div.  
Sunnyvale, Calif.

A method is presented by which interplanetary trajectories may be calculated extremely rapidly and to a degree of accuracy suitable for design studies. By splitting the three-center problem associated with interorbital ballistic transfer into three one-center segments which overlap somewhat at their junctions, solutions may readily be found by machine iteration. The extreme speed of the method enables wholesale amounts of worthwhile numerical results to be obtained. Examples presented in the paper include velocity requirements for trips to and from Mars during the year 1960. Considering that the orbits of Earth and Mars are elliptical and mutually inclined, the Hohmann minimum energy transfer criterion disappears, and the occurrence of several local minimum energy trajectories is observed; this phenomenon is expected to be typical of all interplanetary orbit studies.

WITH the advent of interplanetary voyages, it becomes important to have at hand complete information regarding velocity requirements for journeys between the various planets. If comprehensive data of this nature are made available, they can provide a useful basis for analyzing propulsion requirements, for planning ultimate system configurations, and for conducting feasibility studies relating to any mission contemplated. What is required is a method of calculation rapid enough to allow wholesale amounts of computations to be performed cheaply and efficiently, yet whose accuracy need be limited only to a degree expected in design studies.

It is natural, when such moderate accuracy is required, to approximate the single three-center ballistic problem by three distinct one-center motions, the latter being soluble in closed form (4).<sup>4</sup> Instead of joining conic segments at particular radial distances, the solution is constructed by imagining the heliocentric segment extending to the very centers of the terminal planets, whereas each planet-centered hyperbola meeting the heliocentric arc does so at its asymptote. This construction materially simplifies the calculation procedure and is expected to introduce only tolerable amounts of error into the computations.

By employing a high speed computer to fabricate the combined solutions, literally thousands of orbits per hour may be calculated, and their parameters presented in standardized charts and tables for the various solar planets. These may then be consulted to find the launch, midcourse and arrival information relating to a variety of missions.

A gridwork is selected, each of whose points corresponds to a particular departure date and a specific transfer time. Upon these points are overlaid contours of constant departure speed, constant arrival speed or other quantities of interest. These plots may be readily scanned, not only to select optimum trips for any given mission, but also to observe tradeoff relations for nonoptimal trips.

It is supposed that the planets are moving in fixed ellipses around the sun, every two orbits mutually inclined at some particular angle. Upon selection of appropriate ellipse parameters for the time interval of interest (7-9), preliminary input data may be readily computed by the machine. Fol-

lowing the approach of (2), a modified form of Lambert's theorem is then utilized to find the energies of all heliocentric arcs connecting the departure and arrival planets at the correct dates. For transfer arcs with included central angle  $\leq 2\pi$ , it is shown that exactly two such segments exist for any specified pair of dates, one orbit aimed with and the other against the departure planet's orbital motion; each time the central angle increases by  $2\pi$ , up to four further solutions are added.

After the proper energies are determined, the heliocentric velocities at both ends of the arc are evaluated. These values are transformed into relative vector velocities at the planets by subtracting the motions of the latter bodies. The right ascensions, declinations and speeds corresponding to such "hyperbolic excess velocities" are listed as outputs, together with the useful heliocentric data for the flight.

Total average computing time for each orbit amounts to approximately 0.1 sec on the IBM 7090, using Fortran. All variables are expressed in nondimensional form; lengths are normalized with respect to the astronomical unit, speeds with respect to Earth's mean orbital speed.

## Analysis of Results

It is instructive to begin by considering the transfer problem under the assumption that the planetary orbits be coplanar, concentric circles. Fig. 1 illustrates contours of constant hyperbolic excess departure speeds for trips to Mars. Departure dates cover the period from March 1960 to April 1961, a span which straddles the planetary opposition of Jan. 1, 1961.

All transfer arcs are co-planar with the planetary motions, with the exception of those described by the dashed lines. These latter trips involve central transfer angles of 180 deg, and the planes of transfer for journeys of this type may be inclined at any arbitrary angle to the two planets' motions. Since to any point on the dashed lines there corresponds a multiplicity of transfer orbit inclinations, it follows that each point represents a variety of departure velocities. The dashed lines are therefore singular in nature and will be seen to have additional significance in the more realistic cases to be discussed following. Viewing Fig. 1 as a geodetic contour map, these dashed lines correspond to sharp ridges of negligible thickness, having maximum heights determined by the largest values of departure velocity, i.e., by trips leaving perpendicularly to the ecliptic plane (rearward, or retrograde launchings are not shown in Fig. 1).

Presented at the ARS 14th Annual Meeting, Washington, D. C., Nov. 16-20, 1959.

<sup>1</sup> Staff Scientist.

<sup>2</sup> Research Specialist. Member ARS.

<sup>3</sup> Research Scientist. Member ARS.

<sup>4</sup> Numbers in parentheses indicate References at end of paper.

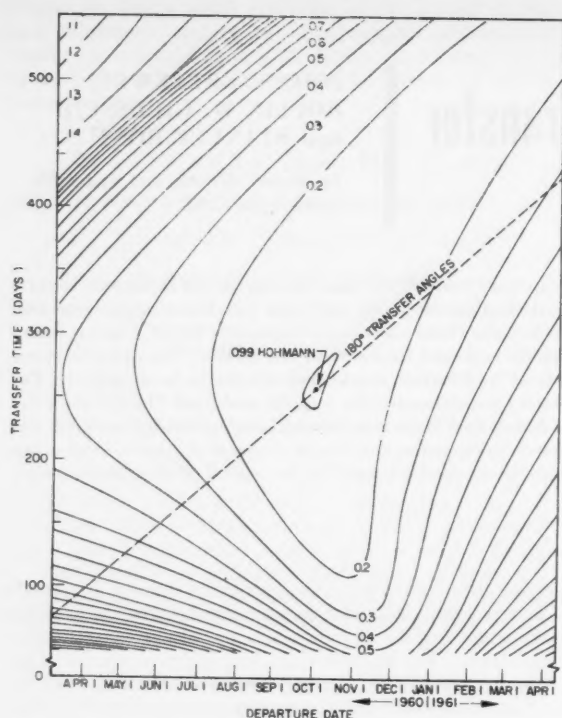


Fig. 1 Earth to Mars (co-planar, circular planetary orbits). Hyperbolic excess departure speeds (increments of 0.1). Normalized with respect to Earth's mean orbital speed

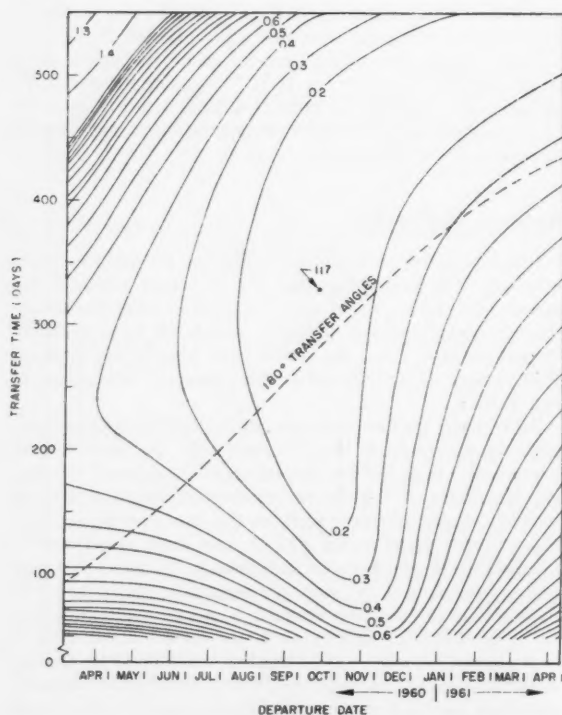


Fig. 2 Earth to Mars (co-planar, elliptical planetary orbits). Hyperbolic excess departure speeds (increments of 0.1). Normalized with respect to Earth's mean orbital speed

The equations of such lines in general are determined by the relation between departure and arrival times for 180-deg transfer. Using  $L_1$  and  $L_2$  to denote planetary longitudes measured from an arbitrary fixed line in space, we have

$$L_2 = \pi + L_1$$

and therefore that

$$d(\Delta t)/dt_1 = n_1/n_2 - 1$$

where

- $t_1$  = departure date
- $\Delta t$  = transfer time
- $n_1, n_2$  = respective planetary mean motions

For trips from Earth to Mars, the slope is about 0.88, for return orbits  $-0.468$ .

In close agreement with (3 and 4), the "Hohmann" point of minimum departure speed is found at Oct. 1, 1960, with an associated journey of 259 days. Since this is a trip involving a transfer angle of 180 deg, it also lies on the dashed line ridge.

Thus, it is found that the ridges corresponding to 180-deg transfer occur once every synodic period, each passing through a Hohmann point, and each having a slope of  $n_1/n_2 - 1$ . An infinite number of these equally spaced lines exist and may be found by expanding the figure's scope. The greater the difference in mean motions between the two planets, the shorter the synodic period, and therefore the closer the spacing of these dashed lines.

Another type of ridge may be observed in Fig. 1, occurring in the upper left-hand corner. This corresponds to transfer angles of 0 or 360 deg. Its direction is also given by  $n_1/n_2 - 1$  although the contours here build up somewhat more gently than those for 180-deg transfer. The two types of ridges displayed in Fig. 1 are to be found evenly interspersed between one another.

As a matter of fact, any particular line drawn with a slope of  $n_1/n_2 - 1$  represents an infinitude of transfers between the two planets, each of which involves the same transfer angle. However, successive points on any such line correspond to transfers of longer and longer duration. Following any one line upward, we find that its associated solutions steadily approach parabolic arcs, all of which traverse the same transfer angle. We conclude, therefore, that for long transfer times the contours of constant departure speed asymptotically approach straight lines parallel to the ridges.

Fig. 2 describes the situation when planetary orbit eccentricities are introduced. Both orbits are still assumed to be co-planar. The date for minimum departure speed has shifted to Sept. 26, 1960, and it no longer involves a transfer of 180 deg (the transfer angle is now about 210 deg). Travel time for this point has increased to 360 days, whereas the speed itself has changed from a value of 0.099 in Fig. 1 to the presently indicated value of 0.117. This increase of 18 per cent illustrates the disadvantages in basing calculations on the "Hohmann" type of analysis. Note also that the ridges, as well as the constant velocity asymptotes, have become undulating lines, owing to the introduction of orbital eccentricities.

Fig. 3 is similar in nature to Fig. 15 of (3), with refinements having been introduced here by the choice of a finer grid size. It illustrates the consequences of introducing planetary orbit inclinations as well as eccentricities into the problem.

The chief resulting modification is observable near the lowest ridge, which has now broadened. The summit line no longer represents orbits perpendicular to the departure plane, but arises from a rather more complicated relation for those points at which a balance is achieved between forward and retrograde firings.

Since the mutual inclination between the orbits of Earth

<sup>6</sup> Figs. 1 to 8 do not include results for transfer through more than 360 deg.



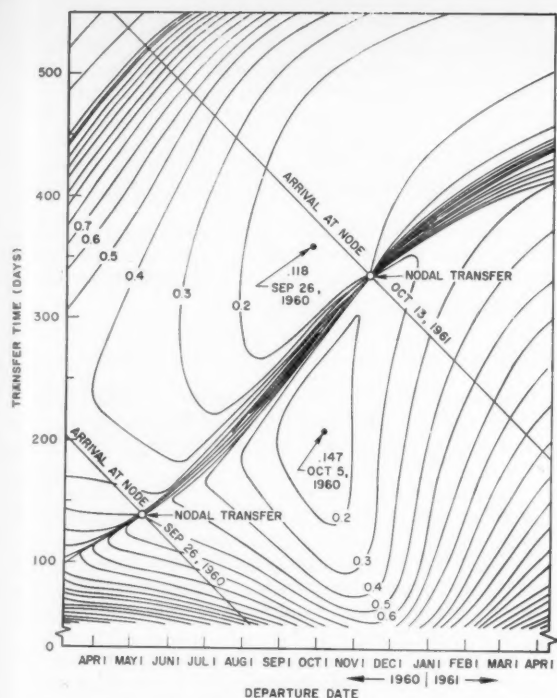


Fig. 3 Earth to Mars. Hyperbolic excess departure speeds (increments of 0.1). Normalized with respect to Earth's mean orbital speed

and Mars is quite small (about 2 deg), this particular ridge is still narrow, and since the eccentricities of both planetary orbits are small, its undulations are also limited. Vestiges of the co-planar transfer model remain at the points of nodal transfer for which many similar orbits are possible, each with a different inclination to the ecliptic.

It is convenient to imagine Fig. 3 to have arisen from Fig. 2 by having held the nodal transfer points clamped and having a wedge forced up from below the thin ridge. This useful analogy is further validated by the fact that the disturbance is indeed localized in the vicinity of the ridge. At points moderately far removed from this ridge, the contours for Figs. 2 and 3 agree closely.

Now the original Hohmann point of Fig. 1 has bifurcated into two local minimum orbits, these occurring at about  $\pm 5$  days from Oct. 1, 1960. The smaller of the two in value, 0.118, is only 1 per cent different from its value in Fig. 2. The other, 0.147 (a trip of 209-days duration) arose purely as a result of introducing relative orbital inclinations. The former point, incidentally, corresponds to an orbit which lies almost in the ecliptic plane, having a transfer angle of about 220 deg. This particular trip leaves Earth at approximately the time when Mars is at the ascending node, and arrives at Mars when it is at the descending node.

These nodal arrival lines, together with the ridges, subdivide the diagram into diamond-shaped regions. In adjacent segments, the character of the motion alternates between orbits aimed above and those aimed below the ecliptic plane.

Although the overall character of the curves is similar for each synodic period, particular details vary from one opposition to the next. Thus, for the period 1966-1968, for instance, the overall minimum departure velocity is 0.098, considerably lower than the present one, and evidently smaller in value than the Hohmann case! The apparent discrepancy is a result of the planetary orbit eccentricities and the fact that Mars' mean (and not its minimum) radius was chosen for the Hohmann analysis of Fig. 1.

A final point of interest concerning this phase of the trips

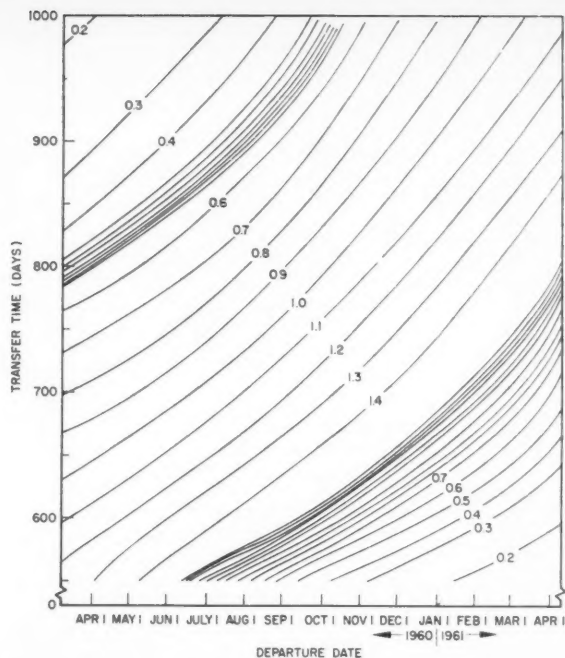


Fig. 4 Earth to Mars, long transfer times. Hyperbolic excess departure speeds (increments of 0.1). Normalized with respect to Earth's mean orbital speed

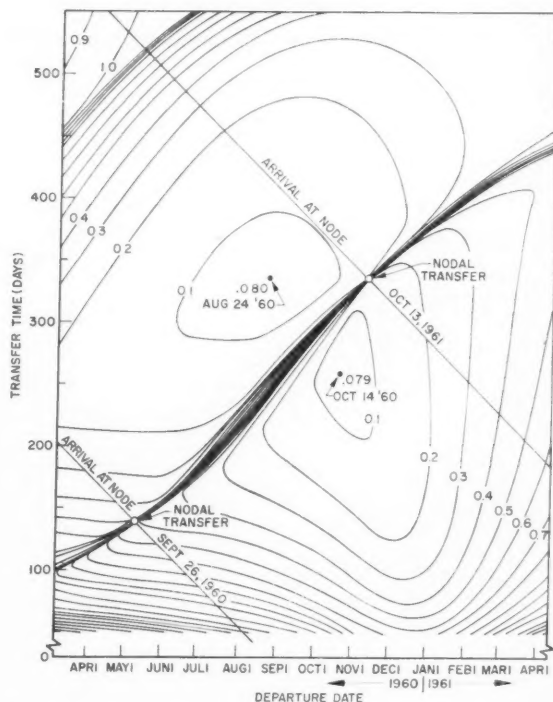


Fig. 5 Earth to Mars. Hyperbolic excess arrival speeds (increments of 0.1). Normalized with respect to Earth's mean orbital speed

is shown in Fig. 4, which depicts the asymptotic solutions for long transfer time. These curves, as explained previously, are all virtually parallel to the ridges. Such regions are of possible interest for nonstop round-trip journeys on which an unfavorable return region from Mars may be encountered for the shorter trips going, but not for the longer.

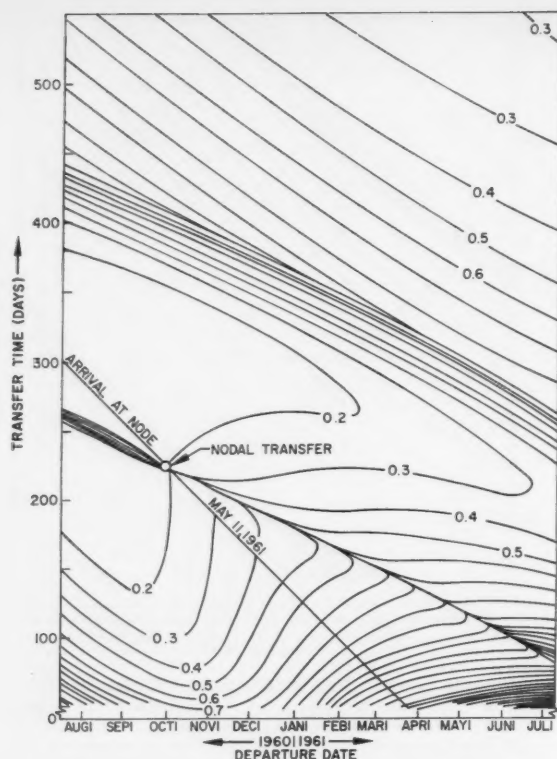


Fig. 6 Mars to Earth. Hyperbolic excess departure speeds (increments of 0.1). Normalized with respect to Earth's mean orbital speed

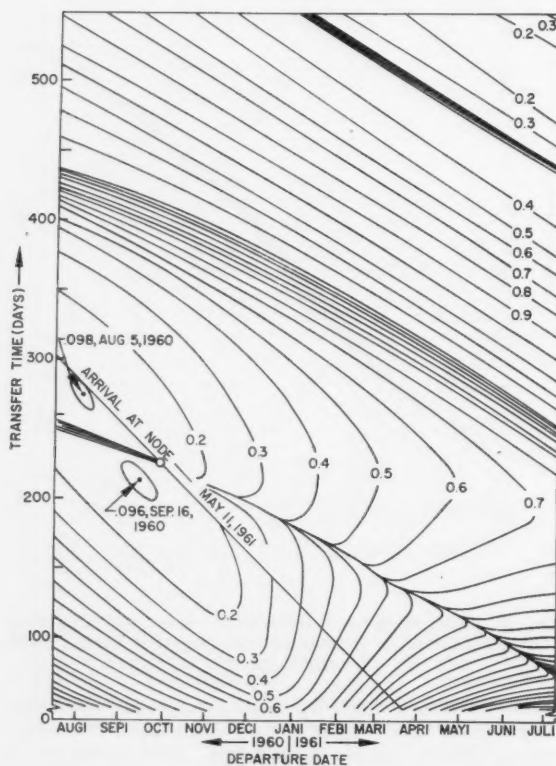


Fig. 7 Mars to Earth. Hyperbolic excess arrival speeds (increments of 0.1). Normalized with respect to Earth's mean orbital speed

This is indeed the case, as inspection of Fig. 6 reveals. Many shorter, physically realistic trips leaving Earth arrive (Fig. 5) at Mars with quite low speeds. When an attempt is made to match a low arrival speed at Mars with an identical departure speed on the same day, it is found that the only return trips for which this is possible are those encompassing longer transit times. Thus, the choice of either a short trip going or a short return trip, but not both, is possible in such cases.

Planning of round trips involves simultaneous manipulation of the various sets of curves, Figs. 3 to 8, until acceptable conditions at all points are realized. These trips will be investigated in a paper now in preparation.

## Summary

A useful method of computing interplanetary ballistic transfer orbits and associated planet-centered flight parameters has been presented, along with typical plots of output data. The method is intended for use in:

1 Overall surveys of trajectory requirements, location of trip optima and studies of nonoptimal alternatives to given nominal flights.

2 Indication of local areas of interest for more careful study with precise orbit calculation programs. Using this method as a coarse locator will result in considerable savings of both time and money.

3 Matching of arbitrary planetary escape (or approach) trajectories to the central coasting segment. In this way, the flight planner need not burden himself with the mechanics of an entire flight; instead, his only concern need be how to arrive at (or depart from) "infinity" in a specified direction, 'possessing a given speed there.

4 Planning of multi-legged journeys and capture orbits in the solar system. Because of the speed and cheapness of the

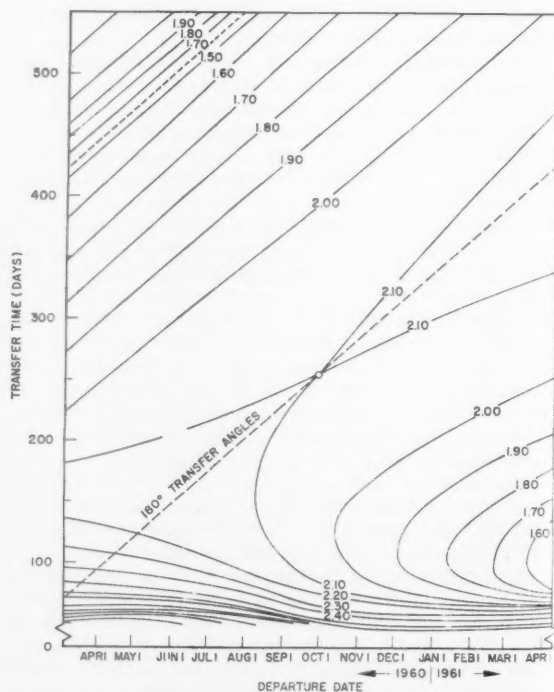


Fig. 8 Earth to Mars, retrograde launchings (co-planar, circular planetary orbits). Hyperbolic excess departure speeds (increments of 0.1). Normalized with respect to Earth's mean orbital speed

calculations, the method represents a most practical way to depict literally thousands of transfers which may be scanned visually or mechanically to find the required components of any broken orbit.

The same method is also applicable to the solution of intercept and rendezvous problems between two satellite orbits about a central body, assuming that oblateness, air drag and other perturbing effects are negligible during the period of transfer.

## Acknowledgment

The authors would like to express their sincere appreciation to B. B. Gragg, of Lockheed Missiles and Space Division, for his able assistance in preparing the computer program for the calculations.

## Appendix: Kinematical Relations

### Heliocentric Orbit

In Fig. 9, geometrical relationships during transfer are illustrated. For any particular trajectory, let  $S$  represent the sun,  $P_1$  the planet of departure at the time of departure,  $P_2$  the planet of arrival at the arrival date, and  $\Pi_1$  and  $\Pi_2$  the planes of planetary motion. Since the transfer plane  $\Pi$  must contain  $P_1$  and  $P_2$  as well as the sun, and since these three points are, in general, noncollinear,  $\Pi$  is immediately determined. From the diagram,  $P_1$  and  $P_2$  define the angles  $L_1$  and  $L_2$  (both measured eastward from  $\Omega$ );  $I$ , the mutual inclination of the planetary orbits, is a fixed constant. Then, well-known relationships from solid trigonometry yield

$$\cos L = \cos L_1 \cos L_2 + \sin L_1 \sin L_2 \cos I \quad [A-1]$$

In order to find all heliocentric orbits which pass through  $P_1$  and  $P_2$  in the stipulated time, it is necessary to investigate not only the two transfer angles  $L$  which lie between 0 and  $2\pi$ , but also all other cases,  $L + 2m\pi$ , satisfying Equation [A-1].

Now, denote by  $s$  the semiperimeter of triangle  $P_1P_2S$  (Fig. 10)

$$s = (1/2)(r_1 + r_2 + c)$$

where  $c$ , the chord joining  $P_1$  and  $P_2$ , is found from

$$c^2 = r_1^2 + r_2^2 - 2r_1r_2 \cos L$$

Let  $E$  be given by

$$E = \frac{\text{heliocentric energy of transfer orbit}}{|\text{heliocentric energy of elliptic orbit with semimajor axis} = s/2|}$$

$$= \begin{cases} -s/2a, & \text{for elliptic transfer} \\ +s/2a, & \text{for hyperbolic transfer} \end{cases}$$

$a$  is the transfer orbit's semimajor (or semitransverse) axis. Finally, let

$$T = \frac{n\Delta t}{(s/2)^{3/2}} = \frac{2\pi \times \text{time of transfer}}{\text{period of elliptic orbit with semimajor axis} = s/2}$$

$\Delta t = t_2 - t_1$ ;  $t_1, t_2$  are the Julian dates of departure and arrival, and  $n$  is the Earth's mean motion.

Then, according to Lambert's theorem (1), the correct elliptic transfer path may be determined by finding  $E$  in

$$T = (-E)^{-3/2} [2m\pi + (f - \sin f) - (g - \sin g)] \quad [A-2]$$

where

$$\begin{aligned} \sin^2 f/2 &= -E \\ \sin^2 g/2 &= -EK \\ K &= 1 - c/s \end{aligned}$$

FEBRUARY 1961

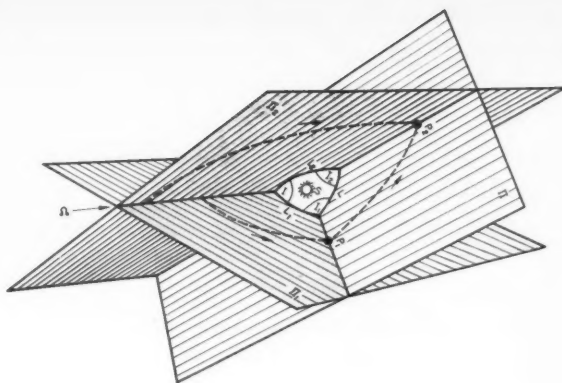


Fig. 9 Transfer geometry

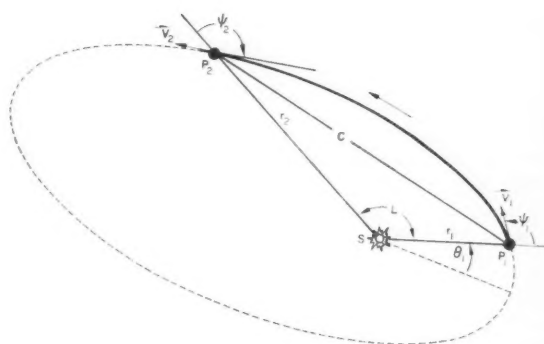


Fig. 10 Relationships in the transfer plane

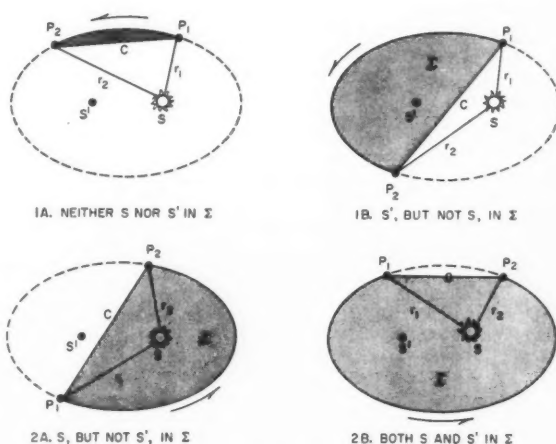


Fig. 11 Different regions for Lambert's theorem

$m = 0, 1, 2, 3, \dots$  denotes the number of complete circuits on the transfer orbit before  $P_2$  is reached.

These latter equations, however, define  $f$  and  $g$  ambiguously. It is thus necessary to differentiate among several possible subcases.  $\Sigma$  is the sector bounded by  $c$  and the transfer arc; these cases are illustrated in Fig. 11:

Case 1A)  $\sin L \geq 0$ ; neither  $S$  nor  $S'$  in  $\Sigma$

$$T = (-E)^{-3/2} [2m\pi + (f - \sin f) - (g - \sin g)] \quad [A-3]$$

Case 1B)  $\sin L \geq 0$ ;  $S'$ , but not  $S$ , in  $\Sigma$

$$T = (-E)^{-3/2}[2(m+1)\pi - (f - \sin f) - (g - \sin g)] \quad [A-4]$$

Case 2A)  $\sin L \leq 0$ ;  $S$ , but not  $S'$ , in  $\Sigma$

$$T = (-E)^{-3/2}[2m\pi + (f - \sin f) + (g - \sin g)] \quad [A-5]$$

Case 2B)  $\sin L \leq 0$ ; both  $S$  and  $S'$  in  $\Sigma$

$$T = (-E)^{-3/2}[2(m+1)\pi - (f - \sin f) + (g - \sin g)] \quad [A-6]$$

where

$$\begin{aligned} S' &= \text{vacant locus of the transfer orbit} \\ f &= 2 \sin^{-1} \sqrt{(-E)} \\ g &= 2 \sin^{-1} \sqrt{(-EK)} \\ E &\leq 0 \end{aligned}$$

and  $f/2, g/2$  are each chosen in  $(0, \pi/2)$ .

Hyperbolic motion can occur only when  $0 \leq L \leq 2\pi$ . The appropriate formulas are then:

Case 1H)  $0 \leq L \leq \pi$

$$T = (E)^{-3/2}[(\sinh f' - f') - (\sinh g' - g')] \quad [A-7]$$

Case 2H)  $\pi \leq L \leq 2\pi$

$$T = (E)^{-3/2}[(\sinh f' - f') + (\sinh g' - g')] \quad [A-8]$$

where

$$\begin{aligned} E &\geq 0 \\ f' &= 2 \sinh^{-1} \sqrt{E} \\ g' &= 2 \sinh^{-1} \sqrt{EK} \end{aligned}$$

Fig. 12 illustrates curves of  $E$  vs.  $T$  for representative values of  $K$ . The lines drawn for  $K = 1$  define regions corresponding to successive values of  $m$ . Points lying within the sector marked  $m = 2$ , for instance, relate to journeys which traverse two complete circuits of the transfer orbit before  $P_2$  is encountered.

As  $K$  decreases, each pair of curves, referred to in the foregoing as 1 and 2, draws together, merging finally into the set of dashed lines representing the case  $K = 0$ . This latter family of orbits is characterized by transfer angles of  $L = (2m+1)\pi$ .

Where  $E = 0$ , corresponding elliptic and hyperbolic solu-

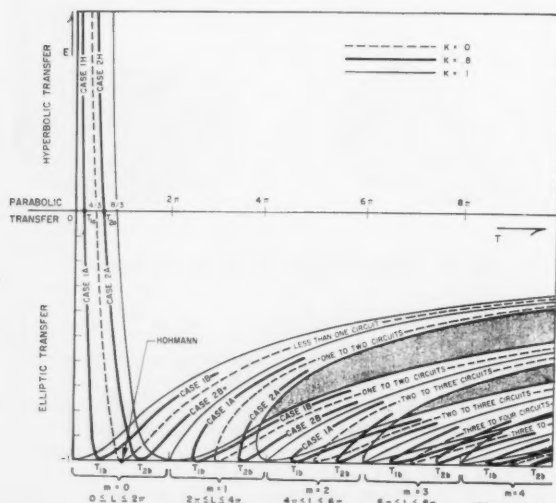


Fig. 12  $E$  vs.  $T$  for typical values of  $K$

tions meet. This situation represents parabolic transfer, and occurs at

$$T_{1a} = (4/3)(1 - K^{3/2}), \text{ for } 0 \leq L \leq \pi$$

$$T_{2a} = (4/3)(1 + K^{3/2}), \text{ for } \pi \leq L \leq 2\pi$$

When  $S'$  lies on  $\overline{P_1P_2}$ , elliptic cases 1A and 1B coincide. This occurs at  $E = -1$  (its minimum value), where

$$T_{1b} = (2m+1)\pi - 2 \sin^{-1} \sqrt{K} + 2 \sqrt{K} \sqrt{1-K} \quad \sin L \geq 0$$

Similarly

$$T_{2b} = (2m+1)\pi + 2 \sin^{-1} \sqrt{K} - 2 \sqrt{K} \sqrt{1-K} \quad \sin L \leq 0$$

and  $E$  is equal to  $-1$  here also.

Having once specified the constellation of  $P_1$  and  $P_2$ , we may immediately form  $T$ . And, depending upon its position in relation to  $T_{1a}, T_{2a}, T_{1b}$  and  $T_{2b}$ , we may then solve for all solutions  $E$  which define the various transfer paths. In the region  $m = 0$ , there exist two, and only two, values of  $E$ , for any given  $T$ . This is evident from Fig. 12 and can, moreover, be rigorously shown as follows.

To the left of points  $T_{1b}$  and  $T_{2b}$ , respectively, we find that

$$dT/dE = f(E) \mp K^{5/2} f(EK)$$

according as we consider cases 1H, 1A or 2H, 2A, where

$$f(E) = (3/E^{5/2}) \sinh^{-1} \sqrt{E} - (E+3)/E^2 \sqrt{1+E} \quad \text{if } E > 0$$

$$f(E) = [3/(-E)^{5/2}] \sin^{-1} \sqrt{-E} - (E+3)/E^2 \sqrt{1+E} \quad \text{if } -1 < E < 0$$

Note that  $f(0^+) = f(0^-) = -3/8 < 0$ , and that  $f(E) \rightarrow \infty$  as  $E \rightarrow -1$ .

Now, if  $E > 0$

$$(d/dE)[E^{5/2} f(E)] = -E^{3/2}/(1+E)^{3/2} < 0$$

Since  $0 \leq K < 1$ , and  $f(0)$  is bounded, it follows that, if  $E > 0$

$$E^{5/2} f(E) < (EK)^{5/2} f(EK) \leq 0$$

and, hence, that  $dT/dE < 0$ , when  $E > 1$ .

Similarly, when  $-1 < E < 0$

$$(d/dE)[(-E)^{5/2} f(E)] = +(-E)^{3/2}/(1+E)^{3/2} > 0$$

so that

$$(-E)^{5/2} f(E) < (-EK)^{5/2} f(EK) \leq 0$$

and, hence, when  $-1 < E < 0$

$$dT/dE < 0$$

Since  $T \rightarrow 0$  as  $E \rightarrow +\infty$ , we observe that as  $E$  decreases from  $+\infty$  to  $-1$ ,  $T$  increases monotonically from zero to  $T_{1b}, T_{2b}$ , respectively. To the right of points  $T_{1b}, T_{2b}$ , respectively (in any  $m$  region, incidentally), on the other hand

$$dT/dE = 3\pi(m+1)(-E)^{5/2} - f(E) \pm K^{5/2} f(EK)$$

which is necessarily positive. Thus,  $T$  increases monotonically from  $T_{1b}, T_{2b}$ , respectively, to  $+\infty$  as  $E$  increases from  $-1$  to zero.<sup>6</sup>

The monotonic character of the  $E, T$  curves, therefore, establishes the existence of two, and only two, solutions for  $E$ , given a particular value of  $T$ , in the region  $m = 0$ . Each successive  $m$  region furnishes up to four additional solutions

<sup>6</sup> By somewhat similar arguments, it can be shown that  $T'' > 0$  to the left of  $T_{1b}, T_{2b}$ , and changes sign just once to the right of these points





so that the relative velocity of the departing vehicle, as seen from  $P_i$ , is

$$\mathbf{v}_1 = [V_1 \cos \psi_1 - \dot{R}_1, V_1 \cos I_1 \sin \psi_1 - (h_1/R_1), V_1 \sin I_1 \sin \psi_1] \quad [\text{A-14}]$$

$$|\mathbf{v}_1| = \sqrt{V_1^2 + \dot{R}_1^2 + (h_1/R_1)^2 - 2V_1(\dot{R}_1 \cos \psi_1 + [h_1/R_1] \cos I_1 \sin \psi_1)}$$

Similar formulas also serve to define  $\mathbf{v}_2$ .

Equation [A-14] expresses the hyperbolic excess velocity requirement for the launching. That is,  $\mathbf{v}_1$  represents the residual velocity vector at "infinity" which the vehicle must possess so that the prescribed heliocentric path be negotiated.

The velocity components are frequently more favorably resolved, however, in terms of a polar-equatorial reference frame than in the heliocentric system of Equation [A-14]. The change of coordinates is effected through two rigid rotations. The first turns  $\hat{x}$ , the solar radial direction toward  $P_i$ , into  $\hat{X}$ , the direction of the sun's ascending node as viewed in the local planetary equatorial system (for the case of Earth,  $\hat{X}$  is directed toward the vernal equinox), through an angle of  $\phi_i - T_i$ .

By the second transformation, ecliptic north  $\hat{z}$  is rotated into polar north,  $\hat{Z}$ , in a left-handed sense about  $\hat{X}$ , through an equatorial inclination angle  $i_i$ , which is a property of the planet in question.

New coordinate axes  $\hat{X}$ ,  $\hat{Y}$ ,  $\hat{Z}$  have now been established in the following sense:

$\hat{X}$  lies in the equatorial plane of  $P_i$ , aimed at the sun's ascending node

$\hat{Z}$  points toward equatorial north

$\hat{Y}$  completes the right-handed system of coordinates, and the full transformation may be characterized by the single orthogonal matrix

$$D \equiv \begin{pmatrix} \cos(\phi_i - T_i) & \sin(\phi_i - T_i) \cos i_i & \sin(\phi_i - T_i) \sin i_i \\ -\sin(\phi_i - T_i) & \cos(\phi_i - T_i) \cos i_i & \cos(\phi_i - T_i) \sin i_i \\ 0 & -\sin i_i & \cos i_i \end{pmatrix}$$

As seen in the equatorial system of  $P_i$ , then, the velocity at infinity is found by matrix multiplication to be

$$\mathbf{v}_i = \mathbf{v}_1 \cdot D$$

Finally, the right ascension and declination of  $\mathbf{v}_i$  are

$$\alpha_i = \sin^{-1} [(\mathbf{v}_i)_Y / \sqrt{(\mathbf{v}_i)_X^2 + (\mathbf{v}_i)_Y^2}] \quad 0 \leq \alpha_i \leq 2\pi$$

$$= \cos^{-1} [(\mathbf{v}_i)_X / \sqrt{(\mathbf{v}_i)_X^2 + (\mathbf{v}_i)_Y^2}]$$

$$\delta_i = \tan^{-1} [(\mathbf{v}_i)_Z / \sqrt{(\mathbf{v}_i)_X^2 + (\mathbf{v}_i)_Y^2}] \quad -\pi/2 \leq \delta_i \leq \pi/2$$

## References

- 1 Plummer, H. C., "An Introductory Treatise on Dynamical Astronomy," Cambridge University Press, 1918, also Dover Publications, Inc. N. Y., 1960, paperback reprint, chapter V.
- 2 Battin, R. H., "The Determination of Round-Trip Planetary Reconnaissance Trajectories," *J. Aero/Space Sci.* vol. 26, no. 9, Sept. 1959, pp. 545-567.
- 3 Gunkel, R. J., Lascody, D. N. and Merrilees, D. S., "Impulsive Mid-course Correction of an Interplanetary Transfer," *Proc. Tenth International Astronautical Congress*, London, Sept. 1959.
- 4 Karrenberg, H. K. and Arthur, P. D., "Interplanetary Ballistic Orbits," ARS preprint 870-59, June 1959.
- 5 Ehricke, K. A., "Zur Auswahl von Flugbahnen für bemannte Raumfahrzeuge zu den Planeten Mars und Venus," *Raketentechnik und Raumfahrtforschung*, Heft 1, Band 4, Jan.-March, 1960, pp. 16-22.
- 6 Vertregt, M., "Interplanetary Orbits," *J. Brit. Interplanet. Soc.*, vol. 16, no. 6, March-April, 1958, pp. 326-354.
- 7 "The American Ephemeris and Nautical Almanac for the Year 1960," U.S. Govt. Printing Office, Wash., D. C., 1958.
- 8 "Planetary Coordinates for the Years 1960-1980," Her Majesty's Stationery Office, London, 1958.
- 9 "Astronom. Ezheg. SSSR na 1960 g.," *Izdat. Akad. Nauk*, Moscow, 1957, pp. 621-623.

# Ballistic Re-Entries With a Varying $W/C_D A$

R. V. WARDEN<sup>1</sup>

Aeronutronic Div., Ford Motor Co.  
Newport Beach, Calif.

An analytical method is presented for evaluating the velocity and deceleration history of a ballistic vehicle experiencing a change in  $W/C_D A$  during re-entry. Mass is assumed to be transferred through the process of either ablation or fluid injection into the boundary layer. Vehicle geometry is represented by  $C_D$  and  $A$  which vary through altitude dependent functions. Gravity and centrifugal forces on the vehicle are neglected, thereby restricting the analysis to large entrance angles and flight velocities. These simplifying assumptions permit a closed form solution of the re-entry trajectory with variable  $W/C_D A$ . The governing equation reduces to an incomplete gamma function or exponential integral, depending upon the sign of  $d(W/C_D A)/dy$ . Results show that the maximum deceleration of the re-entry vehicle is a function of the rate of change of  $W/C_D A$ . Furthermore, variable geometry can produce a significant effect on trajectory parameters, such as velocity, deceleration, impact location and heating.

Received May 27, 1960.

<sup>1</sup> Senior Engineer; Project Engineer, Air Force Scout Re-Entry Vehicle. Member ARS.

ALTERING the ballistic parameter  $W/C_D A$  during re-entry will permit some degree of control over a vehicle's trajectory. The importance of this control will be apparent to the designer from the standpoint of heating, deceleration loads, enemy evasion, target dispersion, etc. (1,2).<sup>2</sup>

Mass, area and drag coefficient are allowed to vary during re-entry; the mechanism which causes the variation is not considered. For a closed form solution certain simplifying assumptions are made. In particular,  $W/C_D A$  is a function only of  $y$ . However, the applicability of the analysis may be extended, as given in the Appendix, to allow mass to vary as a function of the total heat absorbed.  $W/C_D A$  might be programmed in time or dynamic pressure, rather than altitude. Also, a controlled variation using different rates between given cutoff altitudes can be incorporated.

## Equations of Motion

The basic equation of motion, as taken from Newton's second law

$$(d/dt)(mV) = m(dV/dt) + (V - V_p)(dm/dt) = \sum F \quad [1]$$

where

- $m$  = vehicle's mass at any instant of time
- $dm/dt$  = rate of change of the mass
- $V_p$  = velocity of a transferred mass particle

Let  $V_p$  be equal to  $V$ , which restricts the problem to low velocity mass discharges. Then for a zero lift trajectory

$$\begin{aligned} m(d^2y/dt^2) &= -mg \sin \theta + (C_{Dp}AV^2/2) \sin \theta \\ m(d^2x/dt^2) &= (C_{Dp}AV^2/2) \cos \theta \end{aligned} \quad [2]$$

It is allowable to neglect gravity provided that small entrance angles are not considered (3). The flight path is then linear with the coordinate system as shown in Fig. 1.

Let a normalized ballistic parameter be given

$$\text{constant } X[1 - K(1 - \bar{y})]^{N-1}$$

For the solution of specific physical problems, the usual properties may be defined separately

$$\begin{aligned} m &= m_0[1 - K(1 - \bar{y})]^n \\ A &= A_0[1 - K(1 - \bar{y})]^p \\ C_D &= C_{D_0}[1 - K(1 - \bar{y})]^s \end{aligned}$$

where  $K$  may be thought of as determining the mass ratio remaining at sea level ( $0 \leq K \leq 1$ ), and the exponents as influencing the rates of change of mass or geometry.

Using an isothermal atmosphere, the density variation with altitude is  $\rho = \rho_{SL}e^{-\beta y}$ , where

$$\begin{aligned} \bar{\beta} &= y_0/\text{scale height} = \text{constant} \\ y_0 &= \text{initial altitude} \end{aligned}$$

For Earth, defining the altitudes of interest, let

$$\begin{aligned} \bar{\beta} &= y_0/22,000 \\ \rho_{SL} &= 0.0034 \end{aligned}$$

Define a relative density parameter  $\mu = m/\rho_{SL}A_0y_0$ , and normalize the velocity such that

$$\begin{aligned} dy/dt &= -V \sin \theta / V_E = -\bar{V} \sin \theta \\ d^2y/dt^2 &= -(d\bar{V}/dt) \sin \theta \end{aligned}$$

The normalized equation of motion is now

$$-d\bar{V}/dt = (C_{D_0}/2)[1 - K(1 - \bar{y})]^{(p+s-n)} \bar{V}^2 e^{-\bar{\beta}y} \quad [3]$$

The quantity  $(p + s - n)$  controls the total variation of  $W/C_D A$  during flight. (If, for instance, the quantity is positive, the ballistic parameter increases during descent.)

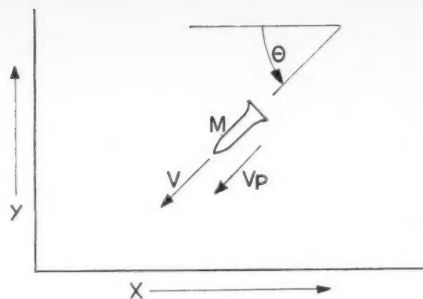


Fig. 1 Coordinate system

Using

$$d\bar{V}/dt = -\bar{V} \sin \theta (d\bar{V}/d\bar{y})$$

the parameter

$$Z = (\bar{\beta}/K)[1 - K(1 - \bar{y})]$$

and equating  $p + s - n = N - 1$ , integration yields

$$\ln \bar{V} = \frac{C_{D_0} e^{\bar{\beta}(1-K)/K}}{2\mu \bar{\beta}(k/\bar{\beta})^{1-N} \sin \theta} \int_{Z_1}^{Z_2} Z^{N-1} e^{-Z} dZ + C_1 \quad [4]$$

where the constant of integration  $C_1 = 1$ , since  $\bar{V} = 1$  at  $Z = Z_1$ .

The remaining integral, when integrated over the limits 0 to  $\infty$ , is the well-known gamma function,  $\Gamma(N)$ . See (4 and 5). The special case of  $N$  equal to 0 results in the "exponential integral" (6,7). It is reasonable to take the upper limit as infinity, since  $y_0$  will be large. However, a lower limit of zero is not of interest, so the incomplete gamma function must be considered when  $N$  is not equal to 0. To integrate from  $Z_1$  to infinity it is convenient to evaluate  $[\Gamma(N) - \Gamma_x(N)]$  where the incomplete gamma function  $\Gamma_x(N)$  is

$$\Gamma_x(N) = \int_0^x e^{-Z} Z^{N-1} dZ$$

$\Gamma_x(N)$  may be replaced by a form of the error integral [see (6)]  $E_n(x)$ , such that

$$\begin{aligned} \frac{1}{n}! E_n(x) &= \int_0^x e^{-B} dB = \\ \frac{1}{n} \int_0^x e^{-S} S^{1/n-1} dS &= \frac{\Gamma(1/n, x^n)}{n} \end{aligned}$$

but

$$\Gamma\left(\frac{1}{n} + 1\right) = \frac{1}{n}! = \frac{1}{n} \Gamma\left(\frac{1}{n}\right)$$

Let the parameter  $Z$  be equal to  $x^n$  and  $1/n$  be equal to  $N$ . Then

$$E_{1/N}(Z^N) = \Gamma(N, Z)/\Gamma(N) = \Gamma_x(N)/\Gamma(N)$$

Thus

$$\Gamma(N) - \Gamma_x(N) = \Gamma(N) [1 - \Gamma_x(N)/\Gamma(N)] = \Gamma(N) [1 - E_{1/N}(Z^N)] \quad [5]$$

The asymptotic expression for large  $Z$  is (6)

$$\begin{aligned} \Gamma(N) [1 - E_{1/N}(Z^N)] &= \\ e^{-Z} \left[ 1 - \frac{1/N - 1}{(1/N)Z} + \frac{(1/N - 1)(2/N - 1)}{[(1/N)Z]^2} - \dots \right] & [6] \end{aligned}$$

<sup>2</sup> Numbers in parentheses indicate References at end of paper.

## Velocity

Using Equation [5] the velocity expression becomes

$$\bar{V} = \exp \left\{ -\frac{C_{D_0}(K/\beta)^{N-1}}{2\mu\beta \sin \theta} \times \Gamma(N) [1 - E_{1/N}(Z^N)] e^{\frac{\beta(1-K)}{K}} \right\} \quad [7]$$

or using Equation [6] for large  $Z$

$$\bar{V} = \exp \left\{ -\frac{C_{D_0}[(K/\beta)Z]^{N-1}}{2\mu\beta \sin \theta} \times \left[ 1 - \frac{1-N}{Z} + \frac{(1-N)(2-N)}{Z^2} \dots \right] e^{-\beta y} \right\} \quad [8]$$

For  $K = 0$  the velocity expression reduces to the constant  $W/C_{D_0}A$  case as in (3).

## Deceleration

$$d\bar{V}/dt = -\bar{V} \sin \theta (d\bar{V}/d\bar{y}) = -\bar{V}\beta \sin \theta (d\bar{V}/dZ)$$

This results in the deceleration (dropping the bars henceforth)

$$\frac{dV}{dt} = -\frac{C_{D_0}}{2\mu} \left( \frac{K}{\beta} Z \right)^{N-1} e^{-\beta y} e^{-\frac{C_{D_0}(K/\beta)^{N-1}}{\mu\beta \sin \theta} \Gamma(N) [1 - E_{1/N}(Z^N)] e^{\frac{\beta(1-K)}{K}}} \quad [9]$$

from Equation [7]; here again use may be made of Equation [6] for large  $Z$ .

## Altitude for Maximum Deceleration

To find the altitude where the deceleration is a maximum, it is convenient to use

$$\frac{d}{dy} \left( \frac{dV}{dt} \right) \left( \frac{dy}{dt} \right) = \beta \frac{d}{dZ} \left( \frac{dV}{dt} \right) \frac{dy}{dt}$$

when  $dy/dt$  is well behaved. Upon differentiating Equation [9],  $(d/dZ)(dV/dt)$  vanishes if

$$(N-1) \left( \frac{K}{\beta} \right) + \left( \frac{K}{\beta} Z \right)^N \frac{C_{D_0} e^{-\beta y}}{\mu\beta \sin \theta} - \frac{K}{\beta} Z = 0 \quad [10]$$

When  $Z$  is expressed in terms of  $y$ , the corresponding altitude is

$y_{\max} =$

$$\frac{1}{\beta} \ln \left( \frac{C_{D_0} [1 - K(1 - y_{\max})]^N}{\mu \sin \theta \{ \beta - K[\beta(1 - y_{\max}) + N - 1] \}} \right) \quad [11]$$

which reduces to

$$y_{\max} = \frac{1}{\beta} \ln \frac{C_{D_0}}{\mu\beta \sin \theta} \quad [12]$$

for constant  $W/C_{D_0}A$ .

Although a transcendental equation is involved, usually only one trial is necessary to obtain a solution within  $\pm 500$  ft. An iterative process was found to be much faster than the alternative graphical solution.

## Maximum Deceleration

Substituting Equation [11] into Equation [9] one obtains

$$\left( \frac{dV}{dt} \right)_{\max} = \frac{\beta \sin \theta (Z + 1 - N)}{2Z} e^{-[1 - (1/Z^N)\{(1-N)^2 - (1-N)(2-N)\} - (1/Z^2)\{(1-N)^2(2-N) \dots - (1-N)(2-N)(3-N)\}]} \quad [13]$$

or, approximately

$$(dV/dt)_{\max} \approx \beta \sin \theta (Z + 1 - N)/2Ze \quad [14]$$

Maximum deceleration vs.  $Z$  is plotted on Fig. 2 which shows the influence of varying rates of change of  $W/C_{D_0}A$ . The rate functions are both  $Z$  (through the parameter  $K$ ) and  $N$ . As the absolute values of either  $K$  or  $N$  increase (thus

increasing the variation in  $W/C_{D_0}A$ ), the magnitude of maximum deceleration is more greatly effected. The  $N = 1$  line on Fig. 2 corresponds to constant  $W/C_{D_0}A$ , and any curve above or below this line would represent an increasing or decreasing  $W/C_{D_0}A$ , respectively. The fact that  $N = 1$  does correspond to a straight line, and the other values for  $N$  converge asymptotically to this line as  $Z$  approaches  $\infty$ , substantiates the independence of maximum deceleration from mass, drag coefficient and geometry only when  $W/C_{D_0}A$  remains constant.

## Numerical Examples

The following examples illustrate some uses of the equations which have been developed.

### Example 1

A comparison is made of the velocity and deceleration histories of several variable geometry, zero-lift, re-entry vehicles. The results illustrate a significant rate of change

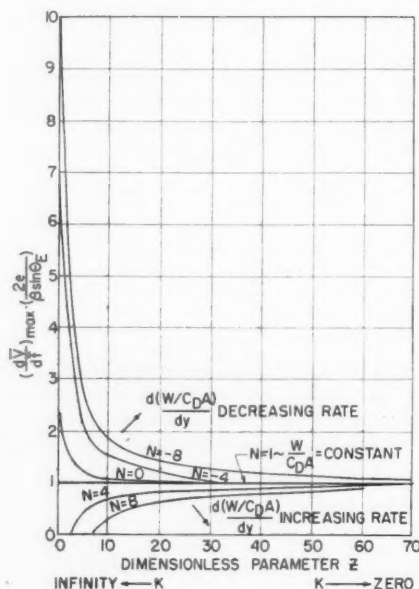


Fig. 2 Maximum deceleration vs.  $Z$

of  $W/C_{D_0}A$  during descent; in fact, for illustrative purposes,  $C_D$  and  $A$  are varied more than is probably practical. The vehicles may be thought of as having an adjustable skirt to vary the area and drag coefficient as shown in Fig. 3.

The initial conditions of  $W/C_{D_0}A = 510$  lbs/ft<sup>2</sup>,  $y_0 = 200,000$  ft, and  $\theta_0 = 15$  deg are the same for each vehicle. The individual cases are described in Table 1.





Fig. 3 Concept for varying  $W/CDA$  in flight

Fig. 4 is a plot of the approximate variation with altitude of  $(W/CDA)/(W/CDA)_0$  for each vehicle. Fig. 5 shows the comparative velocity histories and Fig. 6 shows the deceleration histories of the four vehicles. It is shown that the altitude for maximum deceleration can be varied considerably. The large reduction in  $C_D$  and  $A$  for vehicle (c) have caused it to impact at slightly more than half of its entrance velocity. On the other hand vehicle (a) has been arrested to a terminal falling velocity at almost 35,000-ft altitude. The physical interpretation of the zero velocity at an altitude above sea level is that the vehicle has decelerated to a terminal falling velocity subject to the (neglected) force of gravity.

The implications of being able to control a manned re-entry vehicle are apparent. It is noted that an increasing rate of change of  $W/CDA$  during re-entry lowers the maximum deceleration. Because of thermal considerations it is of benefit to decrease the heated surface area, provided that the ratio of skin friction drag to total drag does not increase. The amount of area reduction would be limited by the requirement that the velocity approach a low value permitting parachute deployment prior to impact, if a man or sensitive equipment were to be safely returned.

#### Example 2

Mass transfer effects on velocity and deceleration are shown for two cases: Constant volume as in porous injection, and diminishing volume as in ablation. Let

$$C_{D0}/\mu = 41.9 \quad [(W/CDA)_0 = 510 \text{ lb/ft}^2]$$

and  $\theta_E = 45^\circ$ . Assuming a spherical body:  $n = 1$ ,  $p = 0$ ,  $s = 0$ , so that  $N = 0$  for the first case;  $n = 1$ ,  $p = \frac{2}{3}$  and  $s = 0$ , so that  $N = \frac{2}{3}$  for the second case which can be shown for a randomly rotating sphere of uniform density which maintains a constant drag coefficient of unity.

The velocity-altitude and deceleration-altitude profiles are plotted on Figs. 7 and 8, respectively, for  $K = 0, 0.2, 0.4$  and 1.0. The magnitude of the decelerations are shown in Fig. 8 for  $V_E = 20,000$  fps. It may be seen that for up to 40 per cent of the mass transferred, there is very little resultant effect on the velocity and deceleration histories. This effect is even less for the ablating case wherein  $W/CDA$  remains more nearly constant.

The locus of maximum deceleration moves to a higher altitude and higher deceleration as the mass transfer rate increases. When the area is reduced during descent for the ablating sphere, the deceleration is lower as would be expected. Of course, an ablating body with a conical shape

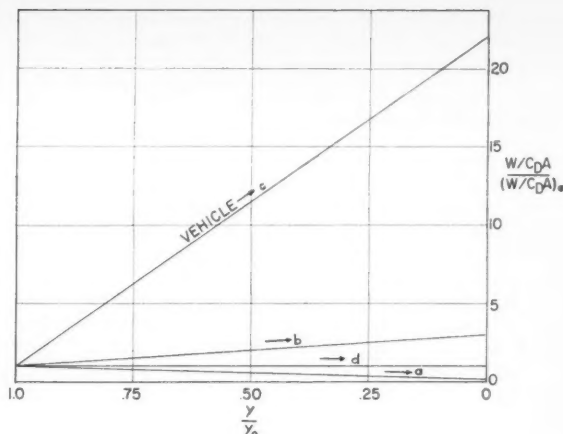


Fig. 4  $W/CDA$  vs. altitude for four vehicles

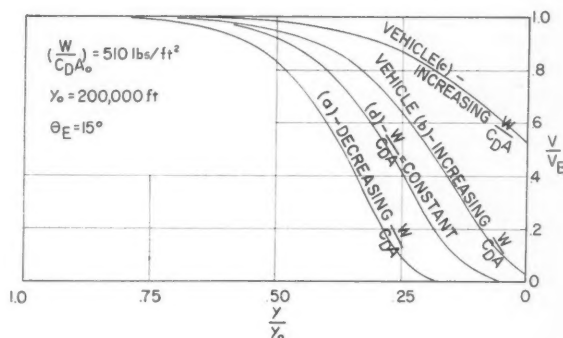


Fig. 5 Velocity vs. altitude for four vehicles. Three of the vehicles have varying  $W/CDA$  during re-entry

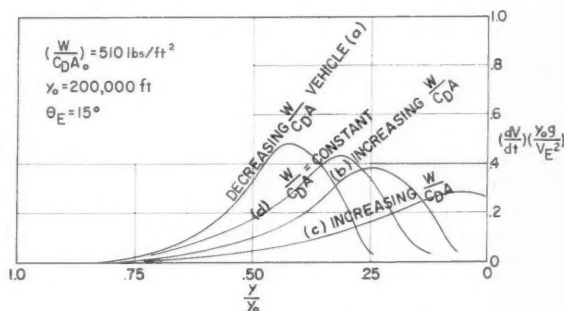


Fig. 6 Deceleration vs. altitude for four vehicles. Three of the vehicles have varying  $W/CDA$  during re-entry

Table 1 Example re-entry bodies with varying  $W/CDA$

Vehicle	$\frac{A_0}{A_{SL}}$	$\frac{C_{D0}}{C_{DSL}}$	$\frac{(W/CDA)_0}{(W/CDA)_{SL}}$	$p$	$s$	$n$	$N$	$K$
a	$\frac{1}{2}$	$\frac{1}{2}$	4.76	-3	-3	1	-6	0.2
b	2	2	0.33	3	3	1	6	0.2
c	4	6	0.046	13.2	17	1	30.2	0.1
d	1	1	1	0	0	0	1	0

could ablate at the nose and still maintain the same frontal area at its base. However,  $C_D$  would increase in this case, and a higher deceleration would be expected.

## Results and Conclusions

Equations have been presented for the velocity and deceleration of a ballistic re-entry vehicle which has a changing  $W/C_D A$  along the trajectory. These equations may be used to investigate variable geometry and mass transfer effects. This was done for several examples, from which it may be concluded that:

1 The maximum deceleration is not independent of the rate of change of  $W/C_D A$ , although it is well known that maximum deceleration is independent of  $W/C_D A$  when  $W/C_D A$  remains constant. Variable geometry has, in fact, a significant effect upon the re-entry trajectory, i.e., velocity, heating, impact location, etc.

2 By increasing  $C_D A$  during re-entry the maximum deceleration is shifted to a higher altitude, and the value of peak deceleration is increased. Decreasing  $C_D A$  has the opposite effect.

3 In the case of an ablating re-entry vehicle, the mass transfer process tends to increase the maximum deceleration and shift the position of maximum deceleration to a higher altitude. (The effect would be small for an efficient heat shield.)

4 If surface ablation takes place in such a manner that the drag area is reduced, the increased deceleration owing to mass transfer is less than if the area had remained constant.

5 Generally, for a fixed geometry vehicle with an efficient heat shield, the change in  $W/C_D A$  upon re-entry has a small influence upon its trajectory. However, aside from the variable geometry vehicle, the preceding analysis has a

useful application with regard to the behavior of separated missile stages or destructed components which may experience significant ablation after separation. Present range safety practice requires a knowledge of the behavior of these components up to impact or disintegration.

## Appendix: Coupling the Motion and Heating Equations

For large flight velocities, the effective heat absorbed within the boundary layer of an ablating body is large compared with the internal heat absorption. Thus

$$H_{eff} = q_s/\dot{m} = H_e + H_i \doteq H_e \quad [A-1]$$

where

$$H_i = C_{pi} \Delta T_i, \text{ internal body heat absorption}$$

$$H_e = 2/3 \bar{C}_p \Delta T_s, \text{ external heat absorbed within the boundary layer (for laminar stagnation point flow)}$$

$$\bar{C}_p = \text{a mean specific heat dependent upon concentration of coolant gas in boundary layer}$$

The laminar heat transfer rate at the stagnation point of an axisymmetric body is (Prandtl number = 1)

$$q_s = 0.765 (\rho_s \mu_s C)^{1/2} H_e \quad [A-2]$$

where

$$H_e = C_{pe} \Delta T_s \doteq (V^2/2) (\text{ft-lb/slug})$$

The heating rate  $q_s$  may be expressed solely as a function of velocity and altitude when: There is an adiabatic shock; the viscosity is proportional to the square root of the temperature; and the velocity gradient is as measured on a hemisphere by Crawford and McCauley (8)

$$q_s = 1.03 \times 10^{-4} \sqrt{\rho_{SL}/r_b} V^3 e^{-\beta y/2} (\text{ft-lb/ft}^2\text{-sec}) \quad [A-3]$$

Using the effective heat of ablation approximately proportional to the enthalpy difference leads to the relation

$$\dot{m} = \left( \frac{dm}{dy} \right) \left( \frac{dy}{dt} \right) = \frac{q_s}{H_{eff}} = -V \left( \frac{dm}{dy} \right) \sin \theta_E$$

where  $dm/dy$  is not a function of  $V$ .

Then the body mass lost per foot of altitude for a gas injected coolant in laminar flow becomes (9)

$$m' = \frac{6.43 \times 10^{-7} C_Q A e^{-\beta y/2} \text{ slugs}}{\sqrt{r_b} \left[ \frac{C_{p1}}{C_{p2}} + 2 \right] \sin \theta_E \text{ ft altitude}} \quad [A-4]$$

where  $C_Q$  is the integrated ratio of average body heating to stagnation point heating. Let

$$m' = dm/dy = S e^{-\beta y/2} \quad [A-5]$$

where  $S$  is a constant for a given body and re-entry angle at high flight velocities. Integrating  $m'$

$$m(y) = m_0 - \frac{2S}{\beta} e^{-\beta y/2} \quad [A-6]$$

Boundary conditions are

$$m = m_0, \text{ when } y = \infty$$

$$m = m_0 - (\text{mass lost through heating}), \text{ when } y = 0$$

The solution for the flight velocity as a function of mass transfer is as follows (using Eqs. [1 through 3] in the text)

$$m(y) \frac{dV}{dt} = \frac{1}{2} C_D \rho_{SL} A V^2 e^{-\beta y} \quad [A-7]$$

as before

$$dV/dt = -V \sin \theta_E (dV/dy) \quad [A-8]$$

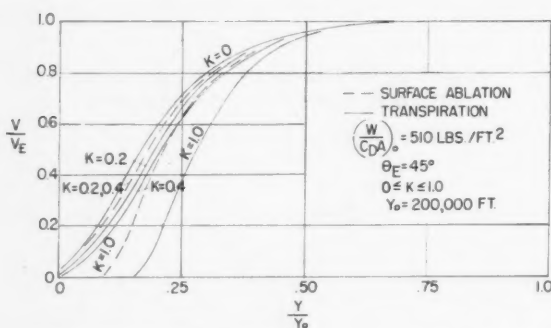


Fig. 7 Velocity vs. altitude for surface ablation and transpiration cooling

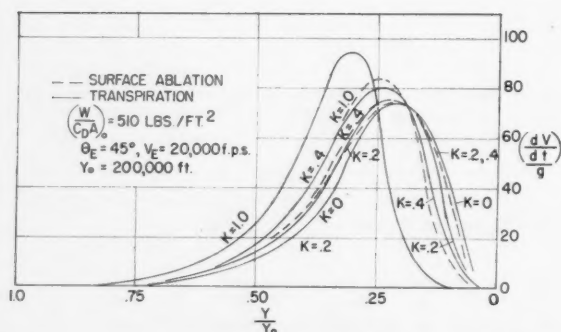


Fig. 8 Deceleration vs. altitude for surface ablation and transpiration cooling

Thus

$$[m(y)/V](dV/dy) = -Be^{-\beta y} \quad [A-9]$$

can be shown to have the solution

$$V = C_m^{-\frac{B\beta m_0}{2S^2}} e^{\frac{B\beta m}{2S^2}} \quad [A-10]$$

where

$$B = C_D \rho_{SL} A / 2 \sin \theta_E \quad [A-11]$$

From Equation [A-6]

$$V = C \left( m_0 - \frac{2S}{\beta} e^{-\beta y/2} \right) - \frac{B\beta m_0}{2S^2} \frac{B\beta}{2S^2} \left( m_0 - \frac{2S}{\beta} e^{-\beta y/2} \right) \quad [A-12]$$

To evaluate the constant, it is necessary that  $V = V_E$  at  $y = \infty$ . Thus

$$C = V_E \left( \frac{m_0}{e} \right)^{\frac{B\beta m_0}{2S^2}} \quad [A-13]$$

Assigning two dimensionless constants

$$k = B\beta m_0 / 2S^2 \quad P = 2S / \beta m_0$$

then

$$V = V_E \left( \frac{m_0}{e} \right)^k (m_0 - P m_0 e^{-\beta y/2})^{-k} \cdot \frac{e^k}{e^{kPe^{-\beta y/2}}} \\ = V_E \left( \frac{e^{-Pe^{-\beta y/2}}}{1 - Pe^{-\beta y/2}} \right)^k \quad [A-14]$$

which is the flight velocity of a ballistic re-entry vehicle that is ablating and therefore experiencing a variable  $W/C_D A$ .

## Nomenclature

$A$	= drag area of body
$C$	= velocity gradient along wall, $du/dx$ ; also used as a constant
$C_D$	= drag coefficient
$C_p$	= specific heat at constant pressure
$\bar{C}_p$	= mean specific heat at constant pressure
$C_q$	= heating coefficient for $q/q_s$ over body
$e$	= Napierian number, 2.7182
$g$	= gravitational acceleration
$H$	= enthalpy, $C_p \Delta T$
$K$	= nondimensional factor for controlling $W$ , $C_D$ and $A$ during re-entry

$m$	= body mass
$M$	= Mach number
$N$	= exponent for rate of change of $W/C_D A$ ; $N = p + s - n + 1$
$q$	= heat transfer rate per unit time, per unit area
$r_b$	= radius of body
$t$	= time
$T$	= temperature
$V$	= flight velocity
$W$	= vehicle weight
$x, y$	= horizontal and vertical space coordinates
$Z$	= dimensionless mass transfer parameter, $Z = (\beta/K) \times [1 - K(1 - \bar{y})]$
$\beta$	= reciprocal scale height for density distribution
$\Gamma(N)$	= gamma function
$\Gamma_x(N)$	= incomplete gamma function
$\Delta$	= increment
$\theta$	= flight path angle, measured from the horizontal
$\mu$	= coefficient of viscosity; or relative density = $m_0/\rho_{SL} A_0 y_0$
$\rho$	= density

## Subscripts

$E, 0$	= initial re-entry value
$s$	= stagnation point value
$SL$	= sea level value
$\infty$	= free stream condition
$1$	= coolant gas
$2$	= air
$(\ )$	= time derivative
$(\ )'$	= altitude derivative
$(\ )$	= mean value (thermal); or normalized value, initial re-entry condition

## References

- Phillips, R. L. and Cohen, C. B., "Use of Drag Modulation to Reduce Deceleration Loads During Atmospheric Entry," *ARS JOURNAL*, vol. 29, no. 6, June 1959, p. 414-422.
- Lees, L., "Similarity Parameters for Surface Melting of a Blunt Nose Body in a High Velocity Gas Stream," *ARS JOURNAL*, vol. 29, no. 5, May 1959, p. 345-354.
- Allen, H. J. and Eggers, A. J., Jr., "A Study of the Motion and Aerodynamic Heating of Missiles Entering the Earth's Atmosphere at High Supersonic Speeds," *NACA TN 4047*, Oct. 1957.
- Person, K., "Tables of the Incomplete Gamma Function," Cambridge University Press, London, 1922. (Reprinted.)
- Jeffreys, Sir H. and Jeffreys, B. S., "Methods of Mathematical Physics," Cambridge University Press, London, 1956, chap. 15.
- Jahnke, E. and Emde, F., "Tables of Functions," Dover Publications, Inc., N. Y., 1945, pp. 1-25.
- Computer Section of Federal Works Agency, "Tables of Sine, Cosine, and Exponential Integral," Federal Works Agency, N. Y., 1940.
- Crawford, D. H. and McCauley, W. D., "Investigation of a Hemisphere-Cylinder in the Langley 11" Hypersonic Tunnel at Mach Number 6.8," *NACA Rep. 1323*, 1957. (Supersedes TN 3706.)
- Warden, R. V., "Mass Transfer Effects on a Re-Entry Vehicle," S. M. Thesis, MIT, Cambridge, Mass., Jan. 1959.

## 1960-61 ARS Meeting Schedule

Date	Meeting	Location	Abstract Deadline
March 13-16	Missile and Space Vehicle Testing Conference	Los Angeles, Calif.	Past
April 4-6	Lifting Re-Entry Vehicles: Structures, Materials, and Design Conference	Palm Springs, Calif.	Past
April 26-28	Propellants, Combustion, and Liquid Rockets Conference	Palm Beach, Fla.	Past
May 3-5	Space Nuclear Conference	Gatlinburg, Tenn.	Past
May 22-24	National Telemetering Conference	Chicago, Ill.	Past
June 13-16	Joint ARS-IAS Meeting	Los Angeles, Calif.	Past
Aug. 7-9	Guidance and Control Conference	Palo Alto, Calif.	March 15
Aug. 16-18	International Hypersonics Conference	Cambridge, Mass.	March 31
Aug. 23-25	Biennial Gas Dynamics Symposium	Evanston, Ill.	Past
Oct. 2-7	XIIth International Astronautical Congress	Washington, D.C.	May 1
Oct. 9-14	ARS SPACE FLIGHT REPORT TO THE NATION	New York, N.Y.	April 15

Send all abstracts to Meetings Manager, ARS, 500 Fifth Ave., New York 36, N.Y.

# Limits for Stable Near-Circular Planetary or Satellite Orbits in the Restricted Three-Body Problem

S. H. DOLE<sup>1</sup>

The Rand Corp.  
Santa Monica, Calif.

In the vicinity of two massive bodies rotating in circles around their common center of mass there are regions in which near-circular orbits of a third body are stable, and other regions in which near-circular orbits are unstable. Expressions for calculating the limiting radii of the regions where stable near-circular orbits can exist are developed from Jacobi's integral to the equations of motion of a particle, and computed quantitative values for these radii are given in graphical and tabular form for mass ratios from  $10^{-8}$  to 0.5. An example is given of the application of these limits to an idealized Earth-moon system (mass ratio, 0.012128563).

A FUNDAMENTAL set of limits in the restricted three-body problem<sup>2</sup> may be established by exploring the question: In what regions of space in the vicinity of two massive bodies can a third body of infinitesimal mass remain in a stable near-circular orbit?

Since the computation of these limits is time consuming, and since the limits may be applied as approximations to a number of real problems in astronomy and orbit mechanics, we hope the results given here will be of general usefulness and interest.

The data, presented in tabular and graphical form, are solutions to a series of problems which are stated as follows. Determine the distance at which particles in circular orbits around either mass or around both masses together can exist, without exceeding the energy levels corresponding to certain critical values of the Jacobian constant  $C$ .

In the restricted three-body problem (reference coordinates rotating at the same angular velocity as the two massive bodies) it is well known that a set of zero relative velocity surfaces may be described around each of the individual bodies and around both bodies together. An example of the intersection of these surfaces with the  $xy$  plane is given in Fig. 1. Sketches of the approximate shapes of these surfaces in the  $xz$  plane and the  $yz$  plane are given by Buchheim (1)<sup>3</sup> and Moulton (2). These zero velocity surfaces are approximately spheres in the immediate vicinity of each of the masses, and approximately cylinders enclosing both masses at a distance from the masses, and are associated with high numerical values of the Jacobian constant. As the value of  $C$  is gradually reduced, the closed "spherical" surfaces around each of the massive bodies gradually expand, and the "cylindrical" surfaces around both bodies gradually contract. As  $C$  is reduced to a certain value  $C_1$  the expanding spheres around the two massive bodies impinge at a point  $p_1$ , the first Lagrangian libration point. As  $C$  is reduced further, the closed contours around the two bodies coalesce into a closed shape resembling a budded yeast cell, while the cylindrical curtains continue to contract. At  $C = C_2$ , the expanding "yeast cell" and the contracting curtain impinge at  $p_2$ , the second Lagrangian point. Further reduction of  $C$  results

in coalescence and formation of a single surface. At  $C = C_3$  another impingement of surfaces takes place at the third Lagrangian point  $p_3$ , and at  $C = C_4$  the surfaces shrink down to two points and disappear at the fourth and fifth Lagrangian points  $p_4$  and  $p_5$ , points in the  $xy$  plane which form equilateral triangles with the two massive bodies.

These zero velocity surfaces have the following significance for the present problem: A real third body has associated with it a specific and conserved value of the Jacobian constant  $C_n$  determined by its position and velocity. It cannot cross a surface of zero relative velocity corresponding to  $C_n$ , but is forever constrained to remain in regions of space where the zero velocity surfaces have a numerical value  $C \geq C_n$ . For example, if a particle has associated with it a value of  $C = C_1$ ,

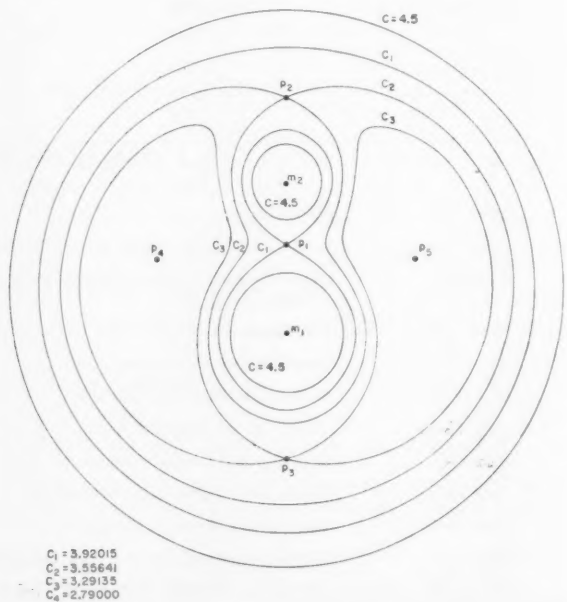


Fig. 1 Zero velocity curves in  $xy$  plane for mass ratio  $\mu$  equal to 0.3

Received June 6, 1960.

<sup>1</sup> Group Leader, Aero-Astronautics Dept. Member ARS.

<sup>2</sup> Two massive bodies rotate in circles around their common center of mass. The third body, of infinitesimal mass, moves in the same plane as do the massive bodies.

<sup>3</sup> Numbers in parentheses indicate References at end of paper.



and is initially within a closed envelope surrounding the larger of the two massive bodies, it cannot escape from the region around  $m_1$  delimited by the  $C_1$  contour. If it is initially outside the outer  $C_1$  contour, it cannot penetrate inside the space enclosed by this contour. On the other hand, if a particle has associated with it a value of  $C \leq C_1$ , it can potentially invade all parts of the space in the  $xy$  plane, no region being excluded.

Now let us consider a particle within the closed  $C_1$  contour around  $m_1$  which has associated within it  $C = C_1$ . Since it cannot escape from this region, it will either orbit endlessly or eventually impact on  $m_1$ . Qualitatively the most stable orbit it can have will be a near-circular orbit around  $m_1$ . Even more stable would be near-circular orbits of particles having  $C > C_1$ .

If we now depart somewhat from the restricted three-body problem and assume that, as in the real world, small perturbing influences are present which can effectively increase or decrease the value of  $C$ , or change the velocity vector by a small amount, it may be seen that a high degree of stability is required in order to enable the third body to survive for long periods of time. Thus if a third body has a value of  $C < C_1$ , even if it is initially in a near-circular orbit around  $m_1$ , one would have doubts as to its long term stability, since it can potentially enter the regions surrounding both  $m_1$  and  $m_2$ , and the probabilities of eventual collision with one of these bodies are much increased. Unfortunately, methods for assessing the long term stability of orbits in multi-body systems are not available. It may be said qualitatively, however, that near-circular orbits of particles with  $C = C_1$  represent the outermost stable orbits which can exist in the closed space about  $m_1$ ; this applies, also, for near-circular orbits around  $m_2$ . For particles in near-circular orbits around both bodies the associated value of  $C$  must be related to the outer  $C_2$  zero velocity curve such that  $C \geq C_2$ .

A graphical representation of the relationship between the Jacobian constant and particles moving at orbital velocity is given in Fig. 2. For an idealized Earth-moon case, values of  $C$  were computed for particles moving at orbital velocity in the  $xy$  plane and in a direction normal to the line joining the two masses. As may be seen from this figure, retrograde satellites of Earth have  $C$  values greater than  $C_1$ , and may be regarded as stable out to a distance of 0.239 lunar units<sup>4</sup> (ca. 57,000 miles), but less than  $C_1$  beyond this. Similarly, direct satellites of Earth are stable between Earth's surface and 0.635 lunar units (152,000 miles) and beyond 1.6056 lunar units (384,000 miles), but not between 0.635 and 1.6056 lunar units.

Direct satellites of the moon on near-circular orbits are stable out to 0.073 units (17,400 miles from the moon's center), whereas retrograde satellites are stable out to 0.043 units (10,300 miles from the center of the moon).

Using similar criteria it is possible to establish regions in which particles on near-circular orbits can exist in the neighborhood of two massive bodies as a function of the mass ratio  $\mu$ .

The expressions for computing the dimensions of these regions are developed from Jacobi's integral in the latter part of this paper.

For the example illustrated in Fig. 3 (where  $\mu = 0.1$ ), stable direct near-circular orbits around  $m_1$  can exist only inside region A, radius 0.44 units; stable retrograde near-circular orbits around  $m_1$  can exist only inside region B, radius 0.21; stable direct near-circular orbits around  $m_2$  can exist only inside region D, radius 0.14; stable retrograde near-circular orbits around  $m_2$  can exist only inside region E, radius 0.086 units; stable direct near-circular orbits around both masses can exist only outside of region F, radius 2.24 units;

<sup>4</sup> A lunar unit is taken to be 239,000 miles. Numerical agreement with 0.239 is coincidence.

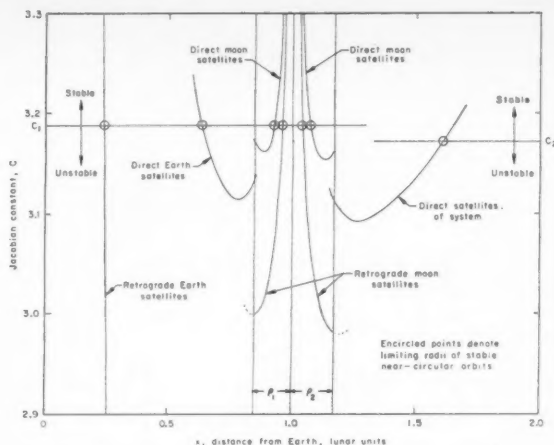


Fig. 2 Values of Jacobian constant  $C$  associated with particles crossing the  $x$ -axis perpendicular with orbital velocity, as a function of distance along  $x$ -axis. Mass ratio  $\mu$  equal to 0.012128563

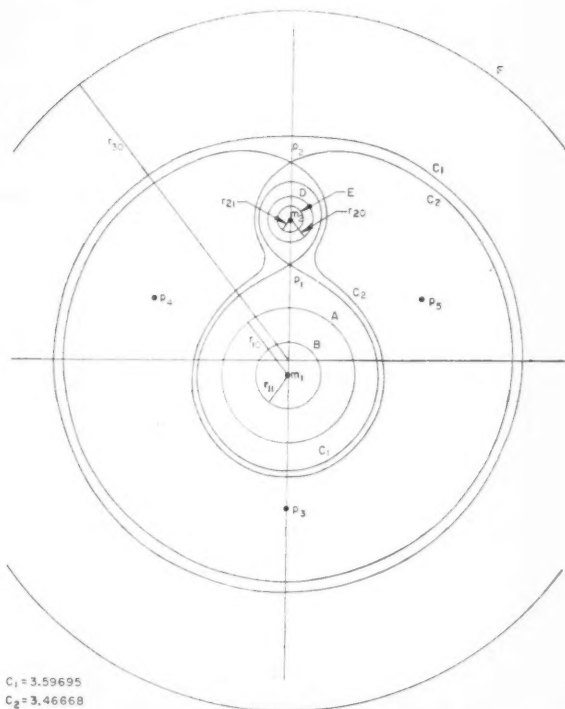


Fig. 3 Zero velocity curves in  $xy$  plane for mass ratio  $\mu$  equal to 0.1. Extreme limits for stable near-circular satellite orbits indicated

apparently none of the near-circular retrograde orbits around both masses are stable.

The regions inside the contours A, B, D and E and outside contour F might be called "permitted regions" for direct and retrograde inferior planets, for direct and retrograde satellites, and for direct superior planets, respectively. All regions outside of those enclosed by B and E might be called "forbidden regions" for retrograde planets and satellites, whereas regions outside of A and D but inside F might be called forbidden regions for direct planets and satellites. If we con-

Table 1 Location of libration points and radii of limiting regions for various mass ratios

$\mu$	$10^{-8}$	$10^{-6}$	$10^{-4}$	$10^{-3}$	0.01	$1/82.45^a$	0.1	0.2	0.3	0.4	0.5
$\rho_1$	$1.493 \times 10^{-3}$	$6.918 \times 10^{-3}$	0.03183	0.06771	0.14192	0.15085	0.29096	0.36192	0.41387	0.45838	0.50000
$\rho_2$	$1.495 \times 10^{-3}$	$6.950 \times 10^{-3}$	0.03253	0.07092	0.15677	0.16773	0.35970	0.47105	0.55673	0.63081	0.69841
$\rho_3$	$5.833 \times 10^{-7}$	$5.833 \times 10^{-5}$	$5.833 \times 10^{-3}$	$5.833 \times 10^{-4}$	$5.833 \times 10^{-3}$	$7.075 \times 10^{-3}$	$0.05839$	0.11716	0.17679	0.23705	0.30159
$C_1 - 3^b$	$2.009 \times 10^{-6}$	$4.294 \times 10^{-4}$	$8.989 \times 10^{-3}$	$0.03995$	0.10754	0.19814	0.59695	0.92015	0.96681	1.00000	1.00000
$C_2 - 3^b$	$2.005 \times 10^{-6}$	$4.280 \times 10^{-4}$	$8.856 \times 10^{-3}$	0.03851	0.15422	0.17199	0.46668	0.55239	0.55641	0.48196	0.45080
$C_3 - 3^b$	$1.000 \times 10^{-6}$	$1.000 \times 10^{-4}$	$1.000 \times 10^{-3}$	$1.000 \times 10^{-3}$	$9.998 \times 10^{-3}$	0.01213	0.09958	0.19732	0.29135	0.37908	0.45980
$3 - C_3^b$	$1.000 \times 10^{-6}$	$9.999 \times 10^{-6}$	$9.999 \times 10^{-4}$	$9.990 \times 10^{-4}$	$9.900 \times 10^{-3}$	0.00198	0.09000	0.16000	0.21000	0.24000	0.25000
1 (D)( $r_{20}$ )	$7.311 \times 10^{-4}$	0.01565	0.03316	0.06910	0.073 <sup>c</sup>	0.14140	0.13869	0.20564	0.20110	0.25115	0.25725
2 (E)( $r_{21}$ )	$7.327 \times 10^{-4}$	0.01559	0.03292	0.06822	0.043 <sup>c</sup>	0.13669	0.13635	0.20110	0.20110	0.25115	0.25725
3 (F)( $r_{22}$ )	$4.187 \times 10^{-4}$	$1.946 \times 10^{-3}$	0.01924	0.04091	0.043 <sup>c</sup>	0.08635	0.08635	0.12537	0.12537	0.15267	0.15267
4 (A)( $r_{10}$ )	$4.188 \times 10^{-4}$	$1.946 \times 10^{-3}$	0.01923	0.04087	0.04087	0.08618	0.08618	0.12510	0.12510	0.15235	0.15235
5 (B)( $r_{11}$ )	0.99543	0.97903	0.90729	0.81396	0.65436	0.625 <sup>c</sup>	0.43514	0.31878	0.31878	0.25725	0.25725
6 (C)( $r_{12}$ )	0.99484	0.97643	0.89764	0.79882	0.63693	0.625 <sup>c</sup>	0.42296	0.31065	0.31065	0.25725	0.25725
7 (D)( $r_{20}$ )	0.25000	0.24998	0.24949	0.24772	0.24022	0.239 <sup>c</sup>	0.21182	0.17883	0.17883	0.15267	0.15267
8 (E)( $r_{21}$ )	0.25000	0.24998	0.24949	0.24772	0.24019	0.239 <sup>c</sup>	0.21164	0.17853	0.17853	0.15235	0.15235
9 (F)( $r_{22}$ )	1.00459	1.02153	1.10448	1.23847	1.56291	1.60556	2.24305	2.41239	2.40770	2.22160	2.16517
10	1.00519	1.02420	1.11534	1.25773	1.59084	1.63396	2.27921	2.44086	2.43289	2.24289	2.16517

<sup>a</sup> Mass ratio for idealized Earth-moon system,  $\mu = 0.012125563$ .  
<sup>b</sup> Values for  $C_1 - 3$ ,  $C_2 - 3$ ,  $C_3 - 3$  and  $3 - C_3$  are tabulated, since  $C_1$ ,  $C_2$ ,  $C_3$  and  $C_4$  all approach 3 very closely for small values of  $\mu$ .  
<sup>c</sup> Approximate values (interpolated).

sider only direct planets of  $m_1$ , the larger of the two massive bodies, it may be seen that  $m_2$  has created a broad band around  $m_1$  in which no planets on near-circular orbits could be expected to exist. Such planets would be expected only inside contour  $A$  and outside contour  $F$ .

Dimensions of permitted regions in the restricted three-body problem for the range of  $\mu$  from  $10^{-8}$  to 0.5 are given in Table 1, and some illustrations drawn to scale of these regions for various mass ratios are given in Fig. 4.

### Analysis

Jacobi's integral to the equations of motion of a particle in the vicinity of two massive bodies that are rotating in circles around their common center of mass may be written as given by Buchheim (1)

$$v^2 = \omega^2(x^2 + y^2) + 2K(1 - \mu)/r_1 + 2K\mu/r_2 - c$$

Fig. 5 illustrates the nomenclature used in this paper.

If we normalize by letting the distance between the two masses equal unity, and the sum of the masses equal unity, for circular motion of the two massive bodies

$$\omega^2 = K$$

by setting  $c/\omega^2 = C$  and  $v/\omega = V$ , the integral may be rewritten

$$C = x^2 + y^2 + 2(1 - \mu)/r_1 + 2\mu/r_2 - V^2$$

Now consider a particle in circular orbit around the smaller of the two masses in the  $xy$  plane and with motion in the direct sense (CCW). At time  $t = 0$ , it is assumed to be on the  $x$ -axis ( $y = 0$ ,  $\dot{x} = 0$ ) between the two masses, and its velocity in intertial space is

$$-\sqrt{K\mu/r_2} = -\omega\sqrt{\mu/r_2}$$

However its velocity in rotating space

$$v = -\omega\sqrt{\mu/r_2} + \omega r_2$$

and

$$V^2 = \mu/r_2 - 2\sqrt{\mu/r_2} + r_2^2$$

also

$$x = 1 - \mu - r_2$$

and

$$r_1 = 1 - r_2$$

and Jacobi's integral becomes

$$C = (1 - \mu - r_2)^2 + 2(1 - \mu)/(1 - r_2) + \mu/r_2 + 2\sqrt{\mu/r_2} - r_2^2$$

If  $C$  is set equal to  $C_1$  and the equation solved for  $r_2$ , we obtain the maximum distance ( $r_{20}$ ) from the smaller mass  $\mu$  that a particle can be moving CCW at orbital velocity, without having so much energy that it could potentially (if perturbed slightly) cross the  $C_1$  zero relative velocity surface and escape from the neighborhood of the smaller mass.

Direct, between

$$C_1 = (1 - \mu - r_{20})^2 + \frac{2(1 - \mu)}{1 - r_{20}} + \frac{\mu}{r_{20}} + 2\sqrt{\mu/r_{20}} - r_{20}^2 \quad [1]$$

A similar expression which considers a particle in direct motion around  $\mu$ , but on a point on the  $x$ -axis on the side away from the larger mass, yields closely similar results.

Direct, beyond

$$C_1 = (1 - \mu + r_{20})^2 + \frac{2(1 - \mu)}{1 + r_{20}} + \frac{\mu}{r_{20}} + 2\sqrt{\mu/r_{20}} - r_{20}^2 \quad [2]$$



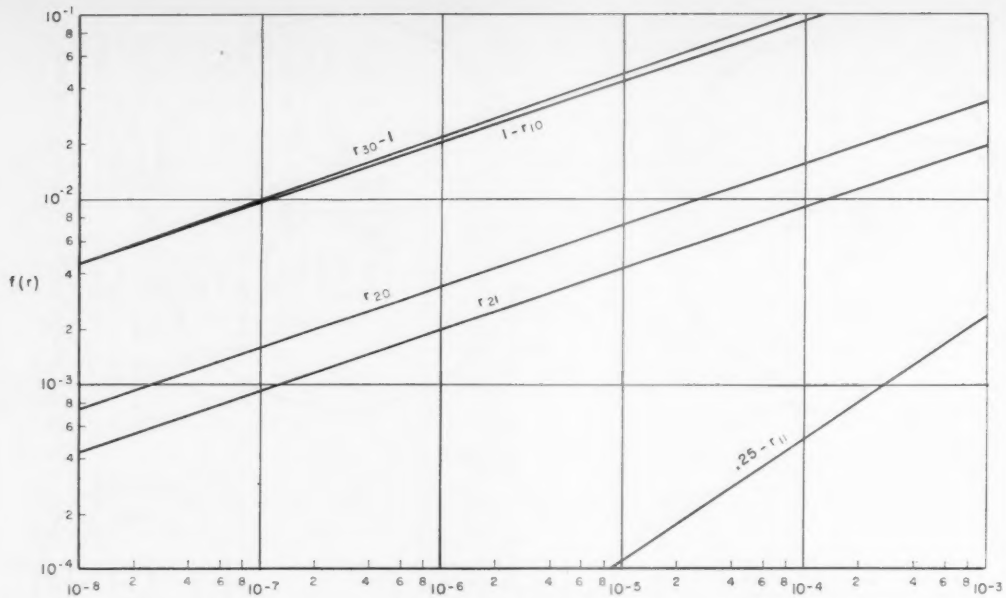


Fig. 6 Limiting radii of stable near-circular planetary and satellite orbits in restricted three-body problem as a function of mass ratio  $\mu$

Following is the equation for the minimum distance of particles in near-circular orbit around both masses, outside the outer  $C_2$  contour where velocities and distances correspond to  $C_2$  and where  $r_{30}$  is the distance from the common center of mass to the particle.

"Direct," beyond

$$C_2 = 2\sqrt{r_{30}} - \frac{1}{r_{30}} + \frac{2(1-\mu)}{r_{30} + \mu} + \frac{2\mu}{r_{30} - (1-\mu)} \quad [9]$$

"Direct," behind

$$C_2 = 2\sqrt{r_{30}} - \frac{1}{r_{31}} + \frac{2(1-\mu)}{r_{30} - \mu} + \frac{2\mu}{r_{31} + (1-\mu)} \quad [10]$$

"Retrograde," beyond

$$C_2 = -2\sqrt{r_{31}} - \frac{1}{r_{31}} + \frac{2(1-\mu)}{r_{31} + \mu} + \frac{2\mu}{r_{31} - (1-\mu)} \quad [11]$$

"Retrograde," behind

$$C_2 = -2\sqrt{r_{31}} - \frac{1}{r_{31}} + \frac{2(1-\mu)}{r_{31} - \mu} + \frac{2\mu}{r_{31} + (1-\mu)} \quad [12]$$

Results of machine computations of the roots of Equations [1 through 10] are given in Table 1. Equations [11 and 12] have no roots for values of  $r_{31} > 1 - \mu + \rho_2$ , hence "retrograde" motion of particles at orbital velocity corresponding to  $C \geq C_2$  apparently is not possible, and no stable "retrograde" near-circular orbits around both masses can exist. (Particles moving at orbital velocity around both masses will always have retrograde motion with respect to the rotating coordinate system. The terms "direct" and "retrograde" refer to motion with respect to inertial space.)

Results are shown graphically in Figs. 6 and 7. The functions  $(1 - r_{10})$ ,  $(0.25 - r_{11})$  and  $(r_{30} - 1)$  are plotted against  $\mu$ , since  $r_{10}$  and  $r_{30}$  both approach 1.0 asymptotically, and  $r_{11}$  approaches 0.25 for small values of  $\mu$ .

## Nomenclature

A = region around larger mass  $m_1$  within which stable direct

- near-circular inferior planetary orbits can exist, radius =  $r_{10}$
- B = region around larger mass  $m_1$  within which stable retrograde near-circular inferior planetary orbits can exist, radius =  $r_{11}$
- C = Jacobian constant, absolute units
- C = Jacobian constant, canonical units,  $C = c/\omega^2$
- $C_1$  = value of Jacobian constant associated with zero relative velocity surface passing through first Lagrangian libration point  $p_1$
- $C_2$  = value of Jacobian constant associated with zero relative velocity surface passing through second Lagrangian libration point  $p_2$
- $C_3$  = value of Jacobian constant associated with the zero relative velocity surface passing through third Lagrangian libration point  $p_3$
- $C_4$  = value of Jacobian constant at fourth and fifth Lagrangian libration points (equilateral points)  $p_4$  and  $p_5$
- $C_5 = 3 - \mu(1 - \mu)$
- D = region around smaller mass  $m_2$  within which stable direct near-circular satellite orbits can exist, radius =  $r_{20}$
- E = region around smaller mass  $m_2$  within which stable retrograde near-circular satellite orbits can exist, radius =  $r_{21}$
- F = region around both masses outside of which stable direct near-circular superior planetary orbits can exist, radius =  $r_{30}$
- G = gravitational constant
- K = product of gravitational constant  $G$  and total mass  $m_0$  of system
- $m_0$  = total mass of system,  $m_0 = m_1 + m_2$
- $m_1$  = mass of larger body
- $m_2$  = mass of smaller body
- $p_1$  = first Lagrangian libration point, in-line point between  $m_1$  and  $m_2$
- $p_2$  = second Lagrangian libration point, in-line point between  $m_2$  and  $+\infty$
- $p_3$  = third Lagrangian libration, in-line point between  $m_1$  and  $-\infty$
- $p_4, p_5$  = fourth and fifth Lagrangian libration points, "equilateral points"



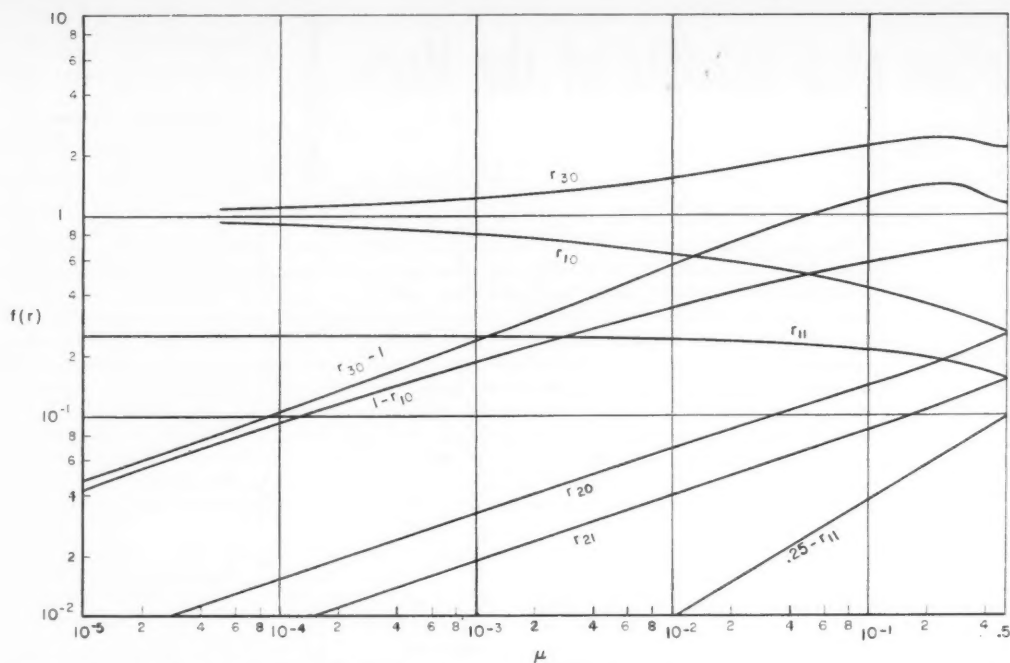


Fig. 7 Limiting radii of stable near-circular planetary and satellite orbits in restricted three-body problem as a function of mass ratio  $\mu$

- $r_1$  = radial distance from larger mass to particle  
 $r_2$  = radial distance from smaller mass to particle  
 $r_3$  = radial distance from center of mass to particle  
 $r_{10}$  = radius of outermost stable direct near-circular inferior planetary orbit of larger mass  $m_1$   
 $r_{11}$  = radius of outermost stable retrograde near-circular inferior planetary orbit of larger mass  $m_1$   
 $r_{20}$  = radius of outermost stable direct near-circular satellite orbit of smaller mass  $m_2$   
 $r_{21}$  = radius of outermost stable retrograde near-circular satellite orbit of smaller mass  $m_2$   
 $r_{30}$  = radius of innermost stable direct near-circular superior planetary orbit around center of mass  
 $t$  = time  
 $v$  = magnitude of velocity of a particle in rotating space  
 $V$  = particle velocity in rotating space, canonical units  
 $V = v/\omega$   
 $x$  = component of distance between particle and center of mass of system, measured parallel to line joining the two massive bodies (rotating coordinate system)  
 $y$  = component of distance between particle and center of mass of system, measured perpendicular to line joining the two massive bodies (rotating coordinate system)

- $\mu$  = ratio of smaller of the two masses to total mass of system  
 $= m_2/m_1 + m_2 = m_2/m_0$   
 for  $m_0 = 1$ ,  $\mu = m_2$  and  $1 - \mu = m_1$   
 $\rho_1$  = distance from  $m_2$  to  $p_1$   
 $\rho_2$  = distance from  $m_2$  to  $p_2$   
 $\rho_3$  = one minus distance from  $m_1$  to  $p_3$   
 $\omega$  = angular velocity of the two massive bodies

$\rho_1$ ,  $\rho_2$  and  $\rho_3$  were computed from the following quintic expressions derived by Moulton (2)

$$\begin{aligned}
 \rho_1^5 - (3 - \mu)\rho_1^4 + (3 - 2\mu)\rho_1^3 - \mu\rho_1^2 + 2\mu\rho_1 - \mu &= 0 \\
 \rho_2^5 + (3 - \mu)\rho_2^4 + (3 - 2\mu)\rho_2^3 - \mu\rho_2^2 - 2\mu\rho_2 - \mu &= 0 \\
 \rho_3^5 - (7 + \mu)\rho_3^4 + (19 + 6\mu)\rho_3^3 - (24 + 13\mu)\rho_3^2 + (12 + 14\mu)\rho_3 - 7\mu &= 0
 \end{aligned}$$

## References

- 1 Buchheim, R. W., "Motion of a Small Body in Earth-Moon Space," The Rand Corp., Research Memo. RM-1726, June 4, 1956.
- 2 Moulton, F. R., "An Introduction to Celestial Mechanics," The Macmillan Co., N. Y., 1959, 2nd revised edition, chap. VIII.

## Motion of a Satellite of the Moon

HARRY LASS<sup>1</sup> and  
CARLETON B. SOLLOWAY<sup>2</sup>

**Jet Propulsion Laboratory,  
California Institute of Technology  
Pasadena, Calif.**

The motion of a satellite of the moon depends chiefly on the force fields of the moon, Earth and sun. If one chooses a frame of reference attached to the moon, it can be shown that the force field resulting from the sun can be neglected when compared with Earth's field on the satellite. The effect of the Earth's field is shown to be of the same order of magnitude as is the moon's perturbing field resulting from its oblateness. The distance between Earth and moon will be assumed to be constant, and satellite orbits of small eccentricity will be studied. The averaging process of Kryloff-Bogoliuboff is applied to the equations of motion for an analysis of this restricted three-body problem, which is further complicated owing to the moon's oblateness. It is shown that a nearly circular polar orbit will digress less than 1 deg from a true polar orbit, and that the change in eccentricity of the orbit is less than a factor of  $e$  in one half of a year. An integral of the motion is obtained, such that accurate observations of a nearly circular orbit (not necessarily a polar orbit) will yield values of two fundamental constants related to the principal moments of inertia of the moon.

### Comparison of the Effects of Earth and Sun on the Motion of a Satellite of the Moon

LET THE masses of the satellite, sun, moon and Earth be indicated by  $m$ ,  $M_0$ ,  $M_1$  and  $M_2$ , respectively. We assume that a coordinate system centered at the sun is an inertial frame of reference. The motion of the satellite (see Fig. 1) is given by

$$m(d^2\mathbf{p}/dt^2) = \mathbf{F}_m(M_0) + \mathbf{F}_m(M_1) + \mathbf{F}_m(M_2) \quad [1]$$

with  $\mathbf{F}_m(M_0)$  the force of the sun on the satellite, etc. The motion of the moon is given

$$M_1(d^2\mathbf{s}/dt^2) = \mathbf{F}_{M_1}(M_0) + \mathbf{F}_{M_1}(M_2) \quad [2]$$

neglecting the force of the satellite on the moon,

From  $\mathbf{r} = \mathbf{p} - \mathbf{s}$  and Equations [1 and 2], it follows that

$$m \frac{d^2 \mathbf{r}}{dt^2} = \mathbf{F}_m(M_1) + \left[ \mathbf{F}_m(M_0) - \frac{m}{M_1} \mathbf{F}_{M_1}(M_0) \right] +$$

$$\left[ \mathbf{F}_m(M_2) - \frac{m}{M_1} \mathbf{F}_{M_1}(M_2) \right]$$

$$= \mathbf{F}_m(M_1) + GmM_0 \left[ \frac{\mathbf{s}}{|\mathbf{s}|^3} - \frac{\mathbf{p}}{|\mathbf{p}|^3} \right] +$$

$$GmM_2 \left[ \frac{\mathbf{w}}{|\mathbf{w}|^3} - \frac{\mathbf{v}}{|\mathbf{v}|^3} \right] \quad [3]$$

The magnitude of the middle term of Equation [3] can be approximated by  $GmM_0|\mathbf{r}|/|\mathbf{s}|^3$  for  $|\mathbf{r}| \ll |\mathbf{s}|$ ; the magnitude of the last term of Equation [3] can be approximated by  $GmM_2|\mathbf{r}|/|\mathbf{w}|^3$  for  $|\mathbf{r}| \ll |\mathbf{w}|$ . The ratio of these terms is

$$(M_0/M_2)|\mathbf{w}/\mathbf{s}|^3 \approx (330,000)(24/9300)^3 \approx (1/2)10^{-2} \quad [4]$$

which justifies omission of the effect of the sun.

### Quasi-Eulerian Coordinates

A description of the quasi-Eulerian coordinates associated with a moving point  $P$  is given in Fig. 2. The  $x, y, z$  coordinate system is a moon-fixed rectangular coordinate system with

origin at the center of the moon. The positive  $x$ -axis is directed toward Earth, the positive  $y$ -axis is in the moon's equatorial plane pointing in the direction of the orbit of the moon about Earth, and the positive  $z$ -axis is the moon's polar (spin) axis. The  $X, Y, Z$  coordinate system is an inertial frame of reference coinciding with  $x, y, z$  at  $t = 0$ . The  $x, y, z$  system rotates with constant angular speed,  $-\Omega$  about the  $Z$ -axis, relative to the  $X, Y, Z$  frame. The instantaneous orbital plane of a particle defined by the instantaneous position and velocity vectors  $\mathbf{r}$  and  $\dot{\mathbf{r}}$  intersects the  $x, y$  plane in the line of nodes  $N$ , and is inclined to that plane at the angle  $\beta$ . The unit vector  $\mathbf{N}$  is directed along the line of nodes making an angle  $\alpha$  with the  $x$ -axis, and  $\mathbf{H}$  is a unit vector normal to the orbital plane. A trihedral is formed by defining  $\mathbf{M} = \mathbf{H} \times \mathbf{N}$ . Finally, the position vector  $\mathbf{r}$  makes an angle  $\psi$  with the line of nodes.

### Potential Field of Moon and Earth

Neglecting higher order terms, the moon's potential is given by (1)<sup>3</sup>

<sup>3</sup> Numbers in parentheses indicate References at end of paper.

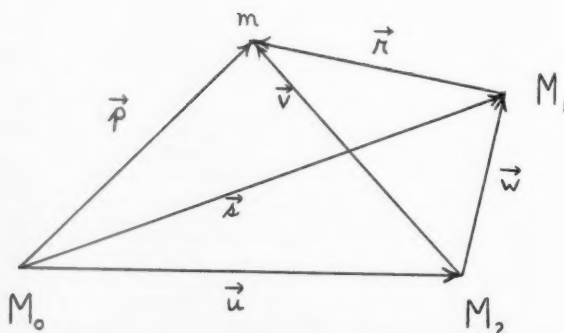


**Fig. 1** Position vectors of satellite, moon and Earth, relative to the sun

Received June 20, 1960.

<sup>1</sup> Research Specialist.

<sup>2</sup> Research Specialist.

$$V_1 = -\frac{GM_1}{R} \left\{ \frac{R}{r} + \frac{R^3 J}{r^3} \left( \frac{1}{3} - \sin^2 \psi \sin^2 \beta \right) + \frac{R^3 K}{r^3} [\cos 2\alpha (\cos^2 \psi - \sin^2 \psi \cos^2 \beta) - \sin 2\alpha \sin 2\psi \cos \beta] \right\} \quad [5]$$

The principal moments of inertia of the moon about the  $x, y, z$  axes, respectively, are  $A, B$  and  $C$ , with  $M_1$  equal to the mass of the moon, and  $R$  equal to the radius of the moon in the direction of the moon's orbit. The numerical values of  $J$  and  $K$  are obtained from (2). The values of  $J$  and  $K$  are

$$\begin{aligned} J &= (3/2M_1R^2)[C - (1/2)A - (1/2)B] \approx 0.00034 \\ K &= (3/4M_1R^2)(B - A) \approx 0.000035 \end{aligned} \quad [6]$$

One must also obtain Earth's potential. The  $x$ -axis points toward Earth, so that the third term of Equation [3] can be written (for a unit mass) as

$$\mathbf{F} = -GM_2 \left[ \frac{(x-D)\mathbf{i} + y\mathbf{j} + z\mathbf{k}}{[(x-D)^2 + y^2 + z^2]^{3/2}} + \frac{\mathbf{i}}{D^2} \right] \quad [7]$$

For  $x^2 + y^2 + z^2 \ll D^2$ , with  $D$  the fixed distance between Earth and the moon, Equation [7] can be replaced by

$$\mathbf{F} \approx (GM_2/D^3)(2x\mathbf{i} - y\mathbf{j} - z\mathbf{k}) = -\text{grad}[(GM_2/2D^3)(r^2 - 3x^2)] \quad [8]$$

Thus, Earth's potential is

$$V_2 = (GM_2/2D^3)r^2[1 - 3(\cos \psi \cos \alpha - \sin \psi \sin \alpha \cos \beta)^2] \quad [9]$$

The total potential is  $V_1 + V_2$  as given by Equations [5] and [9]. Comparing  $GM_1R^2K/r^3$  with  $GM_2r^2/2D^3$  for a satellite near the moon yields

$$\frac{GM_1R^2K/r^3}{GM_2r^2/2D^3} \approx 2 \left( \frac{M_1}{M_2} \right) \frac{D^3}{R^3} K \approx 10 \quad [10]$$

Thus, the  $K$  term of  $V_1$  is slightly more important than the  $V_2$  term in determining the motion of the satellite. Actually, one should compare  $\text{grad } V_1$  with  $\text{grad } V_2$ . If this is done, the  $K$  term still remains slightly more dominant than the force field of Earth.

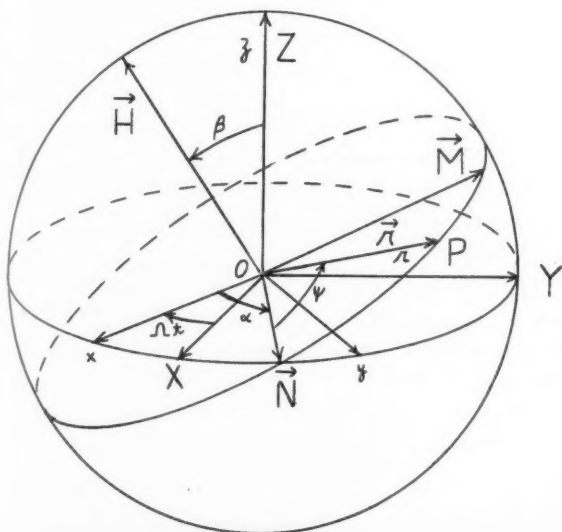


Fig. 2 Quasi-Eulerian coordinates

## Equations of Motion

The kinetic energy per unit mass can be shown to be given by

$$T = (1/2)[\dot{r}^2 + r^2\dot{\psi}^2 + r^2\sin^2 \psi \dot{\beta}^2 + r^2(1 - \sin^2 \psi \sin^2 \beta)(\dot{\alpha} - \Omega)^2 - 2r^2\sin \psi \cos \psi \sin \beta \dot{\beta}(\dot{\alpha} - \Omega) + 2r^2\cos \beta(\dot{\alpha} - \Omega)\dot{\psi}] \quad [11]$$

The Lagrangian governing the motion is  $L = T - (V_1 + V_2) = T + (GM_1/r) - V$ , where  $V$  is the perturbing potential of the moon and Earth. If we let  $r = (h^2/GM_1) \times [1 + \epsilon \cos(\psi - w)]^{-1}$ , it can be shown that Lagrange's equations of motion yield

$$\begin{aligned} d\alpha/dt &= \Omega - (1/h \sin \beta)(\partial V/\partial \beta) \\ d\beta/dt &= -(\cot \psi/h)(\partial V/\partial \beta) \\ dh/dt &= -\partial V/\partial \psi \\ d\psi/dt &= h/r^2 + (\cot \beta/h)(\partial V/\partial \beta) \\ d\epsilon/dt &= -\frac{h}{GM_1} \sin(\psi - w) \frac{\partial V}{\partial r} - \frac{1}{h\epsilon} \left[ (\epsilon^2 - 1) + \frac{h^4}{G^2 M_1^2 r^2} \right] \frac{\partial V}{\partial \psi} \\ dw/dt &= \frac{h}{GM_1 \epsilon} \cos(\psi - w) \frac{\partial V}{\partial r} + \frac{\cot \beta}{h} \frac{\partial V}{\partial \beta} - \frac{\sin(\psi - w)}{h\epsilon} \left( 1 + \frac{h^2}{GM_1 r} \right) \frac{\partial V}{\partial \psi} \end{aligned} \quad [12]$$

Equations [12] are the equations for the variations of the elements; see (3). Since  $\psi$  is a cyclic variable, replace  $d\alpha/dt$  with  $(d\alpha/d\psi)(d\psi/dt) \approx (h/r^2)(d\alpha/d\psi)$ , neglecting  $(\cot \beta/h) \times (d\alpha/d\psi)(\partial V/\partial \psi)$ , since  $(d\alpha/d\psi)(\partial V/\partial \psi)$  is a product of two small terms. Similarly, one considers  $d\beta/d\psi$ ,  $dh/d\psi$ ,  $d\epsilon/d\psi$  and  $dw/d\psi$ . Since the elements are slowly varying, the averaging process of Kryloff-Bogoliuboff [see (4)] can be applied to the new system of equations by integrating  $\psi$  over the range  $(0, 2\pi)$ . The following results are then obtained with  $\mu = GM_1$  and  $\epsilon \ll 1$

$$\begin{aligned} \frac{d\alpha}{d\psi} &= \frac{\Omega h^3}{\mu^2} - \frac{\mu^2 R^2}{h^4} \cos \beta \times \\ &\quad \left( J - K \cos 2\alpha + \frac{3M_2 h^{10}}{2M_1 \mu^5 R^2 D^3} \sin^2 \alpha \right) \\ \frac{d\beta}{d\psi} &= \frac{\mu^2 R^2}{h^4} \left( K + \frac{3M_2 h^{10}}{4M_1 \mu^5 R^2 D^3} \right) \sin 2\alpha \sin \beta \\ \frac{dh}{d\psi} &= 0 \\ \frac{d\epsilon}{d\psi} &= \frac{3\mu^2 R^2 K \epsilon}{4h^4} \times \\ &\quad [\sin 2\alpha \cos 2w \cos \beta + \cos 2\alpha \sin 2w(1 + \cos^2 \beta)] + \\ &\quad \frac{15M_2 h^6}{4M_1 D^3 \mu^3} [\sin 2\alpha \cos 2w \cos \beta + \\ &\quad \sin 2w(\cos^2 \alpha - \sin^2 \alpha \cos^2 \beta)] \end{aligned} \quad [13]$$

An integral of the motion can be obtained from the first three equations of Equations [13] in the form

$$-(2\Omega h^7/\mu^4 R^2) \cos \beta + [J - K \cos 2\alpha + (3M_2 h^{10}/2M_1 \mu^5 R^2 D^3) \sin^2 \alpha] \sin^2 \beta = \text{constant} \quad [14]$$

Accurate observations of a nearly circular orbit would yield values of  $\alpha, \beta$  and  $h$ , from which one could obtain values of  $J$  and  $K$  from Equation [14].

In order to investigate stability of a nearly circular polar

orbit, let  $\beta = \pi/2 - \sigma$ ,  $\sigma \ll 1$ ,  $\sin \beta \approx 1$ ,  $\cos \beta \approx \sigma$ . Thus, from Equations [13]

$$\frac{d\alpha}{d\psi} \approx -\frac{\Omega h^3}{\mu^2}$$

$$d\sigma/d\psi \approx -(\mu^2 R^2/h^4)(K + 3M_2 h^{10}/4\mu^5 R^2 D^3) \sin 2\alpha \quad [15]$$

An integration, with  $\sigma = 0$  for  $\psi = \psi_0$ , yields the inequality

$$|\sigma| \leq (\mu^4 R^2/\Omega h^7)(K + 3M_2 h^{10}/4M_1 \mu^5 R^2 D^3) \quad [16]$$

For a satellite near the moon's surface

$$h^2 \approx \mu R \approx R^4 \psi^2$$

$$\Omega \approx (2\pi/4300)(\text{rad/min})$$

$$|\sigma| \leq (1.5) 10^{-2} \text{ rad} < 1 \text{ deg}$$

Thus, an almost circular polar orbit near the moon's surface will deviate, at most, 1 deg from the polar plane.

Since the preceding analysis requires an orbit of small eccentricity, it is necessary to examine  $d\epsilon/d\psi$ . From Equations [12] and for  $\beta \approx \pi/2$  it follows that

$$\epsilon \leq \epsilon_0 \exp [(3\mu^2 R^2 K/4h^4 + 15M_2 h^8/4M_1 D^3 \mu^3) \psi]$$

$$\leq \epsilon_0 \exp [(5.5) 10^{-5} \psi] \quad [17]$$

with  $\epsilon_0$  the initial eccentricity. The eccentricity will increase at most, by a factor of  $e$  when  $(5.5)10^{-5} \psi = 1$ . The time associated with this increase of eccentricity is approximately one half of a year. Thus, a satellite of the moon will tend to remain in an almost circular polar orbit for a considerable length of time.

## References

- 1 Jeffreys, H., "The Earth, Its Origin, History, and Physical Constitution," University Press, Cambridge, Eng., 1952, p. 140.
- 2 Allen, C. W., "Astrophysical Quantities," University of London Press, 1955, p. 162.
- 3 Moulton, F. R., "Celestial Mechanics," The Macmillan Co., London, 1914, pp. 404-406.
- 4 Minorsky, N., "Introduction to Non-Linear Mechanics," J. W. Edwards, Publ., Ann Arbor, Mich., 1947, pp. 183-206.

# Stanford University 1961 Summer Institute on Space Technology (Rockets)

June 26-August 5, Stanford, Calif.

Directed by Professor Howard S. Seifert and administered by Stanford University for the National Science Foundation. Other members of the teaching staff include: Dr. Robert W. Buchheim, Rand Corp.; Ernest E. Sechler, CalTech; Profs. Irvin Glassman, Jerry Grey and Martin Summerfield, Princeton; Jack Vogel and Herbert R. Lawrence, United Technology Corp.; Dr. Robert Dillaway, Rocketdyne; and Dr. John Teem, Electro-Optical Systems.

Participants will be selected primarily on the basis of their potentiality for teaching courses in rocketry at the engineering college level. Minimum requirements: Baccalaureate degree, the equivalent of two years of full-time college level teaching by July 1961, and mathematics background through ordinary differential equations.

The major objective of this Institute is to supply a full set of notes and a rich background of reference material so that each participant may return to his own university equipped to offer a sound graduate level course in rocket design.

Request applications and further information from:

Mr. Lyman Nickel  
DEPARTMENT OF AERO ENGINEERING  
STANFORD UNIVERSITY, STANFORD, CALIF.



# Slotted Tube Grain Design<sup>1</sup>

MAX W. STONE<sup>2</sup>

Rohm & Haas Co.  
Huntsville, Ala.

A mathematical analysis was made of the internal burning slotted tube configuration, which has distinct advantages for certain solid propellant applications. Those advantages are zero sliver, high loading density and thick web capability, low stress concentration, and mandrels that can be made cheaply and in a relatively short time. The central disadvantage is that an insulating liner is required to protect the motor wall in the slot region. The results of the mathematical analysis were programmed for an electronic computer, and calculations made for a wide range of the parameters of interest. These data have been prepared in graphical form for greater utility.

THE INCREASING demand for missiles with greater thrust capability has caused rocket designers to investigate all means of improving the efficiency of rockets. The desirability of having higher impulse propellants, and lighter and stronger metal parts has, properly, been emphasized. In recent years the design of solid propellant grain configurations has taken on new meaning with the requirement that the greatest efficiency be realized in every phase of rocket performance. The technical literature has recorded this increased interest in an activity that was for a time classed as an art rather than a science. A recent survey paper (1)<sup>3</sup> on grain design lists many such papers. The time has passed when a grain designer must know from experience and memory, or evolve by trial and error with compass and straight edge, the configuration which most nearly meets the particular requirements.

The present paper is a continuation of grain design work in which Rohm & Haas has been interested since 1954. Previously published work (2) has centered around the star, wagonwheel and modified wagonwheel designs.

## Discussion

The slotted tube configuration,<sup>4</sup> as shown in Fig. 1, consists of a cylindrical tube of propellant into which has been cast or cut a number of slots. These slots connect the inner and outer surfaces of the tube and extend part of its length.

The configuration offers some striking advantages for the ballistician. Perhaps the most obvious is its inherent lack of sliver in a nonerosive situation, since it is basically an internal burning cylinder. Because of its simplicity the configuration, with two exceptions, is essentially free from regions of stress concentration such as appear in the star and other more complex designs. The region at the interior end of each slot is, of course, an exception; however, this is not a source of major trouble. The second exception is that very thick webs may be obtained in this configuration. In some propellants the stresses arising from the casting and curing

of such webs are relieved only by cracking, even though there are no points of stress concentration in the configuration. The design simplicity is also an important factor in mandrel machining and fabrication; the mandrels are less costly and can be made in less time than more complicated cores, such as the star and wagonwheel.

Loading fraction increases with increasing web thickness, or burning distance, which permits use of high burning rate propellants in highly loaded designs, or of low burning rate propellants to obtain very long burning times. In a thick web cylindrical design, the throat area to port area ratio ( $J$ ) would be critical; however, slots make possible loading fractions up to and above 95 per cent with reasonable  $J$  values.

The one apparent disadvantage of the slotted tube design is in the exposure of the motor wall in the slots to the hot, high velocity combustion gases. This condition requires an effective insulating liner, the requirement becoming more critical with longer burning times.

Some basic assumptions were made about the grain and the manner in which it may be used. It is considered to be case-bonded and inhibited at the nonslotted end. Elliptical and hemispherical head and/or tail end filling is not considered; the grain is a right-circular cylinder with slots spaced at equal intervals around the periphery. Although the slots are generally at the tail end of the grain, they may be

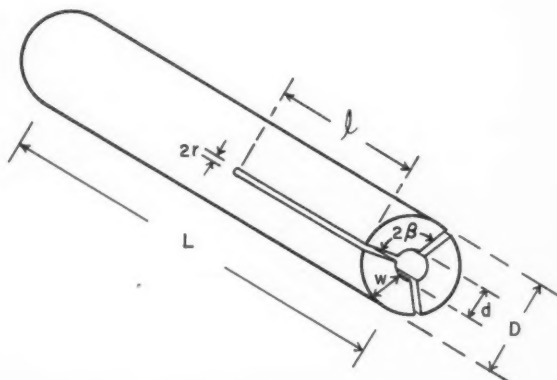


Fig. 1 Slotted tube design

Presented at the ARS Solid Propellant Rocket Research Conference, Princeton, N. J., Jan. 28-29, 1960.

<sup>1</sup> The work reported in this paper was carried out for the U. S. Army under Contract no. DA-01-021-ORD-11878.

<sup>2</sup> Scientist, Interior Ballistics Research Group, Redstone Arsenal Research Div. Member ARS.

<sup>3</sup> Numbers in parentheses indicate References at end of paper.

<sup>4</sup> This configuration apparently was pioneered by the Hercules Powder Co. at the Allegany Ballistics Laboratory.

placed at the head end at the discretion of the ballistician. The only calculated quantity of concern would be the area of port, which will, of course, significantly affect the  $J$  ratio. It is assumed that burning obeys the normal laws, and the propellant regresses in parallel layers. Erosive burning is ignored. Exact representation of surface and volume is tedious in places, as reference to the equations will indicate. Since the configuration cannot be considered only from a two-dimensional standpoint, it is necessary to use double integration formulas with some of the small sections of the grain. This may seem unnecessarily burdensome when approximations could be used, and indeed there are indications that these small areas and volumes can be ignored with negligible effect on total values. An attempt has been made to show the derivations in sufficient detail to permit visualization and to adequately describe the sections referred to.

The ballistic quantities of interest are defined in a manner similar to that of the star design, except that three-dimensional rather than cross-sectional values are used. Thus, the  $L/D$  ratio is important because this defines the length of the unit or 1-in. diameter grain. Scaling is utilized, as will be noted later.

### Mathematical Analysis

Initial surface is found by calculating the following collection of surfaces: Surface of inner perforation, minus surface lost to slots, plus area of the uninhibited end, minus area in end lost to slots, plus area within the slots. Following this order

$$S_i = \pi dL - Nd \arcsin \frac{2r}{d} - Nd \int_0^r \frac{\sqrt{r^2 - y^2}}{\sqrt{(d/2)^2 - y^2}} dy + \frac{\pi}{4} (D^2 - d^2) - Nr(\sqrt{D^2 - 4r^2} - \sqrt{d^2 - 4r^2}) + \frac{Nd^2}{8} \left[ 2 \arcsin \left( \frac{2r}{d} \right) - \frac{4r}{d^2} \sqrt{d^2 - 4r^2} \right] - \frac{ND^2}{8} \left[ 2 \arcsin \left( \frac{2r}{D} \right) - \frac{4r}{D^2} \sqrt{D^2 - 4r^2} \right] + Nl(\sqrt{D^2 - 4r^2} - \sqrt{d^2 - 4r^2}) + \frac{\pi}{2} Nr(\sqrt{D^2 - 4r^2} - \sqrt{d^2 - 4r^2}) + \left[ \frac{\pi}{2} Ndr - 2Nr \int_0^r \sqrt{\frac{x^2 + (d/2)^2 - r^2}{r^2 - x^2}} dx \right] - \left[ \frac{\pi}{2} NDr - 2Nr \int_0^r \sqrt{\frac{x^2 + (D/2)^2 - r^2}{r^2 - x^2}} dx \right] \quad [1]$$

If the grain may be considered to have coordinate axes as shown in Fig. 2, with the origin at the intersection of the centers of the two cylinders which meet at right angles, the equation of the large cylinder is

$$x^2 + z^2 = (d/2)^2 \quad [2]$$

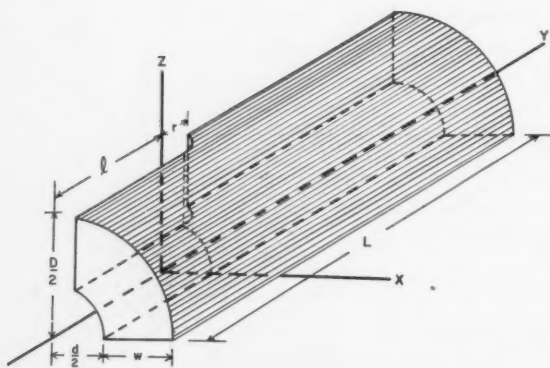


Fig. 2 Sector of slotted tube configuration showing location of coordinate axes

whereas the equation of the smaller cylinder is

$$x^2 + y^2 = r^2 \quad [3]$$

The larger cylinder is the center perforation; the smaller is the rounded end of the slot, actually half of a cylinder. The small areas left over at the intersection of the two cylinders can then be found using the following general formula for the area on a curved surface

$$\text{Area} = \int_S \sqrt{1 + (\partial z / \partial x)^2 + (\partial z / \partial y)^2}^{1/2} dy dx \quad [4]$$

Application of this formula and integration with respect to  $y$  yields the three integrals in  $x$  found in Equation [1]. By suitable transformations the first integral (the third term) becomes

$$A_1 = 2r^2 N \int_0^{\pi/2} \frac{\cos^2 \phi d\phi}{\sqrt{1 - k_1^2 \sin^2 \phi}} \quad [5]$$

where  $k_1 = 2r/d < 1$ . This is a complete elliptic integral of the form  $A_1 = 2Nr^2 B(k_1^2)$  of which  $B(k_1^2)$  is a tabulated function (3). This integral represents the curved surface on the inner perforation that is displaced by the semicylindrical slot end and is subtracted from the surface of the inner perforation.

The major part of the surface inside the semicylindrical slot end is found by considering a right circular half cylinder from the outer propellant surface to the inner perforation parallel to the  $Z$ -axis (Fig. 2). The second integral of the  $S_i$  equation, along with the preceding term in the same equation,

deals with the surface around the side of the small cylinder below the plane normal to the  $Z$ -axis at the intersection of the inner perforation with the  $Z$ -axis. This surface is added. The last integral and its preceding term are analogous, but this is at the outer surface of the grain, and this area is subtracted.

The latter two integrals can also be transformed into complete elliptic integrals; however, because they tend to cancel each other and are relatively small, it was decided that their effect would be negligible, and so they are omitted from actual calculations.

The final surface presents a new problem for consideration. In some cases the web will burn out before the slots burn through the "wall" separating them. In other cases, where the slots are closer together and/or the web thicker, the slots may "join" before web burnout, so that final surface will be limited entirely to the unslotted portion of the grain. However, since burning also occurs in the end of the slot, progressing toward the unslotted end of the grain, a scalloped effect will be noted on the final surface as viewed perpendicular to the  $Y$ -axis (see Fig. 4).

Since different equations will be required in the two cases described, it is well to define a condition that specifies which situation exists for the particular grain under consideration. From Fig. 3 it may be seen that

$$m = (D/2) \sin \beta - r \quad [6]$$

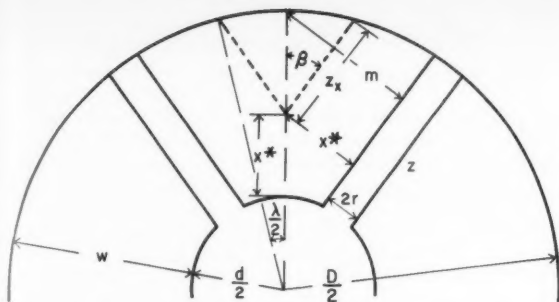


Fig. 3 Cross section of slotted tube configuration

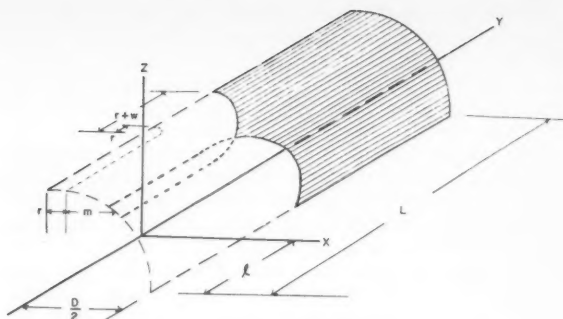


Fig. 4 Final surface when  $m < w$

If  $m = w$ , the sides of the slots meet at the motor wall at web burnout. If  $m > w$ , they will not meet before web burnout; but if  $m < w$ , they will intersect to give the scalloped effect mentioned previously and shown in Fig. 4.

In the cases where  $m \geq w$ , the following formula for final surface will suffice

$$S_f = w\{\pi D - ND \arcsin [2(r+w)/D]\} + \pi D - 2N(r+w)^2 B(k_2^2) + \pi D L = \pi D(L-w) - ND(l-w) \arcsin [2(r+w)/D] - 2N(r+w)^2 B(k_2^2) \quad [7]$$

where  $k_2 = 2(r+w)/D < 1$ . The function  $B(k_2^2)$  is analogous to  $B(k_1^2)$  which was obtained from Equation [5], and the same tabulation (3) is used for its evaluation.

Final surface in the case  $m < w$  is given by Equation [8]

$$S_f = \pi D[L - (l+r+w)] + 2N \int_0^{(D/2) \sin \beta} \int_{\sqrt{(r+w)^2 - x^2}}^{\sqrt{(D/2)^2 - x^2}} \{1 + [-x/\sqrt{(D/2)^2 - x^2}]^{1/2}\} dy dx \quad [8]$$

The double integral represents the scalloped part of the shaded area in Fig. 4. Integration with respect to  $y$  transforms Equation [8] into Equation [9]

$$S_f = \pi D[L - (l+r+w)] + \pi D(r+w) - ND \int_0^{(D/2) \sin \beta} [\sqrt{(r+w)^2 - x^2}/\sqrt{(D/2)^2 - x^2}] dx \quad [9]$$

The integral (including the factor  $ND$ ) reduces to the difference of incomplete elliptic integrals of the first and second kind. By suitable transformations it can be put into the form

$$I = 2N(r+w)^2 \int_0^\phi \cos^2 \psi d\psi / \sqrt{1 - k_3^2 \sin^2 \psi} \\ = 2N(r+w)^2 \int_0^\phi [(\sqrt{1 - \sin^2 \psi})^2 / \sqrt{1 - k_3^2 \sin^2 \psi}] d\psi \quad [10]$$

which becomes

$$I = 2N(r+w)^2 \left[ \int_0^\phi \frac{d\psi}{\sqrt{1 - k_3^2 \sin^2 \psi}} - \int_0^\phi \frac{\sin^2 \psi d\psi}{\sqrt{1 - k_3^2 \sin^2 \psi}} \right] \quad [11]$$

where

$$\phi = \arcsin [(D/2) \sin \beta / (r+w)]$$

$$k_3 = 2(r+w)/D = k_2$$

Legendre's standard form of the elliptic integral of the first kind is

$$F(k, \phi) = \int_0^\phi d\psi / \sqrt{1 - k^2 \sin^2 \psi} \quad [12]$$

and of the second kind is

$$E(k, \phi) = \int_0^\phi \sqrt{1 - k^2 \sin^2 \psi} d\psi \quad [13]$$

If Equation [13] is rewritten as

$$E(k, \phi) = \int_0^\phi [(\sqrt{1 - k^2 \sin^2 \psi})^2 / \sqrt{1 - k^2 \sin^2 \psi}] d\psi \\ = \int_0^\phi d\psi / \sqrt{1 - k^2 \sin^2 \psi} - k^2 \int_0^\phi \sin^2 \psi d\psi / \sqrt{1 - k^2 \sin^2 \psi} \quad [14]$$

then

$$\int_0^\phi \sin^2 \psi d\psi / \sqrt{1 - k^2 \sin^2 \psi} = (F - E)/k^2 \quad [15]$$

Therefore, Equation [9] can be reduced to the form

$$S_f = \pi D(L-l) - 2N(r+w)^2 [F - (F-E)/k^2] \quad [16]$$

The functions  $F(\alpha, \phi)$  and  $E(\alpha, \phi)$ , where  $k = \alpha$ , are tabulated (3). Because it is theoretically nonexistent, no equation is required for sliver.

The volumetric loading fraction is given by the following equation

$$\epsilon = \frac{\text{volume of propellant}}{\text{volume of motor}} = \frac{4}{\pi D^2 L} \left[ \frac{\pi}{4} L(D^2 - d^2) - r l N (\sqrt{D^2 - 4r^2} - \sqrt{d^2 - 4r^2}) + \frac{d^2 l N}{8} \left( 2 \arcsin \frac{2r}{d} - \frac{4r}{d^2} \sqrt{d^2 - 4r^2} \right) - \frac{D^2 l N}{8} \left( 2 \arcsin \frac{2r}{D} - \frac{4r}{D^2} \sqrt{D^2 - 4r^2} \right) - \frac{\pi}{4} N r^2 (\sqrt{D^2 - 4r^2} - \sqrt{d^2 - 4r^2}) \right] \quad [17]$$

In this equation the small volumes analogous to the surfaces represented by elliptic integrals have been ignored. As in the case of the surfaces, they tend to cancel, and the labor involved in obtaining the equations and hence the numerical values appears to be much out of proportion to their effect on the whole value for loading fraction.

It is usually desirable, if not necessary, for the rocket grain designer to know the shape of the pressure-time curve which will be produced by his grain. It is essential to be able to calculate the propellant surface area as a function of the distance burned normal to the surface.

The burning surface of a slotted tube grain may pass through three distinct phases during the course of its consumption. Initially the propellant will burn outward in the interior cylinder, and sideways and lengthwise in the slots. If the web is thick enough and the slots close enough together, eventually the curved cylindrical interior surface separating adjacent slots will disappear into a line contact between the two slots. This is pictured in cross section in Fig. 3, and it may be seen that this occurs when  $x = x^*$ , which is defined as

$$x^* = (d \sin \beta - 2r)/2(1 - \sin \beta) \quad [18]$$

As  $x$  increases further, the propellant between the adjacent slots diminishes rapidly and will vanish before  $x = w$ . Thus the third phase of burning involves only the unslotted, cylindrical section of the grain. This section is inhibited on one end, but burns on the other end which now has a scalloped appearance.

When  $x > x^*$ , the distance  $Z_x$  (see Fig. 3) must be calculated by a formula different from that used when  $x < x^*$ . An additional complication occurs when the slot length is less than web, permitting the end burning effect to extend into the region characterized by the semicylindrical slot ends. Equations are given which, in the interest of practicality, approximate to a sufficient degree of accuracy the surface changes required when  $l < w$ . The equations for all cases are as follows.

Case 1A:  $x < x^*, x \leq l$

$$S_x = \pi(d + 2x)(L - x) + \frac{\pi}{4} [D^2 - (d + 2x)^2] - 2N(r + x)^2 B(k_x^2) + \frac{N}{4} (d + 2x)(d + 6x - 4l) \arcsin \frac{2(r + x)}{d + 2x} + N(l + 1.070796 r + 0.070796 x) Z_x - \frac{ND^2}{4} \arcsin \frac{2(r + w)}{D} \quad [19]$$

where

$$k_x = [2(r + x)/(d + 2x)] < 1$$

$$Z_x = \sqrt{D^2 - 4(r + x)^2} - \sqrt{(d + 2x)^2 - 4(r + x)^2}$$

Case 1B:  $x < x^*, x \leq m, x > l$

$$S_x = \pi(d + 2x)(L - l) + \frac{\pi}{4} [D^2 - (d + 2x)^2] + N(r + x) \left( \frac{\pi}{2} - \zeta - \cos \zeta \right) Z_x - [\pi(d + 2x)(r + x)] \left[ \frac{(\pi/4)(r + x)^2 + (r + m)(x - l) - (1/2)(r + x)(\cos \zeta)(x - l) - (1/2)(r + x)^2 \zeta}{(r + x)(r + m)} \right] \quad [20]$$

where

$$\zeta = \arcsin [(x - l)/(r + x)]$$

$$Z_x = \text{same as in Equation [19]}$$

$$m = (D/2) \sin \beta - r$$

Case 2A:  $x \geq x^*, x \leq m, x \leq l$

$$S_x = \pi(d + 2x)(L - l) + 2NZ_x(l - x) + (NZ_x^2/2) \sin 2\beta + (ND^2/8)(\lambda_x - \sin \lambda_x) + \pi N(r + x)Z_x - 2N(r + x)^2 B(k_x^2) \quad [21]$$

where

$$Z_x = (1/2) \sqrt{D^2 - 4(r + x)^2} - (r + x)/\tan \beta$$

$$\lambda_x = 2\{\beta - \arcsin [2(r + x)/D]\}$$

$$k_x = 2(r + x)/(d + 2x) < 1$$

Case 2B:  $x \geq x^*, x \leq m, x > l$

Use Equation [20] (case 1B).

Case 3:  $x > x^*, x > m$

$$S_x = \pi(d + 2x)(L - l) -$$

$$2N(r + x)^2 \left[ F_x - \frac{F_x - E_x}{k_x^2} \right] \quad [22]$$

where

$$k_x = 2(r + x)/(d + 2x) < 1$$

$$F_x, E_x = \text{functions of } \alpha \text{ and } \phi$$

$$\alpha = \arcsin k_x$$

$$\phi = \arcsin [(d + 2x) \sin \beta / 2(r + x)]$$

### Calculation and Presentation of Data

The equations listed in the previous section, which describe the interrelationship of the design parameters, have been programmed using a small, digital electronic computer, the Royal Precision LGP-30. Quantities specified to be varied over a fairly wide range were progressivity ratio, web, grain length and number of slots. With those quantities specified, the computer determined  $l$  the slot length, and then calculated the initial and final surfaces, the volume and loading fraction, and the port area.

All calculations were made for  $D = 1.0$ , so that  $L$  is actually equivalent to the  $L/D$  ratio. Scaling is accomplished by



multiplying all linear dimensions  $d, w, l, L$  and  $r$  by the desired diameter; by multiplying propellant surface areas and grain port area by the diameter squared; and by multiplying volume by the diameter cubed. Progressivity ratio and loading fraction are, of course, independent of diameter.

The radius  $r$ , essentially a stress relief fillet, was chosen to be  $0.03D$ , the same value as that used in earlier star design work. No difficulty has been experienced in using this value in a number of slotted tube grains.

In order for the results of the computer program to be generally available and used more easily, it was decided to exhibit on graphs as much of the data as possible. Accordingly, graphs of the type shown in Fig. 5 have been prepared. There are 83 graphs covering the range of  $N$  from 2 through 5 and of  $L/D$  ratios from 1 through 15. Length to diameter ratios of less than 1 were calculated; however, analysis of the result led to the conclusion that they would be of little or no value. Grains which are as short as that will surely require head and/or tail filling and an inhibitor arrangement different from that proposed here; the graphs could not be extrapolated to cover these possibilities.

From the graphs one can obtain information relating  $N, L, l, \epsilon, PR, w$  and  $S_i$ . Also, of course,  $S_f$  can be found from  $S_i$  and  $PR$ . There are two sets of web lines: The wider lines with the arrow heads pointing down relate  $w, \epsilon, l$  and  $PR$ , the narrower lines with arrow heads pointing up relate  $w, l$  and  $S_i$ .

In using the graphs, one might have specified the web (or loading fraction), the progressivity ratio and the  $L/D$  ratio. After deciding upon the number of slots to be used, reference to the proper wide web lines will show the slot length required. Relating the particular slot length to the corresponding narrow web line will show the initial surface of the design.

Important information that could not be included on these design graphs is the shape of the surface-time trace. The characteristic shape of the trace of a slotted tube grain is initially progressive; then it rounds over smoothly and decreases until web burns out or the slots burn through, whichever occurs first. In designs where there are enough slots and the web is thick enough ( $w > m$ , see Table 1), so that the slotted end is consumed before web burnout, the final portion of the trace will again become progressive. In short  $L/D$  motors, say  $L/D = 2$ , the effect of burning the scalloped end left by the slots will pretty well neutralize the progressive tendency of the cylindrical portion of the grain.

Something can be done, however, to give the ballisticon some idea of the severity of the "hump" in the surface-time trace without solving the equations for surface as a function of distance burned. In Fig. 6 the maximum height of the hump as a per cent of initial surface is plotted as a function of web, with  $L/D$  as a parameter,  $PR$  constant at 1.00 and  $N = 2$ . Additional information of this type and the design graphs described are provided in (4).

## Application

Ten slotted tube designs have been made by Rohm & Haas Co. for use in test motors. These have loading fractions ranging from 46 to 95.5 per cent, and have been used in motors ranging from 2 to 23 in. in diameter. The design has lived up to expectations, and the problem of insulation in the slots has not been too difficult in the motors used.

Table 1 Values of  $m$

$N$	$m$
2	> radius
3	0.4030
4	0.3235
5	0.2638

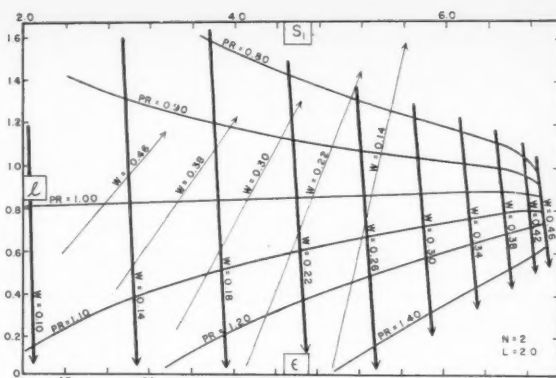


Fig. 5 Design graph for slotted tube configuration

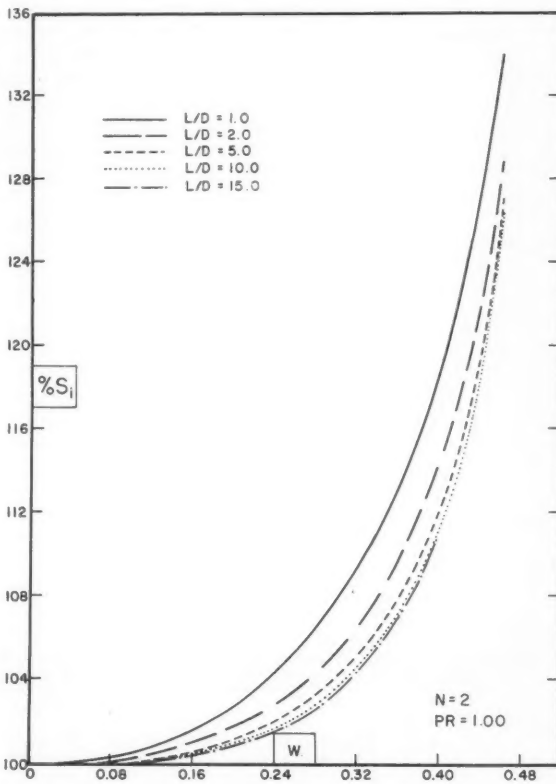


Fig. 6 Maximum height of surface-time trace relative to initial surface

Certainly, as burning times are increased the problem will increase in severity and better liners will be required. A 23-in. diameter motor containing a thousand pounds of propellant has been fired successfully.

An example of a pressure-time trace obtained from the static firing of a slotted tube configuration is shown (Fig. 7, solid line). Inasmuch as this motor had a hemispherical head end, the trace is more regressive than is indicated by the theoretical surface-time trace for the cylindrical portion of the grain (Fig. 7, dotted line). When the additional surface area in the head end, and the decrease in length of the grain from this effect is included, the theoretical trace is as shown by the dashed line in Fig. 7. The propellant used had a pressure exponent of 0.55.

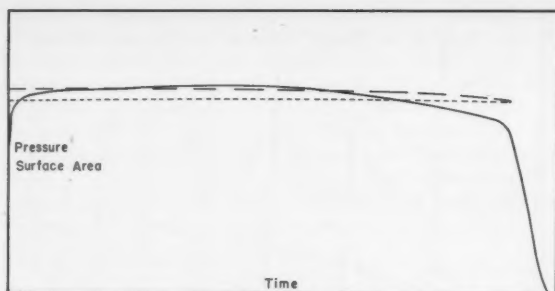


Fig. 7 Surface-time and pressure-time traces for a slotted tube design

This particular design has three slots, a web of  $0.184 D$ ,  $L/D = 5.66$ ,  $l = 2.40 D$ ,  $\epsilon = 58.3$  per cent,  $PR = 1.01$  (right circular cylinder), area of port of  $0.349 D^2$ , and  $S_i = 14.706 D^2$  (including head end). The actual motor size was  $6 \times 33$  in., and the  $J$  value for this particular shot was  $0.214$ . The ratio of the pressure integral during burning time to the total pressure integral was  $0.967$ , comparable to that obtained with purely cylindrical grains under nonerosive conditions. The regressivity exhibited in the firing was probably caused by the differential in burning rates between the head and tail as the result of pressure drop along the grain length.

#### Acknowledgments

The author wishes to express his appreciation to Mrs. M. L.

Cagle for invaluable assistance in performing the calculations, and to H. Wilson for locating an error in the mathematical work.

#### Nomenclature

- $D$  = OD of grain, ID of lined motor
- $d$  = ID of grain
- $L$  = length of grain
- $l$  = length of slot side (to point of tangency with half cylinder at interior end of slot)
- $N$  = number of slots
- $r$  = radius of stress relief cylinder at interior end of slot, half the width of slot
- $m$  = burning distance for slot burnout, perpendicular distance from point of slot burnout to side of original slot (see Fig. 3)
- $\beta = \pi/N$
- $w$  = web,  $(D - d)/2$ , burning distance
- $S_i$  = initial propellant surface area
- $S_f$  = final propellant surface area
- $\epsilon$  = volumetric loading fraction
- $PR$  = progressivity ratio,  $S_f/S_i$

#### References

- 1 Vandenkerckhove, J. A., "Recent Advances in Solid Propellant Grain Design," *ARS JOURNAL*, vol. 29, no. 7, July 1959, pp. 483-491.
- 2 Stone, M. W., "A Practical Mathematical Approach to Grain Design," *JET PROPULSION*, vol. 28, no. 4, April 1958, pp. 236-244.
- 3 Jahnke, E. and Emde, F., "Table of Functions," Dover Publications, Inc., N. Y., 4th ed., 1945.
- 4 Stone, M. W., "The Slotted-Tube Grain Design," Rohm & Haas Co. Rep. no. 8-27, Huntsville, Ala., distributed according to Joint Army-Navy-Air Force Solid Propellant list, additional copies available from author on request.

## Proposed Ground and Flight Program to Develop Space Age Materials

M. A. STEINBERG,<sup>1</sup>  
J. L. FOX<sup>2</sup> and  
B. W. AUGENSTEIN<sup>3</sup>

Lockheed Aircraft Corp.  
Sunnyvale, Calif.

The motivations for extending our knowledge of the behavior of materials in space are given. A proposed program is developed for accomplishing this. The program is set up to: Obtain fuller measurements of the geophysical environments; compile and collate critical geophysical data now scattered throughout a multitude of printed sources; support and extend existing theoretical studies to aid in designing experiments, interpreting and extrapolating the data; extract maximum benefits from presently limited testing opportunities; study means of interpreting tests measuring response to extreme environment forces; and coordinate ground with space testing phases. A description is given of an extensive program presently under way contributing to the attainment of these goals. Requirements for extension of this and similar programs are discussed.

Presented at ARS Structural Design of Space Vehicles Conference, Santa Barbara, Calif., April 6-8, 1960.

<sup>1</sup> Manager, Materials, Propulsion and Ordnance Research. Member ARS.

<sup>2</sup> Manager, Flight Sciences. Member ARS.

<sup>3</sup> Scientific Advisor, Satellite Systems. Member ARS.

## Motivation for Materials Research

**T**HE DEVELOPMENT of space systems is in its early stages today. By space systems we mean those which involve a satellite network of which the primary purpose is to gather, process and transmit information. Economic and operational factors generally indicate that such systems are most attractive when they can function reliably for as long as possible, while satisfying stated mission goals. For such systems to be effective, a number of functional operations must become simply routine as our research and development program unfolds. Some of these operations involve getting into orbit, others involve all the ancillary functions required in orbit, such as two-way communication and command links, operation of power supplies, operation of stabilization and orbit adjust systems where required, etc.

Until these operations are purely routine, we cannot fully exploit the information gathering effectiveness of satellite systems. Until we can concentrate on the design of special payloads to exploit properly this unique kind of data gathering platform, assured that our vehicles will get into orbit properly, and that all the ancillary functions will continue to be performed for a long time, we will not have reached our research and development goals.

We have obtained a considerable amount of scientific information on some early satellite and space flights; however, there is still much detailed engineering information required before we can make the successful operation of the vehicle and its subsystems a routine and commonplace occurrence. Vital to this is increased knowledge of the performance of basic materials in space. Our knowledge of the effects of the space environment on the behavior of materials is not complete, especially as regards the designing of satellite systems for reliable operation for prolonged periods of time.

There are distinct problem areas connected with the behavior of materials in space, and design problems connected with choosing proper materials. We must: First, learn more about the actual environment, especially the many simultaneous environmental conditions existing in space; second, determine the effects of these special environments on our materials; and third, determine ways of improving our materials, and of establishing criteria for selecting materials for appropriate jobs with confidence that these materials will operate successfully and usefully. We do not yet have the background of information needed to state several solutions to design problems, and thus to have the flexibility to design high confidence, but not over conservative systems, matched to the primary purpose of the vehicle. We must be in a position to concentrate on making specific applications of the system our primary objective, without having to compromise this because of possible unknown or deleterious effects on ancillary components of the vehicle system.

### Environmental Factors in Space

We estimate some of the effects of the following forces, and indicate specific needs for greater knowledge of these forces:

Electromagnetic radiation from the sun and Earth. We need data on the solar energy spectrum with emphasis on the ultraviolet and x-ray regions.

Primary cosmic radiation.

Local radiation regions, as in the Van Allen Belts. We need data about auroral zone radiation and the dependence upon the strength of solar activity.

Dust particle concentration from meteoric and earlier corpuscular matter, atomic and molecular matter in Earth's vicinity.

Corpuscular radiation from the sun. We require, for normal and intense solar activity periods, these data: Energy spectrum and density; near-Earth shielding by Earth's magnetic field; measurement of neutral and charged particles for many atomic weights.

The presence of ultra-low vacua in the environment, and

the corresponding high pumping rates for material in the vehicle. We must account for the local atmosphere produced by chemical reactions, sublimation, evaporation, sputtering, the result of dust collisions, and the interaction of these with the general external environment and with other parts of the vehicle.

Nuclear bursts in space and internally generated nuclear radiation represent perturbations of the natural environment and constitute special problems.

These environments may exist singly or in combinations. They may be causally related; e. g., a major solar flare and its associated phenomena will perturb several environments. They may act with varying or disparate force upon materials; one environment may accelerate or-compensate for the degrading effects of another. They may be of unequal force over periods of time; i.e., the cycle of intense solar flare activity over the past few years will probably be followed by a cycle of quiescence. Finally, some environments will exert only a momentary force as a vehicle passes through on the way to orbit altitudes.

In designing high confidence space systems we are confronted on one hand by a limited ability to simulate simultaneously all these special environments, and on the other by the absolute need to study and plan against their complex interworking. Further, we should know time-space average values, variations over Earth (large and small scale), variations in time, etc., for a number of possible orbits.

Successful space design is a result of successful test activity. This depends upon a well-defined integrated program, a firm understanding of problems we must overcome or allow for in space materials, and an unabating test effort, both on the ground and in space.

### Problems Posed by the Environment

The following list is a representative one, including problems of varying severity. Lower risk problems have been included with the knowledge that uncertainty about these should soon be removed by ground or space experiments.

Erosion of surfaces and finishes by meteoric matter. The removal of surface layers degrades thermal control. Pitting distorts optical characteristics and causes light scattering, etc.

Long-term radiation effects of such backgrounds as the Van Allen radiation on solid state materials, dielectrics and organic materials like lubricants or Teflon.

Sublimation and evaporation of materials in high vacua. Surfaces and substrata may be affected by the modification of the gas layer on the vehicle. Organics are particularly sensitive to material loss.

Friction on bearing surfaces, switching contacts, gear trains, etc. Questions here are: What is the best method of preventing seizing where metal parts come in contact? What is the significance of changes in the surface gas film? What are lubrication requirements?

Degradation of organic materials by the shortwave end of the solar spectrum. We need to investigate the inhibitive force of a vacuum on the degradation, photo-ionization of surface layers of solids, and mechanisms of charge transfer between the vehicle and the environment.

Permeability of thin shells, such as space structures rigidized by internal pressure.

Behavior of thin films of material. These are used to control transmissive characteristics, or emissive or radiative properties of vehicle and component surfaces. Even within the vehicle they may be influenced by environmental factors.

Sputtering of materials by incident atomic and molecular surface bombardment of an intensity to change surface properties and cause system malfunctions. To assess the difficulties, we must determine yield ratios (surface atoms removed per incident particle) and measure the factors, i.e., pressure and surface preparation, which influence yield ratios

for several incident particle types at the actual energy of the encounter.

Solar plasma or corpuscular radiation which produces these varied effects relative to altitude and location: High energy sputtering (1),<sup>4</sup> radiation damage to plastic surfaces and a consequent hydrogen evolution charring and carbonizing at high exposures. One source pessimistically suggests that a single major flare could accelerate both sputtering and radiation damage, either one of which may result from normal events (2).

Special problems may arise because of leakage radiation produced by nuclear devices which have requirements for thermal dissipation of energy. These are merely noted, since they depend on specific details of source design, shielding properties, etc.

The effects of these are uncertain and may turn out to be phantom problems; however, each has the potential to damage electrical, mechanical or optical properties of the vehicle and its components. Until we eliminate uncertainty about environmental forces and our space materials' response to those forces, we must continue to seek answers to these three determinative questions: What are the actual environmental conditions? What are the effects of these upon our materials? How can we select and improve materials for use in space?

#### Implications of Thermal Control Design

The distance we have to travel before we can supply these answers can best be gaged by reviewing some aspects of thermal control and the means we have evolved for studying and testing effects of the degradation of organic vehicles, and the roughening or erosion by atom and particle impact of exposed surfaces.

To begin with, allowable temperature variations differ between components. Electron tubes and transistors can operate over a temperature range between 0 and 100 C with relatively small variation of failure rate. On the other hand, paper capacitors and film resistors may increase in failure rate by a factor of about 5 as the ambient temperature rises from 0 to 100 C. Photographic devices or film may become seriously affected unless the temperature range is held to rather small limits with a reasonable mean temperature. Some of these effects result from the nature of film materials, others from thermal perturbations of optical properties; e.g., variations of focal length should be held to well within a value  $f R_E$ , where  $f$  is the focal ratio and  $R_E$  is the resolution if the optical precision is to remain high.

Similarly, there is a relatively significant effect of temperature on semiconductor devices used for photovoltaic solar energy conversion (3). Silicon cell efficiency is roughly halved as the temperature rises from 0 to 100 C. Other equipment, by contrast, operates most effectively at extremes of the temperature range. For example, in an ideal thermal receiver approximating an infrared radiation detector, the minimum detectable power (and the signal to noise ratio) varies approximately as the  $\frac{5}{2}$  power of the absolute temperature (4). Such high sensitivity to temperature has been essentially demonstrated (5) by experiments with photoconductive materials in which the main noise was generation-recombination (the dominant noise at the temperatures considered, 100 to 300 K). Consequently, there is a positive benefit in operating photoconductive devices at rather low temperatures, particularly in a passive fashion, which would allow us to take advantage of this characteristic of photoconductive detectors without a complex active system.

Conventional bearings are also relatively temperature sensitive. Their mean operating life can degrade rapidly in 100 C local temperatures, whereas gyros, clocks or generators of very stable frequencies will function precisely only within tight temperature limits.

Our thermal control methods, whether in active or passive

systems, must be of a high confidence level. At this time passive techniques seem most capable of building confidence; first, because they operate with less degradation than active ones, and second, because they can perform supplementally in the complex active systems. But whichever technique we employ must be evolved slowly and surely through a program of testing.

#### Problems of Testing

Can we gather data as effectively on the ground as under actual flight conditions? We do not fully know the space environment.

Why not simulate the space environment for testing even though we are still probing real space environments? We may not be able to reproduce space conditions on the ground. We cannot simulate the shortwave length portion of the solar spectrum, corpuscular radiation, ultra-low vacuums, or the impact of atoms, ions, molecules and dust particles. It is most difficult to create the simultaneous and interacting effects of micrometeorites, sputtering sources, ultraviolet radiation and thermal cycling.

Which is the better technique for data gathering from space flights, telemetering or recovery of the specimens? These may complement one another. For example, telemetered temperatures can indicate thermal control device degradation, but to pinpoint the precise sources of the degradation requires recovery and study of the material.

How useful is ground testing? Space testing as we know has many advantages. It does not require the elaborate bulk of equipment that ground testing does, and it verifies beyond doubt the validity of our calculations and our ground testing. Still, ground testing is readily controlled, and it has a growing range of applications. For instance, laboratory methods might be devised for testing components which must have long operating lives by accelerating aging tests through increased stresses and maintenance of extreme levels of the parameters involved. Ground testing can, in this way, compress the time required for measuring vehicle and component reliability.

In conclusion, an optimum testing program will be one which correlates ground with space gathered results, one which conserves time wherever possible, and which requires nominal commitments of equipment.

#### Summary of Suggested Program

The following five point program for testing materials incorporates complementary and concurrent activities. Some of these are already being done, while others have a high priority. The ballistic missile test program, keyed to ground testing, is directly served by this suggested ground and space program, because, despite initial differences between the two, ultimately most testing will be done on the ground once facilities and techniques become available. The program will:

- 1 Obtain fuller measurements of the geophysical environments; enable us to build into our designs flexibility now lost, owing to the gross measuring parameters of current scientific programs; provide fine structure knowledge (time, space, location variations) to support the sophisticated engineering for third generation systems. This knowledge will be derived, whenever possible, from ground testing. When it results from space tests, it will cover both the environment and the materials' response to the environment.

- 2 Compile and collate all critical geophysical data now scattered throughout a multitude of printed sources. Such data consisting of test results and theoretical studies must be brought together and continually updated for designers and others with short time lapses. The need for this is attested to by two early attempts at organization, the Lockheed

<sup>4</sup> Numbers in parentheses indicate References at end of paper.



Missiles and Space Division symposium on space materials<sup>5</sup> and the 1959 meeting of an ad hoc committee of the Materials Advisory Board of the National Academy of Sciences.<sup>6</sup>

3 Support and extend existing theoretical studies to design unambiguous ground and space experiments, to extrapolate both theoretical and experimental data to other situations, and to aid in extracting maximum benefits from presently limited testing opportunities.

4 Study means of interpreting tests measuring response to extreme environmental forces. These studies would, in some cases, simplify problems of measuring instrumentation. In others, the material response to hyperenvironments would provide critical tests of a theory and allow confidence in the extrapolation of that theory to a variety of situations. Most important, ground testing time could be compressed where correlations are shown between long duration tests in a conventional environment and accelerated tests in hyperenvironments.

5 Coordinate ground with space testing phases. Initially, space testing will be an urgent requirement because of difficulties of ground simulation, paucity of ground facilities, and scheduling conflicts resulting from long duration testing. Following this first period we will be able to establish routine ground tests for material responses, development of new materials, etc. The limited space testing will be coordinated with our ground experiments. Reliance on ground experiments will increase as our knowledge expands, permitting us to design them sensibly and realistically.

Some current LMSD activities are next described within the frame of reference of this five point program.

### Development of Space Design Techniques

Two striking trends in space material development have marked the space age: A rapid increase in the types of materials being considered, and a marked increase in the number of physical properties of concern. Fig. 1 indicates the growth of material types, and Fig. 2 shows the increase in the properties of concern (6).

Although laboratory experiments are invaluable for estimating the behavior of materials in space, they should be augmented by controlled experiments in the actual space environment. In the following sections we propose to resolve these difficulties by indicating present laboratory materials research and areas where material research in space should be undertaken.

### Temperature Control Surfaces

The need to control temperatures within the limits set by payload requirements is determinative in choosing outer surface materials for spacecraft. Passive systems, in which materials are selected for a proper alpha over epsilon ratio (absorptivity for solar radiation to emissivity of infrared radiation ratio), have predominated in controlling temperatures in satellites. Though extremely close control calls for an active system, passive control will continue in importance because of its low weight and operating power requirements.

Control surfaces must withstand for prolonged periods and without change in radiation characteristics or loss of adherence to the substrate the wide range of forces from micrometeorite erosion and thermal degradation to high energy particle radiation. In addition, they should have good reproducibility, ease of production and repair and be impervious to ascent heating.

Four types of coatings that fulfill these requirements have

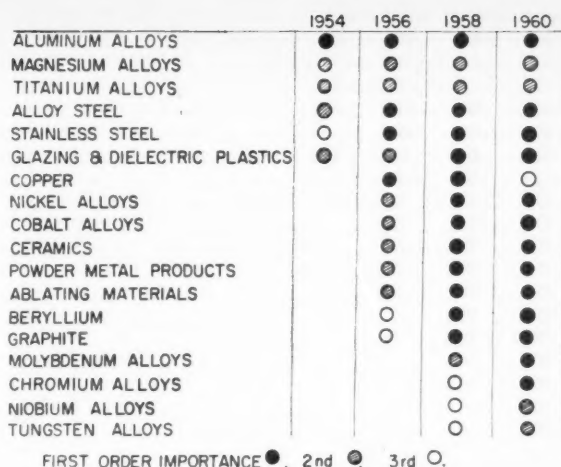


Fig. 1 Construction materials for missiles and spacecraft (6)

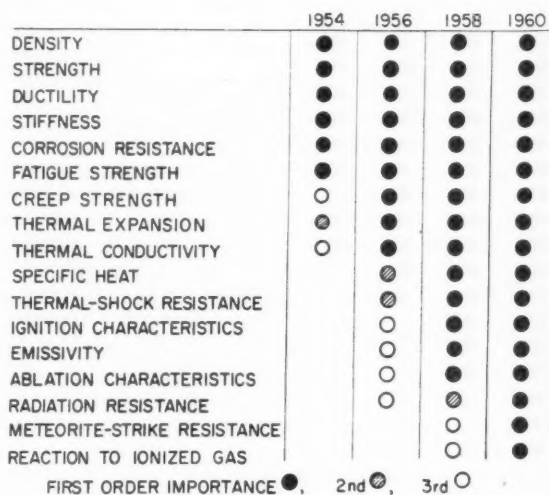


Fig. 2 Significant properties of structural materials for missiles and spacecraft (6)

been developed at LMSD through a program of measurements of the total hemispherical, total normal, and spectral emittance of opaque solids (7). New special equipment for extending spectral and temperature ranges has made the program possible. The coatings, to be used in amounts as indicated by thermal analysis of the vehicle and its trajectory, are of these types:

Flat absorber, high emissivity at all wave lengths.

Solar absorber, high ratio of emissivity in the solar region to emissivity in the infrared region.

Flat reflector, low emissivity at all wave lengths.

Solar reflector, low ratio of emissivity in the solar region (below about 4-μ wave length) to emissivity in the infrared region.

A program to study the stability of these coatings under combined vacuum, temperature, ultraviolet radiation and rapid ascent heating includes the development and formulation of inorganic coatings and semi-inorganic paints to incorporate stability with the other advantages of organic paints.

Flat absorbers are these coatings and black paints: The Dow 9 surface on magnesium-thorium alloy, and black chromium electroplate; commercially available silicon based black paints with carbon black or graphite pigmentation

<sup>5</sup> First Symposium, "Surface Effects on Spacecraft Materials," Palo Alto, Calif., May 12-13, 1959.

<sup>6</sup> Meeting of Ad Hoc Committee on Thermal Control of Space Vehicles of the Materials Advisory Board, Woods Hole, Mass., June 22-26, 1959.

promise good resistance to ascent heating; soluble silicate, titanium ester and silicone ester paint vehicles with suitable black pigments show definite promise.

Lightly oxidized aluminum and metal plated surfaces, as well as some polished metals, act as solar absorbers. Electrodeposition offers a greater range of thicknesses than does vacuum deposition, but both methods are unsatisfactory on magnesium. These are promising: Tabor coated metal surfaces, sulfamate of nickel, silver, crack free rhodium and platinum.

Polished metals generally have low  $\alpha$  and  $\epsilon$  values, serving as good approximations of flat reflectors.

Here is the status of some typical solar reflectors: Magnesium oxide powder, or paints containing the pigment; polished metals with transparent coatings such as lacquer, silicon monoxide or mylar are all acceptable. Strontium titanate, flat absorber paint vehicles combined with white pigments; emathyl white (white pigments anodically deposited on aluminum) are being investigated; titanium dioxide powder is possibly unstable in space environments.

Porcelain enamels and are sprayed coatings could be developed with the characteristics of all four surfaces. However, application of these to aluminum and magnesium affects the mechanical properties of the substrate. Vitreous enamels, more promising than porcelain enamels and are sprayed coatings, are being pursued as both flat (black) absorbers and solar (white) reflectors. Ablative materials and strippable paints are being studied for prelaunch environments only, whereas other coatings are being considered only for ascent protection (to be sublimed in space). For both purposes vinyl base coatings are suitable and commercially available.

Production processes for all these are extremely sensitive: Surfaces must be carefully handled; opaque film buildups must be so controlled as to ensure a minimum thickness to preserve the surfaces' emissivity characteristics independent of the substrate (special surfaces like the Tabor interference coating indicate possible use of eddy-current skin effect principle gages for production control); exposure response measurements must be continuous. For example, we are subjecting specimens to these environmental factors to test adhesion and abrasion resistance and weight changes:

Vacuum of  $10^{-6}$  mm Hg—minimum, in equipment capable (empty) of  $10^{-9}$  mm of Hg.

Temperature, steady state and cyclic, in the 50 to 300 F temperature regime.

Ultraviolet radiation, to  $0.2\mu$  at the shortwave length end.

Time of exposure (1 to 50 days).

We will also test the radiation characteristics after laboratory exposure to atomic and molecular sputtering (8), surface erosion (9), high energy radiation, and simulated ascent heating. The effects of the first two items warrant additional treatment at this point.

### Sputtering and Erosion

Sputtering, defined chemically, is a process of an incoming atom reacting with a molecule or atom of a surface material to form a product that does not adhere to the surface. The sputtering with which we are concerned here is the ejection of an atom, molecule or ion of a surface material as a result of bombardment by an external atom, molecule or ion. Such bombardment, directed against orbiting satellites, may be by sun originated high energy protons, or, more significant to our study, by stationary atmospheric atoms and molecules. This kind of sputtering seems energetically possible, since the incoming particles are generally above the energy level with which the atoms of the surface material are held. The results are drastic modifications of passive temperature controls, mirrors, solar cells and functional surfaces dependent upon uniform optical properties.

Some excellent work by Wehner (10) has established sput-

tering thresholds for normal incidence of mercury ions upon various metal surfaces. These thresholds seem to lie safely above the energy values of the bombarding particles, and this could suggest that sputtering will not be very likely. However, later work by both Wehner (11) and Morgules (12) has shown that these initial measurements were not sensitive enough, and indeed that the threshold is a function of measuring sensitivity. Morgules and Tischenko (12) discovered sputtering down to 7v for the case of argon on cobalt, and Wehner has observed a yield of  $5 \times 10^{-5}$  atoms per ion for 10 ev mercury ions. Other work by Wehner has shown that the yield is greatest when particles are incident upon the surface at an angle of 45 deg from the normal, and the threshold for sputtering at this angle of incidence is appreciably lower than for normal incidence. Wehner has also simulated the bombardment of the Vanguard silicon monoxide surface by immersion in a glow discharge, and observed a sputtering rate of 1 Å per hr or about  $10^{-6}\mu$  per year. This appears to affirm that sputtering could be a problem; still, these experiments were performed with ions, and evidence is too scant to prove that neutrals will sputter with the effectiveness of ions, as Wehner contends. It is generally accepted that most ions (alkali metal ions are an exception) are neutralized as they approach a surface by grabbing an electron. There does not appear to be sufficient time for this energy of ionization to be released in the form of light, and one would expect that the energy would be used up or added to the energy of interaction of the first collision on the surface. If such is the case, neutrals would be expected to sputter far less than the ions.

Data on low energy sputtering may be subject to further qualification because all measurements were made in a glow discharge, thus obscuring the actual constituency of the bombarding particles, the elements of which may or may not have been doubly charged ions falling through the same voltage gradient and registering at 7v when in reality they were 14-v ions. Further, the work on silicon monoxide surfaces called for a balancing of the electron flow to the surface equal to that of the ion flow, since the surface is a nonconductor, and it is probably difficult to know exactly what the energy of these bombarding ions was.

Finally, none of these experiments simulated space vacuum

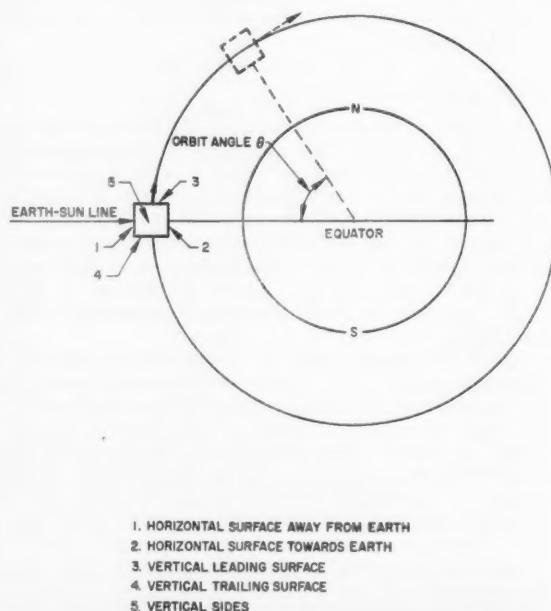


Fig. 3 Oriented cube in noon polar orbit

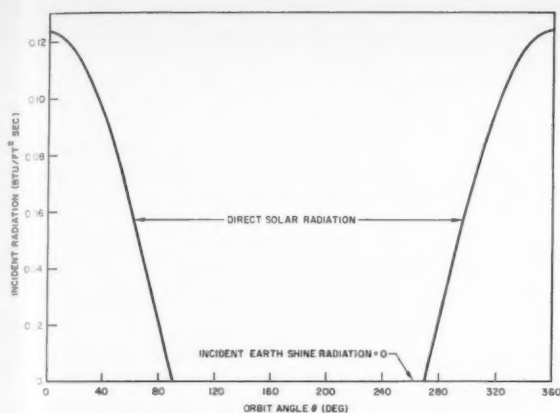


Fig. 4a Irradiation of horizontal surface away from Earth

conditions, and, as a result, did not establish the effect of absorbed surface layers. We must conclude that the difficulties of attaining sensitive measuring systems, and of developing a flux equivalent to those found in space prevent our knowing the magnitude of sputtering which will confront our satellite vehicles.

Erosion by small solid particles is equally difficult to assess (9). Micrometeorites or interplanetary dust can pit and gradually erode vehicle surfaces (13). Recent calculations indicate that the number of impacts by dust particles with diameters on the order of several  $\mu$  will be about 30 per year per  $\text{cm}^2$  for an object traveling just beyond Earth's atmosphere, with some possibility for as many as 300 to 3000 impacts per year per  $\text{cm}^2$ . Impact velocities can be as high as 80 km per sec (179,000 mph).

Laboratory experiments with micrometeorites cannot be accurately extrapolated to space conditions, for they have been an order of magnitude too low in velocity and three orders too high in the size of impacting particles. Experiments have used solid metal pellets, but micrometeorites are believed to be light and fragile "fluff balls" with densities less than 0.05 gm per  $\text{cm}^3$ . It is improbable that erosion by these will affect our oxide coated surfaces, but we can prove this only through in-flight experiments.

All the advantages of ease of measurement, isolation of effects, correlation of discrete data, and built in control of results are attainable in a single flight experiment that we propose at this juncture. The experiment could provide much information we now lack in the total and critical area of thermal control surfaces.

#### Oriented Cube Space Vehicle

Basic to this experiment is a cube (the term "cube" is used conceptually only) in a noon polar circular orbit (Fig. 3). An oriented cube means that all faces maintain a fixed orientation with respect to the instantaneous inertial velocity vector. The irradiation of the faces of the cube is shown in Figs. 4a through 4e. The horizontal surface away from Earth receives only direct solar isolation, while the horizontal surface facing Earth receives mostly Earth shine and Earth reflected solar radiation with some direct solar insolation just prior to and after eclipse. The leading and trailing vertical sides see a combination of all three sources of irradiation, whereas the other two vertical faces receive only Earth shine and Earth reflected solar irradiation at a low level of intensity.

Transient temperature responses of each face (assuming all surfaces thermally insulated) have been calculated for these parameters utilizing the methods of (14):

1. Orbital altitude: 300, 2300 miles.

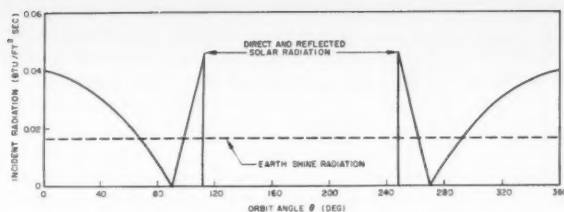


Fig. 4b Irradiation of horizontal surface toward Earth

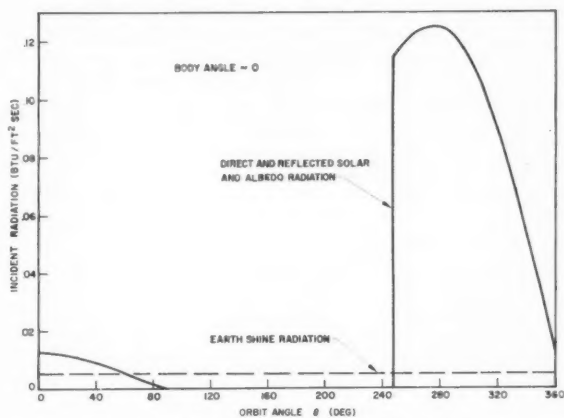


Fig. 4c Irradiation of vertical leading surface

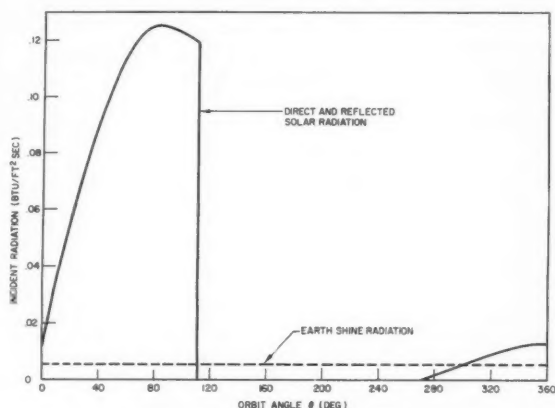


Fig. 4d Irradiation of vertical trailing surface

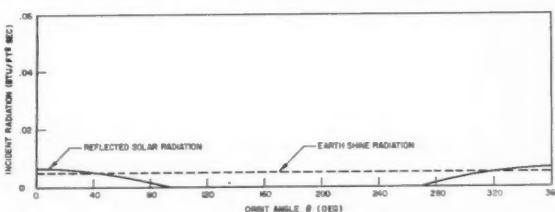


Fig. 4e Irradiation of vertical sides

2. Ratio of solar absorptivity to infrared emissivity  
 $\alpha/\epsilon = 0.15, 0.30, 1.00, 2.00, 4.00$
3. Thermal capacity parameter  
 $Wc\delta/\epsilon = 0.1, 1.0, 10.0$

where

$W$  = specific weight  
 $c$  = specific heat  
 $\delta$  = thickness

Fig. 5 shows the periodic temperature variation for the horizontal surface facing away from Earth in a 300-mile noon orbit for a range of thermal capacities. Included for interest are the analytical results for an infinitely thin plate of zero capacity. Note that for plates of small thermal capacity the peak temperature is a measure of the ratio of  $\alpha/\epsilon$ , whereas in the eclipse the temperature response can be simply calculated as that of  $T^4$  radiation to free space of a finite thermal capacity plate, and is only a function of the infrared low temperature emissivity  $\epsilon$ .

Maximum temperatures that could potentially be reached by thin plates with variable  $\alpha/\epsilon$  ratios are shown in Fig. 6.  $\alpha/\epsilon$  ratios in the range 0.1 to 0.3 can be achieved with special

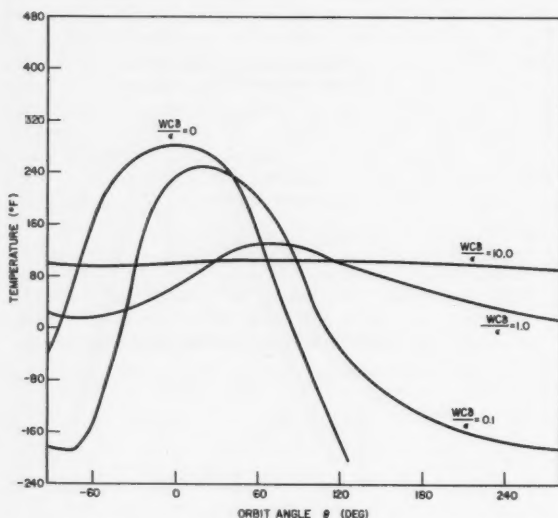


Fig. 5 Transient temperature history of horizontal surface away from Earth

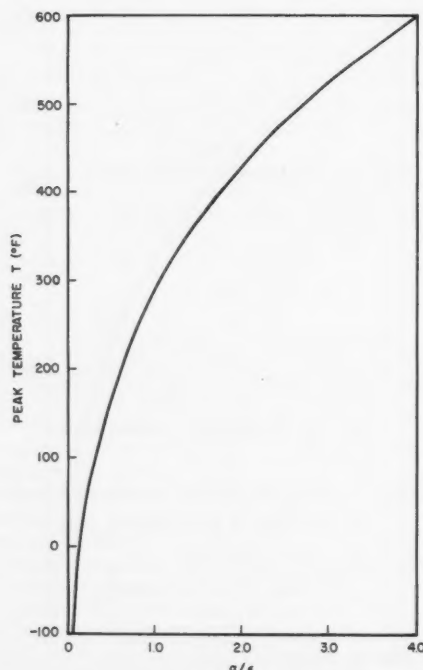


Fig. 6 Peak temperature,  $Wc\delta/\epsilon = 0$

points, whereas ratios of 2.00 to 3 are typical of polished metals; higher values can be achieved by special spectrally selective solar absorbers.

The effect of spatial orientation upon the maximum temperature oscillations experienced is shown in Fig. 7 for the four thermally distinct cube surfaces.

Following are some definite statements about space environment effects on satellites, when we correlate preferred thermal orientations with preferred environmental orientations.

**Solar irradiation**—greatest dosage of x-rays and short wave length ultraviolet radiation will be on the horizontal surface facing away from Earth and the vertical leading and trailing sides.

**Sputtering**—greatest impact by nitrogen and oxygen atoms at lower orbital altitudes will be on the vertical leading face of the cube.

**Micrometeoritic erosion**—micrometeorites are mostly confined to the plane of the ecliptic and are attracted by Earth's gravitational field, so as to travel in spiraling paths towards Earth's surface. These trajectories, relative to Earth, when combined with the satellite motion at velocities of approximately  $\frac{1}{2}$  of the velocity of the most probable micrometeoritic particles, imply that the surfaces of the cube will experience widely separated fluxes of particle impacts. The leading vertical edge has by far the highest flux, whereas the horizontal surface facing Earth and the trailing vertical side receive almost none. The other sides will experience approximately equal numbers of hits, but at a reduced flux.

**Solar corpuscular radiation**—Earth's magnetic field will perturb this to some extent and complicate orientation statements.

**Auroral radiation**—electrons in the 30-kev and protons in the 100-kev range will not disturb the horizontal surface facing Earth. Protons in this energy range may cause surface sputtering as nominally experienced in the laboratory.

**Van Allen belt and solar flare protons**—two additional sources of radiation show only a limited degree of orientation because of complex interactions of the particles with Earth's magnetic field. However, these particles are generally thought to be so highly energetic as to penetrate to depths below those which might cause surface sputtering.

The fact that the upper horizontal surface undergoes

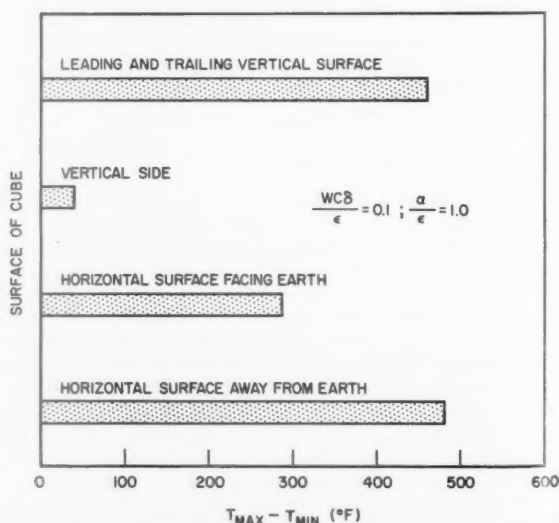


Fig. 7 Comparison of temperature oscillations of four faces of cube in 2300-mile noon orbit,  $Wc\delta/\epsilon = 0.1$ ,  $\alpha/\epsilon = 1.0$



**Table 1 Material response to vacuum**

Coating type	Weight loss in vacuum after 24 hr, %	
	300 F	500 F
polyurethane	66	100
epoxy (4 species)	7-14	61-83
alkyd	17	39
silicone	7	7 (9 at 600 F)
acrylic	43	62
phenolic	6	15
Kel-F	2	3 (98 at 600 F)
nitrocellulose	82	88
polysulfide	63	65

greatest temperature changes and yields  $\alpha/\epsilon$  and  $\epsilon$  values in relation to time gives us an unmatched opportunity to measure the surface property changes of various coatings under each of the oriented space environments. We can do this by indexing any desired face of the cube into this position for several orbits, to establish a periodic temperature history that will yield the changed values of surface properties as affected differently by the environments described. A simple 180-deg rotation of the cube will interchange the leading and trailing vertical surfaces isolating the effects of micrometeorite erosion and sputtering. Orientation of the cube at some arbitrary angle would give an indication of the effects of incidence angle upon erosion and sputtering. In general, the information on all surface orientations is valuable in that many satellite vehicles will fly in preferred orientations as dictated by their missions, and hence various portions of the vehicle surface will exhibit different reactions to the space environment.

### Test Program Parameters

The ground and in-flight program for testing space materials should be directed toward analysis and evaluation of problems related to these areas: Surface coatings, materials and parts, lubrication and mechanical properties. We have already treated these in general, and now a summary is in order before our conclusions.

### Surface Coatings

No organic coating can be expected to resist the combined force of radiation, temperature change and high vacuum. Ultraviolet radiation causes molecular changes which produce crosslinked structures of decreased ductility. An oxygen absence plus an efficient ultraviolet reflecting pigment will inhibit ultraviolet radiation, but the degrading effects of high vacuum cannot be contravened, since they are a function of the finite vapor pressures of such materials. These are greatly increased by the formation of low molecular weight scission fragments in elevated temperature regimes. The data in Table 1 show the weight losses of a wide range of organic coatings exposed for 24 hr to various temperatures in vacuum of  $10^{-5}$  mm Hg (a 90-mile altitude equivalent). Note that only a straight silicone resin and Kel-F did not suffer a rapid and severe loss of integrity (15).<sup>7</sup>

### Materials and Parts

Organic materials have a number of functional applications in spacecraft, and their use requires the retention of properties under conditions quite dissimilar from conventional uses on Earth. Seals and gaskets, for example, must provide tight joints and be unreactive with materials with which they

come into contact, such as high energy fuels or other special fluids. These conditions must be obtained even though one side of the seal or gasket is exposed to an ultra-high vacuum, and the entire body is subjected to direct space radiation or to secondary radiation induced by it. Adhesives must also maintain tight leakproof joints and structural strength under similar conditions. Where adhesives are used to cement optical components together, the effect of the space environment on their refractive indices is another consideration. Electrical applications of organic materials, such as for insulation on wires, dielectrics for capacitors, relay structures and circuit boards, requires that such parts not undergo degradation in space.

A recent summary of radiation data obtained from U. S. and USSR space probes suggests these facts about the resistance of parts in space (16). Structural metals will be relatively insensitive to radiation. Elastomers and organic fluids will be quite subject to radiation damage, as will transistors and diodes, but the latter's normal cladding and location in space vehicles will protect them even in the more intense radiation zones. Semiconductor devices and other sensitive electronic components are subject to rate effects as well as relatively low permanent damage thresholds. Solar cells are generally directly exposed to space unless a more complex scheme of reflected or piped light is used. Proton experiments with solar cells at RCA and at LMSD indicate that an appreciable decrease in power output can occur after a few months in the midst of the intense Van Allen proton belt. Relief may be obtained by the use of protective windows, to a point dictated by weight restrictions.

### Lubrication

Lubrication of moving parts is essential to minimize power requirements and to prevent gross seizures (17). The surface films of absorbed gases present on all surfaces in the atmosphere are irreparably removed by wear and evaporation in space. As a result, base metal surfaces make direct contact and may coldweld together. This potential danger affects bearings, gears, cams and electrical parts, such as sliding contacts, relays and switches. Lubrication in a vacuum is difficult because of the increased evaporation rate and because fatty acids, lacking oxygen, cannot form protective metallic soaps.

Low vapor pressure oils and greases, such as the oils used as pumping fluids in vacuum diffusion pumps, have low evaporation rates but are lacking in good lubricating qualities. Such oils used in a bearing test in vacuum (order of  $10^{-6}$  mm Hg) permitted bearing lives of only about 1000 hr. Projected bearing tests under way for both ground and space simulation testing will measure the running torque by strain gage transducers to obtain torque-time histories. Pressure in the bearing testor will be measured by an ionization gage to give pressure-time history, and motor power consumption will be measured.

Other approaches to lubrication problems in space include the study of thin film solid lubricants—vacuum deposited plates of soft metals like silver, gold and bonded films of laminar solids; of self-lubricating solids—plastics such as Teflon and porous compacts, impregnated or filled with molybdenum disulfide; and of dissimilar materials—sapphire, Pyroceram, or carbides in contact with hardened steel.

### Mechanical Properties

Experiments to measure exo-atmospheric induced changes in mechanical properties of materials such as fatigue and creep-rupture strength require a high degree of simulation. We must also gain experience on large area, low mass structures which could find use as passive communications antennae, optical reflectors and radiation collectors. The statics and dynamics of tori-stiffened circular membranes have been studied in preliminary fashion (18). We will have

<sup>7</sup> The data in (15) were gathered in studies made at Wright Air Development Command and by Litton Industries, and were summarized by G. F. Matacek.

to concentrate in our studies on materials, pressurization and other modes of causing rigidity. A number of methods of bringing about rigidity have already been proposed (19). These include: Making rigid a flexible membrane by gas reaction; the membrane would consist of a linear polymer which will undergo a cross linking reaction to form a rigid network under stimulation of a reactive vapor; using water soluble silicates which, on inflation of the structure in space, will lose water to yield a rigid network of silicic acid (the reaction can be augmented by using carbon dioxide as an inflation propellant); making rigid organic films by the loss of volatiles, primarily high vapor pressures plasticizers; causing rigidity by chemical reaction foams or by volatilization foams.

Each will have to be investigated on the ground, and we will continue to plan space experiments for the near future.

## Summary and Conclusions

The projected result of the integrated test and evaluative activity will be a series of design handbooks which will enable designers to select, with little or no experimental verification, the exact thermal control surface coating for a given application. Reliability and time savings will be heightened because of the wealth of data that will be organized clearly and unambiguously by these handbooks. Complete information will be available on spectral emissivity and total hemispherical emissivity at various temperatures, including the effect on these values of varying durations and severities of the various environments. Manufacturing instructions, methods of application and control and any special handling instructions, such as the necessity for the use of a specific strippable paint, will be set down in detail.

Instructions for the determination of solar absorptivity and total hemispherical emissivity from spectral emissivity curves will be included. Using information on the spectral distribution of the radiation emitted by a given body (e.g., the moon) and data on the spectral emissivity of a specific surface  $\epsilon_\lambda$ , it is possible to determine  $\alpha_B$ , the total absorptivity of that surface for that particular irradiation. Analytical methods will be included, to be used in arriving at a mosaic pattern of two surfaces which would achieve emissivity properties intermediate between those of the two separate surfaces.

This handbook will be cross indexed according to type of surface (i.e., paint, vacuum deposited metal),  $\alpha/\epsilon$ ,  $\epsilon$ , and classification of surface by usage (i.e., non re-entry, interior only), including the duration and intensity of the exposure to specific environments that the particular surface should be expected to withstand.

These books, together with our other efforts to extend basic geophysical knowledge represent the most direct approach to the basic considerations of advanced spaceflight. We want to exploit fully the data gathering potential of satellite systems; we must know more about the space environments; we have to be able to estimate the response of our materials to risk and degradation factors; we can, finally, abrogate

uncertainty only by concerted testing and evaluation.

In the beginning of the program we propose a greater reliance on space testing as an adjunct to ground testing than was the case with the ballistic missile program. However, as we lessen environmental uncertainties and simulation difficulties, the techniques for routine development testing will tend to become comparable with those of the ballistic missile program.

## References

- 1 Yonta, O., Normand, C. and Harrison, D., "High-Energy Sputtering," *J. Appl. Physics*, vol. 31, no. 3, March 1960, pp. 447-450.
- 2 Reiffel, L., "Structural Damage and Other Effects of Solar Plasmas," *ARS JOURNAL*, vol. 30, no. 3, March 1960, pp. 258-262.
- 3 Wysocki, J. and Rappaport, P., "Effect of Temperature on Photovoltaic Solar Energy Conversion," *J. Appl. Physics*, vol. 31, no. 3, March 1960, pp. 571-578.
- 4 Smith, R. A., Jones, F. E. and Chasmar, R. P., "The Detection and Measurement of Infrared Radiation," Oxford University Press, London, 1957, pp. 213-215.
- 5 Spencer, H., "Noise and Signal Response in Lead Sulfide Photoconductive Films," *J. Appl. Physics*, vol. 31, no. 3, March 1960, pp. 505-510.
- 6 Rhode, R. V. and Houbolt, J. C., "The Impact of Space Technology on Research and Development—Structures and Materials," NASA Rep. no. L-128, Washington, D. C., Oct. 20, 1958.
- 7 Shaw, C. C., Berry, J. and Lee, T., "Spectral and Total Emissivity Apparatus and Measurements of Opaque Solids," LMSD Rep. 48488, Lockheed Missiles and Space Div., Sunnyvale, Calif., March 1959; see also Shaw, C. C., "Apparatus for the Measurement of Spectral and Total Emissivity of Solids," in "First Symposium—Surface Effects on Spacecraft Materials," John Wiley & Sons, Inc., N. Y., 1960, pp. 220-237.
- 8 Bershader, D., "Skin Erosion Studies," Status Review Lockheed Missiles and Space Div., Sunnyvale, Calif., unpublished data; see also Stein, R. P., "Variation of Emissive Properties of Surfaces Due to Atomic and Molecular Bombardment," in "Third Symposium—Hypervelocity Impact," Vol. 1, pp. 309-315, Armour Research Foundation of Illinois Institute of Technology, Chicago, February 1959; see also Stein, R. P., "Atomic and Molecular Sputtering," in—"First Symposium, Surface Effects on Spacecraft Materials," John Wiley & Sons, Inc., N. Y., 1960, pp. 391-402.
- 9 Beard, D. B., "Interplanetary Dust Distribution and Erosion Effects," in "First Symposium—Surface Effects on Spacecraft Materials," John Wiley & Sons, N. Y., 1960, pp. 378-386.
- 10 Wehner, G. R., "Advances in Electronics and Electron Physics," Vol. 7, Academic Press, N. Y., 1955, pp. 239-298.
- 11 Wehner, G. R., "Study of Erosion and Drag Under Simulated Satellite Flight Conditions," General Mills, Inc., Minneapolis, Rep. no. 1864, May 1958.
- 12 Morgules, N. D. and Tischenko, V. D., "The Investigations of Cathode Sputtering in the Near Threshold Region I," *J. Exp. & Theor. Phys.*, vol. 30, no. 1, June 1956, pp. 54-59.
- 13 Huth, J., "Power Supplies for Orbital and Space Vehicles," in "Advances in Space Science," Vol. 1, Academic Press, N. Y., 1959, pp. 111-157. (Additional references given.)
- 14 Camack, W. G. and Edwards, D. K., "Effects of Surface Thermal-Radiation Characteristics on the Temperature Control Problem in Satellites," in "First Symposium—Surface Effects on Spacecraft Materials," John Wiley & Sons, N. Y., 1960, chap. 1.
- 15 Matacek, G. F., "Volatility of Organic Coating," in "First Symposium—Surface Effects on Spacecraft Materials," John Wiley & Sons, Inc., N. Y., 1960, pp. 263-283.
- 16 Hess, R. E. and Badertscher, R. F., "Space Radiation as an Environmental Constituent," REIC Memo. no. 19, Battelle Memorial Institute, Columbus, Ohio, 19 Jan. 1960.
- 17 Clauss, F. J., "Surface Effects on Materials in Near Space," presented to San Francisco Section of the Institute of the Aeronautical Sciences, Dec. 17, 1959.
- 18 Jahsman, W. E., Cline, G. G., Jr., Hahne, H. V. and Nachbar, W., "Mechanics Problems of Space Flight," LMSD Rep. no. 288073, Lockheed Missiles and Space Div., Sunnyvale, Calif., 16 Nov. 1958.
- 19 Whitby, L., "Feasibility Study on Gas and Vacuum Hardening of Inflatable Membranes," Lockheed Missiles and Space Div., Sunnyvale, Calif. (Private communication.)

# Stability of Orthotropic Cylindrical Shells Under Combined Loading

T. E. HESS<sup>1</sup>

General Electric Co.  
Philadelphia, Pa.

The increasing use of fiber and whisker reinforced materials makes necessary the availability of methods of analyzing cylinders and cones composed of an orthotropic material. This paper treats the buckling of such shells under a combination of axial compression and uniform external pressure. The differential equation approach of Flugge is used, and the resulting buckling equation is presented in terms of axial and circumferential bending rigidities, shear rigidity, Poisson's ratio, geometry parameters and mode shapes. Design curves are presented which allow quick determination of critical loads on cylinders, and, by using the equivalent cylinder concept, on conical shells of small included angle. The curves also lend themselves to "tailoring" of materials to fit the load carrying requirements of the structure.

IN THE design of modern missiles and space vehicles, increasing use is made of the newer materials, such as reinforced plastics, whisker materials and fiber reinforced metals. Materials of this sort are elastically orthotropic; that is, they have three mutually perpendicular planes of elastic symmetry. This means that the material composing the wall of a shell has a modulus of elasticity and Poisson's ratio different in the axial than in the circumferential direction, and a shear modulus which is completely independent of these.

The critical item in the design of structures utilizing these materials may be stability, depending on the strength, ductility and stiffness of the material. If such is the case, a method of predicting the buckling load is required. One possibility is to use an isotropic analysis such as given in (1),<sup>2</sup> assuming some average material properties. However, this approach could lead to results that would be unduly conservative in some cases, and disastrously nonconservative in other cases. Therefore, the purpose of this report is to present a method of determining the buckling loads on shells composed of an orthotropic material.

In this report the small deflection differential equations describing the action of an orthotropic cylindrical shell under arbitrary loading are derived. These equations are then transformed into the large deflection equations effectively, describing the stability of the shell under the action of external pressure and axial compression (2). The solution of the latter equations yields an expression for the critical loads in terms of shell geometry, material properties and buckling modes. There is an infinite number of possible buckling modes but the only one of practical interest is the one corresponding to minimum load. A family of curves is plotted giving the critical axial load and critical external pressure for an orthotropic cylinder.

For a conical shell of small vertex angle, the equivalent cylinder method developed by Bijlaard (7) and discussed in (1) is recommended.

Presented at the ARS Structural Design of Space Vehicles Conference, Santa Barbara, Calif., April 6-8, 1960.

<sup>1</sup> Engineer, Space Structures Engineering, Missile and Space Vehicle Dept.

<sup>2</sup> Numbers in parentheses indicate References at end of paper.

## Derivation of Cylindrical Shell Equations

Consider a cylindrical shell of length  $L$ , thickness  $h$ , and middle surface radius  $R$ , subjected to an arbitrary loading with components of  $\Phi$ ,  $\Theta$  and  $Z$  (Fig. 1). Consider also the differential element of shell at point  $P(r, \theta, z)$  shown in Fig. 2. The element is located by the three coordinates  $r$ ,  $\theta$  and  $z$ , and  $\eta$  is the distance from the middle surface to any point, so that the coordinate  $r$  is equal to  $R + \eta$ . Fig. 3 shows the element with the stresses acting on it. The equilibrium of forces in the  $r$ ,  $\theta$  and  $z$  directions on the element is described by

$$\begin{aligned} \frac{\partial \sigma_{zz}}{\partial z} + \frac{1}{R(1 + \eta/R)} \frac{\partial \sigma_{\theta z}}{\partial \theta} + \frac{1}{R(1 + \eta/R)} \sigma_r - \frac{1}{R(1 + \eta/R)} \sigma_\theta + \frac{\partial \sigma_r}{\partial r} &= 0 \\ \frac{\partial \sigma_{z\theta}}{\partial z} + \frac{1}{R(1 + \eta/R)} \frac{\partial \sigma_{\theta\theta}}{\partial \theta} + \frac{2}{R(1 + \eta/R)} \sigma_{r\theta} + \frac{\partial \sigma_{r\theta}}{\partial r} &= 0 \\ \frac{\partial \sigma_z}{\partial z} + \frac{1}{R(1 + \eta/R)} \frac{\partial \sigma_{\theta z}}{\partial \theta} + \frac{1}{R(1 + \eta/R)} \sigma_{rz} + \frac{\partial \sigma_{rz}}{\partial r} &= 0 \end{aligned} \quad [1]$$

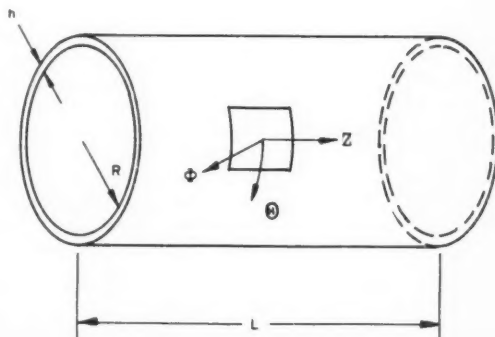


Fig. 1 Cylindrical shell with arbitrary loading

The strain displacement relations for cylindrical coordinates are (5)

$$\begin{aligned} \epsilon_r &= \partial u / \partial r \\ \epsilon_\theta &= [1/R(1 + \eta/R)](\partial v / \partial \theta + u) \\ \epsilon_z &= \partial w / \partial z \\ \epsilon_{z\theta} &= [1/2(1 + \eta/R)](\partial w / \partial \theta) + (1/2)(\partial v / \partial z) \\ \epsilon_{rz} &= (1/2)(\partial w / \partial r + \partial u / \partial z) \\ \epsilon_{r\theta} &= (1/2)(\partial v / \partial r) - [1/2R(1 + \eta/R)](v - \partial u / \partial \theta) \end{aligned} \quad [2]$$

where  $u$ ,  $v$  and  $w$  are the displacements of the point  $P(r, \theta, z)$  in the  $r$ ,  $\theta$  and  $z$  directions, respectively. The stress resultants are given by (Fig. 4)

$$\begin{aligned} N_\theta &= \int_{-h/2}^{h/2} \sigma_\theta d\eta & N_z &= \int_{-h/2}^{h/2} \sigma_z(1 + \eta/R)d\eta \\ Q_{z\theta} &= \int_{-h/2}^{h/2} \sigma_{z\theta}(1 + \eta/R)d\eta & Q_{\theta z} &= \int_{-h/2}^{h/2} \sigma_{\theta z}d\eta \\ Q_{\theta r} &= \int_{-h/2}^{h/2} \sigma_{\theta r}d\eta & Q_{zr} &= \int_{-h/2}^{h/2} \sigma_{zr}(1 + \eta/R)d\eta \\ M_z &= -\int_{-h/2}^{h/2} \sigma_z\eta(1 + \eta/R)d\eta & M_\theta &= \int_{-h/2}^{h/2} \sigma_\theta\eta d\eta \\ M_{z\theta} &= \int_{-h/2}^{h/2} \sigma_{z\theta}\eta(1 + \eta/R)d\eta & M_{\theta z} &= -\int_{-h/2}^{h/2} \sigma_{\theta z}\eta d\eta \end{aligned} \quad [3]$$

At this point we introduce the stress-strain relations for an orthotropic medium (6), namely,

$$\begin{aligned} \sigma_\theta &= [E_\theta / (1 - \nu_{\theta z}\nu_{z\theta})](\epsilon_\theta + \nu_{\theta z}\epsilon_z) \\ \sigma_z &= [E_z / (1 - \nu_{\theta z}\nu_{z\theta})](\epsilon_z + \nu_{z\theta}\epsilon_\theta) \\ \sigma_{\theta z} &= 2G\epsilon_{\theta z} \end{aligned} \quad [4]$$

These equations contain four independent elastic constants, which are  $E_\theta$ ,  $E_z$ ,  $G$  and  $\nu_{\theta z}$ . Poisson's ratio  $\nu_{\theta z}$  is not independent, since Maxwell's reciprocal theorem states that the circumferential strain due to a unit axial stress must equal

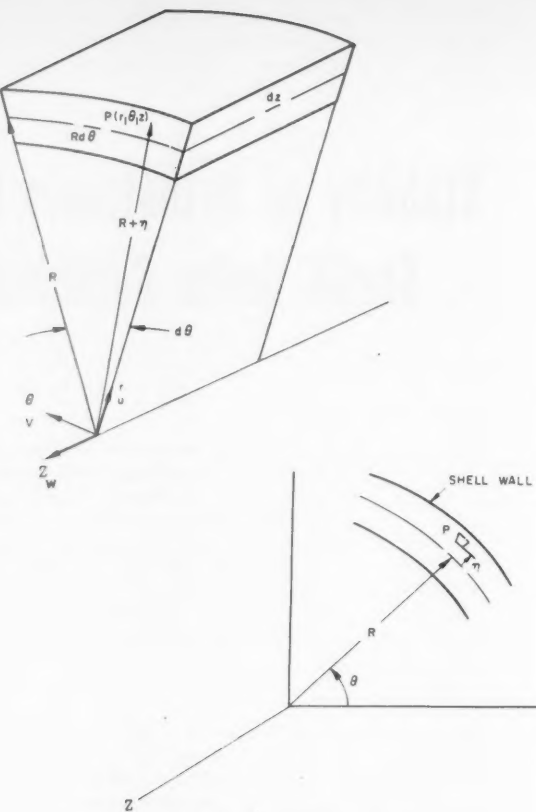


Fig. 2 Cylindrical coordinate system

the axial strain due to a unit circumferential stress, which leads to

$$\nu_{z\theta}/E_z = \nu_{\theta z}/E_\theta$$

or

$$\nu_{\theta z} = (E_\theta/E_z)\nu_{z\theta}$$

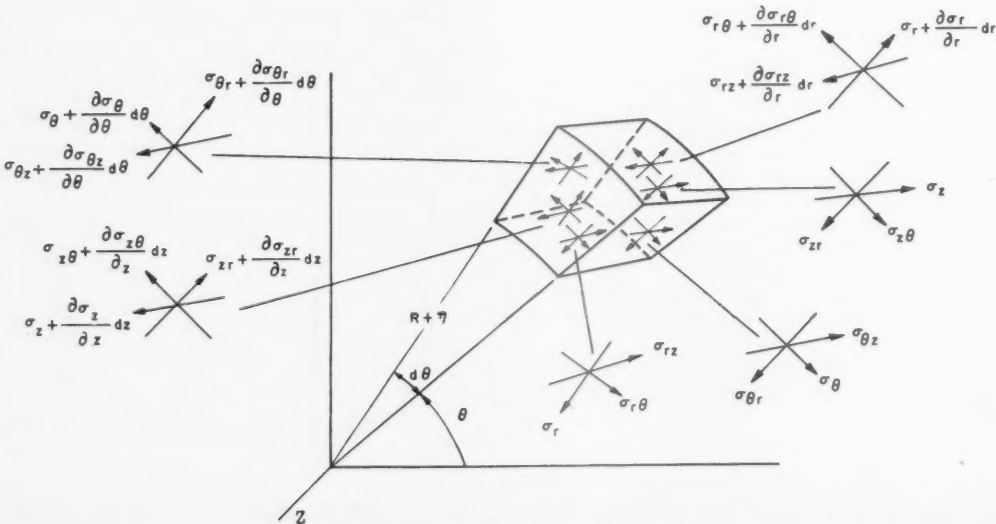
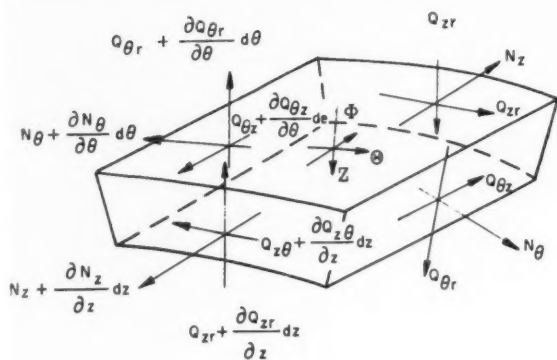
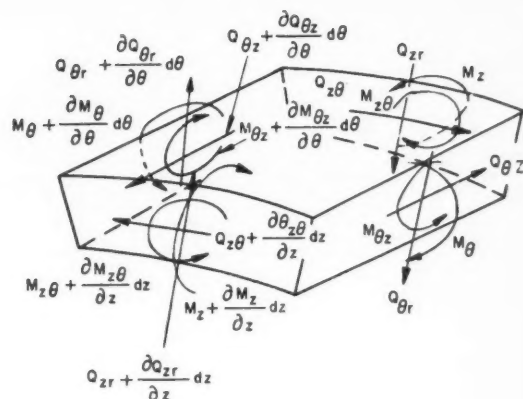


Fig. 3 Stresses on element of shell wall





a. EQUILIBRIUM OF FORCES



b. EQUILIBRIUM OF MOMENTS

Figs. 4 Stress resultants

The usual shell assumptions are then made, namely, elements perpendicular to the middle surface before deflection remain perpendicular during deflection and experience no strain, only rotation and translation. This results in a very small value for  $\sigma_r$ , compared with the other stresses and  $\epsilon_r = \epsilon_{\theta r} = \epsilon_{\theta \theta} = 0$ . Then, integrating the equilibrium equations through the thickness of the shell wall and combining the previously noted equations, the stresses, strains and finally the stress resultants can be expressed in terms of the middle surface displacements, shell geometry and the following stiffness constants

$$\begin{aligned} D_s &= E_s h^3 / 12(1 - \nu_{\theta s} \nu_{s \theta}) & H_s &= E_s h / (1 - \nu_{\theta s} \nu_{s \theta}) & D_\theta &= E_\theta h^3 / 12(1 - \nu_{\theta \theta} \nu_{\theta \theta}) \\ H_\theta &= E_\theta h / (1 - \nu_{\theta \theta} \nu_{\theta \theta}) & D_k &= G h^3 / 12 & H_k &= G h \end{aligned} \quad [5]$$

Finally, the following governing equations for a flexure resistant orthotropic cylindrical shell under arbitrary loading are

$$\begin{aligned} \frac{1}{R} \left[ \frac{u_0}{R} + \frac{1}{R} \frac{\partial v_0}{\partial \theta} + \nu_{s\theta} \frac{\partial w_0}{\partial z} \right] + \frac{D_\theta}{H_\theta} \left[ \frac{1}{R^4} \left( \frac{\partial^4 u_0}{\partial \theta^4} + 2 \frac{\partial^2 u_0}{\partial \theta^2} + u_0 \right) + \frac{\nu_{s\theta}}{R^2} \frac{\partial^4 u_0}{\partial \theta^2 \partial z^2} \right] - \frac{D_k}{H_\theta} \left[ \frac{3}{R^2} \frac{\partial^3 v_0}{\partial \theta \partial z^2} - \frac{4}{R^2} \frac{\partial^4 u_0}{\partial \theta^2 \partial z^2} - \frac{1}{R^3} \frac{\partial^3 w}{\partial \theta^2 \partial z} \right] + \\ \frac{D_s}{H_\theta} \left[ \frac{\nu_{\theta s}}{R^2} \frac{\partial^4 u_0}{\partial \theta^2 \partial z^2} + \frac{\partial^4 u_0}{\partial z^4} - \frac{\nu_{\theta s}}{R^2} \frac{\partial^3 v_0}{\partial \theta \partial z^2} - \frac{1}{R} \frac{\partial^3 w_0}{\partial z^3} \right] - \frac{\Phi}{H_\theta} = 0 \\ \frac{1}{R} \left[ \frac{1}{R} \frac{\partial u_0}{\partial \theta} + \frac{1}{R} \frac{\partial^2 v_0}{\partial \theta^2} + \nu_{s\theta} \frac{\partial^2 w_0}{\partial \theta \partial z} \right] + \frac{H_k}{H_\theta} \left[ \frac{\partial^2 v_0}{\partial z^2} + \frac{1}{R} \frac{\partial^2 w_0}{\partial \theta \partial z} \right] - \frac{D_\theta}{H_\theta} \left[ \frac{\nu_{s\theta}}{R^2} \frac{\partial^3 u_0}{\partial \theta \partial z^2} \right] + \frac{D_k}{H_\theta} \left[ -\frac{3}{R^2} \left( \frac{\partial^3 u_0}{\partial \theta \partial z^2} - \frac{\partial^2 v_0}{\partial z^2} \right) \right] + \frac{\Theta}{H_\theta} = 0 \\ \frac{1}{R} \left[ \frac{\nu_{\theta s}}{R} \frac{\partial u_0}{\partial z} + \nu_{s\theta} \frac{\partial^2 v_0}{\partial \theta \partial z} \right] + \frac{\partial^2 w_0}{\partial z^2} + \frac{D_k}{H_s} \left[ \frac{1}{R^3} \frac{\partial^3 u_0}{\partial \theta^2 \partial z} + \frac{1}{R^4} \frac{\partial^2 w_0}{\partial \theta^2} \right] + \frac{H_k}{H_s} \left[ \frac{1}{R} \frac{\partial^2 v_0}{\partial \theta \partial z} + \frac{1}{R^2} \frac{\partial^2 w_0}{\partial \theta^2} \right] - \frac{D_s}{H_s} \frac{1}{R} \frac{\partial^3 u_0}{\partial z^3} + \frac{Z}{H_s} = 0 \end{aligned} \quad [6]$$

where  $u_0$ ,  $v_0$  and  $w_0$  are middle surface displacements.

### Development of Stability Equations

In order to determine the stability requirements for an orthotropic cylindrical shell under the combination of axial compression and external radial pressure, one may regard the differential equations for the flexure resistant shell (see Eq. [6]), as the required buckling equations, provided they are interpreted correctly. The initial state for buckling is not the unloaded state, but the initially compressed state *A* (Fig. 5), caused by the action of  $q$  and  $N$ . The displacements  $u_0$ ,  $v_0$  and  $w_0$  then are the displacements from this initially compressed state to another state of equilibrium *B* (Fig. 6) immediately adjacent to the initial state. Also, the forces  $\Phi$ ,  $\Theta$  and  $Z$  are no longer external loading forces but additional forces developed in the transition from state *A* to state *B*. During this transition, the forces  $q$  and  $N$  remain constant, since buckling

presupposes two adjacent states of equilibrium under the same external loading. Therefore, the forces  $\Phi$ ,  $\Theta$  and  $Z$  act to maintain equilibrium, since the element upon which  $q$  and  $N$  are acting undergoes strain and rotation in going from state *A* to state *B*.  $\Phi$ ,  $\Theta$  and  $Z$  may be evaluated by considering the deformation of the element in Fig. 5. For example,  $\Phi$  consists of three parts due to the expansion of the middle surface, the change in angle between adjacent axial sections and the change in angle between adjacent circumferential sections. The forces are then seen to be

$$\begin{aligned} \Phi &= -q \left[ u_0/R + \partial w_0/\partial z + (1/R)(\partial^2 u_0/\partial \theta^2) \right] - N(\partial^2 u_0/\partial z^2) \\ \Theta &= -N(\partial^2 v_0/\partial z^2) \\ Z &= q[\partial u_0/\partial z - (1/R)(\partial^2 w_0/\partial \theta^2)] \end{aligned} \quad [7]$$

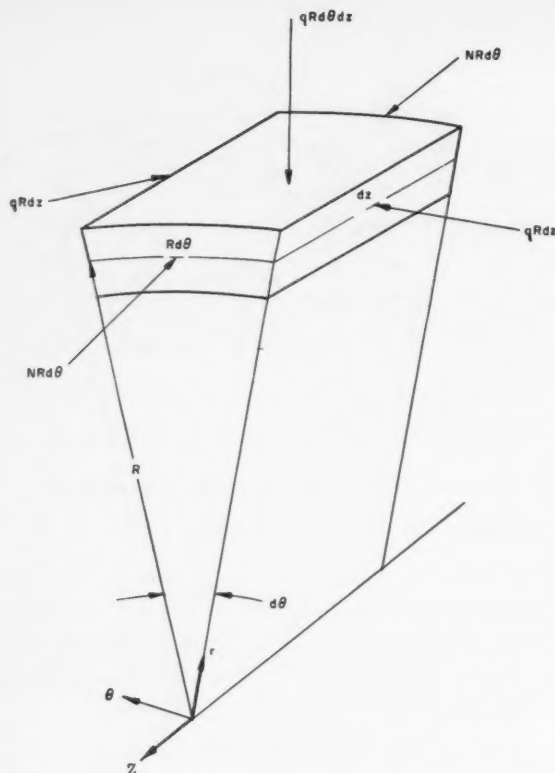


Fig. 5 Stress state A

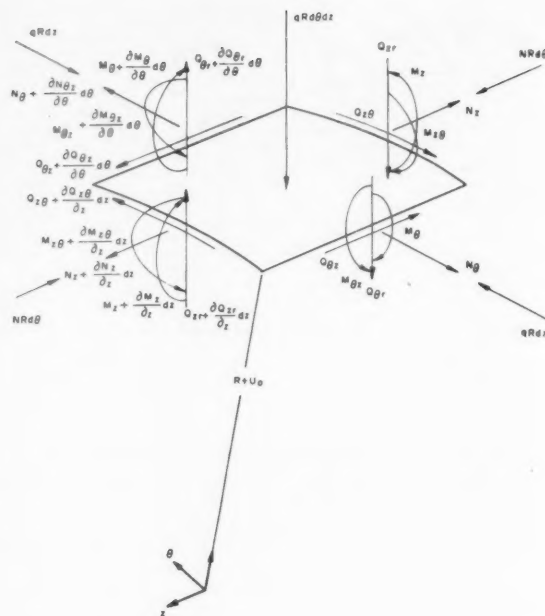


Fig. 6 Stress state B

Then, substituting these into Equations [6] yields the following, which are the required stability equations

$$\begin{aligned}
 & \left[ u_0 + \frac{\partial v_0}{\partial \theta} + \nu_{z\theta} R \frac{\partial w_0}{\partial z} \right] + \frac{D_\theta}{H_\theta} \left[ \frac{1}{R^2} \left( \frac{\partial^4 u_0}{\partial \theta^4} + 2 \frac{\partial^2 u_0}{\partial \theta^2} + u_0 \right) + \nu_{\theta z} \frac{\partial^4 u_0}{\partial \theta^2 \partial z^2} \right] - \frac{D_k}{H_\theta} \left[ 3 \frac{\partial^3 v_0}{\partial \theta \partial z^2} - 4 \frac{\partial^4 u_0}{\partial \theta^2 \partial z^2} - \frac{1}{R} \frac{\partial^3 w_0}{\partial \theta^2 \partial z} \right] + \\
 & \frac{D_z}{H_\theta} \left[ \nu_{\theta z} \frac{\partial^4 u_0}{\partial \theta^2 \partial z^2} + R^2 \frac{\partial^4 u_0}{\partial z^4} - \nu_{\theta z} \frac{\partial^3 v_0}{\partial \theta \partial z^2} - R \frac{\partial^3 w_0}{\partial z^3} \right] + \phi_{1\theta} \left[ u_0 + R \frac{\partial w_0}{\partial z} + \frac{\partial^2 u_0}{\partial \theta^2} \right] + \phi_2 R^2 \frac{\partial^2 u_0}{\partial z^2} = 0 \\
 & \left[ \frac{\partial u_0}{\partial \theta} + \frac{\partial^2 v_0}{\partial \theta^2} + \nu_{\theta z} R \frac{\partial^2 w_0}{\partial \theta \partial z} \right] + \frac{H_k}{H_\theta} \left[ R^2 \frac{\partial^2 v_0}{\partial \theta \partial z} + R \frac{\partial^2 w_0}{\partial \theta \partial z} \right] - \frac{D_\theta}{H_\theta} \nu_{\theta z} \frac{\partial^3 u_0}{\partial \theta \partial z^2} + \frac{D_k}{H_\theta} \left[ -3 \left( \frac{\partial^3 u_0}{\partial \theta \partial z^2} - \frac{\partial^2 v_0}{\partial z^2} \right) - \phi_2 R^2 \frac{\partial^2 v_0}{\partial z^2} \right] = 0 \\
 & R \left[ \nu_{\theta z} \frac{\partial u_0}{\partial z} + \nu_{\theta z} \frac{\partial^2 v_0}{\partial \theta \partial z} \right] + R^2 \frac{\partial^2 w_0}{\partial z^2} + \frac{D_k}{H_z} \left[ \frac{1}{R} \frac{\partial^3 u_0}{\partial \theta^2 \partial z} + \frac{1}{R^2} \frac{\partial^2 w_0}{\partial \theta^2} \right] + \\
 & \frac{H_k}{H_z} \left[ R \frac{\partial^2 v_0}{\partial \theta \partial z} + \frac{\partial^2 w_0}{\partial \theta^2} \right] - \frac{D_z}{H_z} R \frac{\partial^3 u_0}{\partial z^3} + \phi_{1z} \left[ R \frac{\partial u_0}{\partial z} - \frac{\partial^2 w_0}{\partial \theta^2} \right] = 0
 \end{aligned}
 \tag{8}$$

where

$$\phi_{1z} = q(1 - \nu_{\theta z} \nu_{z\theta}) R / E_z h$$

$$\phi_{1\theta} = q(1 - \nu_{\theta z} \nu_{z\theta}) R / E_\theta h$$

$$\phi_2 = N(1 - \nu_{\theta z} \nu_{z\theta}) / E_\theta h$$

The general solution of Equations [8] leads to serious difficulties. Therefore, solutions are confined to a simple form. Then, assuming the cylinder to be simply supported at the ends, solutions of the following form are looked for (3)

$$u_0 = U \cos n\theta \sin \lambda(z/R)$$

$$v_0 = V \sin n\theta \sin \lambda(z/R)$$

$$w_0 = W \cos n\theta \cos \lambda(z/R)$$

$$\dots \dots \dots [9]$$

where  $\lambda = m\pi R/L$  and  $U$ ,  $V$  and  $W$  are constants. The solution defined by  $m$  and  $n$  characterizes a loading that causes the cylinder to buckle with  $2n$  half waves in the circumferential direction and  $m$  half waves in the axial direction (Fig. 7). Substituting the assumed displacements, Equations [9], into the differential equations [8] gives three equations in  $U$ ,  $V$  and  $W$ .

For a solution other than zero to exist, the determinant of

the coefficients must be zero. Carrying this through results in the required buckling equation which is

$$A\lambda^4(h/R) + (K\lambda^6 + L\lambda^6n^2 + B\lambda^4n^4 + C\lambda^2n^6 + Fn^8)(h^3/12R^3) + (Mn^2\lambda^4 + H\lambda^2n^4 - Fn^6)w_2 + (H\lambda^4n^2 + M\lambda^6 - Fn^4\lambda^2)W_2 = 0 \quad [10]$$

This is the required equation of stability. The constants  $A$ ,  $B$ ,  $C$ , etc., are given by

$$\begin{aligned} A &= (D_k/D_\theta)(D_z/D_\theta) - \nu_{\theta\theta}^2(D_k/D_\theta) \\ B &= 6(D_k/D_\theta)(D_z/D_\theta) - 8\nu_{\theta\theta}(D_k/D_\theta)^2 - 8\nu_{\theta\theta}^2(D_k/D_\theta) + 2\nu_{\theta\theta}(D_z/D_\theta) - 2\nu_{\theta\theta}^3 \\ C &= (D_z/D_\theta) + 4(D_k/D_\theta) - \nu_{\theta\theta}^2 \\ F &= (D_k/D_\theta) \\ H &= 2\nu_{\theta\theta}(D_k/D_\theta) + \nu_{\theta\theta}^2 - (D_z/D_\theta) \\ K &= (D_k/D_\theta)(D_z/D_\theta)^2 \\ L &= -\nu_{\theta\theta}^2(D_z/D_\theta) + 4(D_k/D_\theta)^2(D_z/D_\theta) + (D_z/D_\theta)^2 \\ M &= -(D_k/D_\theta)(D_z/D_\theta) \end{aligned} \dots\dots\dots [11]$$

and

$$\begin{aligned} D_z &= E_z h^3/12[1 - \nu_{\theta\theta}^2(E_\theta/E_z)] \\ D_\theta &= E_\theta h^3/12[1 - \nu_{\theta\theta}^2(E_\theta/E_z)] \\ D_k &= Gh^3/12 \end{aligned}$$

The quantities  $H_k$ ,  $H_z$ ,  $H_\theta$ ,  $\nu_{\theta\theta}$  and  $\phi_{1\theta}$  were eliminated by the following relationships

$$\begin{aligned} H_k &= 12D_k/h^2 & H_\theta &= 12D_\theta/h^2 & H_z &= 12D_z/h^2 \\ \nu_{\theta\theta} &= \nu_{\theta\theta}(E_\theta/E_z) & \phi_{1\theta} &= \phi_{1\theta}(E_\theta/E_z) \end{aligned}$$

The terms  $\phi_{1\theta}$  and  $\phi_2$  were replaced by  $w_1$  and  $w_2$ , thus

$$\begin{aligned} w_1 &= \phi_{1\theta} \frac{h}{R} = \frac{q[1 - \nu_{\theta\theta}^2(E_\theta/E_z)]}{E_\theta} \\ w_2 &= \phi_2 \frac{h}{R} = \frac{N[1 - \nu_{\theta\theta}^2(E_\theta/E_z)]}{E_\theta R} = \frac{P[1 - \nu_{\theta\theta}^2](E_\theta/E_z)}{2\pi E_\theta R^2} \end{aligned}$$

Equation [10] contains only linear terms in  $w_1$  and  $w_2$ . Higher order terms have been eliminated, since it was shown that they are small compared with the linear terms.

The important parameters in determining the constants are the ratios of the rigidities, which can be expressed as

$$\frac{D_z}{D_\theta} \equiv \frac{E_z}{E_\theta} \quad \frac{D_k}{D_\theta} \equiv \frac{G[1 - \nu_{\theta\theta}^2(E_\theta/E_z)]}{E_\theta}$$

So, for a given shell geometry and material, the only unknown quantities are  $m$  and  $n$ , the mode shapes. For a given value of these quantities there is a linear relationship between  $w_1$  and  $w_2$ . The minimum envelope of all the possible linear relationships is the critical load envelope, and it can be used to determine the critical values of axial load and radial pressure (see Fig. 8).

### Simplification of General Buckling Equation

It is desirable to simplify the equation of stability, Equation [10], so that it can be put in curve form, thereby reducing the amount of labor and time involved in its use. It can be shown that the constants  $A$ ,  $B$ ,  $C$ , etc., defined in Equations [11] can

$$\begin{aligned} &\left(\frac{D_k}{D_\theta}\right)\left(\frac{D_z}{D_\theta}\right)\left(\frac{h}{R}\right)\lambda^4 + \left[\left(\frac{D_k}{D_\theta}\right)\left(\frac{D_z}{D_\theta}\right)^2\lambda^8 + \left\{4\left(\frac{D_k}{D_\theta}\right)^2\left(\frac{D_z}{D_\theta}\right) + \left(\frac{D_z}{D_\theta}\right)^2\right\}\lambda^6n^2 + 6\left(\frac{D_z}{D_\theta}\right)\left(\frac{D_k}{D_\theta}\right)\lambda^4n^4 + \left\{\left(\frac{D_z}{D_\theta}\right) + 4\left(\frac{D_k}{D_\theta}\right)^2\lambda^2n^6 + \right. \right. \\ &\quad \left. \left. \left(\frac{D_k}{D_\theta}\right)n^8\right]\frac{h^3}{12R^3} - \left[\left(\frac{D_k}{D_\theta}\right)\left(\frac{D_z}{D_\theta}\right)n^2\lambda^4 + \left(\frac{D_z}{D_\theta}\right)\lambda^2n^4 + \left(\frac{D_k}{D_\theta}\right)n^6\right]w_1 + \left[\left(\frac{D_z}{D_\theta}\right)\lambda^4n^2 + \left(\frac{D_k}{D_\theta}\right)\left(\frac{D_z}{D_\theta}\right)\lambda^6 + \left(\frac{D_k}{D_\theta}\right)n^4\lambda^2\right]w_2 = 0 \end{aligned} \quad [13]$$

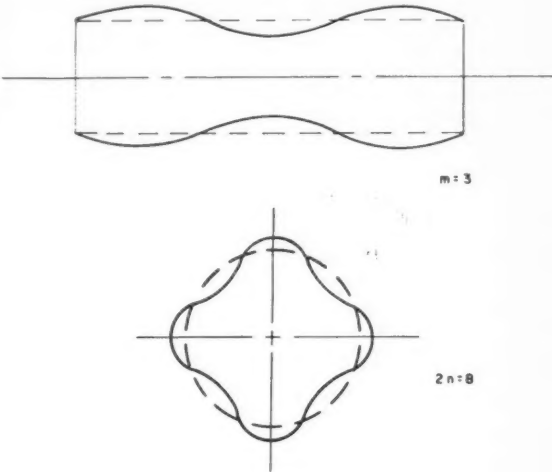


Fig. 7 Buckling modes

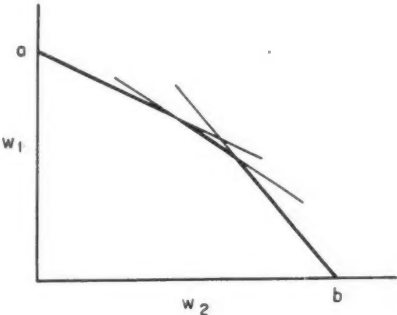


Fig. 8 Critical load interaction

be reduced to the following, with negligible error

$$\begin{aligned} A &= (D_k/D_\theta)(D_z/D_\theta) \\ B &= (D_k/D_\theta)(D_z/D_\theta)6 \\ C &= (D_z/D_\theta) + 4(D_k/D_\theta) \\ F &= (D_k/D_\theta) \\ H &= -(D_z/D_\theta) \\ K &= (D_k/D_\theta)(D_z/D_\theta)^2 \\ L &= 4(D_k/D_\theta)^2(D_z/D_\theta) + (D_z/D_\theta)^2 \\ M &= -(D_k/D_\theta)(D_z/D_\theta) \end{aligned} \dots\dots\dots [12]$$

It is seen that the essence of this reduction is the neglecting of the terms containing Poisson's ratio,  $\nu_{\theta\theta}$ . See (4). Equation [10] can then be written

For a given shell geometry and material, it develops that the critical load envelope giving the interaction between  $w_1$  and  $w_2$  is slightly above a straight line (see Fig. 8). It can also be seen that the critical load envelope will never be below a straight line. To assume a straight line interaction is, at most, conservative. This assumption was made here, and the preceding equation was divided into two separate equations—one gives the critical axial load parameter in the absence of pressure  $w_{1\max}$ , and the other gives critical pressure parameter in the absence of axial load  $w_{2\max}$ . These two points are the end points of the curve of Fig. 8. Thus

$$w_{1\max} = \frac{\left(\frac{D_k}{D_\theta}\right)\left(\frac{D_z}{D_\theta}\right)\left(\frac{h}{R}\right)\lambda^4 + \left[\left(\frac{D_z}{D_\theta}\right)\left(\frac{D_z}{D_\theta}\right)^2\lambda^3 + \left\{4\left(\frac{D_z}{D_\theta}\right)\left(\frac{D_k}{D_\theta}\right)^2 + \left(\frac{D_z}{D_\theta}\right)^2\right\}\lambda^6 n^2 + 6\left(\frac{D_k}{D_\theta}\right)\left(\frac{D_z}{D_\theta}\right)\lambda^4 n^4 + \left\{4\left(\frac{D_z}{D_\theta}\right)^2 + \left(\frac{D_z}{D_\theta}\right)\right\}\lambda^2 n^6 + \left(\frac{D_k}{D_\theta}\right)n^8]}{12R^3} \quad [14]$$

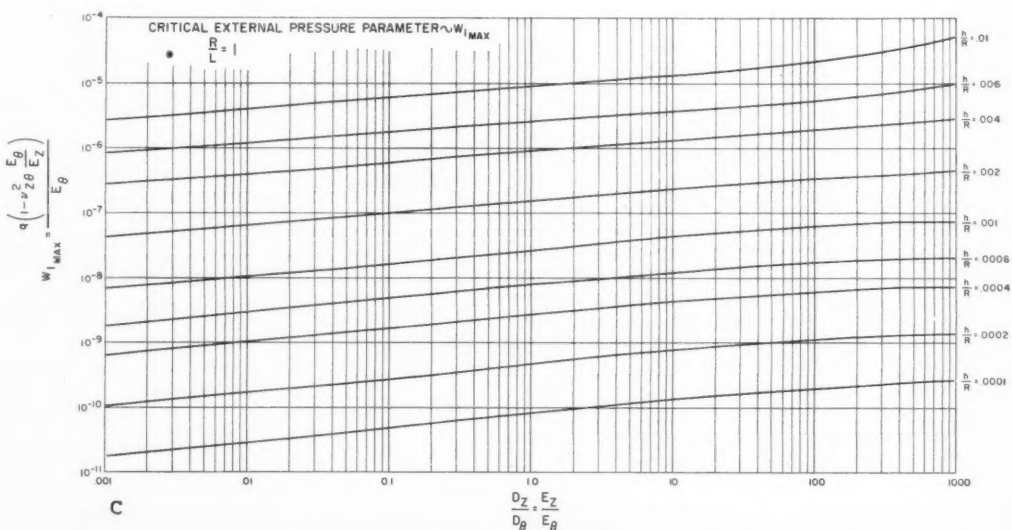
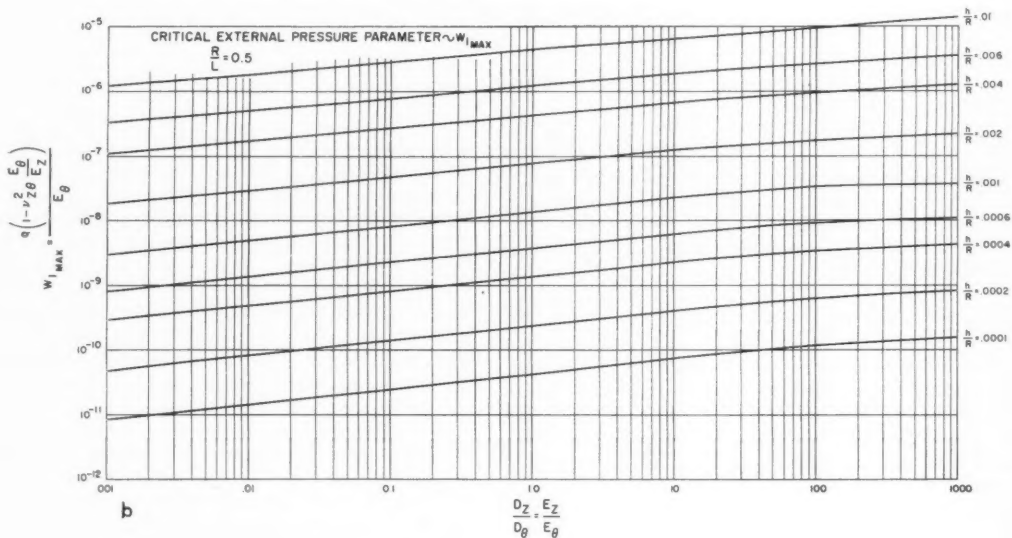
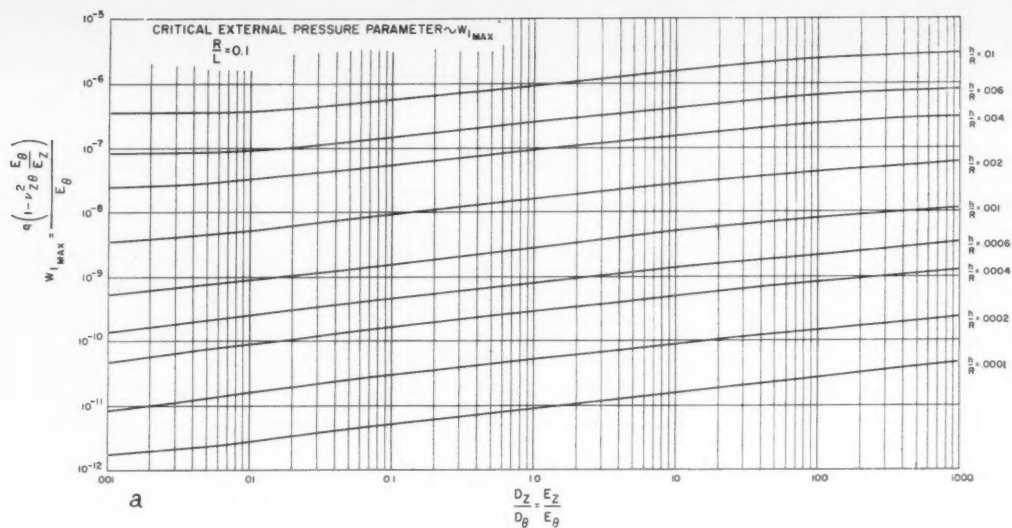
$$w_{2\max} = \frac{\left(\frac{D_k}{D_\theta}\right)\left(\frac{D_z}{D_\theta}\right)\left(\frac{h}{R}\right)\lambda^4 + \left[\left(\frac{D_z}{D_\theta}\right)\left(\frac{D_z}{D_\theta}\right)^2\lambda^3 + \left\{4\left(\frac{D_z}{D_\theta}\right)\left(\frac{D_k}{D_\theta}\right)^2 + \left(\frac{D_z}{D_\theta}\right)^2\right\}\lambda^6 n^2 + 6\left(\frac{D_k}{D_\theta}\right)\left(\frac{D_z}{D_\theta}\right)\lambda^4 n^4 + \left\{\left(\frac{D_z}{D_\theta}\right) + 4\left(\frac{D_k}{D_\theta}\right)^2\right\}\lambda^2 n^6 + \left(\frac{D_k}{D_\theta}\right)n^8]}{12R^3} \quad [15]$$

Furthermore, it was found, by calculating  $w_{1\max}$  for a wide range of values of  $D_k/D_\theta$ , that  $w_{1\max}$  is almost independent of  $D_k/D_\theta$ . Similarly, it was found that  $w_{2\max}$  is independent of  $R/L$ . So  $D_k/D_\theta$  can be eliminated from Equation [14], and  $R/L$  can be eliminated from Equation [15].  $D_k/D_\theta$  is taken as 0.5 in Equation [14], and  $R/L$  is taken as 1 in Equation [15]. These values were assigned because they are midrange values of the two parameters. Thus Equations [14 and 15] become

$$w_{1\max} = \frac{0.5\left(\frac{D_z}{D_\theta}\right)\left(\frac{h}{R}\right)\left(\frac{m\pi R}{L}\right)^4 + \left[0.5\left(\frac{D_z}{D_\theta}\right)\left(\frac{m\pi R}{L}\right)^8 + \left\{\left(\frac{D_z}{D_\theta}\right) + \left(\frac{D_z}{D_\theta}\right)^2\right\}\left(\frac{m\pi R}{L}\right)^6 n^2 + 3\left(\frac{D_z}{D_\theta}\right)\left(\frac{m\pi R}{L}\right)^4 n^4 + \left\{\left(\frac{D_z}{D_\theta}\right) + 1\right\}\left(\frac{m\pi R}{L}\right)^2 n^6 + 0.5n^8]}{12R^3} \quad [16]$$

$$w_{2\max} = \frac{\left(\frac{D_k}{D_\theta}\right)\left(\frac{D_z}{D_\theta}\right)\left(\frac{h}{R}\right)(m\pi)^4 + \left[\left(\frac{D_k}{D_\theta}\right)\left(\frac{D_z}{D_\theta}\right)^2(m\pi)^8 + \left\{4\left(\frac{D_z}{D_\theta}\right)\left(\frac{D_k}{D_\theta}\right)^2 + \left(\frac{D_z}{D_\theta}\right)^6 n^2 + 6\left(\frac{D_k}{D_\theta}\right)\left(\frac{D_z}{D_\theta}\right)(m\pi n)^4 + \left\{\left(\frac{D_z}{D_\theta}\right) + 4\left(\frac{D_k}{D_\theta}\right)^2\right\}(m\pi)^2 n^6 + \left(\frac{D_k}{D_\theta}\right)n^8}\right]}{12R^3} \quad [17]$$





Figs. 9a, b, c Critical external pressure parameter

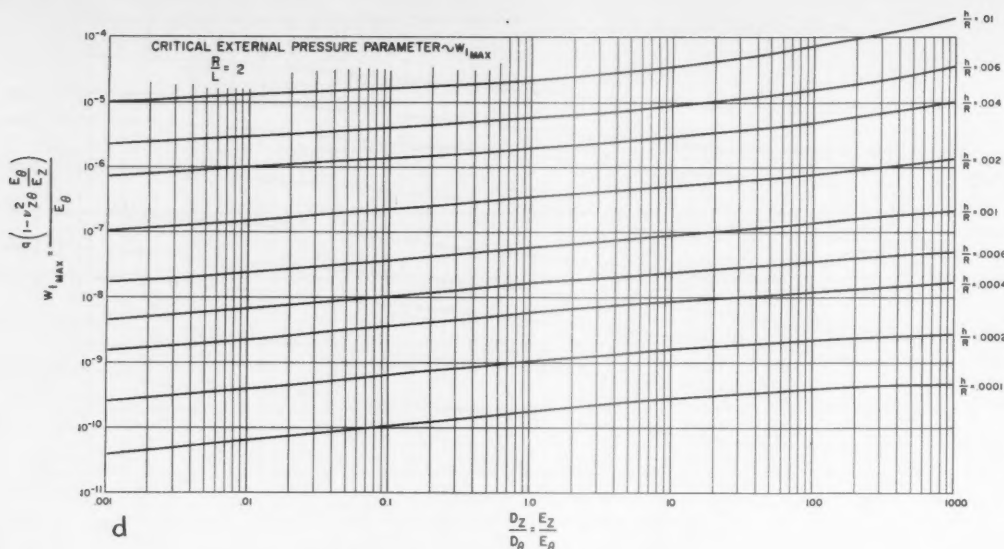


Fig. 9d Critical external pressure parameter

Equations [16 and 17] give  $w_{lmax}$  and  $w_{\theta max}$  as a function of shell geometry and material properties. They are plotted in Figs. 9 and 10 for a range of geometries and material properties. The critical external pressure and axial load can then be found, and critical combinations of these values, by assuming the linear interaction.

## Conclusions

The curves of this report can be used to determine the critical axial load and critical external pressure on cylindrical and conical shells whose walls are composed of an orthotropic material. Assuming linear interaction between the two, one can determine combined loading capabilities of a given shell. For cylindrical shells the curves can be used directly, but for conical shells it is necessary to transform into the equivalent cylinder.

One conservative aspect of this theory is that simple-supported ends are assumed. An actual shell design would probably have rings at the ends, giving a support somewhat better than a simple one. However, it is reasonable to assume the existence of a simply supported end condition considering some of the other nonconservative aspects of buckling theories.

Some tests are planned for the purpose of confirming the theoretical results of this study, or for determining a reasonable safety factor to be used with this theory. No test results on cylinders of a purely orthotropic material could be found. However (1), which gives experimental results, served as a basis for a limited amount of comparison with test. This was done as follows. A value of  $E_z/E_{\theta} = 1$  corresponds to an isotropic material. Therefore, the corresponding values of  $w_{lmax}$  were compared with the theory given in (1), and very good agreement was found. Testing is still needed, however, as this comparison is very limited.

It can also be seen from this theory that minimum weight can be attained by a proper orientation of the greater modulus of elasticity. For example, consider a cylindrical shell under an external pressure of 10 psi. The shell has a radius of 20 in. and a length of 20 in. Fig. 11 shows that if  $E_z$  equals  $E_{\theta}$ , a thickness of 0.110 is required.  $E_z$  and  $E_{\theta}$  were taken as  $5 \times 10^6$  here, but any value could have been used, since relative magnitudes and trends are being examined. Now if the

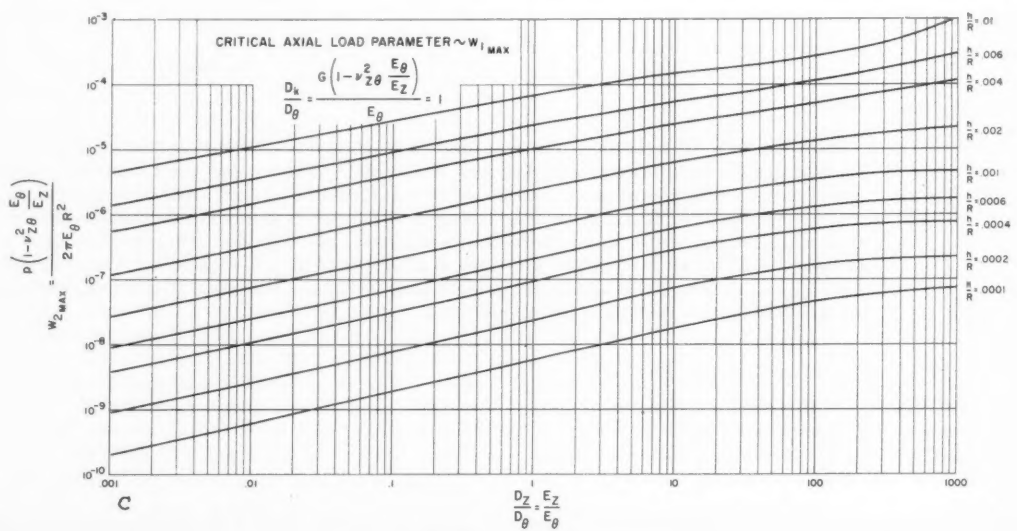
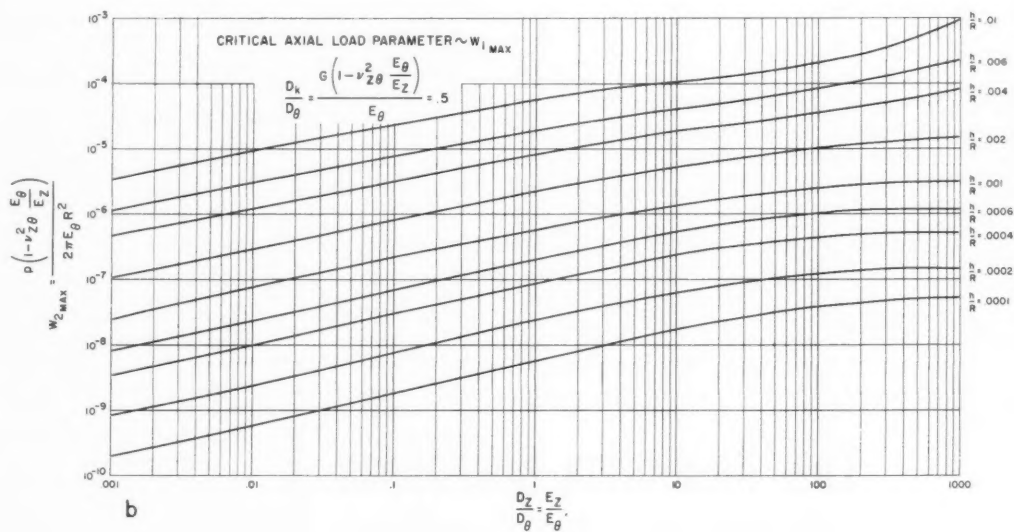
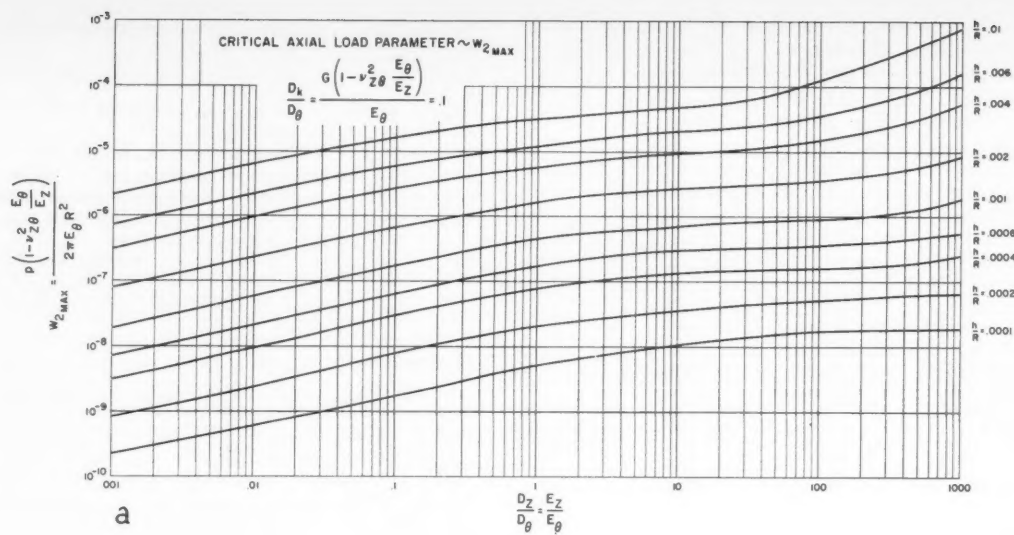
axial modulus of elasticity  $E_z$  is tripled, making  $E_z/E_{\theta}$  equal to 3, the thickness required is 0.102. This represents a 7.3 per cent decrease in thickness. If, however, the circumferential modulus of elasticity  $E_{\theta}$  is tripled instead, bringing  $E_z/E_{\theta}$  equal to 0.33, the required thickness is 0.077, or a 30 per cent decrease in thickness. It can easily be seen that, given the choice of increasing either  $E_z$  or  $E_{\theta}$ , the more advantageous choice is to increase  $E_{\theta}$ . The same trend can be seen for the case of axial load. Therefore, it can be concluded that thickness, and therefore weight, is much more sensitive to  $E_{\theta}$  than to  $E_z$ , and that, where possible, the shell should have a valued  $E_z/E_{\theta}$  less than 1.

The 7.3 and 30 per cent decreases in thickness do not mean the same percentage decreases in weight, since conceivably some weight has to be added to increase the moduli. However, it is reasonable to assume that this added weight is approximately the same whether used to triple  $E_z$  or  $E_{\theta}$ , and so there is still more advantage to be gained in using the weight to triple  $E_{\theta}$ .

This discussion also points out that there is a significant weight saving potential in the use of orthotropic materials, and that every effort should be made to develop capabilities for analyzing them, so that these materials may be used to the fullest extent.

## Nomenclature

$h$	= shell thickness, in.
$m$	= axial buckling half waves
$n$	= circumferential buckling waves
$q$	= external radial pressure, psi
$u, v, w$	= displacements in $r, \theta, z$ directions, respectively, in.
$r, \theta, z$	= cylindrical coordinates
$w_1$	= $q[1 - \nu_{\theta}^2(E_{\theta}/E_z)]/E_{\theta}$ , critical external pressure parameter
$w_2$	= $P[1 - \nu_{\theta}^2(E_{\theta}/E_z)]/2\pi E_{\theta} R^2$ , critical axial load parameter
$D_z$	= $E_z h^3/12(1 - \nu_{\theta} \nu_{\theta z})$ , flexural rigidity in axial direction, in.-lb
$D_{\theta}$	= $E_{\theta} h^3/12(1 - \nu_{\theta} \nu_{\theta z})$ , flexural rigidity in circumferential direction, in.-lb
$D_k$	= $Gh^3/12$
$E_z$	= modulus of elasticity in axial direction, psi



Figs. 10 Critical axial load parameter

$E_\theta$  = modulus of elasticity in circumferential direction, psi  
 $G$  = shear modulus of elasticity, psi  
 $H_z$  =  $E_z h / (1 - \nu_{\theta z} \nu_{z\theta})$ , lb/in.  
 $H_\theta$  =  $E_\theta h / (1 - \nu_{\theta z} \nu_{z\theta})$ , lb/in.  
 $H_k$  =  $Gh$ , lb/in.  
 $L$  = shell length, in.

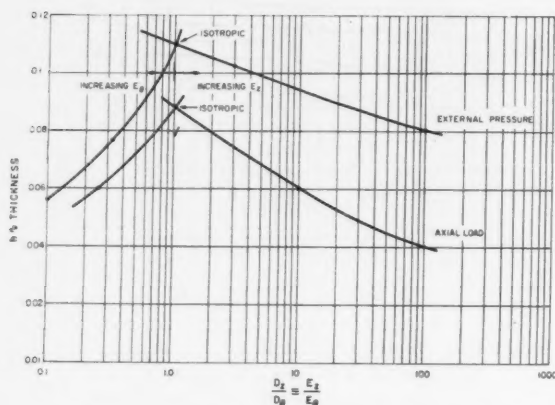


Fig. 11 Variation of thickness with rigidity ratio

$M_z, M_\theta, M_{z\theta}, M_{\theta z}$  = moment stress resultants, in-lb/in.  
 $N$  = axial load, lb/in.  
 $N_z, N_\theta$  = force stress resultants, lb/in.  
 $P$  = axial load, lb  
 $Q_{z\theta}, Q_{\theta z}, Q_{\theta r}, Q_{zr}$  = shear stress resultants, lb/in.  
 $R$  = shell radius, in.  
 $\epsilon$  = strain components, in./in.  
 $\sigma$  = stress components, psi  
 $\nu_{\theta\theta}$  = Poisson's ratio, relating strain in the  $\theta$  direction to strain in the  $z$  direction owing to stress in  $z$  direction.  
 $\nu_{z\theta}$  = Poisson's ratio, relating strain in the  $z$  direction to strain in the  $\theta$  direction owing to stress in the  $\theta$  direction

## References

- 1 Hess, T. E. and Garber, A. M., "Stability of Ring-Stiffened Conical Shells Under Simultaneous Lateral Pressure and Axial Compression," TIS no. R58SD226, General Electric Co., Philadelphia, Pa., April, 30, 1958.
- 2 Biezeno, C. B. and Grammel, R., "Engineering Dynamics," Vol. II, Blackie & Son, Ltd., London, 1956.
- 3 Timoshenko, S., "Theory of Elastic Stability," McGraw-Hill Book Co., Inc., N. Y., 1936.
- 4 Becker, H., "General Instability of Stiffened Cylinders," NACA TN 4237, July 1958.
- 5 Hess, T. E., "Design of Orthotropic Beams and Plates Under Uniform Lateral Pressure," Memo no. 123-78, General Electric Co., Philadelphia, Pa., March 13, 1959.
- 6 Hess, T. E., "Thermal Stresses in an Orthotropic Spherical Shell With a Radial Temperature Gradient," TIS no. R59SD344, General Electric Co., Philadelphia, Pa., April 13, 1959.
- 7 Bijlaard, P. P., "Critical External Pressure of Conical Shells That Are Simply Supported At The Edges," Rep. no. 02-941-027, Bell Aircraft Corp., Buffalo, N. Y., Feb. 1953.

# Low Resolution Unchopped Radiometer for Satellites

RUDOLF A. HANEL<sup>1</sup>

Goddard Space Flight Center,  
NASA  
Washington, D. C.

Knowledge of the blackbody temperature and the albedo of Earth and other planets, and the variation of both parameters with latitude, longitude and time, is of great value in understanding the climatic and meteorological conditions of the particular planet. An unchopped radiometer of a wide but restricted field of view is capable of such temperature and albedo measurements. Coated thermistors mounted in highly reflective cones serve as detectors. Their performance as sensor elements is analyzed in detail to prove the feasibility of the measurement. The simplicity of the instrumentation and the low information bandwidth required make the experiment equally attractive for Earth satellites and space probes.

THE MEASUREMENT of optical and thermal properties of Earth and other planets is one of the basic physical experiments that can be performed with satellites and space probes. Incoming and outgoing radiation determines the

energy budget of the astronomical body and is responsible for climate and weather in the broadest sense. Measurements in narrow spectral regions permit the determination of composition and temperatures of the atmospheres and give information on surface conditions.

The goal in this field of research could be to produce detailed maps of the planets, showing the visual picture, tem-

Received May 31, 1960.

<sup>1</sup> Research Scientist.



peratures and radiation in characteristic bands. All high resolution maps obtainable by photography, television and spot scanning techniques require a high information rate capability in transmission and possibly storage facilities in the probe. For many purposes, especially if overall global or planetary studies are involved, only average values over rather large areas, e.g.,  $300 \times 300$  miles, are of interest. Even in Earth satellites, where a high resolution picture is possible with present day communication capabilities, the integrating property of the wide field detector justifies simultaneous measurements by high and low resolution devices.

The simplest form of such a wide field radiation measurement is the heat balance experiment, suggested by Suomi and Wesler in connection with the IGY program (1).<sup>2</sup> The temperature of small spheres, coated to discriminate between solar and terrestrial radiation, is sensed by thermistors. However, the omnidirectional device has restrictions in accuracy and resolution. It is especially desirable in conjunction with an image forming experiment, such as the television cameras of Tiras, to match the field of view of both high and low resolution instruments. Interesting correlations between cloud cover and radiation balance might be expected. The main problem in such a simple, unchopped radiometer is the loss in sensitivity resulting from the restrictions in the field of view. A technique which overcomes this limitation has been developed and is analyzed in this paper.

## Method

In the suggested version of the detector, a thermistor is mounted in the apex of a highly reflecting cone. The detector can be classified as a thermal detector predominantly cooled by radiation. The temperature of the detector is governed by the equation of energy balance

$$\epsilon_t \sigma T_t^4 = k_1 \sigma T_E^4 + k_2 \sigma T_s^4 + k_2' 4\sigma T_0^3 (T_s - T_t) + k_3 A S \sin \beta \quad [1]$$

Thermal radiation emitted by the thermistor balances radiation from Earth, radiation and heat conduction from the satellite, and finally Earth's reflected solar energy. The coefficients  $k_i$  consolidate optical as well as geometrical factors. The two unknowns, the blackbody temperature of Earth  $T_E$  and the albedo  $A$ , can be determined if a second linearly independent equation is available.

In the experiment, the second equation is provided by a second thermistor of different optical properties. One detector is coated "black"; it is equally sensitive to reflected sunlight and long wave terrestrial radiation. The second detector is coated to be highly reflective in the visible and near infrared out to about  $3\mu$ . See (2). The surface appears "white" to the eye even though its emissivity in the infrared is very high. Since 99.9 per cent of the terrestrial radiation is emitted at wave lengths longer than  $4\mu$ , both detectors will show the same equilibrium temperature when they face the dark side of Earth. On the illuminated side, the temperature of the "black" detector will rise in contrast to the white one which is hardly affected by reflected sunlight. A careful measurement of the temperature of both detectors and an accurate calibration of all  $k$  values permits the determination of albedo and terrestrial radiation.<sup>3</sup> It has been assumed that the influence of the satellite temperature  $T_s$  can be kept small ( $k_2$  and  $k_2' \ll k_1$ ); otherwise the thermistor would read what is essentially the satellite temperature. A high thermal isolation of the detectors from the satellite structure is essential to the experiment, and the major part of this paper is devoted to this problem.

<sup>2</sup> Numbers in parentheses indicate References at end of paper.

<sup>3</sup> This is exactly true only if radiation from Earth follows Lambert's cosine law. But, since the atmosphere with its peculiar absorption bands in the infrared and its temperature gradients does not emit like a diffuse surface, certain corrections in the interpretation of data must be made.

## Geometry of Cone

The field of view of a thermistor mounted in a cone can be visualized best by the mirror image of the detector (Fig. 1). The conical detector is equivalent to a spherical one which is restricted in its field of view by an aperture equal to the base of the cone. Reflection losses could be taken into account by the assumption of a reduced emissivity of each image. It is reasonable to consider a sphere of uniform emissivity  $\epsilon_t$ , since evaporated metal surfaces have high reflectivity (90-99 per cent) and since only a few reflections are involved. Figs. 2 show the field of view of such a detector for various relative sizes of the thermistor and various aperture angles.

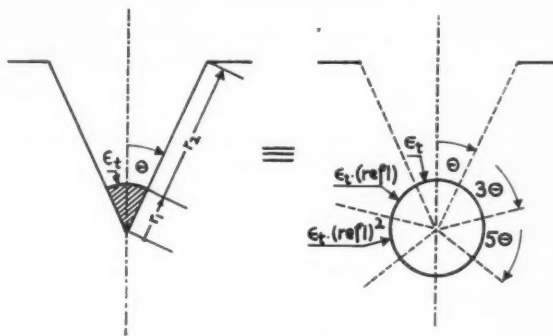


Fig. 1 Wide field of view radiometer; equivalent detector, imaging of the thermistor

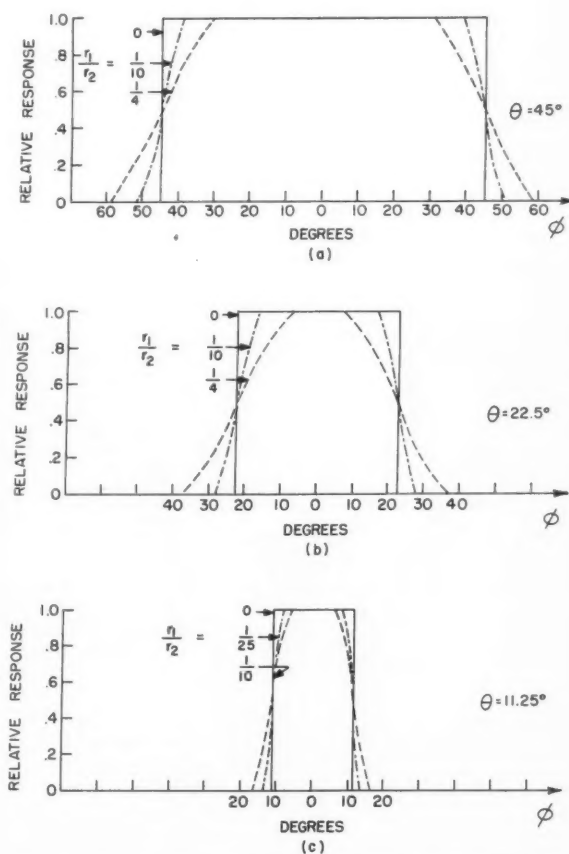


Fig. 2 Field of view of wide field radiometer as a function of thermistor to cone ratio ( $r_1/r_2$ ) and aperture angle

The energy exchange is judged better by a second mode of imaging, namely, by imaging of the source as shown in Fig. 3. The detector surface appears completely surrounded by the target. Radiation exchange between thermistor and Earth is then described by Equation [2]

$$P = \epsilon_i \sigma (T_E^4 - T_i^4) a_i \quad [2]$$

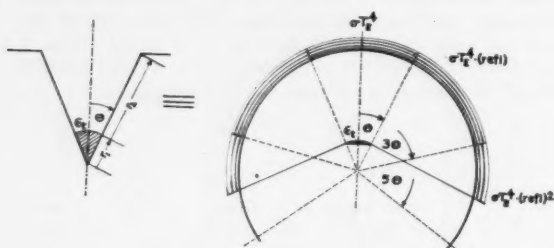


Fig. 3 Wide field of view radiometer; equivalent detector, imaging of the radiation source

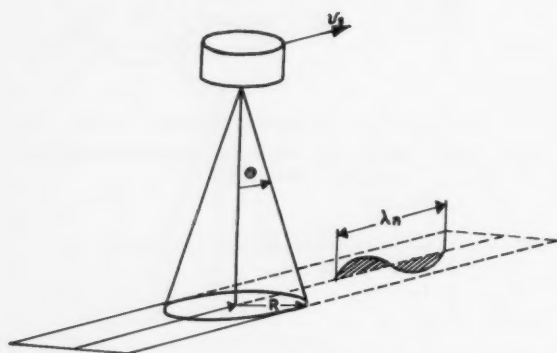


Fig. 4 Schematic of detector scanning Earth as the satellite moves along vector  $v$

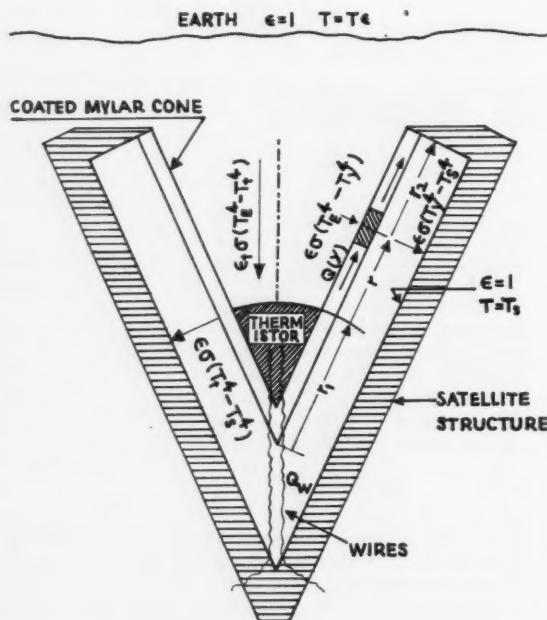


Fig. 5 Wide field radiometer; energy transfer within the conical detector

The term  $a_i = 2\pi r_i^2 (1 - \cos \Theta)$  represents the detector area. Without the conical reflector the same detector would receive approximately  $P \sin^2 \Theta$ . The "gain" introduced by the cone becomes about 5 for  $\Theta = 25$  deg. The same method of imaging enables us to estimate radiation between cone and detector. Since the emissivity of the cone material can be kept as low as 0.02, and since large portions of the cone will be at the satellite temperature, this effect, small to begin with, can be incorporated into the radiation exchange of the unexposed side of the thermistor mount.

## Resolution and Bandwidth

The spatial resolution of the system and the electrical bandwidth which is required to process the gathered information are determined by the field of view, the altitude and the speed of the vehicle. The detector, slowly scanning Earth as the satellite moves along, responds to the average radiation within its field of view as shown in Fig. 4. Any arbitrary intensity distribution in the scanning direction can be taken into consideration by superposition of periodic distributions of wavelength  $\lambda_n$ . A small slit perpendicular to the scan motion or a small square field of view exhibit a  $\sin x/x$  characteristic. The first null of this function is at  $x = \pi$ . The relationship between tape speed, gap width and frequency response for magnetic tape recorders, for example, shows complete analogy to formulas describing optical scanning processes.

A small circular field of view has a  $2J_1(x)/x$  scanning function, and the first null appears at  $x = 3.8$ . If the field of view is circular but not negligibly small as it is in the case under consideration, then the scanning characteristic of the detector can be described by a sum of Bessel functions rather than only one of the first order. For an altitude of 300 miles and a total field of view of 50 deg, however, the first null of the scanning function shifts only insignificantly from 3.8 to 4; a black and white pattern on the ground of a periodicity of  $\lambda_1 = 2\pi R/4$  cannot be resolved by the detector. The electrical frequency which corresponds to the first null in the scanning function is given by the subsatellite velocity  $v$  divided by  $\lambda_1$ . The numerical values mentioned yield about 0.02 cps. The thermal time constant of the detector has to be chosen to accommodate up to this frequency. Compared with other detection systems the bandwidth requirements are very low indeed.

## Energy Transfer Within the Cone

A cross section of the detector assembly (Fig. 5) shows the thermistor imbedded in the central area on the tip of the cone. The thermistor material could be deposited directly on the lower inner part of the Mylar cone. For small angles  $\Theta$  the "black" detector being truly gray, since its emissivity is about 0.8, would resemble an ideal blackbody. This procedure is not too advisable for the white detector, since the reflectivity for visible light is also reduced. The cover plate which shields the cone or cones from the interior of the satellite is made highly reflective ( $\epsilon = 0.02$ ). However, in the calculations an emissivity of unity ( $\epsilon_s = 1$ ) was assumed. This seems justified for the following reasons.

Owing to multireflections the effective emissivity of two parallel surfaces of emissivity  $\epsilon_1$  and  $\epsilon_2$ , facing each other, is

$$\epsilon_{eff} = \epsilon_1 \epsilon_2 / (\epsilon_1 + \epsilon_2 - \epsilon_1 \epsilon_2) \quad [3]$$

If both emissivities  $\epsilon_1$  and  $\epsilon_2$  are small and equal,  $\epsilon_{eff}$  becomes  $\epsilon/2$ . However, if radiation emitted by the rear surface of the thermistor is not reflected back to the detector, but bounces back and forth between cone and cover plate until it is finally absorbed, then the cavity between cone and cover acts like a blackbody independent of wall emissivity, and  $\epsilon_{eff}$  becomes equal to  $\epsilon$  rather than  $\epsilon/2$ . The physical structure will be somewhere between both cases, probably closer to the black cavity model. Therefore, and also to incorporate a small

amount of radiation from the front surface of the detector to the outer areas of the cone, the emissivity of the cover plate was chosen equal to unity for the purpose of this calculation.

The energy flux  $Q(r)$  in the cone material is proportional to the temperature gradient

$$Q(r) = -cD2\pi r \sin \Theta \, dT_{(y)}/dr \quad [4]$$

$$a = \frac{(\xi r_1/4\epsilon \sin \Theta) [\epsilon(\rho + \sin \Theta)(1 - H_{01}/H_{02}) - \epsilon_2(1 - \cos \Theta)(1 + H_{01}/H_{02})] - i(H_{11}/H_{02})}{(\xi r_1/4\epsilon \sin \Theta) [\epsilon(\rho + \sin \Theta) + \epsilon_2(1 - \cos \Theta)](J_{01}H_{02} - J_{02}H_{01}) + i(J_{11}H_{02} - J_{02}H_{01})} \quad [16]$$

Simultaneously,  $Q(r)$  is the flux into the cone tip plus the received or emitted radiation

$$Q(r) = Q(r_1) + \int_{r_1}^r \epsilon \sigma (T_E^4 - T_y^4) da - \int_{r_1}^r \epsilon \sigma (T_y^4 - T_s^4) da \quad [5]$$

In Equation [16]  $\rho$  stands for

$$\rho = c_w q_w / \epsilon \sigma 4 T_0^3 \pi r_1^2 \quad [17]$$

Since the general solution for  $y$  equals  $t$  for  $r = r_1$ , the thermistor temperature is given by

$$t = H_{01}/H_{02} + a(J_{01}H_{02} - J_{02}H_{01})/H_{02} \quad [18]$$

and finally by substitution of  $a$  and rearranging terms

$$t = \frac{[\epsilon(\rho + \sin \Theta) - \epsilon_2(1 - \cos \Theta)]/4\epsilon \sin \Theta + (i/\xi r_1)[(J_{11}H_{02} - J_{02}H_{11})/(J_{01}H_{02} - J_{02}H_{01})]}{\{[\epsilon(\rho + \sin \Theta) + \epsilon_2(1 - \cos \Theta)]/4\epsilon \sin \Theta\} + (i/\xi r_1)[(J_{11}H_{02} - J_{02}H_{11})/(J_{01}H_{02} - J_{02}H_{01})]} \quad [19]$$

The areal element  $da$  in Equation [5] is  $da = 2\pi r \sin \Theta dr$ . The balance between incoming and outgoing radiation of the thermistor is

$$Q(r_1) = \epsilon_i \sigma (T_E^4 - T_i^4) 2\pi r_1^2 (1 - \cos \Theta) - \int_0^{r_1} \epsilon \sigma (T_i^4 - T_s^4) da - 2c_w q_w (T_s - T_i)/l \quad [6]$$

These equations can be solved after linearization using a reference temperature  $T_0$

$$\begin{aligned} T_y &= T_0 + y & T_y^4 &= T_0^4 + 4T_0^3 y + \dots \\ T_i &= T_0 + t & T_i^4 &= T_0^4 + 4T_0^3 t + \dots \\ T_s &= T_0 + S & T_s^4 &= T_0^4 + 4T_0^3 S + \dots \\ T_E &= T_0 + E & T_E^4 &= T_0^4 + 4T_0^3 E + \dots \end{aligned} \quad [7]$$

The error which is introduced by the omission of second-order terms can be kept small if  $T_0$  is chosen close to the midrange value of temperatures involved. Furthermore, without a loss in generality, the satellite temperature  $S$  can be taken equal to plus unity (+1) and the equivalent Earth temperature equal to minus unity (-1).

Equations [4 through 6] then become

$$Q(r) = -cD2\pi r \sin \Theta \, dy/dr \quad [8]$$

$$Q(r) = Q(r_1) - 2\epsilon \sigma 2\pi \sin \Theta 4T_0^3 \int_{r_1}^r y r dr \quad [9]$$

$$Q(r_1) = \sigma 4T_0^3 \pi r_1^2 [-\epsilon_i(1 + t)2(1 - \cos \Theta) + \epsilon(1 - t) \sin \Theta] + 2c_w q_w (1 - t)/l \quad [10]$$

Differentiation of Equations [8 and 9] leads to a Bessel differential equation

$$y'' + (1/r)y' - 2\epsilon \sigma 4T_0^3 y/cD = 0 \quad [11]$$

which is solved by Bessel and Hankel functions of zero order and imaginary argument (3)

$$y = aJ_0(i\xi r) + bH_0^{(1)}(i\xi r) \quad [12]$$

The parameter  $\xi$  is introduced for brevity

$$\xi^2 = 2\epsilon \sigma 4T_0^3/cD \quad [13]$$

Boundary conditions determine the constants  $a$  and  $b$  in Equation [12]. One boundary condition states that the temperature of the base of the cone must be the satellite temperature

$$y(r = r_1) = +1 \quad [14]$$

The introduction of Equation [14] into Equation [12] yields

$$y = H_0(i\xi r)/H_{02} + a[J_0(i\xi r)H_{02} - J_{02}H_0(i\xi r)]/H_{02} \quad [15]$$

At the other boundary,  $r$  equals  $r_1$ ; the thermal flux must be  $Q(r_1)$  as specified by Equation [10] which determines the remaining constant  $a$

The thermistor temperature  $t$  expressed by Equation [19] is shown in Fig. 6 (4). The thermistor temperature is within the two limits, the satellite temperature  $S$  (+1) and the Earth temperature  $E$  (-1). A variety of parameters which have been consolidated in  $x_1$  and  $x_2$  determines  $t$ . The abscissa in Fig. 6 is  $x_1$ , and the depicted curves correspond to a particular value of  $x_2$ . The parameters  $x_1$  and  $x_2$  are proportional to the dimensions of the thermistor ( $r_1$ ) and the cone ( $r_2$ ). They should be chosen so that  $t$  approaches the Earth temperature  $E$  as closely as possible without unnecessarily increasing the physical dimensions of the detector. The value  $x_1 = 3$  seems to be a good compromise. For thermal reasons alone  $x_2 \geq 6$  would be sufficient; however, a well-defined field of view requires  $x_2 \geq 4x_1$ . The radii  $r_1$  and  $r_2$  can then be determined

$$r_1 = x_1 \sqrt{\frac{cD}{2\epsilon \sigma 4T_0^3}} \quad r_2 = x_2 \sqrt{\frac{cD}{2\epsilon \sigma 4T_0^3}} \quad [20]$$

Numerical values for a 1-mil Mylar cone yield a thermistor size of about 1 cm<sup>2</sup>, which is quite a reasonable dimension.

Up to this point the influence of wires which connect the thermistor electrically to the resistance measuring instrument has been neglected. This is justified as can be seen from Equation [19] as long as  $\rho$  is less than  $\sin \Theta$  or  $c_w q_w$  is less than  $\epsilon \sigma 4T_0^3 \pi r_1^2 \sin \Theta$ , a condition which can easily be met by a thin platinum wire (gage number 30,  $l = r_2$ ). Heat conduction through the wires can therefore be neglected.

## Calibration

A very important task will be the determination of the coefficients  $k_i$ . The linearized form of Equation [1] for the black and the white thermistor yields two equations with new coefficients

$$\begin{aligned} t_{bl} &= k_{11}E + k_{12}S + k_{13}A \\ t_{wh} &= k_{21}E + k_{22}S + k_{23}A \end{aligned} \quad [21]$$

The constants  $k_{11}$ ,  $k_{13}$  and  $k_{21}$  will be chosen high, perhaps 0.9. With proper coating, the residual responsivity of the white detector to sunlight ( $k_{22}$ ) will be made as small as possible. Calculations in this paper have shown that the combined effect of radiation and conduction from the satellite structure  $k_{12}$  and  $k_{23}$  can be made very small indeed (0.1). The experimental verification and determination of all values of  $k$  are the most important parts of the calibration. The temperatures of the black and white thermistor and the satellite

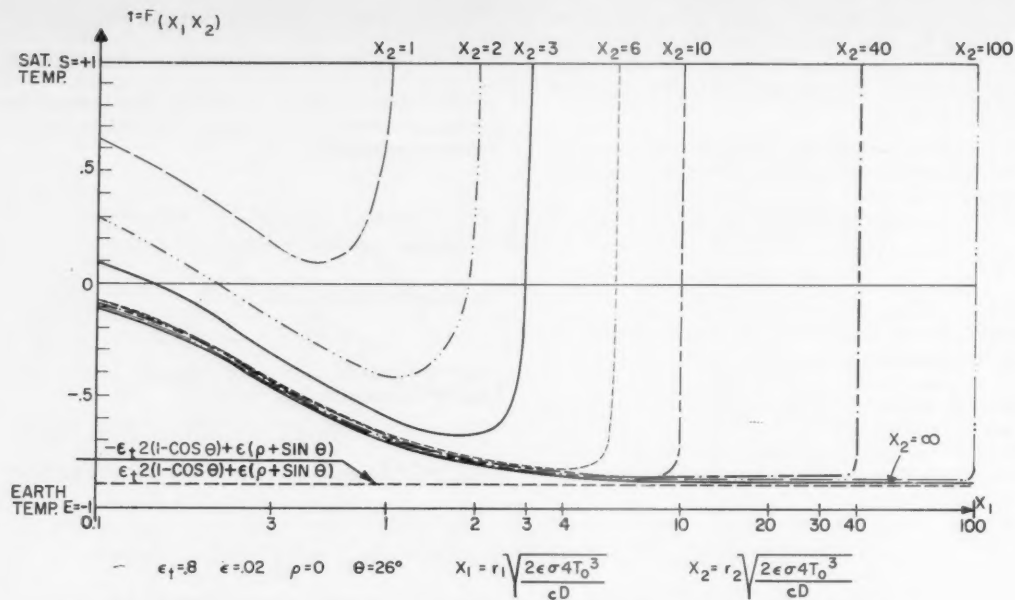


Fig. 6 Thermistor temperature in environment of the satellite and radiation field of Earth

structure will be telemetered back to Earth; then Equations [1] or [21] can be solved for the two unknowns, the blackbody temperature  $E$  and the reflected solar energy  $A$ .

#### Acknowledgments

The author wishes to thank W. G. Stroud, NASA/GSFC, for his constant encouragement, and Dr. V. Suomi, University of Wisconsin, for many discussions on the subject. R. De Waard and E. A. Jackson of Barnes Engineering Co. are presently engaged in construction of an experimental model. R. Wiack and C. Catoe, NASA/GSFC, performed calibration tests; most of the numerical calculations were carried out by J. Fedor, NASA/GSFC.

#### Nomenclature

$\sigma$	= Stefan-Boltzmann radiation constant
$\epsilon$	= emissivity, emissivity of cone surface (= 0.02)
$T$	= absolute temperature, K
$T_0$	= reference temperature
$S$	= solar constant
$y$	= temperature of cone relative to reference temperature
$t$	= temperature of thermistor relative to reference temperature
$S$	= temperature of satellite structure relative to reference temperature
$E$	= temperature of Earth relative to reference temperature
$r$	= radius from cone apex to an arbitrary point
$r_1$	= radius from cone apex to thermistor (Fig. 5)
$r_2$	= radius from cone apex to baseplate (Fig. 5)
$R$	= radius of target area
$\theta$	= aperture angle (one half of field of view)
$\beta$	= elevation angle
$P$	= total radiant flux
$da$	= areal element
$a_t$	= detector area
$v$	= subsatellite speed

$x$	= arbitrary variable
$x_1$	= auxiliary parameter (Fig. 6)
$x_2$	= auxiliary parameter (Fig. 6)
$\lambda_m$	= wave length of intensity distribution (Fig. 4)
$J_m(i\xi r)$	= Bessel's function of $m$ th order of the argument ( $i\xi r$ )
$H_m^{(1)}(i\xi r)$	= Hankel's function of first kind, $m$ th order and of the argument ( $i\xi r$ )
$J_{01}$	= $J_0(i\xi r_1)$
$J_{02}$	= $J_0(i\xi r_2)$
$J_{11}$	= $J_1(i\xi r_1)$
$H_{01}$	= $H_0^{(1)}(i\xi r_1)$
$H_{02}$	= $H_0^{(1)}(i\xi r_2)$
$H_{11}$	= $H_1^{(1)}(i\xi r_1)$
$\xi$	= $\sqrt{2\epsilon\sigma 4T_0^3/cD}$ , Equation [13]
$\rho$	= $c_w q_w / \epsilon\sigma 4T_0^3\pi r_1^2$ , Equation [17]
$c$	= specific conductivity
$D$	= thickness of cone material
$c_w$	= specific conductivity of connecting wire
$q_w$	= cross section of connecting wire
$l$	= length of connecting wire
$Q_{(y)}$	= thermal flux in cone
$A$	= albedo
$f$	= frequency
$a, b, k$	= constants

#### Subscripts

$y$	= cone
$t$	= thermistor
$S$	= satellite
$E$	= Earth

#### References

1. Suomi, V. E. and Wexler, H., "University of Wisconsin Proposal for Measuring Energy Budget of the Earth from an Earth Satellite," National Science Foundation, U. S. National Committee, International Geophysical Year, Project 30.11.
2. Reid, C. D. and McAlister, E. D., "Measurement of Spectral Emissivity from 2 to 15 Microns," *J. Optical Soc. Amer.*, vol. 49, Jan. 1959, pp. 78-82.
3. McLachlan, N. W., "Bessel Functions for Engineers," Oxford University Press, 1955, London.
4. Jahnke, E. and Emde, F., "Tables of Functions," B. C. Teubner, Leipzig, 1933.



# Thermodynamic Calculations of Hydrogen-Oxygen Detonation Parameters for Various Initial Pressures

LOREN E. BOLLINGER<sup>1</sup>  
and RUDOLPH EDSE<sup>2</sup>

Ohio State University  
Columbus, Ohio

Composition, temperature, pressure and density behind a stable detonation wave and its propagation rate have been calculated for seven hydrogen-oxygen mixtures at 1, 5, 25 and 100 atm initial pressure, and at an initial temperature of 40 C. For stoichiometric mixtures the calculations also include an initial temperature of 200 C. According to these calculations the detonation velocities of hydrogen-oxygen mixtures increase with increasing initial pressure, but decrease slightly when the initial temperature is raised from 40 to 200 C. The calculated detonation velocities agree satisfactorily with values determined experimentally. These values will be published in the near future.

THE CALCULATIONS are based on the assumption that complete thermodynamic and chemical equilibrium is established in the wave. Dissipating effects such as viscosity, heat transfer by conduction and radiation, and chemical reaction rate phenomena are disregarded. The calculations were carried out for hydrogen-oxygen mixtures using a rigorous method developed by Edse (1).<sup>3</sup> Other gaseous reactants will be treated in a future paper.

The detonation parameters are derived from the Hugoniot equation for the reacted gas mixture in equilibrium, and from the condition that the detonation velocity is the minimum wave velocity of the possible velocities for the given state of the combustible gas. Thus the results are based

on the Chapman-Jouguet point at which the velocity of the reacted gas relative to the detonation wave is equal to the equilibrium sonic speed (2) in the reacted gas behind the wave. These conditions can be calculated more readily than those for a frozen speed of sound for which the ratio of the specific heats  $k$  must be calculated (3).

## Method of Calculation

Assuming that only the neutral species of  $H_2O$ ,  $H_2$ ,  $O_2$ ,  $OH$ ,  $O$  and  $H$  occur in the detonation wave of hydrogen-oxygen mixtures, the Hugoniot equation can be written

$$\frac{p_a}{p_c} = \frac{\left[ \frac{(T_a/T_b) \sum_i p_{i,a} (\Delta H_f/RT)_i T_a}{2p_{H_2O} + 2p_{H_2} + p_{OH} + p_H} - \frac{(\Delta H_f/RT)_{H_2} T_b + (N_O/N_H)(\Delta H_f/RT)_{O_2} T_b}{2} \right]}{\frac{1 + N_O/N_H}{4} \left\{ 1 + \frac{[2p_b/(1 + N_O/N_H)] \cdot (T_a/T_b)}{2p_{H_2O} + 2p_{H_2} + p_{OH} + p_H} \right\}} + 1 \quad [1]$$

where

$$\sum p_{i,a} (\Delta H_f/RT)_i T_a = p_{H_2O} (\Delta H_f/RT)_{H_2O} T_a + \dots$$

In Equation [1] the partial pressures of  $H_2O$ ,  $H_2$ ,  $O_2$ ,  $OH$ ,  $O$  and  $H$  must satisfy the conditions for chemical equilibrium. With an assumed value for the partial pressure of molecular oxygen, the partial pressures are calculated as

$$p_{O_2} \text{ assumed} \quad p_O = K_{O_2}(p_{O_2})^{1/2} \quad [2]$$

$$p_{H_2} = \left\{ \left[ \frac{K_{OH} \left( 1 - \frac{N_O}{N_H} \right) (p_{O_2})^{1/2} - \frac{N_O}{N_H} K_{H_2}}{2 \left[ \frac{(1 - 2N_O/N_H)(p_{O_2})^{1/2}}{K_{H_2O}} - 2 \frac{N_O}{N_H} \right]} \right]^2 - \frac{2p_{O_2} + K_{O_2}(p_{O_2})^{1/2}}{K_{H_2O}} - 2 \frac{N_O}{N_H} \right\}^{1/2}$$

$$\left\{ \frac{K_{OH} \left( 1 - \frac{N_O}{N_H} \right) (p_{O_2})^{1/2} - \frac{N_O}{N_H} K_{H_2}}{2 \left[ \frac{(1 - 2N_O/N_H)(p_{O_2})^{1/2}}{K_{H_2O}} - 2 \frac{N_O}{N_H} \right]} \right\}^2 \quad [3]$$

$$p_H = K_{H_2}(p_{H_2})^{1/2} \quad [4]$$

Received Sept. 5, 1960.

<sup>1</sup> Assistant Supervisor, Rocket Research Laboratory; also Assistant Professor, Dept. of Aeronautical Engineering. Member ARS.

<sup>2</sup> Director, Rocket Research Laboratory; also Professor, Dept. of Aeronautical Engineering. Member ARS.

<sup>3</sup> Numbers in parentheses indicate References at end of paper.

$$p_{OH} = K_{OH} (p_{H_2})^{1/2} \cdot (p_{O_2})^{1/2} \quad [5]$$

$$p_{H_2O} = p_{H_2}(p_{O_2})^{1/2}/K_{H_2O} \quad [6]$$

For hydrogen-rich mixtures ( $N_O/N_H < 1/2$ ) the assumed value of the molecular oxygen partial pressure must be less than  $[2N_O/(N_H - 2N_O) \cdot K_{H_2O}]^2$ .

Since the sum of all partial pressures must be equal to  $p_a$  as derived from Equation [1], the correct value of  $p_{O_2}$  can be determined by trial and error using Equations [1 through 6]. As a result of these calculations, a pair of  $T_a$  and  $p_a$  values is obtained that satisfies the Hugoniot equation.

The values of  $T_a$  and  $p_a$  together with the corresponding partial pressures are then used to calculate the Mach number for the wave relative to the unreacted gas

$$k_b M^2 =$$

$$1 - \frac{(p_a/p_b) - 1}{1 + N_O/N_H \cdot \frac{2p_b}{2p_{H_2O} + 2p_{H_2} + p_{OH} + p_H} \cdot \frac{T_a/T_b}}{[5]}$$

This procedure is repeated until a pair of  $p_a$  and  $T_a$  values is found which makes this Mach number a minimum. These values and the minimum value of  $M$  represent the detonation conditions of a stable Chapman-Jouguet detonation wave. The velocity of the reacted gas relative to the wave is obtained using the continuity equation

$$u_a = u_D \cdot \frac{v_a}{v_b} = u_D \frac{2p_b}{1 + N_O/N_H} \cdot$$

$$\frac{T_a/T_b}{2p_{H_2O} + 2p_{H_2} + p_{OH} + p_H} \quad [8]$$

where

$$u_D = [(RT_b/\mathfrak{M}_b) \cdot k_b M_{\min}^2]^{1/2}$$

$$M_{\min} = M_D$$

The impact pressure ratio follows from

$$\frac{p_{\text{imp}}}{p_b} = \frac{(u_D - u_a)^2}{p_b \cdot v_a} + \frac{p_a - p_b}{p_b} = \left[ \frac{p_a}{p_b} - 1 \right] \cdot \frac{[5]}{\left[ \frac{2p_{H_2O} + 2p_{H_2} + p_{OH} + p_H}{T_a/T_b} \cdot \frac{1 + N_O/N_H}{2p_b} \right]} \quad [9]$$

The results of these calculations are presented in Tables 1 through 5. A small amount of scatter in the results was unavoidable because of the limited number of iterations used during these calculations, which were made with a Square Root Friden calculating machine.

Assuming that the immediate front of the detonation wave consists of a normal shock wave, propagating at the velocity  $u_D$  through the combustible gas mixture without causing any chemical reactions in the gas, we can calculate the temperature and pressure behind this wave by solving the

Table 1 Composition of combustion gas<sup>a</sup>

Molar per cent fuel in mixture	$p_b$ , atm	$p_{O_2}$ , atm	$p_{O}$ , atm	$p_{H_2}$ , atm	$p_{H}$ , atm	$p_{OH}$ , atm	$p_{H_2O}$ , atm	$p_a, D$ , atm
30	1	8.724624	0.215919	0.041257	0.020413	0.979947	4.397839	14.38
	5	45.54562	0.720766	0.139228	0.052724	4.272417	23.26924	74.00
	25	234.3475	2.173795	0.425371	0.119158	17.42348	121.5107	376.0
	100	958.5706	5.325256	1.051486	0.222619	56.44056	502.3895	1524
45	1	5.59712	0.764398	0.361456	0.230445	2.640986	7.055621	16.70
	5	29.73052	3.023995	1.450444	0.751872	13.09236	38.15074	86.20
	25	158.4731	11.10064	5.408457	2.207236	60.89125	206.8194	444.9
	100	690.0791	33.49343	16.46756	5.372824	229.4414	910.1455	1885
55	1	2.959380	0.982713	1.038860	0.653540	3.502681	8.362823	17.50
	5	15.83605	4.051083	4.462804	2.283650	17.71854	46.74787	91.10
	25	84.45476	16.17427	18.46938	7.615351	87.57169	259.0146	473.3
	100	364.8844	50.79208	59.26096	19.79955	339.6077	1148.655	1983
66.67	1	0.745876	0.638231	2.952802	1.390335	3.036375	9.236365	18.00
	5	3.457926	2.651718	14.53298	5.581083	15.41088	50.86544	92.5
	25	16.20487	10.66765	71.40139	21.67408	78.30594	291.7461	490.0
	100	61.59676	35.43535	279.3280	69.52653	316.8585	1307.255	2070
66.67 <sup>b</sup>	1	0.483911	0.435817	1.867628	0.952529	1.915126	5.544988	11.20
	5	2.277220	1.866690	9.424538	3.954084	9.940380	30.83709	58.30
	25	11.36679	8.142093	49.09055	16.52124	53.89335	184.28593	323.3
	100	41.66044	25.67596	188.1448	50.79253	211.5335	822.1927	1340
75	1	0.115846	0.208676	5.607926	1.618600	1.621170	8.327770	17.50
	5	0.433543	0.749963	29.49570	6.490038	7.612434	45.71833	90.5
	25	1.470763	2.443691	159.1462	25.26848	34.33146	257.3394	480.0
	100	3.720694	5.865815	664.8134	74.87667	115.8869	1134.837	2000
85	1	0.001155	0.005833	9.583973	0.670734	0.191782	5.153881	15.61
	5	0.002658	0.013401	50.28687	2.234858	0.689028	27.13284	80.36
	25	0.004809	0.024271	260.7106	6.655522	2.188263	141.1835	410.77
	100	0.006513	0.032814	1052.562	15.31090	5.192902	571.6204	1645
90	1	0.000005	0.000049	10.01964	0.104141	0.010547	2.865618	13.0
	5	0.000007	0.000066	50.71035	0.268537	0.028007	14.49302	65.5
	25	0.000008	0.000074	252.2448	0.623218	0.065482	72.06635	325.0
	100	0.000009	0.000084	1025.286	1.340041	0.141945	293.2318	1320

<sup>a</sup> Initial temperature = 313.16 K except where noted.

<sup>b</sup> Initial temperature = 473.16 K.

Table 2 Properties of a hydrogen-oxygen detonation wave,  $p_b = 1$  atm

Molar per cent fuel in mixture	$T_b$ , K	$T_{a, D}$ , K	$T_{a, N.S.}$ , K	$p_{a, D}$ , atm	$p_{a, N.S.}$ , atm	$p_{imp}$ , atm	$u_{a1}$ , m/sec	$u_{D1}$ , m/sec	$\frac{\rho_{a, D}}{\rho_b}$	$M_D = \frac{u_D}{a_b}$
30	313.16	2860	1560	14.38	24.174	24.096	1024	1845	1.801	4.567
45	313.16	3320	1795	16.70	28.660	29.296	1169	2182	1.866	4.970
55	313.16	3538	1875	17.50	31.377	30.459	1332	2459	1.846	5.199
66.67	313.16	3646	1981	18.00	32.270	31.572	1522	2826	1.857	5.272
66.67	473.16	3576	2083	11.20	20.666	17.290	1585	2784	1.757	4.225
75	313.16	3567	1976	17.50	32.036	29.917	1750	3173	1.813	5.253
85	313.16	3108	1725	15.61	27.251	26.260	2017	3627	1.798	4.848
90	313.16	2563	1512	13.00	23.215	21.140	2155	3796	1.762	4.476

Table 3 Properties of a hydrogen-oxygen detonation wave,  $p_b = 5$  atm

Molar per cent fuel in mixture	$T_b$ , K	$T_{a, D}$ , K	$T_{a, N.S.}$ , K	$p_{a, D}$ , atm	$p_{a, N.S.}$ , atm	$p_{imp}$ , atm	$u_{a1}$ , m/sec	$u_{D1}$ , m/sec	$\frac{\rho_{a, D}}{\rho_b}$	$M_D = \frac{u_D}{a_b}$
30	313.16	2965	1586	74.00	122.96	124.32	1033	1861	1.802	4.606
45	313.16	3526	1874	86.20	151.12	149.14	1220	2240	1.836	5.103
55	313.16	3790	2018	91.10	164.37	158.34	1368	2517	1.839	5.321
66.67	313.16	3954	2102	92.50	172.10	157.76	1618	2918	1.803	5.444
66.67	473.16	3884	2182	58.30	109.78	92.586	1652	2869	1.737	4.354
75	313.16	3843	2066	90.50	169.13	152.79	1824	3260	1.787	5.397
85	313.16	3244	1777	80.36	141.26	135.17	2058	3692	1.794	4.935
90	313.16	2596	1525	65.50	117.64	106.19	2177	3821	1.743	4.506

Table 4 Properties of a hydrogen-oxygen detonation wave,  $p_b = 25$  atm

Molar per cent fuel in mixture	$T_b$ , K	$T_{a, D}$ , K	$T_{a, N.S.}$ , K	$p_{a, D}$ , atm	$p_{a, N.S.}$ , atm	$p_{imp}$ , atm	$u_{a1}$ , m/sec	$u_{D1}$ , m/sec	$\frac{\rho_{a, D}}{\rho_b}$	$M_D = \frac{u_D}{a_b}$
30	313.16	3049	1635	376.0	639.77	628.09	1061	1898	1.789	4.698
45	313.16	3724	1947	444.9	789.00	764.66	1257	2289	1.821	5.214
55	313.16	4064	2104	473.3	865.92	816.96	1417	2583	1.822	5.461
66.67	313.16	4296	2210	490.0	914.05	839.02	1667	3007	1.804	5.610
66.67	473.16	4241	2306	323.3	588.47	535.57	1653	2970	1.796	4.507
75	313.16	4138	2167	480.0	891.60	819.53	1858	3347	1.801	5.541
85	313.16	3349	1816	410.8	725.31	689.79	2092	3741	1.788	5.001
90	313.16	2606	1535	325.0	592.15	520.75	2209	3834	1.736	4.521

Table 5 Properties of a hydrogen-oxygen detonation wave,  $p_b = 100$  atm

Molar per cent fuel in mixture	$T_b$ , K	$T_{a, D}$ , K	$T_{a, N.S.}$ , K	$p_{a, D}$ , atm	$p_{a, N.S.}$ , atm	$p_{imp}$ , atm	$u_{a1}$ , m/sec	$u_{D1}$ , m/sec	$\frac{\rho_{a, D}}{\rho_b}$	$M_D = \frac{u_D}{a_b}$
30	313.16	3108	1663	1524	2603.2	2543.2	1072	1914	1.786	4.738
45	313.16	3898	2004	1885	3265.2	3327.0	1248	2328	1.864	5.303
55	313.16	4298	2227	1983	3685.0	3395.1	1477	2664	1.803	5.632
66.67	313.16	4641	2296	2070	3819.0	3597.2	1683	3073	1.826	5.733
66.67	473.16	4554	2387	1340	2448.5	2236.3	1674	3019	1.803	4.581
75	313.16	4380	2231	2000	3710.1	3431.2	1890	3413	1.806	5.651
85	313.16	3405	1840	1645	2945.5	2731.8	2132	3770	1.769	5.039
90	313.16	2622	1539	1320	2375.1	2139.7	2189	3839	1.755	4.527

following equations simultaneously

$$\frac{p_{a, N.S.}}{p_b} = \frac{1}{2} + \sum_i \gamma_i' \left[ \left( \frac{H - E_0}{RT} \right)_i^{T_{a, N.S.}} \cdot \frac{T_{a, N.S.}}{T_b} - \left( \frac{H - E_0}{RT} \right)_i^{T_b} \right] - \frac{1}{2} \frac{T_{a, N.S.}}{T_b} + \left( \frac{1}{2} + \sum_i \gamma_i' \times \right. \\ \left. \left[ \left( \frac{H - E_0}{RT} \right)_i^{T_{a, N.S.}} \cdot \frac{T_{a, N.S.}}{T_b} - \left( \frac{H - E_0}{RT} \right)_i^{T_b} \right] - \frac{1}{2} \frac{T_{a, N.S.}}{T_b} \right)^2 + \frac{T_{a, N.S.}}{T_b} \right)^{1/2} \quad [10]$$

$$\frac{p_{a, N.S.}}{p_b} = \frac{1 + k_b M_D^2}{2} + \left[ \left( \frac{1 + k_b M_D^2}{2} \right)^2 - \frac{T_{a, N.S.}}{T_b} \cdot k_b M_D^2 \right]^{1/2} \quad [11]$$

These pressures are the highest that would occur in the detonation wave should complete relaxation prevail in the internal modes of motion of the unreacted gases. Completely inactive vibrational motion in the molecules of the combustible gas mixtures would lead to pressures and temperatures in the wave calculated for a normal shock at  $M_D$  with

$$[(H - E_0)/RT]^{T_a} = [(H - E_0)/RT]^{T_b}$$

The difference between the latter values and those obtained from Equations [10 and 11] is usually quite small.

It is frequently necessary to calculate the parameters behind a steady-state detonation wave for the case where the reaction has proceeded to an arbitrarily assumed chemical composition. For such calculations a method is proposed which is based on an evaluation of the derivative  $d(p_a/p_b)/d(T_a/T_b)$  which, according to the Chapman-Jouguet condition

$$\frac{d \left( \frac{u_D^2}{RT_b/\mathfrak{M}_b} \right)}{d \left( \frac{T_a}{T_b} \right)} = \left\langle \left( 1 - \frac{T_a}{T_b} \right) \cdot \frac{d \left( \frac{p_a}{p_b} \right)}{d \left( \frac{T_a}{T_b} \right)} - \left( \frac{p_a}{p_b} - 1 \right) \left[ \frac{\frac{T_a}{T_b} \cdot \frac{\mathfrak{M}_a}{\mathfrak{M}_b} \frac{d(p_a/p_b)}{d(T_a/T_b)} - \frac{p_a}{p_b} \cdot \frac{\mathfrak{M}_a}{\mathfrak{M}_b} \right] \right\rangle \div \left\langle \left( 1 - \frac{T_a}{T_b} \right) \cdot \frac{d \left( \frac{p_a}{p_b} \right)}{d \left( \frac{T_a}{T_b} \right)} - \frac{p_a}{p_b} \cdot \frac{\mathfrak{M}_a}{\mathfrak{M}_b} \right\rangle = 0 \quad [12]$$

becomes

$$\frac{d \left( \frac{p_a}{p_b} \right)}{d \left( \frac{T_a}{T_b} \right)} = - \frac{\frac{p_a}{p_b} - 1}{\frac{p_a}{p_b} \cdot \frac{\mathfrak{M}_a}{\mathfrak{M}_b} - \frac{T_a}{T_b} \left[ 2 - \frac{1}{(p_a/p_b)} \right]} \quad [13]$$

Upon differentiation of the Hugoniot equation

$$\frac{p_a}{p_b} = \frac{T_a/T_b}{\mathfrak{M}_a/\mathfrak{M}_b} \left[ \sum_i \gamma_i'' \left( \frac{\Delta H_f}{RT} \right)_i^{T_a} - \frac{1}{2} \right] - \left[ \sum_i \gamma_i' \left( \frac{\Delta H_f}{RT} \right)_i^{T_b} - \frac{1}{2} \right] + \left( \left\{ \frac{T_a/T_b}{\mathfrak{M}_a/\mathfrak{M}_b} \left[ \sum_i \gamma_i'' \left( \frac{\Delta H_f}{RT} \right)_i^{T_a} - \frac{1}{2} \right] - \left[ \sum_i \gamma_i' \left( \frac{\Delta H_f}{RT} \right)_i^{T_b} - \frac{1}{2} \right] \right\}^2 + \frac{T_a/T_b}{\mathfrak{M}_a/\mathfrak{M}_b} \right)^{1/2} \quad [14]$$

this derivative becomes

$$\frac{d(p_a/p_b)}{d(T_a/T_b)} = \frac{\sum_i \gamma_i'' (c_p/RT)_i^{T_a} - 1/2}{\mathfrak{M}_a/\mathfrak{M}_b} + \left\langle \left\{ \frac{T_a/T_b}{\mathfrak{M}_a/\mathfrak{M}_b} \left[ \sum_i \gamma_i'' \left( \frac{\Delta H_f}{RT} \right)_i^{T_a} - \frac{1}{2} \right] - \left[ \sum_i \gamma_i' \left( \frac{\Delta H_f}{RT} \right)_i^{T_b} - \frac{1}{2} \right] \right\} \frac{\sum_i \gamma_i'' (c_p/RT)_i^{T_a} - 1/2}{\mathfrak{M}_a/\mathfrak{M}_b} + \frac{1/2}{\mathfrak{M}_a/\mathfrak{M}_b} \right\rangle \div \left\langle \left\{ \frac{T_a/T_b}{\mathfrak{M}_a/\mathfrak{M}_b} \left[ \sum_i \gamma_i'' \left( \frac{\Delta H_f}{RT} \right)_i^{T_a} - \frac{1}{2} \right] - \left[ \sum_i \gamma_i' \left( \frac{\Delta H_f}{RT} \right)_i^{T_b} - \frac{1}{2} \right] \right\}^2 + \frac{T_a/T_b}{\mathfrak{M}_a/\mathfrak{M}_b} \right\rangle^{1/2} \quad [15]$$

The detonation parameters are obtained by solving Equations [13, 14 and 15] simultaneously.

An approximate but explicit solution of the detonation problem is possible when an average value for the specific heat ratio  $k$  is introduced. According to this method, the detonation wave is considered to consist of a shock wave followed by a region in which heat is added to the gas until the Mach number becomes 1. This solution is useful primarily because it yields a quick answer, and it affords a good starting point for the exact calculations. When heat  $q$  is

added to a unit mass of the subsonic flow behind the normal shock, the final Mach number  $M_3$  will be 1 if, for a given value of  $q$ , the proper value of  $M_1$  is selected. The amount of heat  $q$  added to the gas is the heat of reaction of a unit mass of the gas mixture. Allowance must be made for the fact that the reaction does not go to completion in most cases. Since for the normal shock  $M_2^*$  equals  $1/M_1^*$ , and for the flow with heat addition in the present case  $M_3$  equals  $M_3^*$  equals 1 which leads to

$$\frac{[1 - (M_2^*)^2]^2}{4(M_2^*)^2} = \frac{q}{h_1 + u_1^2} = \frac{\frac{q}{(RT_1/\mathfrak{M}_1)}}{\frac{k}{k-1} \left( 1 + \frac{k-1}{2} M_1^2 \right)} \quad [16]$$

we obtain

$$M_1^2 = \frac{k^2 - 1}{k} \frac{q}{(RT_1/\mathfrak{M}_1)} + 1 + \left[ \left( \frac{k^2 - 1}{k} \frac{q}{(RT_1/\mathfrak{M}_1)} \right)^2 - 1 \right]^{1/2} \quad [17]$$

for the Mach number of the detonation wave. Results of these calculations are presented in Figs. 1 and 2 for various values of the specific heat ratio  $k$  as a function of the heat release coefficient

$$C_q = q/(RT_1/\mathfrak{M}_1)$$



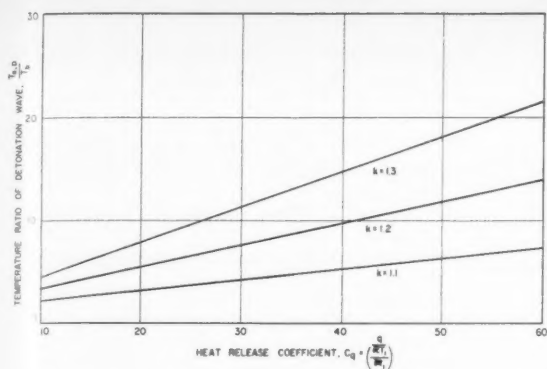


Fig. 1 Effect of heat release coefficient on temperature ratio across detonation wave for hydrogen-oxygen mixtures

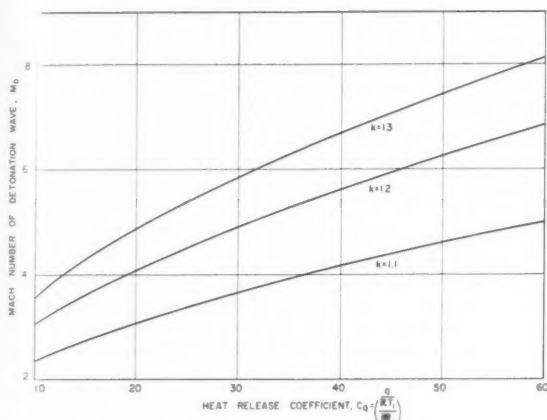


Fig. 2 Effect of heat release coefficient on Mach number of detonation wave for hydrogen-oxygen mixtures

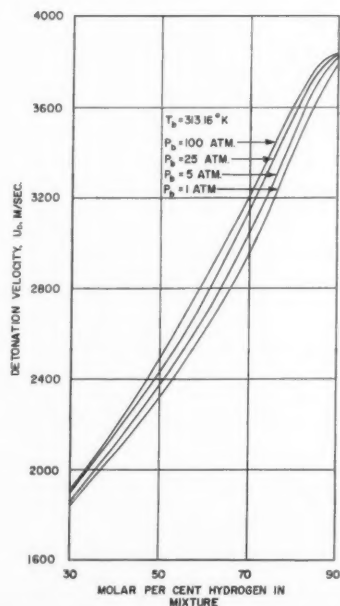


Fig. 3 Calculated detonation velocity of hydrogen-oxygen mixtures as a function of fuel concentration

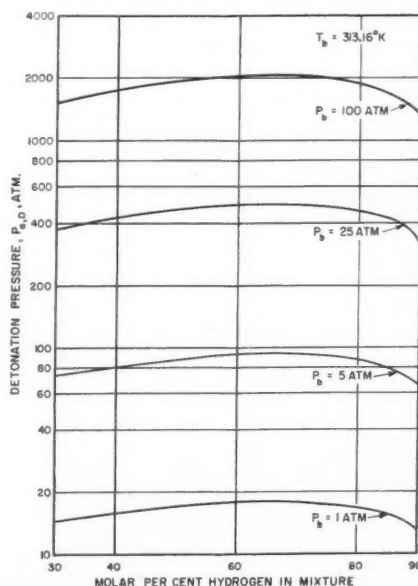


Fig. 4 Pressure behind hydrogen-oxygen detonation wave for various fuel concentrations

## Discussion of Results

The results of the calculations show that the detonation velocities of stoichiometric hydrogen-oxygen mixtures (Fig. 3) increase with initial pressure at the approximate rate of  $d(u_d)/(dp/p) = 54$  m per sec. This coefficient becomes smaller for lean or rich mixtures. The curves of Fig. 3 also show that the detonation velocities of hydrogen-oxygen mixtures increase rather sharply with the concentration of hydrogen in mixtures up to 90 per cent. At higher hydrogen concentrations the advent of a decrease in velocity is indicated by the shape of the curves.

The pressure ratio  $p_a, 2/p_b$  across the detonation wave of near stoichiometric mixtures increases rather significantly when the initial pressure is increased (Fig. 4). For very lean or very rich mixtures the effect is small. The temperature of the gas behind the detonation wave follows a similar pattern (Fig. 5). However, the density ratio  $\rho_a, 2/\rho_b$  across the wave decreases as the initial pressure is increased. For lean or rich mixtures, again, the effect of pressure on this parameter is small.

Variations of the initial temperature have only a small influence on the detonation velocity, the detonation temperature and the density ratio across the wave. However, these variations affect the pressure in the wave very strongly. Whereas an increase of 160 C (50 per cent) in the initial temperature produces a decrease of the detonation velocity by less than 2 per cent, this temperature change decreases the pressure by more than 30 per cent. It is of interest to note that an increase in initial temperature leads to a lower detonation temperature.

The temperatures in the normal shock zone are almost one half the detonation temperatures, whereas the pressures behind the normal shock are almost twice the pressure of the detonation wave and slightly higher than the impact pressures.

The results of these theoretical calculations are being used in an experimental investigation to determine the detonation induction distances of hydrogen-oxygen mixtures under a variety of initial conditions. Velocity measurements and other pertinent data obtained during this experimental study will be presented later.

## Acknowledgment

These studies were conducted under Contract NAW-6551 of the National Aeronautics and Space Administration, whose support is greatly appreciated.

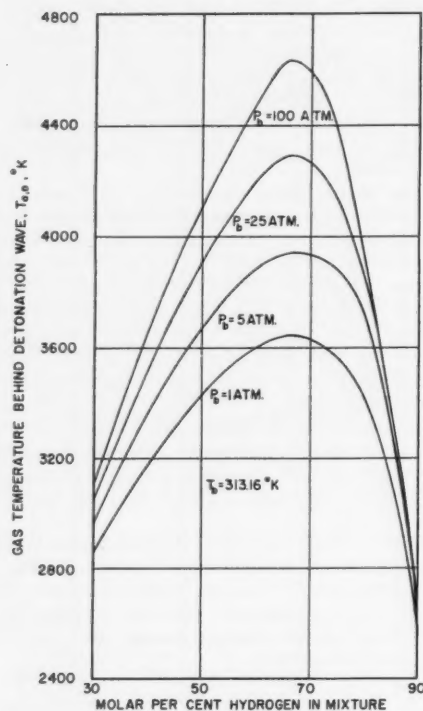


Fig. 5 Gas temperature behind hydrogen-oxygen detonation wave as a function of fuel concentration for various initial pressures

## Nomenclature

$a$	= equilibrium sonic velocity in gas mixture
$c_p$	= specific heat at constant pressure
$C_e$	= heat release coefficient
$E_0$	= zero point energy
$H$	= absolute molar enthalpy
$\left(\frac{\Delta H_f}{RT}\right)_i$	= dimensionless heat of formation of species $i$ at temperature $T$
$k$	= ratio of specific heat at constant pressure to that at constant volume
$K$	= equilibrium constant based on partial pressures
$M$	= Mach number
$M$	= molecular weight
$N$	= total mole number of element in mixture
$p$	= absolute pressure
$p_i$	= partial pressure of species $i$
$q$	= heat added per unit mass of gas
$R$	= universal gas constant
$s$	= entropy per unit mass
$T$	= absolute temperature
$u$	= linear velocity
$v$	= specific volume
$\gamma_i'$	= mole fraction of reactants
$\gamma_i''$	= mole fraction of products
$\rho$	= density

## Subscripts

$a$	= conditions in gas leaving detonation or shock wave
$b$	= conditions in gas entering detonation or shock wave
$D$	= stable detonation wave
$i$	= $i$ th species of mixture
imp	= impact
min	= minimum
N.S.	= normal shock wave
1	= initial state of gas
2	= state of gas behind normal shock when initial Mach number is $M_1$
3	= state of gas behind steady-state detonation wave
*	= critical flow condition

## References

- 1 Edse, R., "Propagation of Shock Waves through Chemically Reacting Gas Mixtures," Proc. Propellant Thermodynamics and Handling Conf., July 20-21, 1959, special rep. 12, Engng. Experiment Station, Ohio State Univ., June 1960, pp. 247-258.
- 2 Chu, S. T. and Edse, R., "Propagation of Sound Waves through Chemically Reacting Gas Mixtures," Proc. Propellant Thermodynamics and Handling Conf., July 20-21, 1959, special rep. 12, Engng. Experiment Station, Ohio State Univ., June 1960, pp. 235-246.
- 3 Edse, R., "Calculations of Detonation Velocities in Gases," WADC Tech. Rep. 54-416, ASTIA no. AD 94173, March 1956.

# Technical Notes

## An Integrated Propellant Performance Analysis Program

STANLEY F. SARNER<sup>1</sup> and JOHN F. DOLLRIES<sup>2</sup>

Flight Propulsion Laboratory, General Electric Co., Cincinnati, Ohio

THIS program is designed to calculate the theoretical performance of rocket propellants. The results are used to guide propellant research by leading the lines of effort toward high performing systems, to aid in engine design by providing information on temperatures, pressures, and composition of products, and to locate the optimum mixture ratios, and to provide input data for flight performance calculations. The program will be available, for calculations, on a contract basis for those outside of General Electric Co.

The program is based on the element potential method developed by Powell (1,2)<sup>3</sup> and is written for use with the IBM-704 and IBM-7090 digital computers. The storage capacity of our IBM-704 digital computer is 32,000 words plus tapes, which allows for wider latitude in approaches than when using the IBM-650, with a 2000-word storage. The element potentials are fewer in number than chemical potentials: One for each element rather than one for each species. Therefore, the matrix to be solved is much smaller than is normally the case, and as a result the program is considerably faster than others with similar capabilities. In addition, the variables of temperature and energy (enthalpy or entropy) are included in the matrix, thus requiring only one convergence for final solution.

### Capabilities

The program can accept any 10 elements contained in any 10 propellants, and consider any 50 of about 300 available species as combustion products. The species may be all gases, or may form up to 16 separate phases, with provision for five species in solution in any condensed phase. It may consider up to five chamber pressures and 25 exit pressures with one input. These limitations are not strictly necessary, but are imposed at present to limit the necessary storage space.

The program determines the equilibrium composition of the combustion products and their thermodynamic properties in the chamber, at the throat and at the exit or any other nozzle station, and various rocket parameters including specific impulse, density impulse, boost velocity, characteristic velocity, thrust coefficient, specific heat ratio and area ratio. A distinguishing feature of IPPA is its ability to calculate all the above parameters in conjunction with any or all of a variety of assumptions regarding chemical, phase, thermal and velocity equilibria. This is quite important when dealing with propellant systems forming condensed phases.

Presented at the ARS Propellants, Combustion and Liquid Rockets Conference, The Ohio State University, Columbus, Ohio, July 18-19, 1960.

<sup>1</sup> Rocket Propellant Thermodynamicist. Member ARS.

<sup>2</sup> Propellant Computations Analyst.

<sup>3</sup> Numbers in parentheses indicate References at end of paper.

### Inhibitions

The program is provided with inhibitions or restrictions which can be imposed on the expansion process. These inhibitions take into account the various assumptions involved pertaining to the type of flow encountered. Since these are thermodynamic rather than kinetic assumptions, they can be considered as boundary conditions for the processes involved. A total of 10 basic inhibitions are available; they are described in the following, and are shown in Table 1.

Five of the basic 10 inhibitions consider condensed phases to be in velocity equilibrium with the gaseous phase. These are the "A" inhibitions. In these cases the equation used to calculate specific impulse is the usual one

$$I_s = \sqrt{2g_0 J(H_c - H_e)/g_0}$$

The first inhibition in this group, 1a, is the standard impulse; namely total equilibrium. This is the least restrictive of all the conditions considered.

The next inhibition, 2a, is more restrictive. The gaseous phase is in chemical equilibrium during expansion, but the condensed phase is fixed at the chamber conditions as to the amount (by weight) and the composition in each condensed phase. Thermal and velocity equilibria are maintained.

Inhibition 3a is identical to 2a in the manner of handling chemical composition, but it restricts the heat transfer between the condensed and gaseous phases. Thus, the condensed phases remain at the chamber temperature, while the gases are cooled during expansion. The exit temperature computed will be that for the gases, while the exit enthalpy will be

$$H_e = \sum_{g,c} [(x_g h_g)_{T_e} + (x_c h_c)_{T_c}]$$

Inhibition 4a fixes the entire composition (both gases and condensed phases) at the chamber conditions, but allows thermal and velocity equilibrium. This inhibition is the normal "frozen flow" case.

The most restrictive inhibition which still maintains velocity equilibrium is 5a, which fixes the composition as in 4a, and also restricts heat transfer between phases as in 3a.

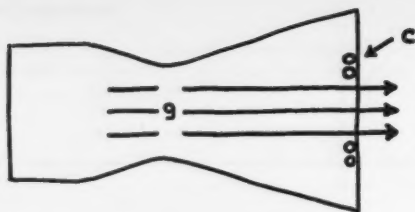
When the "B" inhibitions are imposed, the condensed phases are assumed to contribute nothing to the thrust. They lose all velocity, as if they condensed out on the wall at the

Table 1 Allowable inhibitions

Code no.	Gaseous phase	Condensed phase	Thermal	Velocity
1 a,b	E	E	E	E,F
2 a,b	E	F	E	E,F
3 a,b	E	F	F	E,F
4 a,b	F	F	E	E,F
5 a,b	F	F	F	E,F

Note: "E" denotes equilibrium conditions. "F" denotes frozen or restricted conditions.

EDITOR'S NOTE: The Technical Notes and Technical Comments sections of ARS JOURNAL are open to short manuscripts describing new developments or offering comments on papers previously published. Such manuscripts are usually published without editorial review within a few months of the date of receipt. Requirements as to style are the same as for regular contributions (see masthead page).



$$I_s = \frac{M_g V_g + M_c V_c}{g_0 M_p} = \left[ \frac{M_g}{M_p} \right] I_g$$

Fig. 1 "B" inhibitions

exit plane and were removed from the system with their mass and energy. The normal overall impulse can be given as (see Fig. 1)

$$I_s = (m_g v_g + m_c v_c) / g_0 m_p$$

and since  $v_c$  is defined here as zero, we may calculate an impulse based on the expansion of the gases, and then apply a correction factor so that

$$I_s = [m_g / m_p] I_g$$

Under inhibitions 2b to 5b, the mass fraction of condensed phase remains constant, and it is, therefore, immaterial where in the thrust chamber the correction factor is evaluated. Under inhibition 1b, the factor is evaluated at the exit plane in order to be consistent with the chemical and thermal equilibrium assumptions. For all "B" inhibitions, only the velocity assumption is changed, and all other assumptions or restrictions are identical with the corresponding "A" inhibition. For inhibitions 1b, 2b and 4b, under which thermal equilibrium is maintained, the equation for impulse is then

$$I_s = \left[ \frac{m_g}{m_p} \right] \frac{\sqrt{2g_0 J (H_c - H_e)}}{g_0}$$

since the condensed phases give up energy during expansion which can be used for acceleration of the gases. Under inhibitions 3b and 5b, wherein heat transfer between phases is restricted, only the gaseous enthalpies are involved

$$I_s = \left[ \frac{m_g}{m_p} \right] \frac{\sqrt{2g_0 J [H_c(\text{gases}) - H_e(\text{gases})]}}{g_0}$$

Many more inhibitions could be conceived of, but were ruled out as being unlikely or inconsistent. In this category would be such assumptions as condensed phase equilibrium with a frozen gas composition or restricted heat transfer between phases during chemical equilibrium. It is possible, however, to combine the basic inhibitions if desired. For example, the consideration of equilibrium flow (1a) to the throat followed by frozen flow of any type (2 to 5) in the nozzle.

#### Physical Constants

The constants used in the performance calculations are as follows:

$$\begin{aligned} R &= 1.98726 \text{ cal per mole-deg K} \\ g_0 &= 980.665 \text{ cm per sec}^2 \\ J &= 426.64 \text{ gm-m per cal} \\ 1 \text{ cal} &= 4.1840 \text{ joules} \end{aligned}$$

and therefore, using these constants and with  $\Delta H$  in cal per gm

$$\sqrt{2g_0 J} / g_0 = 9.3279$$

#### Thermodynamic Properties

A library of about 300 potential products of combustion is available for use with the program, although only 50 can be used at one time. The program selects the appropriate species as per instructions from the complete tape. The properties given on the tape, from 100 to 6000 K, are

$$\begin{aligned} \frac{H - H_0}{RT} + \frac{\Delta H}{RT} \\ \frac{F - H_0}{RT} + \frac{\Delta H}{RT} \\ \frac{C_p}{R} \end{aligned}$$

and also, molecular weight and elemental composition; additionally, for condensed species: Melting point, boiling point, specific volume.

The published compilation (3) also includes values at 273.15 and 298.15 K, and an additional column of  $C_p$  (cal per mole-deg K) for comparison purposes. Complete references to the sources of data are included.

#### Input

The program has been written to require an absolute minimum of input information. Only the elemental composition of the propellants and their enthalpies, densities and mole or weight fractions are needed in addition to the operating pressures, expansion assumptions and considered species desired. The calculation set-up has been simplified to the point where only about 5 minutes of preparation is needed for the entire input. The output has been designed to print all results in report form, and may be printed directly on multilith masters for immediate reproduction. The program can also plot curves if requested. The program has been designed to conserve both engineering and calendar time, and as a result, it is entirely possible to issue a technical report on the performance of a system within an hour of initial conception.

#### Nomenclature

$C_p$	= heat capacity
$F$	= free energy
$g_0$	= gravitational constant
$H, h$	= enthalpy
$I, I_s$	= specific impulse
$J$	= mechanical equivalent of heat
$m$	= mass or mass flow
$R$	= gas constant
$T$	= temperature
$v$	= velocity
$x$	= mole fraction

#### Subscripts

$c$	= chamber conditions or condensed phase
$e$	= exit conditions
$g$	= gaseous phase
$p$	= propellants

#### References

1. Powell, H. N. and Sarner, S. F., "The Use of Element Potentials in Analysis of Chemical Equilibria," General Electric Rep. R59FPD796, "Final Report on Contract NOrd-18508 (FBM), Vol. 1," Oct. 15, 1959.
2. Powell, H. N., "The Use of Element Potentials in Analysis of Chemical Equilibria," to be published in *J. Chem. Phys.*
3. Sarner, S. F. and Warlick, D. L., "Thermodynamic Properties of Combustion Products," General Electric Rep. R59FPD796, "Final Report on Contract NOrd-18508 (FBM), Vol. 3," June 14, 1960.



# Optimum Stage-Weight Distribution of Multistage Rockets

JOHN J. COLEMAN<sup>1</sup>

Space Technology Laboratories, Inc., Los Angeles, Calif.

In this analysis a generalized method is developed for determining the optimum stage-weight distribution for multistage rockets. Inclusion of the variations in structural factors with stage weights in the optimization process is shown to lead to a more generalized set of optimum conditions. Expression of all rocket weight parameters in terms of the stage weights allows for convenient optimization as well as for a comparison with previous optimization methods. This approach permits improved optimum design over existing methods for maximizing payload ratios for given theoretical velocities, and for maximizing theoretical velocities for given payload ratios. As presented, the generalized method is equally applicable to satellite and space vehicle launchers as well as for ballistic missiles. An evaluation of previous methods is included for comparison purposes, and the limitations of these previous methods are discussed.

IN RECENT years, the optimization of multistaged rockets has received considerable attention. Since the performance of missiles and space vehicles is sensitive to small changes in design, optimization procedures are of great importance. In (1-11)<sup>2</sup> methods were developed for determining "optimum" stage mass ratio distributions. None of these methods, however, allowed for variations of structural factor with stage weight. Consequently, the referenced methods do not yield truly optimum stage mass ratio distributions.

The purpose of this paper is, first, to derive, in terms of the stage weights, a more general design optimization that allows for variations of structural factors with stage weights and, second, to evaluate the limitations of previous design criteria.

## Optimization Parameters

### Performance parameters

The performance capability of a multistage rocket vehicle can be described by two equations, representing the payload ratio  $P$  and the burnout velocity  $V_{bo}$

$$P = \frac{W_0^{(1)}}{W_L} \quad [1]$$

$$V_{bo} = \sum_{j=1}^N I_j g \ln r_j - \delta V \quad [2]$$

where

- $W_0^{(1)}$  = gross vehicle weight
- $W_L$  = payload weight
- $I_j$  = specific impulse of the  $j$ th stage
- $r_j$  = mass ratio of the  $j$ th stage
- $\delta V$  = velocity losses associated with gravity and drag
- $N$  = total number of stages

The drag losses are primarily dependent upon the initial thrust-to-weight ratio  $N_0$  and on the quantity,  $W_0^{(1)}/C_D A$ .

Equation [2] can be rewritten in terms of range  $R$  for a ballistic missile (12)

$$R = D \left( \prod_{i=1}^N r_i^{I_i/B} - 1 \right) \quad [3]$$

where  $D$  and  $B$  are empirical parameters, and where  $B$  is very insensitive to changes in  $N_0$  and  $W_0^{(1)}/C_D A$ , while the parameter  $D$  is fairly sensitive to such changes.

Let  $\phi$  be defined as

$$\phi = \prod_{j=1}^N r_j^{I_j} \quad [4]$$

and the theoretical velocity

$$V_t = V_{bo} + \delta V \quad [5]$$

Then from Equations [2-4]

$$\phi = \prod_{j=1}^N r_j^{I_j} = e^{V_t/g} \quad [6]$$

or

$$\phi = \prod_{j=1}^N r_j^{I_j} = \left( \frac{R + D}{D} \right)^B \quad [7]$$

Thus, for a given initial thrust-to-weight ratio and mission, the velocity requirements may be lumped into a fixed single term,  $\phi$ . The range equation already provides for velocity losses in the empirical constants  $D$  and  $B$  used for any particular configuration.

When there are at least two stages and when all the specific impulses are known,  $P$  and  $\phi$  do not uniquely define the mass ratios of the various stages. Consequently, proper selection (optimization) of mass ratios for either maximum payload at a given  $V_t$  or maximum  $V_t$  at a given payload ratio is required.

### Structural factor parameters

The structural factor  $\sigma_i$  for the  $i$ th stage is given by

$$\sigma_i = \frac{W_i - W_{pi}}{W_i} \quad [8]$$

Expressed in terms of  $W_i$ , the weight of the  $i$ th stage, the following scaling laws are assumed to hold

$$\sigma_i = C_i W_i^{n_i-1} \quad [9]$$

where  $C_i$  and  $n_i$  are empirical constants for each stage subject to the selection of propellant feed systems, auxiliary systems, etc.

### Use of stage-weight parameters

The mass ratio of the  $i$ th stage can be defined by

$$r_i = \frac{W_0^{(i)}}{W_{bo}^{(i)}} = \frac{W_0^{(i)}}{W_0^{(i)} - W_{pi}} \quad [10]$$

where

$$W_0^{(i)} = \sum_{j=i}^N W_j + W_L \quad [11]$$

and

$$W_{bo}^{(i)} = W_0^{(i)} - W_{pi} \quad [12]$$

where

- $W_{bo}^{(i)}$  = burnout weight of the  $i$ th stage
- $W_0^{(i)}$  = gross weight of the  $i$ th stage
- $W_{pi}$  = propellant weight of the  $i$ th stage

Combining Equations [8-12]

$$r_i = \left( \sum_{j=i}^N W_j + W_L \right) / \left( C_i W_i^{n_i} + \sum_{j=i+1}^N W_j + W_L \right) \quad [13]$$

Substituting Equation [11] into Equation [1]

$$P = \left( \sum_{j=1}^N W_j + W_L \right) / W_L \quad [14]$$

Received July 29, 1960.

<sup>1</sup> Member of the Technical Staff.

<sup>2</sup> Numbers in parentheses indicate References at end of paper.

where the payload ratio is now expressed in terms of the stage weights. By substituting Equation [13] into Equation [6] or [7],  $\phi$  can be expressed in terms of the stage weights

$$\phi = \prod_{k=1}^N \left[ \left( \sum_{j=k}^N W_j + W_L \right) / \left( C_k W_k^{n_k} + \sum_{j=k+1}^N W_j + W_L \right) \right]^{I_k} \quad [15]$$

## General Optimization

### Application of the Lagrangian multiplier technique to optimum rocket design

The Lagrangian multiplier method may be used to optimize  $P$  subject to a fixed  $\phi$  or vice versa.

In general

$$\begin{aligned} \frac{\partial P}{\partial W_1} + \gamma \frac{\partial \phi}{\partial W_1} &= 0 \\ \frac{\partial P}{\partial W_2} + \gamma \frac{\partial \phi}{\partial W_2} &= 0 \\ \frac{\partial P}{\partial W_N} + \gamma \frac{\partial \phi}{\partial W_N} &= 0 \\ &\dots\dots\dots [16] \end{aligned}$$

and either  $\phi$  or  $P$  = constant.

The optimization conditions expressed by Equation [16] guarantee an optimum  $P$  for constant  $\phi$  or vice versa, since variation of structural factor with stage weight is included in the optimization process. In previous methods (1-11), this variation was not included.

### Reduction of the optimization equations to simpler form

From Equation [14], for fixed  $W_L$

$$\frac{\partial P}{\partial W_1} = \frac{\partial P}{\partial W_2} = \dots = \frac{\partial P}{\partial W_N} = \frac{1}{W_L} \quad [17]$$

Substituting Equation [17] into Equation [16] and eliminating common terms, the optimization equations reduce to

$$\frac{\partial \phi}{\partial W_1} = \frac{\partial \phi}{\partial W_2} = \dots = \frac{\partial \phi}{\partial W_N} \quad [18]$$

and either  $\phi$  or  $P$  = constant.

### Application to Optimum Three-Stage Rocket Design

For a three-stage rocket, Equations [14 and 15] become

$$P = (W_1 + W_2 + W_3 + W_L) / W_L \quad [19]$$

and

$$\phi = \left( \frac{W_1 + W_2 + W_3 + W_L}{C_1 W_1^{n_1} + W_2 + W_3 + W_L} \right)^{I_1} \left( \frac{W_2 + W_3 + W_L}{C_2 W_2^{n_2} + W_3 + W_L} \right)^{I_2} \times \left( \frac{W_3 + W_L}{C_3 W_3^{n_3} + W_L} \right)^{I_3} \quad [20]$$

Substituting Equation [20] into the optimization equations given by Equation [18] and factoring out  $\phi$  yields two independent nonlinear equations

$$\frac{I_1 (1 - n_1 C_1 W_1^{n_1-1})}{(1 - C_1 W_1^{n_1-1})} \left[ 1 - C_1 W_1^{n_1-1} \left( \frac{W_1 + W_2 + W_3 + W_L}{C_1 W_1^{n_1} + W_2 + W_3 + W_L} \right) \right] = I_2 \left[ 1 - n_2 C_2 W_2^{n_2-1} \left( \frac{W_2 + W_3 + W_L}{C_2 W_2^{n_2} + W_3 + W_L} \right) \right] \quad [21]$$

and

$$I_2 \frac{(1 - n_2 C_2 W_2^{n_2-1})}{(1 - C_2 W_2^{n_2-1})} \left[ 1 - C_2 W_2^{n_2-1} \left( \frac{W_2 + W_3 + W_L}{C_2 W_2^{n_2} + W_3 + W_L} \right) \right] = I_3 \left[ 1 - n_3 C_3 W_3^{n_3-1} \left( \frac{W_3 + W_L}{C_3 W_3^{n_3} + W_L} \right) \right] \quad [22]$$

Equations [21 and 22] together with the constraint equation,  $\phi$  or  $P$  = constant, constitute three equations in terms of the three unknowns  $W_1$ ,  $W_2$  and  $W_3$ . For specified sets of values of  $I_1$ ,  $I_2$ ,  $I_3$ ,  $C_1$ ,  $C_2$ ,  $C_3$ ,  $n_1$ ,  $n_2$ ,  $n_3$  and  $\phi$  or  $P$  (depending upon which type of optimization is desired), the three equations can be solved by iteration techniques to yield optimum values of  $W_1$ ,  $W_2$  and  $W_3$ . By employing Equations [11 and 12], the other rocket parameters can also be determined.

Another way suggested<sup>3</sup> for optimizing the stage weights is to find  $W_1$ ,  $W_2$  and  $W_3 > 0$  such that Equation [20] is satisfied and Equation [19] is minimized. To do this, Equation [20] could first be solved for  $W_1$  as a function of  $W_2$  and  $W_3$  and then quadratic fits could be made to this expression

$$P(W_1, W_2) = [W_1(W_2, W_3) + W_2 + W_3 + W_L] / W_L \quad [23]$$

minimizing the quadratic fit and iterating this process until there is no improvement in  $P$ .

## Comparison With Previous Methods

For comparison purposes, the relations corresponding to previous methods (1-11) for design criteria can be written in terms of the mass ratios

$$I_1 (1 - \sigma_1 r_1) = I_2 (1 - \sigma_2 r_2) = I_3 (1 - \sigma_3 r_3) \quad [24]$$

which is the familiar form usually seen in the references listed below. Equations [21 and 22] become

$$I_1 [(1 - n_1 \sigma_1) / (1 - \sigma_1)] (1 - \sigma_1 r_1) = I_2 (1 - n_2 \sigma_2 r_2) \quad [25]$$

$$I_2 \frac{(1 - n_2 \sigma_2)}{(1 - \sigma_2)} (1 - \sigma_2 r_2) = I_3 (1 - n_3 \sigma_3 r_3) \quad [26]$$

or combining Equations [25 and 26]

$$I_1 \frac{(1 - n_1 \sigma_1)}{(1 - \sigma_1)} (1 - \sigma_1 r_1) = I_2 (1 - n_2 \sigma_2 r_2) = I_2 (1 - n_2) + n_2 \frac{I_3 (1 - \sigma_2)}{(1 - n_2 \sigma_2)} (1 - n_3 \sigma_3 r_3) \quad [27]$$

which represent more inclusive optimization conditions. Comparison of Equation [24] with Equation [27] indicates the significant difference between previous "optimizations" and the more realistic optimization criteria.

It is obvious that the present method yields a more general result than the constant  $\sigma_i$  solutions of the previous papers (1-11). Equations [24 and 27] indicate the differences in the results of the methods. The constant  $\sigma_i$  solution, as given by Equation [24], may be obtained from Equation [27] by setting  $n_i = 1$ , which eliminates the dependence of  $\sigma$  on the stage weight.

There have been many papers written on the subject of optimum staging, and a good deal of discussion has been presented on aspects of the problem. Common to almost all the papers, however, is the neglect of variations of structural factors with stage weights. Inclusion of these variations in the optimization process has been shown to lead to a more generalized set of solutions. This approach permits improved design optimization over previous methods.

<sup>3</sup> Lincoln R. Turner, Space Technology Laboratories, Inc., private communication.

## Application to N-Stage Rocket Optimization

If iterative techniques can be expanded to include solving  $N$  simultaneous nonlinear equations, then the process described above can be extended to any number of stages. In the case of a large number of stages, computerized random search techniques might be employed to solve for optimum values of the stage weights. Once the optimum stage weights are obtained, these values can be substituted into Equations [11 and 12] to solve for the other rocket parameters.

## References

- 1 Malina, F. J. and Summerfield, M., "The Problem of Escape From the Earth by Rocket," *J. Aeron. Sci.*, vol. 14, Aug. 1947, p. 471.
- 2 Vertregt, M., "A Method for Calculating the Mass Ratios of Step-Rockets," *J. Brit. Interplanetary Soc.*, vol. 15, 1956, p. 95.
- 3 Goldsmith, M., "On the Optimization of Two-Stage Rockets," *JET PROPULSION*, vol. 27, 1957, p. 415.

- 4 Schurmann, E. E. H., "Optimum Staging Technique for Multi-staged Rocket Vehicles," *JET PROPULSION*, vol. 27, 1957, p. 863.
- 5 Weisbord, L., "A Generalized Optimization Procedure for N-Staged Missiles," *JET PROPULSION*, March 1958, p. 164.
- 6 Hall, H. H. and Zambelle, E. D., "On the Optimization of Multistage Rockets," *JET PROPULSION*, vol. 28, July 1958, p. 463.
- 7 Subotowicz, M., "The Optimization of the N-Step Rocket With Different Construction Parameters and Propellant Specific Impulses in Each Stage," *JET PROPULSION*, vol. 28, July 1958, p. 460.
- 8 Faulders, C. R., "Optimization of Multi-Staged Missiles," Tech. Rep., North American Aviation, 1959.
- 9 Hanson, A. A., "A Preliminary Design Method of Optimizing Vehicle Stage Proportions," Rep. no. 59-9110-43-1, Space Technology Laboratories, Inc., Sept. 29, 1959. (Confidential)
- 10 Baer, H. W., "Design of Take-Off Masses of Multi-Stage, ICBM-Type Rockets With Given Range and Payload Objectives," Rep. no. EM 9-8, TN-59-0000-00228, Space Technology Laboratories, Inc., Feb. 2, 1959.
- 11 Summerfield, M. and Seifert, H. S., "Flight Performance of a Rocket in Straight Line Motion," in "Space Technology," John Wiley and Sons, New York, 1959, pp. 3-25.
- 12 Dergarabedian, P. and Ten Dyke, R. P., "Estimating Performance Capabilities of Boost Rockets," TR-59-0000-00792, Space Technology Laboratories, Inc., Sept. 10, 1959.

## Optimum Trajectories Between Two Terminals in Space<sup>1</sup>

HAROLD M. STARK<sup>2</sup>

Systems Corporation of America, Los Angeles, Calif.

The problem of finding rocket trajectories between two terminals in space is considered from the viewpoint of minimizing the velocity increment added to an arbitrary initial velocity at the first terminal, with the restriction that the resulting trajectory pass through the second terminal. A solution for this minimum velocity increment is found. As a special case, the minimum initial velocity for a trajectory between two points in space is found and shown to be elliptical. Numerical examples are given, and the concept of a false optimum is briefly discussed.

THE PROBLEM of finding an optimum rocket trajectory between two terminals with specified velocities at each terminal has been discussed by Lawden (1 and 2).<sup>3</sup> Lawden defines an optimum trajectory to be one which minimizes the characteristic velocity, or the amount of fuel consumed, using two impulses. The purpose of this paper is to determine the optimum trajectory between two terminals in an inverse square gravitational field, with only the velocity at the initial terminal being given. Here, an optimum trajectory is defined as one which minimizes the single velocity increment which is applied at the initial terminal. Such a solution would find application in feasibility studies for the first interplanetary probes whose objective is to intercept the destination planet. Numerical examples for a trip to Mars in both two and three dimensions are given and compared.

## Determination of the Optimum Orbit for Two Dimensions

The requirement that a ballistic (two-body) orbit pass through two given terminals gives a relation between  $V$  and

$\gamma$  at the initial terminal. This relation, which shall be known here as the range equation, is

$$\frac{r_1}{r_2} = \frac{GM}{r_1 V^2} \left( \frac{1 - \cos \phi}{\cos^2 \gamma} \right) + \frac{\cos(\gamma + \phi)}{\cos \gamma} \quad [1a]$$

Equation [1a] can be found in any comprehensive survey on orbital mechanics, such as (3). As given in (3), the transfer angle is  $\phi$  and  $|\gamma| \leq (\pi/2)$ . However, since Equation [1a] can be rewritten as

$$\frac{r_1}{r_2} = \frac{GM}{r_1 V^2} \left[ \frac{1 - \cos(2\pi - \phi)}{\cos^2(\pi - \gamma)} \right] + \frac{\cos[(\pi - \gamma) + (2\pi - \phi)]}{\cos(\pi - \gamma)} \quad [1b]$$

then  $\pi \geq |\gamma| \geq (\pi/2)$  represents a transfer angle of  $2\pi - \phi$ . Thus, Equation [1a] gives all possible transfers between  $r_1$  and  $r_2$ . By expanding  $\cos(\gamma + \phi)$  and letting  $X = V \cos \gamma$ ,  $Y = V \sin \gamma$ , we get

$$X^2(r_1/r_2 - \cos \phi) + XY \sin \phi = GM(1 - \cos \phi)/r_1 \quad [2]$$

In either of the above forms, the range equation expresses the condition that the resulting orbit will pass through  $r_2$ . For elliptic orbits, this is tantamount to saying that the vehicle will reach  $r_2$ ; however, for parabolic or hyperbolic orbits, it is possible that the vehicle is going away from  $r_2$  and, hence, will never actually arrive at  $r_2$ . Such a possibility must be guarded against as it may result in a false optimum.

It is easily seen that for  $\phi \neq 0$  or  $\pi$ , Equation [2] is that of a hyperbola with center at the origin and asymptotes

$$X = 0 \quad [3]$$

$$\frac{Y}{X} = - \frac{(r_1/r_2) - \cos \phi}{\sin \phi} \quad [4]$$

A typical graph of Equation [2] along with the asymptotes of the curve is shown in Fig. 1. As a point of interest, one of the asymptotes passes through  $r_2$  and the other passes through the focus. The dotted portions of the curve depict hyperbolic velocities that direct the transfer vehicle away from the final terminal, rather than toward it.

It is seen that the problem of finding the minimum  $\Delta V$  reduces to the problem of finding the closest point on the hyperbola to  $V_1$ . The vector,  $\Delta V_{\min}$ , must have the property

Received July 11, 1960.

<sup>1</sup> This paper was prepared as part of a study done for Republic Aviation Corporation, under AF Contract 33(616)-6547.

<sup>2</sup> Member of the Scientific Staff.

<sup>3</sup> Numbers in parentheses indicate References at end of paper.

of being perpendicular to the hyperbola. If we let  $V_{opt} \times \cos \gamma_{opt} = X_{opt}$ ,  $V_1 \cos \gamma_1 = X_1$ , etc., this condition may be expressed as

$$\frac{Y_{opt} - Y_1}{X_{opt} - X_1} = - \frac{1}{(dY/dX)(at X_{opt})} \quad [5]$$

Letting

$$A = (r_1/r_2) - \cos \phi \quad [6]$$

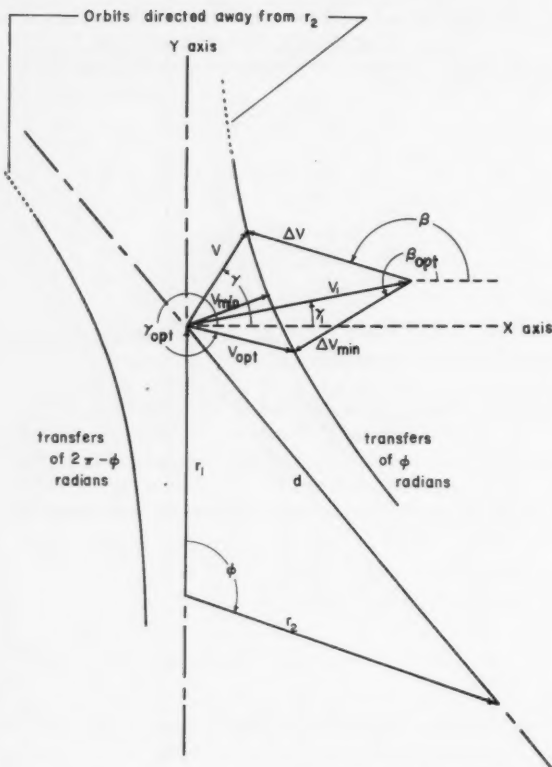


Fig. 1 Configuration for the two-dimensional problem

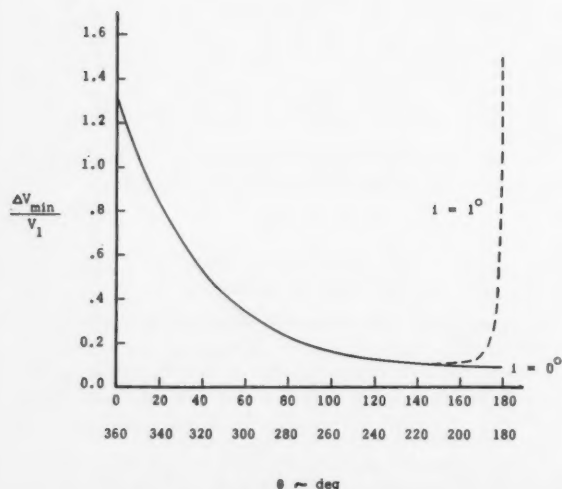


Fig. 2 Results for a trip to Mars

and

$$B = GM(1 - \cos \phi)/r_1 \quad [7]$$

we may use Equation [2] to obtain

$$Y_{opt} = \frac{B - AX_{opt}^2}{X_{opt} \sin \phi} \quad [8]$$

$$\frac{dY}{dX}(at X_{opt}) = - \frac{AX_{opt}^2 + B}{X_{opt}^2 \sin \phi} \quad [9]$$

Eliminating  $Y_{opt}$  and  $(dY/dX)$  (at  $X_{opt}$ ) between Equations [5, 8 and 9] yields

$$(A^2 + \sin^2 \phi)X_{opt}^4 + (AY_1 \sin \phi - X_1 \sin^2 \phi)X_{opt}^3 + (BY_1 \sin \phi)X_{opt} - B^2 = 0 \quad [10]$$

This fourth degree equation<sup>4</sup> may be solved either analytically or numerically for  $X_{opt}$ . Then  $Y_{opt}$  is given from either of Equations [5] or [8]. We may now determine  $\Delta V_{min}$  and  $\beta_{opt}$  from the following equations

$$\Delta V_{min} = \sqrt{(X_{opt} - X_1)^2 + (Y_{opt} - Y_1)^2} \quad [11]$$

$$\beta_{opt} = \tan^{-1}[(Y_{opt} - Y_1)/(X_{opt} - X_1)] \quad [12]$$

A number which is sometimes useful is  $V_{min}$ . This can be found from the above method by setting  $V_1 = 0$ . When this is done, Equation [10] reduces to

$$(A^2 + \sin^2 \phi)X_{opt}^4 - B^2 = 0 \quad [13]$$

$$X_{opt}^2 = B/\sqrt{A^2 + \sin^2 \phi} \quad [14]$$

Using the law of cosines we get

$$A^2 + \sin^2 \phi = [(r_1/r_2) - \cos \phi]^2 + \sin^2 \phi = (r_1^2 + r_2^2 - 2r_1r_2 \cos \phi)/r_2^2 = d^2/r_2^2 \quad [15]$$

so that

$$X_{opt}^2 = \frac{Br_2}{d} \quad [16]$$

Substituting into Equation [5] (and Equation [9]) gives

$$Y_{opt}/X_{opt} = X_{opt}^2 \sin \phi / (AX_{opt}^2 + B) \quad [17]$$

or, using [16]

$$Y_{opt}/X_{opt} = r_2 \sin \phi / (Ar_2 + d) \quad [18]$$

Since  $\Delta V_{min} = V_{min}$ , Equations [11, 18, 15 and 16] yield

$$V_{min}^2 = 2Br_2/(Ar_2 + d) \quad [19]$$

Substituting for  $A$  and  $B$  from Equations [6 and 7] and eliminating  $\cos \phi$  with the law of cosines produces

$$V_{min}^2 = (2GM/r_1)\{1 - [2r_1/(r_1 + r_2 + d)]\} \quad [20]$$

Since escape velocity at  $r_1$  is given by

$$V_{esc}^2 = 2GM/r_1 \quad [21]$$

$V_{min} < V_{esc}$  is an elliptic velocity. Further, for  $\phi = 180$  deg

$$d = r_1 + r_2 \quad [22]$$

and hence

$$V_{min}^2 = (2GM/r_1)[r_2/(r_1 + r_2)] \quad [23]$$

so that  $V_{min}$  is just the Hohmann velocity.

<sup>4</sup> After this paper was submitted, it was brought to the author's attention that T. Godal had stated in "Conditions of Compatibility of Terminal Positions and Velocities," Proc. XIth International Astronautical Congress, Stockholm, July 1960, pp. 40-44, that a fourth degree equation must be solved for this problem. No further details were given.



### Determination of the Optimum Orbit for Three Dimensions

The transfer orbit plane is determined by  $r_1$ ,  $r_2$  and the focus. This means that for any transfer to be effected between the two terminals, the out of (transfer) plane component of  $\Delta V$  must cancel the out of plane component of  $V_1$ . It remains only to minimize the in-plane component of  $\Delta V$ , a problem solved in the previous section where the initial velocity is the in-plane component of  $V_1$ . This reduces the three-dimensional problem to the two-dimensional case.

#### Examples for a Trip to Mars

In the following two examples,  $\Delta V_{\min}$  is presented as a function of  $\theta$  for given  $r_1$ ,  $r_2$ ,  $V_1$  and  $i$ . In one case  $i = 0$ , so that  $r_1$ ,  $r_2$  and  $V_1$  are in the same plane and the problem is purely two dimensional. In this case  $\phi = \theta$ . In the second case  $i = 1$  deg and the problem is three dimensional. In both cases  $r_2 = 1.52 r_1$  and  $V_1$  is the circular velocity at a distance of  $r_1$  from the attracting body. If we let  $r_1 = 1$  a.u., then the results will hold for a trip from Earth's orbit to the orbit of Mars. These results are plotted in Fig. 2.

Battin (4) used a different method to analyze the two dimensional problem with the restriction that  $V_1$  be the circular velocity at  $r_1$ . His curve of  $\Delta V_{\min}$  vs.  $\theta$  for a trip to Mars is identical with the curve for  $i = 0$  in Fig. 2 which was calculated using the more general equations of this paper. None of the  $\Delta V_{\min}$  in Fig. 2 are false optima. However, false optima do occur in examples of this kind. For instance, in Figs. 2 and 3 of (4) Battin presents plots of  $\Delta V_{\min}$  vs.  $\theta$  for trips to Jupiter, Saturn and Uranus. The dotted portions of these curves depict cases where the resulting transfer trajectory is hyperbolic or parabolic. In all of these cases in which  $180 \text{ deg} < \theta < 360 \text{ deg}$ ,  $\Delta V_{\min}$  is a false optimum. The transfer vehicle would be directed away from the final terminal instead of toward it. In these specific instances, there is no optimum orbit (because there are four roots to Equation [10] there are configurations in which there does exist an optimal transfer trajectory even though

the closest point on the hyperbola results in a false optimum). The phenomenon seen in Fig. 2 for  $\theta = 180 \text{ deg}$  is very general. A transfer for  $\theta = 180 \text{ deg}$  will be economical only if  $i = 0$ .

#### Acknowledgment

Appreciation is herewith expressed to Dr. A. Kartveli, Vice President of Republic Aviation Corp., for permission to publish the present study.

#### Nomenclature

$r_1$	= distance from focus to initial terminal
$r_2$	= distance from focus to final terminal
$d$	= distance between initial and final terminals
$\phi$	= angle at focus between $r_1$ and $r_2$
$V_1$	= given initial velocity
$\gamma_1$	= angle between $V_1$ and the local horizontal
$V$	= velocity required to reach final terminal
$\gamma$	= angle between $V$ and the local horizontal
$V_{\min}$	= minimum $V$
$\Delta V$	= velocity increment needed to change $V_1$ into $V$
$\beta$	= angle between $\Delta V$ and the local horizontal
$\Delta V_{\min}$	= minimum $\Delta V$
$\beta_{\text{opt}}$	= angle between $\Delta V_{\min}$ and the local horizontal
$V_{\text{opt}}$	= velocity resulting from adding $\Delta V_{\min}$ to $V_1$
$\gamma_{\text{opt}}$	= angle between $V_{\text{opt}}$ and the local horizontal
$i$	= angle between $r_2$ and projection of $r_2$ on plane of initial orbit
$\theta$	= angle between $r_1$ and projection of $r_2$ on plane of initial orbit
$G$	= gravitational constant
$M$	= mass of attracting body

#### References

- 1 Lawden, D. F., "Stationary Rocket Trajectories," *Quart. J. Mech. Appl. Math.*, vol. 7, 1954, pp. 488-504.
- 2 Lawden, D. F., "Minimal Rocket Trajectories," *JET PROPULSION*, vol. 23, 1953, pp. 360-367.
- 3 Arthur, P. D., "Lectures on Orbital Mechanics," Systems Corporation of America Memo., May 1959.
- 4 Battin, R. H., "The Determination of Round-Trip Planetary Reconnaissance Trajectories," presented at the Inst. Aeron. Sci. Annual Meeting, New York, Jan. 1959, IAS preprint 59-31.

## Peltier Cooling of Electrical Components in Telemetry Packages

RAYMOND MARLOW<sup>1</sup>

Texas Instruments, Inc., Dallas, Texas

Peltier cooling, a direct method of converting electrical energy into usable thermal energy by use of a semiconductor device, is a method of obtaining an adequate thermal environment inside the telemetry package of missiles and satellites. An example of how Peltier cooling may be applied to telemetry packages is discussed in this paper.

CONVERTING various electrical impulses from strain gages, flowmeters, temperature and pressure transducers into electrical signals suitable for transmission to a ground receiving station is the function of a telemetry system in a missile or satellite. During ground checkout, pre-flight and flight, the system determines whether or not the electronic equipment

is operating properly, transmits to the ground receiving station the internal and external environments, reports malfunctions or failure of components, and monitors the overall performance of the missile or satellite.

For optimum telemetry system performance, the components in the system must be protected from extreme high and low temperatures and from sudden temperature changes. This may be accomplished by the use of insulating materials, but the internal heat generated during long ground and pre-flight checkouts poses another problem. Also, satellite vehicles require some method of internal cooling to insure optimum performance under continuous operating conditions. Peltier cooling appears to be an answer to this problem.

#### Principles of the Peltier Effect

In 1834, Jean Peltier observed that an electric current passing across the junction of two dissimilar conductors caused heat to be absorbed at one junction and liberated at the other junction. This phenomenon could be reversed by reversing the direction of the current. Because only small temperature differences were obtainable with electrical conducting materials at that time, the discovery lay dormant for almost a century. During the past decade, the theory of Peltier cooling has been extensively investigated (4,7,9).<sup>2</sup>

This paper is based on ARS Preprint no. 841-59 presented at the ARS Semi-Annual Meeting, San Diego, Calif., June 8-11, 1959.

<sup>1</sup> Missiles Department Engineer, Apparatus Div.

<sup>2</sup> Numbers in parentheses indicate References at end of paper.

The upsurge in the field of semiconductor materials has made it possible to cool or heat electronic equipment in a manner comparable to other methods of cooling presently in use.

Fig. 1 is a typical thermoelectric thermoelement. If a d-c current is passed through the *N*-type and *P*-type semiconductor materials, the temperature *T* of the copper bus will decrease and heat will be absorbed. This heat will be transmitted through the legs by electron transport to the other end of the junction *T*<sub>0</sub> and liberated. Under ideal conditions, the amount of Peltier heat absorbed at the copper bus *T* is dependent on the product of the thermoelectric power  $\alpha$ , the current *I*, and the absolute temperature *T*. The product of the thermoelectric power and the temperature is the Peltier coefficient  $\pi$ .

In practical applications, the Peltier heat that may be absorbed from the surroundings is reduced from two sources—Joule heat *Q*<sub>J</sub> and conducted heat *Q*<sub>C</sub>. Joule heat is generated internally as current passes through the semiconductor. An assumption is made that one half of this heat is generated at the cold end and the other half at the hot end. Conducted heat is transmitted from the hot end to the cold end by thermal conduction. By writing a heat balance equation at the cold junction *T*, the net amount of heat *Q*<sub>net</sub> that would be absorbed per thermoelement is

$$Q_{\text{net}} = Q_P - Q_J - Q_C = \alpha TI - \frac{1}{2} I^2 R - K(T_0 - T)$$

The coefficient of performance in a cooling system is the ratio of the net cooling effect to the amount of input electrical power supplied to produce the cooling. The input power *P*<sub>I</sub> is the sum of the back emf's, or Seebeck effect, and the Joule heat

$$P_I = \alpha(T_0 - T) I + I^2 R$$

Therefore, the coefficient of performance is

$$COP = \frac{Q_{\text{net}}}{P_I} = \frac{\alpha IT - \frac{1}{2} I^2 R - K(T_0 - T)}{\alpha(T_0 - T) I + I^2 R}$$

By differentiating *COP* with respect to the current, the maximum *COP* obtainable is

$$COP_{\text{max}} = \frac{T}{T_0 - T} \frac{\sqrt{1 + \frac{1}{2} Z(T + T_0)} - T_0/T}{\sqrt{1 + \frac{1}{2} Z(T + T_0)} + 1}$$

In this equation, the *Z* term is

$$Z = \alpha^2 \sigma / k = \text{figure of merit}$$

$$\alpha = \text{thermoelectric power}$$

$$\sigma = \text{electrical conductivity}$$

$$k = \text{thermal conductivity}$$

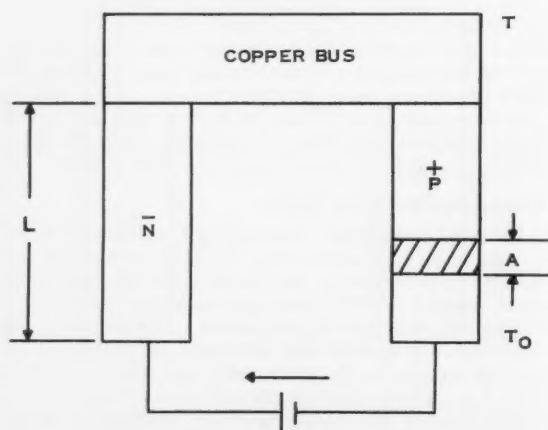


Fig. 1 Typical thermoelectric thermoelement

The figure of merit is important because it is dependent upon only the properties of the material used for the thermoelectric thermoelements. Fig. 2 illustrates why the new advances in semiconductor materials have improved the performance of Peltier cooling and heating. The electrical conductivity is small in insulators and increases as the number density of charge carriers increases. However, the thermoelectric power is large in insulators and decreases as the number density of charge carriers increases. Since the numerator of the figure of merit varies as  $\alpha^2 \sigma$ , there is a maximum value of  $\alpha^2 \sigma$ , and this maximum occurs in semiconductors. To increase the figure of merit, the thermal conductivity should be as small as possible. The total thermal conductivity *k* is the sum of the phonon conductivity *k*<sub>ph</sub> plus the electron conductivity *k*<sub>el</sub> shown in Fig. 2. The electron conductivity should be large, since the electrical conductivity is dependent on the number density of the charge carriers. The phonon conductivity is dependent on the lattice of the material, and it is this quantity of the thermal conductivity that should be reduced to zero.

#### Application of Peltier Cooling

Peltier cooling has recently been applied to many devices (1-3, 5-6, 8, 10-11). In this paper, the transmitter of a telemetry system is to be cooled by the Peltier effect. Assume that a transmitter in a satellite requires an input power of 30 watts to operate with a 5-watt power output, thus requiring 25 watts of heat dissipation to maintain a constant transmitter temperature. The transmitter is to be mounted on a chassis whose temperature is 60°C (333 K). The problem is to design a thermoelement that will maintain the base of the transmitter at 30°C (303 K). The base of the transmitter is 4 in.<sup>2</sup>; therefore, 50 thermoelectric thermoelements with cross-sectional areas of 1 cm<sup>2</sup> and lengths of 2 cm are to be used. The total cross-sectional area of the Peltier cooler is approximately 4 in.<sup>2</sup>.

It is assumed that the electrical resistivity, thermal conductivity, cross-sectional area, length and thermoelectric power are the same for both the *N*-type and *P*-type material.

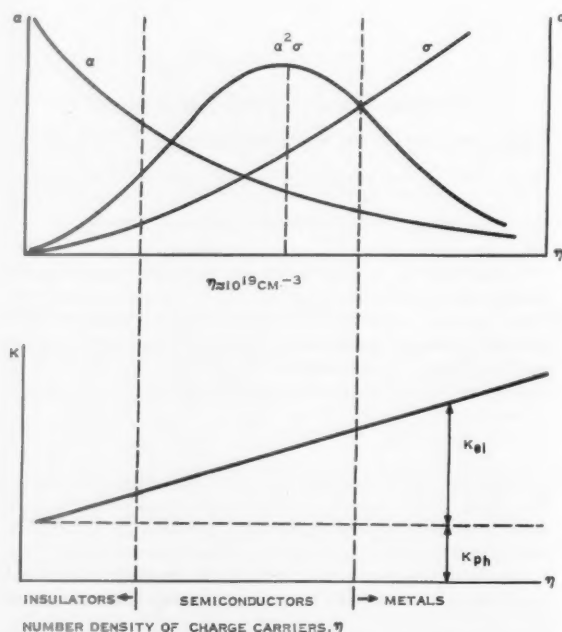


Fig. 2 Material parameters as function of charge carrier density

The following values are to be used for this problem

- $A = 1 \text{ cm}^2 = \text{area of each thermoelement leg}$
- $L = 2 \text{ cm} = \text{length of each thermoelement leg}$
- $k = 0.02 \text{ (watt/cm-C)} = \text{thermal conductivity}$
- $\rho = 10 \times 10^{-4} \text{ ohm-cm} = \text{electrical resistivity}$
- $\alpha = 400 \times 10^{-6} \text{ (volts/K)} = \text{total thermoelectric power}$
- $K = 2kA/L = (2)(0.02)(1/2) = 0.02 \text{ (watt/K)} = \text{thermal conductance per thermoelement}$
- $R = 2\rho L/A = (2)(10 \times 10^{-4})(2/1) = 40 \times 10^{-4} \text{ ohm} = \text{electrical resistance per thermoelement}$

The amount of heat that must be absorbed per thermoelectric thermoelement is  $Q_{\text{net}} = (Q_{\text{Total}}/N) = 25/50 = 0.5 \text{ watt per element}$ , where  $N$  is the number of thermoelements.

Substituting these values into the heat balance equation, the current required to produce this cooling effect is calculated

$$Q_{\text{net}} = \alpha TI - \frac{1}{2}I^2R - K(T_0 - T)$$

$$0.5 = (400 \times 10^{-6})(303)I - \frac{1}{2}I^2(40 \times 10^{-4}) - 0.02(333 - 303)$$

Rearranging and solving for the current gives  $I = 10 \text{ amp}$ . By substituting the current of 10 amp into the input power equation, the amount of input power per thermoelement may be calculated

$$P_i = (400 \times 10^{-6})(333 - 303)(10) + \frac{1}{2}(10)^2(40 \times 10^{-4}) = 0.12 + 0.2 = 0.32 \text{ watt}$$

The coefficient of performance can be calculated as

$$COP = 0.5/0.32 = 1.5$$

## Conclusion

During the ground checkout and after firing, the telemetry system serves as the "eyes" of the missile or satellite. It must function properly over extended periods of time, transmitting information to ground receiving stations. Peltier cooling and heating is one method of providing a thermal environment which will lengthen the life expectancy of the electrical components. Since there are no moving parts, this method of cooling is inherently reliable. As the state of the art in fabricating semiconductor materials advances, the use of Peltier cooling and heating most likely will increase accordingly.

## References

- 1 Benedict, R. P., "Thermoelectric Effects," *Electrical Manufacturing*, vol. 65, no. 2, 1960, pp. 103-118.
- 2 Eichhorn, R. L., "Thermoelectric Refrigeration Design Considerations," Sixth Thermoelectric Effects Colloquium of the Advisory Committee, Thermoelectric Effects Research Program, Franklin Institute, no. 1958.
- 3 Fuschillo, "The Thermoelectric Effects Research Program," Franklin Institute, July 1958.
- 4 Goldsmid, H. J., "Thermoelectric Cooling," *Brit. Communications and Electronics*, vol. 7, no. 2, Feb. 1960, pp. 110-112.
- 5 Huck, William V., "Thermoelectric Heat Pumps," *Electrical Manufacturing*, vol. 65, no. 5, 1960, pp. 281-284.
- 6 Ioffe, A. F., "Semiconductor Thermoelements and Thermoelectric Cooling," Infosearch, Ltd., London, England, 1957.
- 7 Jaumot, Frank E., "Thermoelectric Effects," *Proc. IRE*, vol. 46, no. 3, 1958, pp. 538-554.
- 8 Lackey, R. S., Mees, J. D. and Somers, E. V., "Application of Thermoelectric Cooling and Heating to Novel Household Appliances," 54th Semi-annual Meeting, ASRE, New Orleans, La., Dec. 1958.
- 9 Rittner, E. S., "On the Theory of the Peltier Heat Pump," *J. Appl. Phys.*, vol. 30, no. 5, 1959, pp. 702-707.
- 10 Taylor, J. and Mulicia, A., "Thermoelectric Coolers for Electronic Components," *Electrical Manufacturing*, vol. 65, no. 5, 1960, pp. 284-286.
- 11 Wright, W. L., "Thermoelectric Refrigeration," *Electrical Engineering*, vol. 79, no. 5, 1960, pp. 380-384.

## Estimation of Specific Heats at Normal Temperatures

FRED H. BROCK<sup>1</sup>

Aerojet-General Corp., Azusa, Calif.

A model of wide applicability has been developed for the calculation of the specific heats at constant volume of solids and liquids at or near normal temperatures. By means of simple computations based on a set of self-consistent rules, the specific heats at constant pressure of compounds of such diverse nature as sodium chloride and quinoline may be estimated generally to within 10 per cent. The approach is based on the postulate that the vibrational energies of a molecule's "groups," as defined in this paper, are negligible compared with their translational and rotational energies.

This method is able to: Differentiate between ionic and co-valent compounds, such as the metallic halides and the corresponding oxides and sulfides; explain the low specific heats of the elements beryllium, boron, carbon (diamond and graphite) and silicon; and offer a correlation between specific heat and molecular structure.

A UNIFIED procedure based on a theoretical or on a semi-empirical model for the estimation of heat capacities of both solids and liquids does not appear to be available. Approximate values for very simple compounds may be obtained by Kopp's rule (1).<sup>2</sup> For organic liquids, methods that are based on the use of spectral data to determine the energy of the molecule's bonds are accurate but time consuming, and require the necessary experimental data (2). Calculations for solids, usually concerned with the elements, are generally amplifications of the classical work of Einstein (3) and Debye (4). The method derived in this paper is successful for the rapid estimation of the heat capacities of inorganic and organic liquids and solids.

## Derivation of Equation

This approach is based on the postulate that the vibrational energy of a "group" of a molecule is negligible compared to the translational and rotational energies. The vibrational degrees of freedom are computed by the well-known formulas applied to each "group" of atoms. A "group" is defined as follows:

- a. In ionic compounds, each ion is considered as a group.
- b. In compounds with a linear "backbone" or "main chain," a group consists of the atom in the main chain together with the atoms attached to it.

<sup>1</sup>Received March 21, 1960.

<sup>2</sup>Research Chemist, Chemical Div.

<sup>2</sup>Numbers in parentheses indicate References at end of paper.

c. In branched compounds, a branch is considered as a "sub-chain," the atom in the main chain being included in the group immediately attached to it, provided that no other non main-chain atoms are bonded to it.

d. In compounds containing rigid structures, the number of the degrees of freedom of a group are decreased as shown in the examples below.

The following symbols will be used:

$N$  = number of atoms in the molecule

$n_r$  = number of atoms in the  $r$ th nonlinear group

$n_s$  = number of atoms in the  $s$ th linear group

$i$  = number of simple ions (one ionized atom per group)

$n$  = number of nonlinear groups

$l$  = number of linear groups

$F$  = number of degrees of freedom of all atoms of the molecule

$F_a$  = number of degrees of freedom of all groups at normal temperatures

$F_v$  = number of vibrational degrees of freedom of a group

$R$  = gas constant

$C$  = molar specific heat at constant volume at normal temperatures

$C_p$  = molar specific heat at constant pressure

The equations

$$F_v = 3n_r - 6 \quad [1]$$

$$F_v = 3n_s - 5 \quad [2]$$

hold for nonlinear and linear groups respectively.

It is known that

$$F = 3N \quad [3]$$

and assumed that

$$C = RF_a \quad [4]$$

Hence

$$F_a = 3N - \sum_1^n (3n_r - 6) - \sum_1^l (3n_s - 5) \quad [5]$$

$$F_a = 3N - \sum_1^n 3n_r - \sum_1^l 3n_s + 6n + 5l \quad [6]$$

Since

$$N = \sum_1^n n_r + \sum_1^l n_s + i \quad [7]$$

and using Equation [4]

$$C = R(6n + 5l + 3i) \quad [8]$$

Thus, it may be concluded that the molar specific heat is the same for a series of compounds consisting of the same type and number of groups. Consequently, the specific heat per gram of such compounds will vary inversely as the molecular weight.

Furthermore, in agreement with experimental values, the specific heats of organic compounds consisting of the same kinds of groups may be shown to be almost independent of molecular weight. For ease of computation, assuming the molecules to consist of only one kind of group, say an  $n$  group

$$M = n M_{av} \quad [9]$$

where  $M$  = molecular weight, and  $M_{av}$  = average molecular weight of the groups.

The combination of Equations [8 and 9] yields the specific heat

$$C/M = 6R/M_{av} \quad [10]$$

Since  $M_{av}$  for organic compounds does not vary greatly, the values of the specific heats of these compounds will fall within a narrow range.

In order to explain the application of Equation [8], several examples will be given. Compounds have been divided into classes in terms of similar groups according to Equation [8]. In the examples presented in Figs. 1 and 2, nonlinear groups are circled by heavy lines (—), and linear groups by light lines (—).

#### Inorganic Compounds<sup>3,4</sup>

##### Metallic halides

These halides are assumed to be ionized completely; hence,

<sup>3</sup> Due to space limitations, the experimental values are not listed.

<sup>4</sup> Unless noted, the heat capacity values of the inorganic compounds and of the elements calculated by this method were compared with those listed (in cal per mol C at 25°C) in "Selected Values of Chemical Thermodynamic Properties, Circular of the National Bureau of Standards 500," U. S. Government Printing Office, Washington, D. C., 1952.

Compound No.	Compound	Number of Groups	Calculated C
1.		$l = 1$	5R, i.e., 9.9
2.		$l = 1, n = 1$	11R, i.e., 21.9
3.		$n = 1$	6R, i.e., 11.9
4.		$l = 1, i = 1$	8R, i.e., 15.9
5.		$n = 1, i = 2$	12R, i.e., 23.8
6.		$n = 1, i = 1$	9R, i.e., 17.9
7.		$n = 1, l = 1, i = 1$	14R, i.e., 27.8
8.		$n = 1, l = 1$	11R, i.e., 21.9
9.		For $H_2SO_4$ , $n = 1$ , $l = 1, i = 1$ For every water of hydration, $i = 1$ , $l = 1$	14R + 6R, i.e., 27.8 + 15.9R

Fig. 1 Computations of the heat capacities of inorganic compounds

Compound No.	Compound	Number of Groups	Calculated C	Experimental Values
				Temp. °C
10.		$n = 2, l = 1$	17R, i.e., 33.78	3.8 29.4 34.69 30.6
11.		$n = 2, i = 1$	15R, i.e., 29.8	19.50 29.3 21.6 29.5
12.		$n = 1, b = 5$	16R, i.e., 31.8	-6.37 34.1 25.0 37.4
13.		$n = 2, b = 5$	22R, i.e., 43.7	1.84 42.7 36.84 44.6
14.		$n = 1, i = 1$ , $b = 5$	13R, i.e., 27.8	21.84 34.7 25. 37.1
15.		$n = 1, b = 4$	14R, i.e., 27.8	-5.16 30.6 16.84 31.8
16.		$b = 8, f = 1$	19R, i.e., 37.7	10.93 37.7 21.52 39.6
17.		$n = 1, b = 6$ , $f = 1$	21R, i.e., 41.7	-5.16 44.8 16.84 46.8
18.		$b = 10, f = 2$	26R, i.e., 51.7	50 54.9
19.		$n = 1, a = 5$	21R, i.e., 41.7	-5.49 41.8 12.60 42.9
20.		$n = 2, a = 4$	24R, i.e., 47.7	11.67 48.5 28.28 50.5
21.		$n = 2, l = 1$ , $m = 2$	23R, i.e., 45.7	20-27 43.3 40-47 45.4

Fig. 2 Computations of the heat capacities of organic compounds



**Table 1 Heat capacities of inorganic hydrogen-bonded compounds**

Compound	Calc. $C$	Exp. $C_p$
H <sub>2</sub> O	15.90	18.00
H <sub>2</sub> SO <sub>4</sub>	27.82	32.88
H <sub>2</sub> SO <sub>4</sub> ·3H <sub>2</sub> O	75.51	76.21 (23.26 C) <sup>a</sup>
H <sub>2</sub> SO <sub>4</sub> ·4H <sub>2</sub> O	91.40	92.30 (23.91 C) <sup>a</sup>

<sup>a</sup> See (5).

from Equation [8],  $C = 3Ri$ , where  $i$  is the number of cations and anions per molecule, i.e., the values of  $i$  are 2 and 3 for the halides of monovalent and divalent cations, respectively.

#### Metallic oxides and sulfides

As a first approximation, these structures are considered as separate molecular species, without taking into account their detailed crystalline structures.<sup>5</sup> These compounds are considered to be co-valent.

In Fig. 1, the  $C$ 's of the oxides of the bivalent, trivalent, tetravalent and monovalent metals (compounds 1 to 4), are shown to be 9.9, 21.9, 11.9 and 15.9, respectively. The value of the heat capacity of the oxide of a monovalent metal agrees with that of a metal ion added to an ionized bivalent metal oxide. Similar examples occur for compounds of the form  $M_2A$  where  $M$  is a monovalent metal.

#### Carbonates

These compounds are considered to be ionic. The  $C$ 's of the carbonates of monovalent and divalent cations (compounds 5 and 6) are 23.8 and 17.9, respectively.

#### Sulfates and other oxygen-containing anions

The  $C_p$  of compounds with oxygen-containing anions are greater than that of the corresponding carbonates. In terms of this model, better agreement with experimental values is obtained assuming one metal-oxygen bond to be co-valent. Thus, for monovalent cations (compound 7),  $C = 27.8$ , and for bivalent cations (compound 8),  $C = 21.9$ .

Among the reasons for the divergence between the calculated and experimental values could be: The difference between  $C_v$  and  $C_p$  may be appreciable; and at 25 C, the vibrational modes of the anion probably do make a contribution to the value of  $C_p$ .

#### Effect of hydrogen bonding

In most cases, the effect of hydrogen bonding both in the inorganic as well as in the organic compounds may be neglected. Acids as well as water are considered to be ionized. In combination with the rule stated above for sulfates, the heat capacities of the hydrates of sulfuric acid will be based on the structure of compound 9. The agreements shown in Table 1 are typical for this model.

#### Organic Compounds<sup>6</sup>

These compounds are divided into groups as defined above, similarly to the inorganic compounds. Due to space limitations the method is illustrated by only a small number of examples in Fig. 2. Whenever available, experimental values are listed at two temperatures near room temperature.

<sup>5</sup> Details of structures are found in reference books such as: Pauling, L., "The Nature of the Chemical Bond," Cornell Univ. Press, Ithaca, N.Y., 1939, chapters 5 and 7; also Wells, A. F., "Structural Inorganic Chemistry," Oxford University Press, London, 1945, chapters 11 and 12.

<sup>6</sup> The heat capacity data of the organic compounds were obtained from Timmermans, J., "Physico-Chemical Constants of Pure Organic Compounds," Elsevier Publishing Co., Inc., New York, 1959; also "International Critical Tables," vol. V, McGraw-Hill Book Co., Inc., New York, N. Y., 1929. Units are in cal per mol C and temperatures are in deg C.

#### Aliphatic series

These compounds are represented by acetone and acetic acid (compounds 10 and 11, respectively). The calculated values for paraffins are generally too high by approximately 50 per cent.

#### Aromatic series

It is assumed that due to the rigidity of the double bonds and rings the number of degrees of freedom of the groups are restricted. Every CH group of the benzene molecule may be thought to possess one translational degree of freedom (out of the plane of the ring) instead of three, and one rotational degree of freedom instead of two. In these calculations, the number of CH groups in the benzene ring will be designated by  $b$ . Hence, for benzene,  $b = 6$ , therefore  $C = 12R$ , i.e., 23.8 [cf. 29.6 and 32.4 at  $-2.58$  C(s) and  $21.80$  C (l), respectively].

Substitution of a hydrogen by another "chemical group" forms a new group or groups. The carbon atom of the benzene ring is included in the group immediately attached to it, as shown for toluene, ethyl benzene and benzoic acid (compounds 12, 13 and 14, respectively).

#### Pyridine

Since the "N" is non-ionic, in the sense of the model, it is included with its nearest neighbor in a group (compound 15).

#### Polycyclic compounds

In terms of the model, the group consisting of the two carbon atoms at the junction of the two rings has three degrees of freedom instead of five, i.e., two translational and one rotational, or one translational and one rotational degree less than the unrestricted group. The number of groups of two carbon atoms at the junctions of the fused rings will be designated by  $f$  as for naphthalene, quinoline and anthracene (compounds 16, 17 and 18 respectively).

#### Cyclic hydrocarbons

**Cyclohexane:** Each CH<sub>2</sub> group has three degrees of freedom, i.e., one more than the CH group in benzene. The number of ring CH<sub>2</sub> groups will be designated by  $m$ . Thus, for cyclohexane,  $m = 6$ ; therefore  $C = 18R$ , i.e., 35.8 [cf. 30.9 and 36.5 at  $-2.03$  C(s) and  $11.73$  (l), respectively].

**Methyl-substituted cyclohexanes:** The hydrogen on the substituted carbon atom is included with the C-CH<sub>3</sub> in one non-linear group, as in methyl cyclohexane, and 1,2-trans dimethyl cyclohexane (compounds 19 and 20, respectively).

**Tetrahydrofurfuryl alcohol:** The calculation of the heat capacity of the saturated heterocyclic compound (compound 21) follows from the above discussion.

#### Liquid co-valent compounds containing one central atom, AB<sub>2</sub>

The heat capacity of most of these compounds is generally  $3(x + 1)R$ , i.e., the maximum number of degrees of freedom are excited. A possible explanation is that the atoms are not restricted as in the more complex crystalline compounds.

#### Elements

The atomic heats of the elements carbon, boron, beryllium and silicon are less than  $3R$ . Carbon favors co-valent formation and the others are on the borderline between co-valent and ionic structures. Hence, in terms of the model, it is assumed that the atoms of these elements may not be considered as independent oscillators, but rather, as being bonded in co-valent groups. The number of atoms in a group is designated by  $G$ , so that  $C$  (element) =  $C$  (group)/ $G$ .

#### Carbon

**Graphite:** In this compound, consisting of planar sheets,  $G = 4$ . Due to the rigidity of the rings, it is assumed that the total number of degrees of freedom of this group is four, considered as two translational and two rotational degrees of free-

dom, i.e., the planar structure restricts translations and rotations in the rings' plane, similarly as in the  $f$  groups. Hence,  $C = 4R/4$ , i.e., 1.99 (Lit. value at 25 C, 2.066).

**Diamond:** This structure is tetrahedral, each carbon atom being bonded to four others, so that  $G = 5$ . The structure's rigidity decreases each of the two kinds of degrees of freedom by one each, so that the group's number of degrees of freedom is four. Hence,  $C = 4R/5$ , i.e., 1.59 (Lit. value at 25 C, 1.449).

#### Boron

Since the valence is 3,  $G = 4$ ;  $n = 1$ . Hence,  $C = 6R/4$ , i.e., 2.98 (Lit. value at 20 C, 2.86). Thus, the atomic heat value agrees with that of an unrestricted group.

#### Beryllium

Since boron, of valence 3, is calculated as being in an unrestricted group, it is expected that beryllium, of valence 2, is also in an unrestricted group. Since  $G = 3$ ,  $C = 6R/3$ , i.e., 3.97 (Lit. value at 25 C, 4.26).

#### Silicon

Although this element, of valence 4, possesses the tetrahedral structure similar to diamond, its  $C_p$  agrees with the value calculated for a linear group of  $G = 2$ ,  $l = 1$  viz.,  $C = 5R/2$ , i.e., 4.97 (Lit. value at 25 C, 4.75). This apparent anomaly is explained by the fact that silicon is more ionic than carbon, the increased number of degrees of freedom of the group being reflected in the greater value of the atomic heat.

## Conclusions

In abbreviated form, the expression for the heat capacity may be written as  $C = RKM$ , where  $K$  is a row matrix containing the constants  $[6\ 5\ 3\ 2\ \dots]$ , and  $M$  is a column matrix whose elements are the number of groups corresponding to the elements in  $K$ , i.e.,  $[n, l, i, b, \dots]$ .

The model for the estimation of heat capacity, which has been shown in the foregoing discussion to be capable of yielding fairly accurate results, appears to emphasize that, as defined in the sense of this paper, the concept of groups is valid. Its success, although depending partly on cancellation of errors, is in all probability not fortuitous, but rests on the independence of entities in terms of which a molecular structure may be considered. The mathematical simplifications offered by this concept should be useful in gaining further insight into the theory of molecular structure and in the estimation of required heat capacity values.

## References

- 1 Partington, J. R., "An Advanced Treatise on Physical Chemistry" Vol. III, Longmans, Green and Co., London, 1952, p. 308; also Kopp, P., "Ueber die Beziehung zwischen der spezifischen Waerme und der chemischen Zusammensetzung bei starren organischen Verbindungen," *Berichte der deutschen chemischen Gesellschaft*, vol. 19, 1886, p. 813.
- 2 Sakladis, B. C. and Contes, J., "Prediction of Specific Heat of Organic Liquids," *A. I. Ch. E. J.*, vol. 2, 1956, p. 88.
- 3 Einstein, A., "Die Plancksche Theorie der Strahlung und die Theorie der Spezifischen Waerme," *Ann. Phys.*, vol. 22, 1907, p. 180.
- 4 Debye, P., "Zur Theorie der spezifischen Waerme," *ibid.*, vol. 31, 1912, p. 789.
- 5 Hornung, E. W. and Giauque, W. F., "Heat Capacities and Entropies of  $H_2SO_4$  tri- and tetrahydrates," *J. Amer. Chem. Soc.*, vol. 77, 1955, p. 2983.

# Technical Comments

## Note on "Pierce Gun Design for an Accelerate-Decelerate Ionic Thrust Device"

J. R. PIERCE<sup>1</sup>

Bell Telephone Laboratories, Inc., Murray Hill, N. J.

IT IS gratifying to note that the application of gun design procedures which I originally proposed have been suggested for an ionic thrust device.<sup>2</sup>

In connection with a statement "This beam spreading [by space charge] is dependent upon beam width . . .," I wish to note that for a ribbon beam the absolute amount of spread is not dependent on beam width, though the fractional amount is.

In connection with the lens effect of the entrance and exit apertures to the field-free region, I wish to note that this is quite large. The convergence  $C$  of a slit electrostatic lens is

$$C = \frac{V_2' - V_1'}{2V} \quad [1]$$

Here  $V_2'$  and  $V_1'$  are the potential gradients to the right and

Received Oct. 25, 1960.

<sup>1</sup> Director of Research, Communications Principles. Member ARS.

<sup>2</sup> Raether, M. J. and Seitz, R. N., "Pierce Gun Design for an Accelerate-Decelerate Ionic Thrust Device," *ARS JOURNAL*, vol. 30, pp. 640-642, July 1960.

to the left of the slit, and  $V$  is the potential at the slit.

In the cathode slit region,  $V$  varies as distance from the cathode  $x$  to the  $\frac{1}{3}$  power, and this leads to

$$V' = (4/3) V/x \quad [2]$$

If we assume that the distance between the second aperture and the final low potential anode is equal to the distance between the cathode and the first aperture, that the strength of the lens at the second aperture is roughly equal to that at the first aperture and that the distance between the two apertures is small, we obtain as the sum of the convergences of the lenses formed by the fields of the two apertures

$$C = (4/3) x \quad [3]$$

where  $x$  is the spacing between the cathode and the first aperture.

It is not clear just how great this will make the beam width at the final anode; the deceleration of the beam tends to increase the spread, and the shape of the electrodes tends to provide some focusing if the beam spreads beyond its initial diameter. If the ions traveled in straight lines beyond the second aperture, the final beam width would be  $2\frac{1}{3}$  times that at the cathode. The spreading will in any case be considerable, and if the potential to which the electrons are decelerated in the second region is low enough, the outermost electrons could well turn around and go back toward the cathode. The spreading will of course become greater as the distance between the two apertures is increased.

# Determination of Optimum Insulation Weight<sup>1</sup>

J. A. ORR<sup>2</sup>

Jet Propulsion Laboratory, California Institute of Technology, Pasadena, Calif.

Frequent reference has been made in the literature to hydrogen fueled space propellant systems which require insulation of propellant tanks to reduce the heat absorbed by and rejected with the vaporizing propellant. This note presents a method of determining the amount of insulation and propellant loss which will result in the best performance of a stage subjected to storage periods in space.

ACCORDING to Burry and Degner (1),<sup>3</sup> it should not be difficult to store propellants of noncryogenic nature for considerable periods of time anywhere between the orbits of Venus and Mars. The cryogenic oxidizers are slightly more difficult to store, whereas hydrogen requires considerable precautions. If a mission has a requirement of a long storage (or coast) period anywhere within about 5 astronomical units (a.u.) of the sun, it will be necessary to provide some type of insulation on a hydrogen tank in order to reduce the amount of hydrogen vaporized (and presumed lost—assuming a constant pressure system).

Both the insulation and the lost propellant serve to reduce the effective value of the propellant fraction and, therefore, the payload capability of a given system. This effective propellant fraction ( $\nu_p'$ ) can be calculated using the equation

$$\nu_p' = \frac{W_p}{W_p + W_H + W_I + W_L[1/(\lambda - 1)]} \quad [1]$$

where

- $W_p$  = total tanked propellants less residuals
- $W_H$  = system hardware plus residuals
- $W_I$  = tank insulation
- $W_L$  = propellant lost by boiloff
- $\lambda$  =  $\exp(\Delta V/c)$

It is evident that proper design of the stage would allow any required value of  $W_L$  to be provided without changing the engine mixture ratio which should be achieved, merely by allowing the tanked mixture ratio to differ from the engine

mixture ratio. Therefore, it is desirable to so select  $W_I$  and  $W_L$  that  $\nu_p'$  is maximized. Assuming that  $\partial W_H/\partial W_L$  and  $\partial W_H/\partial W_I$  are small (which is a good first-order assumption), the relation for maximum  $\nu_p'$  is

$$W_I = W_L[1/(\lambda - 1)] \quad [2]$$

Using this relation in Equation [1] yields

$$\nu_p' = W_p/(W_p + W_H + 2W_L) \quad [3]$$

In hydrogen fueled systems, the hydrogen tank presents the larger volume as well as the most severe insulation requirement. Therefore, the insulation weights for the system can be closely approximated by calculating the requirement for the hydrogen tank alone. Assuming a heat balance between the sun and the night sky, Roschke (2) gives, for an isolated spherical tank with uniform liquid temperature

$$\frac{\epsilon}{\alpha} \sigma T_2^4 + \frac{k}{\alpha(\Delta x)} (T_2 - T_L) = \frac{C_s}{4R^2} \quad [4]$$

and

$$q_{2L} = 4\pi a^2(k/\Delta x)(T_2 - T_L) \quad [5]$$

where

- $a$  = tank radius
- $C_s$  = solar intensity at  $R = 1$
- $k$  = average thermal conductivity of insulation
- $q_{2L}$  = net heat flow to liquid
- $R$  = distance to center of sun, a.u.
- $T_2$  = temperature of outer surface
- $T_L$  = temperature of tank wall (and liquid)
- $\alpha$  = solar absorptivity of outer surface
- $\Delta x$  = thickness of insulation
- $\epsilon$  = infrared emissivity of outer surface
- $\sigma$  = Boltzmann's constant

Changing parameters and remembering Equation [2] gives

$$\frac{\epsilon}{\alpha} \sigma \left[ \frac{H_v W_L^2}{16\pi^2 a^4 k \rho_I \Delta t (\lambda - 1)} + T_L \right] + \frac{H_v W_L}{4\pi a^2 \alpha \Delta t} = \frac{C_s}{4R^2} \quad [6]$$

where

- $H_v$  = heat of vaporization of liquid
- $\Delta t$  = storage (coast) period
- $\rho_I$  = density of insulation

Equation [6] can be solved numerically for the optimum value of  $W_L$  for a given set of conditions.

## References

- 1 Burry, R. V. and Degner, V. R., "Liquid Propellant Storage Evaluation for Space Vehicles," in Vol. I, "Bull. of First Meeting JANAF Liquid Propellant Group," New Orleans, La., Nov. 1959, pp. 261-295.
- 2 Roschke, E. J., "Research Summary no. 5," Jet Propulsion Laboratory Pasadena, Calif., Oct. 15, 1959, pp. 24-28. (Confidential)

# Propagation of Errors in a Schuler-Type Inertial Navigation System

JOSEPH G. GURLEY<sup>1</sup>

Hughes Aircraft Co., Culver City, Calif.

THE OBJECT of this paper is to characterize the effects, on the errors of an inertial navigation system used for navigation over the surface of Earth, of the cross coupling between channels caused by an arbitrary motion of the vehicle.

Presented at the ARS Semi-Annual Meeting, May 9-12, 1960, Los Angeles, Calif.

<sup>1</sup> Engineer.

Particular attention is given to effects not elucidated by a single-channel linear analysis. This object is most conveniently attained by examining the motion of a perfectly instrumented platform, caused by small initial errors in position, velocity and attitude.

The inertial navigation system being discussed can have any of a variety of forms, but it must contain the following elements: Three one-degree of freedom gyros or equivalent instruments, in order to establish an inertial attitude reference; two accelerometers oriented so as to measure the lateral acceleration; integrators to compute the lateral velocity; an independent source of radial distance from the center of Earth (e.g., a pressure altimeter); a computer which converts linear velocity to angular velocity over Earth's surface and

integrates that to obtain position coordinates; and provision for orienting the accelerometers as mentioned. Various orientations of the accelerometers (based on local vertical, mass attraction vertical or geocentric vertical), various azimuth orientations (north-oriented or free) and various coordinate systems affect the instrumentation errors and the accuracy and convenience of the computation, but do not affect the type of errors described.

Such a navigation system has seven degrees of freedom, two corresponding to its two position coordinates, two corresponding to its two components of horizontal velocity and three corresponding to its attitude.

Initial errors in the three of these degrees of freedom corresponding to the platform attitude relative to the fixed stars will be permanently retained, and will not couple into the other four degrees of freedom. Assuming that the platform is initially vertical and has the correct initial velocity, then it will remain vertical and retain the correct velocity. However, the indicated position coordinates and azimuth will be related to the correct position coordinates and azimuth by the rotation required in transforming from the indicated platform attitude to the actual platform attitude.

The other four error components represent Schuler-pendulum-type oscillations in two planes. That is, if the vehicle is not moving relative to inertial space, the velocity and position errors will undergo sinusoidal oscillations at the Schuler frequency, which, on the surface of Earth, is about  $2\pi/84$  min.

The propagation of initial velocity and position errors is complicated by the presence of cross-coupling due to the motion of the vehicle. The actual linearized equations satisfied by the east-west position error  $\delta x$  and the north-south position error  $\delta y$  are

$$\frac{d^2\delta x}{dt^2} + \left[ \omega_0^2 - \left( \frac{dL}{dt} \right)^2 \right] \delta x - 2 \frac{dL}{dt} \sin \lambda \frac{d\delta y}{dt} - \left( \frac{d^2L}{dt^2} \sin \lambda + 2 \frac{dL}{dt} \frac{d\lambda}{dt} \cos \lambda \right) \delta y = 0$$

$$\frac{d^2\delta y}{dt^2} + \left[ \omega_0^2 - \left( \frac{dL}{dt} \right)^2 \sin^2 \lambda - \left( \frac{d\lambda}{dt} \right)^2 \right] \delta y + 2 \frac{dL}{dt} \sin \lambda \frac{d\delta x}{dt} + \frac{d^2L}{dt^2} \sin \lambda \delta x = 0$$

where

$L, \lambda$  = longitude and latitude, respectively, of the vehicle  
 $\omega_0$  = Schuler frequency

A general solution to these equations does not appear feasible, but the special case of uniform circular motion has been solved. The errors along the path and normal to the path vary exponentially with time, being proportional to  $e^{\pm \mu t}$  where

$$(k^2 + \omega_0^2 - \omega_m^2)(k^2 + \omega_0^2 - \omega_m^2 \cos^2 \mu) + 4k^2\omega_m^2 \cos^2 \mu = 0$$

In this equation  $\mu$  is the radius of the circle and  $\omega_m$  the angular velocity of the vehicle in the circle.

One immediately obtains from this equation the frequencies observed when an inertial navigation system is operated at a fixed point on Earth. Due to the rotation of Earth, the effect is the same as if one were in a vehicle describing a circular path whose radius is the co-latitude, at a rate of  $2\pi$ -radians per day. At the latitude of Los Angeles, this leads to two periods, one of 81 min and one of 87 min.

Another case of interest is that of motion about a closed path at a period approximating the Schuler period. At exactly the Schuler period, one solution is  $k = 0$ ; the platform has neutral stability. If  $\omega_m$  lies between  $\omega_0$  and  $\omega_0 \sec \mu$ , then the constant term in the characteristic equation changes sign, indicating a condition of instability. However, the exponential increase in error is rather slow for circles of reasonable size. For example, consider a circle of radius 600 nautical miles. The greatest rate of increase would occur when this circle was transversed 1.076 times per Schuler period, or at a speed of 2700 knots. The error, however, would increase only five per cent each trip around the circle.

## An Interesting Observation on the Point Release Into Orbit of a Number of Objects

DONALD B. BRICK<sup>1</sup>

Sylvania Electronic Systems, Waltham, Mass.

CONSIDER the instantaneous point release of  $n$  particles ( $i = 1, \dots, n$ ) of equal mass  $m$  into orbit, under the effect of a central gravitational force. (The perturbation effects due to other bodies, variances from spherical symmetry and rotation of the central mass, and frictional damping are neglected.) The instantaneous release mechanism can be considered to have the effect of imparting to each particle, at the release point, an initial impulsive velocity vector  $V_i$ . This initial velocity (with respect to the inertial frame of reference of the central mass) is normally a function of the direction in which each particle is released, as indicated by the spherical angles  $\theta_i$  and  $\phi_i$  measured about the radial direction  $r_0$  at the release point, as shown in Fig. 1. An interesting observation that has been made is that if the magnitude  $V_i$  of the release velocity vector (the release speed) is not a function

of  $\theta_i$  and  $\phi_i$ , i.e., if the same initial speed, regardless of initial direction, is imparted to each particle,<sup>2</sup> then the orbital periods of all  $n$  particles will be equal, and all particles which are released together will, to within the limitations of the approximations made, coalesce periodically at the initial release point even though they traverse very different orbits. (Of course, this result will suffer important perturbations in any practical situation due to neglected factors, some of which are mentioned in the foregoing.)

The proof of the statement is immediately obvious from examination of the equations of the classical two-body problem. Although the author is convinced that this observation must have been made many times previously, he has never seen it recorded and therefore feels that this note is pertinent now, especially in view of the recent interest in placing many small objects in orbit for communications purposes.<sup>3</sup>

<sup>2</sup> Note that the condition implies that initial speed is uniform with respect to a fixed release point in the inertial frame of the central mass. If the particles are released from a carrier, such as a satellite or missile, traveling with a certain velocity with respect to the central mass, the carrier's velocity must be considered as part of the initial velocity imparted to each particle and, hence, the release must be shaped with respect to this component in order to provide a resultant constant release speed.

<sup>3</sup> See, for example, Klass, P. J., "Techniques of 'Project Needles' Detailed," *Aviation Week*, Sept. 19, 1960, pp. 30-31.

Received Oct. 24, 1960.

<sup>1</sup> Senior Engineering Specialist, Applied Research Laboratory.



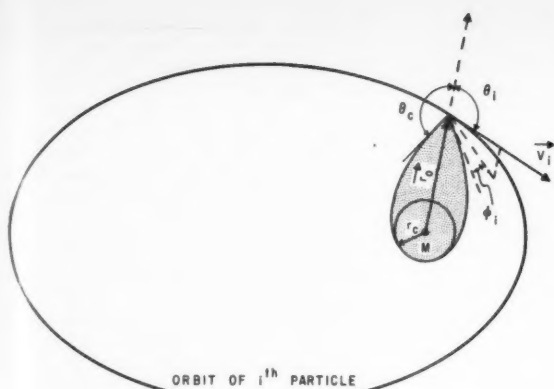


Fig. 1 Geometry of orbit

The derivation is simply as follows: The period of the  $i$ th particle is<sup>4</sup>

$$\tau_i = 2\pi GMm^{1/2} / \sqrt{(-2E_i)^3}$$

where

$M$  = mass of the central body  
 $G$  = gravitational constant

<sup>4</sup> See, for example, Synge, J. L. and Griffith, B. A., "Principles of Mechanics," McGraw-Hill Book Co., Inc., N. Y., 1942, p. 179.

$E_i$ , the energy of the  $i$ th particle is a constant in time subsequent to release, given by  $(1/2) mV_i^2(\theta_i, \phi_i) - (GMm/r_0)$ .

For all particles to have equal periods,  $\tau_i = \tau$ , a constant for all  $i = 1, \dots, n$ . If all particles are of equal mass, then equal periods require equal energy  $E_i = E$ , or, from the above relationship,  $V_i(\theta_i, \phi_i) = V$ , for all  $i$ 's, where  $E$  and  $V$  are constants representing the constant energy and initial or release speed per particle, respectively. The last condition is the one we desired to show. In other words, if all particles are released with the same initial speed, each will have the same orbital period  $\tau$  regardless of the direction  $\theta_i$  and  $\phi_i$  of the initial velocity vector, and thus, if all particles are released at the same time they will return to the release point at the same time.

The actual numerical value of the initial speed  $V$  is given by

$$V(\theta, \phi) = \begin{cases} \sqrt{GM \left[ \frac{2}{r_0} - \left( \frac{4\pi^2}{\tau^2 GM} \right)^{1/3} \right]}, & \pi - \theta_c < \theta < \theta_c \\ 0, & \theta \geq \theta_c, \theta \leq \pi - \theta_c \end{cases}$$

where

$$\theta_c = \sin^{-1} \left[ \frac{r_c}{r_0} \sqrt{\frac{2}{\frac{2}{r_0} - \left( \frac{4\pi^2}{\tau^2 GM} \right)^{1/3}}} \right] \leq \sin^{-1} \frac{r_c}{r_0}$$

The angular cutoff  $\theta_c$  has been introduced somewhat arbitrarily in order to provide the control mechanism to avoid releasing particles that intersect the central body or some sphere surrounding it (as for example Earth or its sensible atmosphere), indicated by radius  $r_c$ , since such particles will not enter periodic orbits.

## Book Notes

**Rocket Propulsion**, Barrère, Marcel (Head, Research Div., National Office for Aeronautical Studies and Researches—ONERA), Jaumotte, André (Professor, University of Brussels), Fraeijs De Veubeke, Baudouin, Professor, Universities of Liège and Louvain) and Vandekerckhove, Jean (Lecturer, Institute of Aeronautics, University of Brussels), Elsevier Publishing Co., Amsterdam, 1960, (sole distributors, U.S.A.: D. Van Nostrand Co., Inc., Princeton, N. J.), 829 pp. \$27.

**Chapters:** 1. Rocket Propulsion Elements (by A. Jaumotte); 2. Nozzle Theory and Characteristic Parameters (by A. Jaumotte and J. Vandekerckhove); 3. Aerochemistry of the Combustion Products (by M. Barrère); 4. Solid

Propellants (by J. Vandekerckhove); 5. Internal Ballistics of Solid-Propellant Rockets (by J. Vandekerckhove); 6. Design of Solid-Propellant Rockets (by J. Vandekerckhove); 7. Liquid-Propellant Rockets (by M. Barrère); 8. Experimental Techniques for Rocket Propulsion (by M. Barrère); 9. Liquid Propellants (by M. Barrère); 10. Combustion Instability in Liquid-Propellant Rocket Motors (by M. Barrère); 11. Elementary Problems of Overall Rocket Performance (B. Fraeijs de Veubeke); 12. Variational Methods in Optimizing Rocket Performance (B. Fraeijs de Veubeke).

This book is a comprehensive treatise on rocket propulsion that can now be regarded as the standard work in the field. It is designed for the research and development engineer and for advanced graduate students in engineering. This book is a new work and not simply a translation of the earlier French book by the same authors. An introduction is written by Dr. Theodore von Kármán, Chairman, AGARD.

**Elements of Flight Propulsion**, Foa, Joseph V. (Professor of Aeronautical Engineering, Rensselaer Polytechnic Institute), John Wiley & Sons, Inc., New York, 1960, 445 pp. \$12.50.

**Chapters:** 1. Basic Laws and Concepts; 2. One-Dimensional Approximations; 3. Propagation of Disturbances; 4. One-Dimensional Steady Flow; 5. Changes of the Frame of Reference; 6. One-Dimensional Nonsteady Flow; 7. Nonuniform Flows; 8. Diffusers and Nozzles; 9. Dynamic Flow Machines; 10. Pressure Exchange; 11. Combustion Chambers; 12. Thrust and Drag; 13. Efficiencies—Propulsive Cycles; 14. Steady-Flow Thrust Generators; 15. Nonsteady-Flow Thrust Generators.

This book is intended for students and practicing engineers. It is based on classroom use in undergraduate courses and in first-year graduate courses at Rensselaer Polytechnic Institute.

**An Introduction to Astrodynamics**, Baker, Robert M. L., Jr. and Makemson,

Maud W. (both of the Department of Astronomy, University of California), Academic Press, New York, 1960, 339 pp. \$7.50.

**Chapters:** 1. Introduction; 2. The Minor Planets; 3. The Comets; 4. Geometry and Coordinate Systems; 5. Astrodynamical Constants; 6. Orbit Determination and Improvement; 7. The N-Body Problem; 8. Special Perturbations; 9. General Perturbations; 10. Nongravitational and Relativistic Effects; 11. Observation Theory; 12. Application to Interplanetary Orbits.

This book is partially based on an intensive summer course given by Dr. Baker, which is derived from a course initiated by Dr. Samuel Herrick in 1946. The text is directed particularly to the engineer or nonastronomer. In this regard, this work is meant to serve both as a brief introduction to the history, nomenclature and practical application of astrodynamics and as a key or handbook of specific astrodynamical techniques.

**Classical Mechanics**, Corben, H. C. (Assoc. Director, Ramo-Wooldridge Research Laboratory) and Stehle, Philip (Professor of Physics, University of Pittsburgh), John Wiley & Sons, Inc., New York, 2nd edition, 1960, 389 pp. \$12.

**Chapters:** 1. Kinematics of Particles; 2. The Laws of Motion; 3. Conservative Systems with One Degree of Freedom; 4. Two-Particle Systems; 5. Time-Dependent Forces and Nonconservative Motion; 6. Lagrange's Equations of Motion; 7. Applications of Lagrange's Equations; 8. Small Oscillations; 9. Rigid Bodies; 10. Hamiltonian Theory; 11. The Hamilton-Jacobi Method; 12. Infinitesimal Contact Transformations; 13. Further Development of Transformation Theory; 14. Special Applications; 15. Continuous Media and Fields; 16. Introduction to Special Relativity Theory; 17. The Orbits of Particles in High Energy Accelerators.

This book is intended for students and practicing physicists. Completely revised to include the applications of the subject during the past 10 years, this edition includes some applications to problems not usually taught in physics departments.

**Fundamentals of Aerodynamic Heating**, Truitt, Robert Wesley (Professor and Head of the Aeronautical Engineering Dept., Virginia Polytechnic Institute), The Ronald Press Co., New York, 1960, 257 pp. \$10.

**Chapters:** 1. Basic Concepts; 2. Fundamental Equations; 3. Properties of the Laminar Boundary Layer; 4. Theoretical Laminar Skin Friction and Heat Transfer; 5. Approximate Methods for Solution of Laminar Boundary Layers; 6. The Turbulent Boundary Layer; 7. Basic Parameters for Low-Density Flow; 8. Slip Flow; 9. Free-Molecule Flow; 10. Stagnation-Point Heat Transfer; 11. Mass-Transfer Cooling in the Stagnation Region; 12. Calculation of Skin Temperature.

The book is based on a course at the senior-graduate level conducted by the

author. It is intended also for practicing engineers, physicists and mathematicians working in the missile field, especially those who have not had the benefit of a formal course in boundary layer theory and heat transfer.

**Principles of Fluid Mechanics**, Kenyon, Richard A. (Asst. Professor of Mechanical Engineering, Clarkson College of Technology), The Ronald Press Co., New York, 1960, 216 pp. \$7.

**Chapters:** 1. Fundamental Concepts and Fluid Properties; 2. Characteristics of Fluids; 3. Fluid Statics; 4. The Principle of Conservation of Mass and the Continuity Equation; 5. The Principle of Conservation of Energy and the Energy Equation; 6. Newton's Second Law of Motion—The Euler Equation of Motion and the Bernoulli Equation; 7. Newton's Second Law of Motion—Impulse and Momentum in Steady Flow; 8. One-Dimensional, Frictionless, Compressible Gas Flow; 9. Dimensional Analysis; 10. Incompressible Flow of a Nonideal Fluid; 11. Introduction to Boundary-Layer Theory.

This text is written for a first course in fluid mechanics. The author's goal is to present the fundamental principles with a greater depth and rigor than is found in other elementary texts. It is his belief that the study of unsteady compressible, or general, flow and the application of the calculus in a basic but rigorous course in fluid mechanics is essential not only for those who will pursue advanced work in fluid flow but for those whose need is fundamental theory.

**Advanced Dynamics for Engineers**, Downey, Glenn L. and Smith, Gerald M., Assoc. Professors of Engineering Mechanics, University of Nebraska), International Textbook Co., Scranton, Pa., 1960.

**Chapters:** 1. Basic Concepts; 2. Kinematics; 3. Kinetics; 4. Work and Energy; 5. Impulse and Momentum; 6. Vibration—Periodic Motion; 7. Systems with Multiple Degrees of Freedom; 8. Basic Analog Computer Theory.

This text is intended for senior level undergraduate engineering students and beginning graduate students who have had the introductory course in dynamics and basic knowledge of differential equations and mechanics of materials. The authors have tried to integrate the principles of dynamics with other subject matter encountered in the engineering curriculum.

**Diffuse Coatings of Iron and Steel**, Gorbunov, N. S. (Institute of Physical Chemistry, Academy of Sciences of the USSR), The Israel Program for Scientific Translations, 1960, 165 pp. Transl. from Russian and available from the Office of Technical Services, U. S. Dept. of Commerce, Washington 25, D. C.; \$1.25.

**Chapters:** 1. The Physico-Chemical Conditions in the Formation of Diffuse Coatings; 2. Methods of Formation of Diffuse Coatings; 3. Determination of the Diffusion Coefficients of Chromium

in Iron by Spectroscopic Methods and by Radioactive Tracer Techniques; 4. The Roentgenographical and Electronographical Analysis of Diffuse Coatings; 5-10. Diffuse Coatings Formed by Copper, Gold, Zinc, Beryllium, Boron, Aluminum, Silicon, Titanium, Vanadium, Chromium, Molybdenum, Tungsten, Manganese and other Chemical Elements.

A considerable part of this book, originally published in Russian in 1958, describes experimental studies carried out at the Institute for Physical Chemistry, Academy of Science USSR. New Methods of applying physico-chemical principles of the formation of diffuse coatings and the experimental results of investigation on the properties of the coatings obtained are described.

**Frequency-Power Formulas**, Penfield, Paul, Jr. (Asst. Professor of Electrical Engineering, Massachusetts Institute of Technology), The Technology Press of MIT and John Wiley & Sons, Inc., New York, 1960, 168 pp. \$4.

**Chapters:** 1. Introduction; 2. The Energy-Function Method; 3. Four Types of Frequency-Power Formulas; 4. Lumped Reactive Systems; 5. Lumped Dissipative Systems; 6. Distributed Systems; 7. Rotating Machine Applications; 8. Communications Applications.

This is the eighth of a series of Technology Press "Research Monographs," designed to make selected timely and important research studies readily accessible to libraries and to the independent worker. This book is based on a thesis submitted toward a Doctor of Science degree in Electrical Engineering at MIT.

**Basic Human Factors for Engineers: The Task Analysis Approach to the Human Engineering of Men and Machines**, Verdier, Paul A. (Engineering Psychologist engaged in industrial and weapons systems work), Exposition Press, New York, 1960, 103 pp. \$4.

**Chapters:** 1. Human Factors and Task Analysis; 2. Analyzing the Task; 3. Human Factors Forms and Worksheets; 4. The Human Engineering Department in the Company; 5. The Future of Human Engineering. **Appendix:** A Suggested Format for a Military Unit Proficiency System Personnel Performance Test.

The method presented in this manual is intended as the first systematic methodology for the new profession of Human Engineering, an essential part of this discipline which has been lacking to date.

**An Introductory Treatise on Dynamical Astronomy**, Plummer, H. C. (Late Professor of Astronomy in the University of Dublin and Royal Astronomer of Ireland), Dover Publications, Inc., New York, 1960, 343 pp. Paperback reprint \$2.35.

**Chapters:** 1. The Law of Gravitation; 2. Introductory Propositions; 3. Motion Under a Central Attraction; 4. Expansions in Elliptic Motion; 5. Relations Between Two or More Positions in an Orbit and the Time; 6. The Orbit in Space; 7. Conditions for the Determina-

tion of an Elliptic Orbit; 8. Determination of an Orbit. Method of Gauss; 9. Determination of Parabolic and Circular Orbits; 10. Orbits of Double Stars; 11. Orbits of Spectroscopic Binaries; 12. Dynamical Principles; 13. Variations of Elements; 14. The Disturbing Function; 15. Absolute Perturbations; 16. Secular Perturbations; 17. Secular Inequalities. Method of Gauss; 18. Special Perturbations; 19. The Restricted Problem of Three Bodies; 20. Lunar Theory I; 21. Lunar Theory II; 22. Precession, Nutation and Time; 23. Libration of the Moon; 24. Formulas of Numerical Calculation.

First published in 1918 and now available in this inexpensive paperback, this book is intended to provide an introduction to those areas of astronomy which require dynamical treatment. Basic principles are stressed throughout to prepare the student for advanced study. It is useful also as a reference book for astronomers.

**A Manual of Spherical and Practical Astronomy**, Chauvenet, William, Dover Publications, Inc., New York, 1960. Paperback reprint in two volumes:

**Vol. 1. Spherical Astronomy**, 708 pp. \$2.75.

*Chapters:* 1. The Celestial Sphere; 2. Time—Use of the Ephemeris—Interpolation—Star Catalogues; 3. Figure and Dimensions of the Earth; 4. Reduction of Observations to the Centre of the Earth; 5. Finding the Time by Astronomical Observations; 6. Finding the Latitude by Astronomical Observations; 7. Finding the Longitude by Astronomical Observations; 8. Finding a Ship's Place at Sea by Circles of Position—Sumner's Method; 9. The Meridian Line and Variation of the Compass; 10. Eclipses; 11. Precession, Nutation, Aberration and Annual Parallax of the Fixed Stars; 12. Determination of the Obliquity of the Ecliptic and the Absolute Right Ascensions and Declinations of Stars by Observation; 13. Determination of Astronomical Constants by Observation.

**Vol. 2. Theory and Use of Astronomical Instruments**, 633 pp. \$2.75.

*Chapters:* 1. The Telescope; 2. Of the Measurement of Angles or Arcs in General—Circles—Micrometers—Level; 3. Instruments for Measuring Time; 4. The Sextant, and Other Reflecting Instruments; 5. The Transit Instrument; 6. The Meridian Circle; 7. The Altitude and Azimuth Instrument; 8. The Zenith Telescope; 9. The Equatorial Telescope; 10. Micrometric Observations. *Appendix:* Method of Least Squares (98 pp.); *Tables:* Bessel's Refraction Table, Tables for Correcting Lunar Distances, etc. (55 pp.)

These two paperback volumes are unabridged and unaltered republications of Chauvenet's fifth revised and corrected classical treatises (copyright 1891). The work is useful as a reference book, as a book of instruction for the student and as a practical manual for navigators.

**An Introductory Treatise on the Lunar Theory**, Brown, Ernest W. (Professor of

Applied Mathematics, Haverford College, Pa., Sometime Fellow of Christ's College, Cambridge), Dover Publications, Inc., New York, 1960, 292 pp. Paperback reprint, \$2.

*Chapters:* 1. Force-Functions; 2. The Equations of Motion; 4. Undisturbed Elliptic Motion; 4. Form of Solution: The First Approximation; 5. Variation of Arbitrary Constants; 6. The Disturbing Function; 7. De Pontécoulant's Method; 8. The Constants and Their Interpretation; 9. The Theory of Delaunay; 10. The Method of Hansen; 11. Method with Rectangular Coordinates; 12. The Principal Methods; 13. Planetary and Other Disturbing Influences.

This book was first published in 1896. It is for scientists and engineers who are interested in orbital calculation, navigation of space, and other areas where the three-body problem is important.

**Theoretical Mechanics: Dynamics of Rigid Bodies**, Macmillan, William Duncan, Dover Publications, Inc., New York, 1960, 478 pp. Paperback reprint, \$2.

*Chapters:* 1. Algebra of Vectors; 2. Moments of Inertia; 3. Systems of Free Particles; 4. General Theorems on the Motion of a Rigid Body; 5. Motion Parallel to a Fixed Plane; 6. Motion of a Rigid Body in Space; 7. Integrable Cases of Motion of a Rigid Body about a Fixed Point; 8. Rolling Motion; 9. Impulsive Forces; 10. The Differential Equations of Analytical Dynamics; 11. The Canonical Equations of Hamilton; 12. The Method of Periodic Solutions.

First published in 1936, this textbook is intended for the advanced student.

**Dynamics of a System of Rigid Bodies. Part I: The Elementary Part**, Routh, Edward John, Dover Publications, Inc., New York, 1960, 443 pp. Paperback reprint, \$2.35.

*Chapters:* 1. On Moments of Inertia; 2. D'Alembert's Principle, etc.; 3. Motion About a Fixed Axis; 4. Motion in Two Dimensions; 5. Motion in Three Dimensions; 6. On Momentum; 7. Vis Viva.

In this elementary half of Routh's work, the student is introduced to the dynamical principles of the subject together with the more elementary applications.

**Principles of Stellar Dynamics**, Chandrasekhar, S. (astrophysicist; Morton D. Hull Distinguished Service Professor, University of Chicago), Dover Publications, Inc., New York, 1960, 313 pp. Paperback reprint, \$2.

*Chapters:* 1. Kinematics; 2. The Time of Relaxation of a Stellar System; 3. Galactic Dynamics: The Dynamics of Differential Motions; 4. General Dynamics of Stellar Systems: Spiral Structure; 5. The Dynamics of Star Clusters. *Later papers:* Dynamical Friction, New Methods in Stellar Dynamics.

For the student of astronomy, this book (originally published in 1942) presents the theory of stellar dynamics as a branch of classical dynamics.



## PIONEERING IN SPACE NAVIGATION RESEARCH



The Jet Propulsion Laboratory in Pasadena, California, has been given the responsibility by the National Aeronautics and Space Administration of managing and executing a number of highly significant explorations in space. They include lunar and planetary missions such as fly-bys, orbiters, and unmanned roving vehicles for the observation of the surface of the moon and the planets. Other missions planned for the future involve trips outside of the ecliptic and beyond the confines of the solar system.

The successful execution of these programs requires extensive research efforts of a basic nature in the areas of celestial navigation and the guidance and control of vehicles operating far out in space. The problem areas being investigated include novel concepts in navigation based on astrophysical phenomena as well as research on inertial, optical, and electro-optical sensors of various types. Other examples of present research activities in this area are cryogenic studies related to gyro and computer techniques, gas lubrication and flotation of sensing masses, research in solid-state physics, and many others.

The Laboratory has a number of positions open for scientists who are interested in working on challenging problems in these areas and who have the ability to investigate novel concepts and try unconventional methods.

Applicants must have an outstanding academic background with a Ph.D. degree, or equivalent experience and a Masters degree, in physics, astronomy, or electrical engineering. A minimum of five years of industrial or academic experience in the following fields will normally be required: optical physics, astrophysics, cryogenics, inertial guidance, celestial navigation, and computer and logic devices.

Qualified scientists will be offered the opportunity to work in an unusually stimulating atmosphere and will have available excellent supporting facilities for experimental and analytical studies.

Send professional resumé to  
Robert C. Dewar  
California Institute of Technology  
**JET PROPULSION LABORATORY**  
4800 Oak Grove Drive  
PASADENA, CALIFORNIA



# New Patents

George F. McLaughlin, Associate Editor

**Gas stream thrust reaction propulsion engines (2,940,252).** W. A. Reinhart, Bellevue, Wash., assignor to Boeing Airplane Co. (ARS corporate member).

Tapered dividers mounted in the discharge end to separate the gas flow into branched streams for noise suppression and thrust reversal.

**Ullage compensation for pressurizing systems (2,940,256).** J. R. Conyers, D. E. Aldrich and G. P. Sutton (ARS members), Washington, D. C., assignors to North American Aviation, Inc. (ARS corporate member).

Expandable container in the propellant tank of a rocket. A flow shifting valve redirects the fast burning charge gases to the thrust chamber at a predetermined point below full tank operating pressure.

**Rocket propellant injector (2,940,259).** R. L. Mantler, Webster Groves, Mo., assignor to NASA.

Parallel co-planar tubes forming a flattened grating ejecting alternate spray sheets of propellants from different sources over the entire injector surface.

**Missile launcher adaptor (2,940,362).** C. N. Paxton, Encino, Calif., assignor to the U. S. Air Force.

Single mounting for supporting the weight of a missile formed on the upper surface of the missile. An adaptor carries the missile until a predetermined shear force of the mount is exceeded.

**Rocket release mechanism (2,940,363).** G. A. Hamilton and R. T. Marete, Cleveland, Ohio, assignors to the Weatherhead Co.

Nonmetallic tube with a latch pivoted and extending into the tube. A cam tilts the latch in response to axial movement of the rocket in the tube.

**Turbine-driven fans (2,940,689).** A. R. Howell, Cove, Farnborough, England, assignor to the British Government.

Delta wing aircraft with ducted fans in the wings. A turbine nozzle supplies working fluid to the rotor blades. Rotor speed is maintained at constant value over the range of output of the fans.

**Aircraft with split flaps and gas jet boundary layer control (2,940,690).** A. D. Wood, Ottawa, Ontario, Canada, assignor to National Research Council.

Ducts from the power units project a gas stream through flaps at the trailing edge of the wings, deflecting the flow downwardly.

**Vertical takeoff powerplant system (2,940,691).** C. V. David, San Diego, Calif., assignor to Ryan Aeronautical Co. (ARS corporate member).

Vertically thrusting fan providing lift when the blade pitch is high, and maintaining its gyroscopic stabilizing effect when feathered.

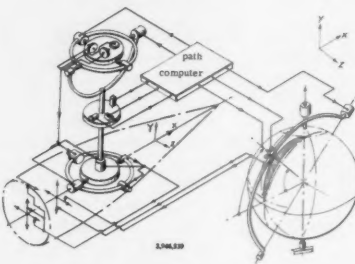
**Solid composite propellants with burning rate catalyst (2,941,352).** W. M. St. John Jr., Waco, Texas, assignor to Phillips Petroleum Co.

Method of developing thrust using as a base a propellant of inorganic oxidizing salt and a binder of a conjugated diene having 4 to 8 carbon atoms per molecule.

**Jet propelled convertiplane (2,941,749).** R. J. Sullivan and H. J. Nozick, Fairfield, Conn., assignors to United Aircraft Corp. (ARS corporate member).

Fixed wings sustain the aircraft in airplane flight. A jet-driven rotor is mounted for rotation about a vertical axis for helicopter flight.

**Guidance system for long range ballistic missile (2,946,539).** E. M. Fischel, Huntsville, Ala., assignor to the U. S. Navy.



Integrated control autonomous after launching, and capable of traversing a great circle course along the trajectory of a Kepler ellipsoid.

**Balloon load launching device (2,941,750).** H. V. Smith, J. Dwyer and J. A. Winkler, Sioux Falls, S. D., assignors to the U. S. Air Force.

Automatically controlled means for separating a cord attaching a parachute to the balloon rigging at a predetermined point in the ascent.

**Rocket propellant (2,942,961).** J. R. Eiszner and W. C. Stanley (ARS member), Seymour, Ind., assignors to Standard Oil Co.

Composition of ammonium nitrate, Prussian blue catalyst, finely divided carbon and a plastic binder material of cellulose acetate.

**Stable rocket propellant (2,942,962).** E. F. Morello, W. A. Porell (ARS member) and N. J. Bowman (ARS member), Hammond, Ind., assignors to Standard Oil Co.

Combustion catalyst of Prussian blue, finely divided carbon, a plastic binder, and plasticizer components consisting of a liquid polyesterification condensation product.

**Solid propellant combustion catalyst (2,942,963).** T. A. Burgwald, Hammond, Ind., assignor to Standard Oil Co.

Gas producing grain of ammonium nitrate and a combustible plastic binder of synthetic resin.

**Stable gas generating composition (2,942,964).** T. A. Burgwald, J. Linsk and E. F. Morello, Joliet, Ill., assignors to Standard Oil Co.

Ammonium nitrate, an inorganic combustion catalyst consisting of ammonium dichromate and insoluble Prussian blue, and a binder containing nitrodiphenyl ether.

**Production of hollow thermal elements (2,942,970).** C. G. Coetzel and J. L. Ellis,

White Plains, N. Y., assignors to Sintercast Corp. of America.

Method comprises forming a core of high melting and inert material of melting point above 1700 deg. F., and providing on the external surface a porous coating of a refractory material.

**Method of propelling rockets and rocket fuels (2,943,439).** C. R. Scott, Bartlesville, Okla., assignor to Phillips Petroleum Co.

Oxidant and fuel components of a bipropellant introduced in the combustion chamber. Components are a mixture of a 5-membered heterocyclic compound and a mercaptan.

**Rocket thrust chamber (2,943,442).** E. F. Baehr, Berea, Ohio.

Regeneratively cooled combustion chamber able to withstand high flux rates. Channels secured together form a hollow enclosure. Rod-like means encircle the exterior, with the channels defining coolant passages.

**Missile safety closure (2,943,445).** J. H. Ritterskamp and C. A. Weise, Pacific Palisades, Calif., assignors to Douglas Aircraft Co., Inc. (ARS corporate member).

Plug-type closure in a container adapted to receive a propellant charge and igniter. A circuit breaker controls operation of the igniter in response to rotation of the plug.

**Stable monopropellants (2,944,385).** E. E. Toops Jr., Terre Haute, Ind., assignor to Commercial Solvents Corp.

Mixtures having a molar ratio of lithium chlorate to ammonia ranging from 1 : 2 to 1 : 3, and a bipropellant oxidant of lox, nitric acid and dinitrogen tetroxide.

**Device for increasing the impulsion of a fluid (2,944,386).** J. H. Bertin and H. F. Schmitt, Bourg-la-Reine, France, assignors to Société Bertin & Cie.

Jet augments for lift or propulsion. Convergent duct ending with an orifice open to the atmosphere. Pressure liquid supplied to a chamber outside the duct. Part of the liquid issues as a divergent jet.

**Air atomizing spray bar (2,944,388).** F. C. Bayer, Euclid, Ohio, assignor to Thompson Ramo Wooldridge, Inc. (ARS corporate member).

Inside tube with air injection orifices at intervals along its length, and surrounded by a second tube for discharging air atomized fuel into the combustion chamber.

**Rotating rocket motor (2,944,389).** C. E. Weinland (ARS member), China Lake, Calif., assignor to the U. S. Navy.

Ring surrounding an insulated metal collar at the rear end of the rocket. Electrical wires from an igniter have one end connected to the collar; the other is grounded.

**Termination of thrust in solid propellant rockets (2,944,390).** A. C. Keathley and N. A. Kimmel, Waco, Texas.

Safety disk having an area sufficiently greater than that of the nozzle, so as to reduce the pressure in the motor case to a degree insufficient to maintain combustion.

**Combustion Chamber for jet propulsion motors (2,944,398).** R. J. Naegele Jr. (ARS member), Menlo Park, Calif., assignor to Lockheed Aircraft Corp. (ARS corporate member).

Ramjet with burner in the air passage

EDITOR'S NOTE: Patents listed above were selected from the Official Gazette of the U. S. Patent Office. Printed copies of patents may be obtained from the Commissioner of Patents, Washington 25, D. C., at a cost of 25 cents each; design patents, 10 cents.



between the housing and center body. Burner has downstream diverging walls to direct combustible mixture into the burner.

**Jet engine noise reducer (2,944,623).** A. G. Bodine Jr., Van Nuys, Calif.

Twisted vanes in the constricted throat of an exit nozzle impart spin to the column of gases which is radially expanded by centrifugal force.

**Aircraft (2,944,762).** T. R. Lane, Cleveland, Ohio, assignor to Thompson Ramo Wooldridge, Inc. (ARS corporate member).

Circular configuration in plan. A compressor enclosed at the center of the saucer-shaped fuselage directs air over particular portions of the upper surface of the airfoil for vertical, horizontal and hovering flight.

**Guidance system (2,944,763).** R. Grandgent and T. Petrides, New York, N. Y., assignors to Republic Aviation Corp. (ARS corporate member).

For controlling the flight of a missile launched from a moving base. Optical means tracks the missile and produces signals indicating its position, and converts the signals into command signals.

**Jet propelled aircraft (2,946,540).** H. Coanda, Paris, France, assignor to Sebac Nouvelle S. A. Corp.

Slits of the Coanda-type extending around the fuselage forward of the wing and along the wing leading edge, adapted to direct emerging fluid rearwardly.

**Air vehicle (2,947,495).** W. M. Hammond Jr., Middle River, Md., assignor to the Martin Co. (ARS corporate member).

Air towed spherical body for carrying detection instrumentation. Stabilizing fins rotatably mounted so as to contribute no lift.

**Jet propelled aircraft (2,947,496).** A. L. Leggett, Los Angeles, Calif.

Space craft with centrally mounted resonant jet engine. Horizontal disk with radial passages provides lift and gyroscopic stabilization.

**Rocket power plants for aircraft (2,947,500).** K. Dreyer, W. Wessel and L. Bölkow, Stuttgart-Degerloch, Germany, assignors to Bölkow-Entwicklungen KG.

Solid fuel rocket power acceleration plant and continuous drive plant. One nozzle from the acceleration plant extends downwardly and rearwardly at an acute angle.

**Jet deflectors for aircraft (2,947,501).** J. A. Flint, Cove, Farnborough, England, assignor to Power Jets (Research and Development) Ltd.

Pipe junction in the form of a T-piece. Butterfly valves guide the deflected jets into a downward path.

**Ejection seat for aircraft (2,947,503).** G. A. Holcomb, Columbus, Ohio, assignor to North American Aviation, Inc. (ARS corporate member).

Rocket attached to a seat to provide a primary seat lifting force. A plate under the seat provides a secondary lift force when moved in an air stream.

**Combined rocket and ramjet engine (2,948,112).** K. W. Smith, Dallas, Texas.

Nose valve in the passageway from the forward end of the body to the combustion chamber provides flow of oxidant when closed, and shuts off flow when open.

**Supersonic wind tunnel for a variable Mach number (2,948,148).** L. M. G. de Jurquet de la Salle d'Anfreville, J. H. Bertin and M. Kadosch, Paris, France, assignors to SNECMA Co.

Nozzle in the form of a slot-like passage opening through the test chamber wall at the throat, and facing upstream. Pressure fluid is supplied to the nozzle.



## DA VINCI AND THE BIRDMAN WARP

**L**EONARDO DA VINCI (1452-1519) was an intellectual giant who loved to discourse on the subject of "*Natural and Mechanical Flight*." He propounded a theory of aerodynamics and recognized the importance of wing warp and airframe stresses. In his treatise on the mechanical birdman he cautions that, "...its joints should be made of strong tanned hide, and sewn with cords of strong raw silk. And let no one encumber himself with iron bands, for these are very soon broken..."

Here at CEA, our scientists and engineers analyze advanced systems. For example, we supply missile and ground support equipment manufacturers with detail data on the response of their structures to thermal and aeroelastic environments. In our studies, we use an invention that would have delighted the probing intellect of Da Vinci: our Direct Analog Computer.



**COMPUTER ENGINEERING ASSOCIATES, INC.**  
350 N. Halstead  
Pasadena, California  
Elgin 5-7121

# Technical Literature Digest

M. H. Smith, Associate Editor

The James Forrestal Research Center, Princeton University

## Combustion and Propellants

Pre flame Reactions in the Autodecomposition of Acetylenic Compounds, by V. U. Henderson Jr., *Experiment Inc. TP-161*, Dec. 31, 1959, 23 pp.

Ion Identification and Ionization Processes in Flames, by A. Van Tiggeleu, *Louvain University Laboratory for Inorganic Chemistry, Final Report*, May 1960, 45 pp.

Ignition and Flame Stabilization of Stream of Combustible Gaseous Mixtures by Hot Jet, by Hiroshi Tsuji, *Tokyo, University Aeronautical Res. Institute, Rep. no. 357*, June 1960, 18 pp.

Propagation of Free Flames in Laminar and Turbulent-Flow Fields, by Ray E. Bolz and Henry Burlage Jr., *NASA Tech. Note D-551*, Sept. 1960, 66 pp.

Liquid-Phase Heat-Release Rates of the Systems Hydrazine-Nitric acid and Unsymmetrical Dimethylhydrazine-Nitric

Acid, by Somogyi, Dezso and Charles E. Feiler, *LeRC., NASA TN D-469*, Sept. 1960, 16 pp.

Stability of Some Potential Rocket Fuels in the Molten State, by R. P. Rastogi, R. K. Nigam and Harbans Lal, *ARS JOURNAL*, vol. 30, Sept. 1960, pp. 905-907.

Concerning the Analogy Between Combustion in a Detonation Wave and in a Rocket Engine, by Yu. N. Denisov, Ya. K. Trashin and K. I. Shchelkin, *ARS JOURNAL*, vol. 30, Sept. 1960, *Russian Suppl.*, pp. 834-840.

The Infrared Fundamental Band of Liquid and Solid Hydrogen, by H. P. Gush, W. F. J. Hare, E. J. Allin and H. L. Welsh, *Canadian J. Phys.*, vol. 38, Feb. 1960, p. 176-193.

Theory of the Infrared and Raman Spectra of Solid Para-Hydrogen, by J. Van Kranendonk, *Canadian J. Phys.*, vol. 38, Feb. 1960, p. 240-261.

The Flame Decomposition of Some Substituted Ethyl Nitrates, by J. Powling, W. A. W. Smith and J. Thynne, *Combustion and Flame*, vol. 4, Sept. 1960, pp. 201-212.

Chlorine Inhibition of Carbon Monoxide Flames, by H. B. Palmer and D. J.

Seery, *Combustion and Flame*, vol. 4, Sept. 1960, pp. 213-222.

Mechanisms of Extinction of Liquid Fires with Water Sprays, by D. J. Rasbash, Z. W. Rogowski and G. W. V. Stark, *Combustion and Flame*, vol. 4, Sept. 1960, pp. 223-234.

Heterogeneous Combustion of Multi-component Fuels, by B. J. Wood, H. Wise and S. H. Inami, *Combustion and Flame*, vol. 4, Sept. 1960, pp. 235-242.

Kinetic Parameters for the Hydrogen and Ethylene Flames from Flashback Measurements, by B. Fine, *Combustion and Flame*, vol. 4, Sept. 1960, pp. 243-252.

Activation Energy and Reaction Order in Methane-Oxygen Flames, by H. Vandenabeele, R. Corbeels and A. Van Tiggelen, *Combustion and Flame*, vol. 4, Sept. 1960, pp. 253-260.

The Formation of Polycyclic Aromatic Hydrocarbons and Carbon Deposits from Normal and Reversed Diffusion Flames, by A. J. Lindsey, *Combustion and Flame*, vol. 4, Sept. 1960, pp. 261-264.

The Spontaneous Ignition of Aliphatic Amines, by C. F. Cullis and B. A. Khokhar, *Combustion and Flame*, vol. 4, Sept. 1960, pp. 265-269.

The Reaction of Hydrogen Atoms with Solid Propene at Low Temperatures, by Ralph Klein, Milton D. Scheer and John G. Walker, *J. Phys. Chem.*, vol. 64, Sept. 1960, pp. 1247-1253.

Chemical Reactions of Free Radicals at Low Temperature, by R. A. Ruehrwein, J. S. Hashman and J. Edwards, *J. Phys. Chem.*, vol. 64, Sept. 1960, pp. 1317-1322.

The Solubility of Nitrogen, Argon, Methane, Ethylene and Ethane in Normal Primary Alcohols, by Franklin L. Boyer and Louis J. Bircher, *J. Phys. Chem.*, vol. 64, Sept. 1960, pp. 1330-1335.

Investigation of the Mass Transfer Behind Flameholders, by G. Winterfeld, *Zeitschrift für Flugwissenschaften*, vol. 8, Aug. 1960, pp. 219-225. (In German.)

## Materials and Structures

Rocket Motor Gear Tooth Analysis (Hertzian Contact Stresses and Times), by E. K. Gatcombe and R. W. Prowell, *J. Engng. for Industry (ASME Trans.)*, vol. 82, Series B, no. 3, Aug. 1960, p. 223.

The Strain Analysis of Solid Propellant Rocket Grains, by M. L. Williams, *J. Aero/Space Sci.*, vol. 27, Aug. 1960, pp. 574-586.

Oxygen Transport and Steel Corrosion, by L. B. Johnson Jr., *I/EC: Indl. & Engng. Chem.*, vol. 52, Aug. 1960, pp. 71-73A.

Spectral Emissivity, Total Emissivity, and Thermal Conductivity of Molybdenum, Tantalum, and Tungsten Above 2300°, by Robert D. Allen, Louis F. Glasier Jr. and Paul L. Jordan, *J. Appl. Phys.*, vol. 31, Aug. 1960, pp. 1382-1387.

The Analysis of Redundant Structures by the Use of High-speed Digital Computers, by Walter J. Crichlow and Gernot

## PROFESSIONAL OPPORTUNITIES IN STRUCTURES ENGINEERING AT AEROJET-GENERAL'S SOLID ROCKET PLANT

In the sixties, as in the forties, Aerojet-General stands foremost in the solid rocket field. Our Solid Rocket Plant near Sacramento, California, is the nation's largest facility for the development and production of solid rocket power plants.

To continue our growth and expansion into new fields of rocketry, we are seeking mature, experienced engineers who have specialized in the areas of structural analysis, shell theory, large-deformation theory, heterogeneous construction (such as filament-winding), photoelastic analysis, and quantitative structural testing. A degree in mechanical, aeronautical or civil engineering is required.

The intricate and highly refined load-carrying components of modern missiles present interesting challenges to our structural engineering staff. Intriguing problems are brought about by the complex interaction of the very large propellant grain, chamber, interstage structures and applied loads which a modern large solid rocket motor must withstand. These problems demand the attention of structural analysts and test engineers of the highest talent.

Our top specialists are given responsibility and freedom to work on a broad spectrum of problems. Excellent salaries are offered, commensurate with proven ability and experience. Our location near Sacramento, between Lake Tahoe and San Francisco, offers the finest living conditions.

We invite you to send your resume and any detailed questions to:

Mr. E. P. James, Head  
Technical and Scientific Personnel  
Box 1947D

**AEROJET-GENERAL CORPORATION**

Sacramento, California

## Fluid Dynamics, Heat Transfer and MHD

**Influence Coefficients for Radiation in a Circular Cylinder**, by E. W. Parkes, *Stanford Univ., Dept. Aeron. Engng., Rep. SUDAER 92*, March 1960, 11 pp.

**Studies in the Heating of a Supersonic Gas Stream by a Radio Frequency Discharge**, by Frederick O. Smetana, *Southern Calif. Univ., Rep. USCEC 56-214*, July 15, 1960, 88 pp.

**Temperature Histories in Ceramic Insulated Heat-sink Nozzle**, by Carl C. Diepluch, *NASA TN D-300*, July 1960, 25 pp.

**Transport Properties of Free Molecule (Knudsen) Flow**, by G. N. Patterson, *Univ. Toronto, Inst. Aerophys., UTIA Rev. 11*, March 1958, 22 pp.

**Design Study of the UTIA Low Density Plasma Tunnel**, by J. B. French and E. P. Muntz, *Univ. Toronto, Inst. Aerophys., UTIA TN 34*, March 1960, 34 pp.

**Oblique Shock Relations for Air at Mach 7.8 and 7200 R Stagnation Temperature**, by H. T. Nagamatsu, J. B. Workman and R. E. Sheer Jr., *ARS JOURNAL*, vol. 30, no. 7, July 1960, pp. 619-622.

**Mass Transfer and Shock Generated Vorticity**, by H. Hoshizaki, *ARS JOURNAL*, vol. 30, no. 6, July 1960, pp. 628-634.

**Magnetohydrodynamic Cavities**, by Bernard Steginsky, *ARS JOURNAL*, vol. 30, no. 7, July 1960, pp. 642-643.

**Analytic Formulation for Radiating Fins with Mutual Irradiation**, by E. R. G. Eckert, T. F. Irvine Jr. and E. M. Sparrow, *ARS JOURNAL*, vol. 30, no. 7, July 1960, pp. 644-646.

**Condensation Shocks in Supersonic Nozzles**, by A. A. Stepankov, *ARS JOURNAL*, vol. 30, no. 7, July 1960, *Russian Supplement*, pp. 695-699.

**Approximate Free Molecule Aerodynamic Characteristics**, by D. M. Schrello, *ARS JOURNAL*, vol. 30, no. 8, Aug. 1960, pp. 765-767.

**Free Molecule Flow over Nonconvex Bodies**, by Ira M. Cohen, *ARS JOURNAL*, vol. 30, no. 8, Aug. 1960, pp. 770-772.

**Aerodynamic Heating Charts for Solid Propellant Rocket Motors**, by Gerald R. Guinn, *ARS JOURNAL*, vol. 30, no. 8, Aug. 1960, pp. 776-778.

**Transient State Heat Transfer and Diffusion Problems**, by Tung Tsang, *I/EC: Indl. & Engng. Chem.*, vol. 52, Aug. 1960, pp. 707-710.

**An Experimental Investigation of the Effect of Ejecting a Coolant Gas at the Nose of a Bluff Body**, by C. H. E. Warren, *J. Fluid Mech.*, vol. 8, part 3, July 1960, pp. 400-417.

**Magnetohydrodynamic Flow of a Viscous Fluid Past a Sphere**, by Richard Van Blerkom, *J. Fluid Mech.*, vol. 8, part 3, July 1960, pp. 432-441.

**Rocket Heat-transfer Literature**, *J. Heat Transfer (ASME Trans.)*, vol. 82, series C, no. 3, Aug. 1960, p. 155.

**Unsteady Turbulent Heat Transfer in Tubes**, by E. M. Sparrow and R. Siegel, *J. Heat Transfer (ASME Trans.)*, vol. 82, series C, no. 3, Aug. 1960, pp. 170-180.

**Improved Lumped Parameter Method for Transient Heat Conduction Calculations**, by H. G. Elrod Jr., *J. Heat Transfer (ASME Trans.)*, vol. 82, series C, no. 3, Aug. 1960, pp. 181-188.



HIGH-POWER ELECTRONICS

**The result of complex challenges**



50 Megawatt "S" Band Radar Transmitter

FXR's advanced techniques and facilities have produced the 50 Megawatt "S" Band Radar Transmitter for Cornell Aeronautical Laboratories. This transmitter, more than twice as powerful as the formerly largest unit of its class, will be used in the electronic exploration of the atmosphere and the ionosphere.

FXR has an extensive achievement record in solving demanding problems. Put this creative ability to work to help solve your High Power Electronics problem.

For detailed information concerning your particular application, contact your FXR applications engineer. He is only a phone call away.



## FXR, Inc.

Design • Development • Manufacture  
25-26 50th STREET • RA 1-9000  
WOODSIDE 77, N. Y. • TWX: NY 43745

**Local and Average Heat Transfer and Pressure Drop for Refrigerants Evaporating in Horizontal Tubes**, by M. Altman, R. H. Norris and F. W. Staub, *J. Heat Transfer (ASME Trans.)*, vol. 82, series C, no. 3, Aug. 1960, pp. 189-198.

**Experiments on Heat Transfer from Spheres Including Combined Natural and Forced Convection**, by T. Yuge, *J. Heat Transfer (ASME Trans.)*, vol. 82, series C, no. 3, Aug. 1960, pp. 214-220.

**Heat Transfer to Freon 12 Near the Critical State in a Natural Circulation Loop**, by J. P. Holman and J. H. Boggs, *J. Heat Transfer (ASME Trans.)*, vol. 82, series C, no. 3, Aug. 1960, pp. 221-226.

**Combined Free and Forced-convection Heat-generating Laminar Flow inside Vertical Pipes with Circular Sector Cross Sections**, by Pau-Chang Lu, *J. Heat Transfer (ASME Trans.)*, vol. 82, series C, no. 3, Aug. 1960, pp. 227-232.

**On Combined Free and Forced Convection in Channels**, by L. N. Tao, *J. Heat Transfer (ASME Trans.)*, vol. 82, series C, no. 3, Aug. 1960, pp. 233-238.

**The Role of the Skin in Heat Transfer**, by A. M. Stoll, *J. Heat Transfer (ASME Trans.)*, vol. 82, series C, no. 3, Aug. 1960, pp. 239-242.

**Heat Transfer by Laminar Flow from a Rotating Cone**, by C. L. Tein, *J. Heat Transfer (ASME Trans.)*, vol. 82, series C, no. 3, Aug. 1960, p. 252.

**The Effect of Mass Transfer on Free Convection**, by R. Eichhorn, *J. Heat Transfer (ASME Trans.)*, vol. 82, series C, no. 3, Aug. 1960, pp. 260-262.

**Boundary Layer Transition and Heat Transfer in Shock Tubes**, by R. A. Hartunian, A. I. Russo and P. V. Marrone, *J. Aero/Space Sci.*, vol. 27, Aug. 1960, pp. 587-594.

**The Thickness of a Melting Ablation-type Heat Shield**, by Ernst Wilhelm

Adams, *J. Aero/Space Sci.*, vol. 27, Aug. 1960, pp. 620-621.

**Mass-transfer Cooling in a Turbulent Boundary Layer**, by J. P. Hartnett, D. J. Masson, J. F. Gross and Carl Gazeley Jr., *J. Aero/Space Sci.*, vol. 27, Aug. 1960, pp. 623-624.

**Some Mass-Transfer Results with External-Flow Pressure Gradients**, by J. R. Baron and P. E. Scott, *J. Aero/Space Sci.*, vol. 27, Aug. 1960, p. 625.

**The Effect of a Deceleration Force on a Melting Boundary Layer**, by Simon Ostrach, Arthur W. Goldstein and Jesse Hamman, *J. Aero/Space Sci.*, vol. 27, Aug. 1960, p. 626.

**Heating of a Plasma by Acoustic Waves**, by Taro Dodo, *J. Phys. Soc., Japan*, vol. 15, July 1960, pp. 1292-1294.

**Statistical Mechanics of Transport in Fluids**, by James A. McLennan Jr., *Phys. of Fluids*, vol. 3, no. 4, July-Aug. 1960, pp. 493-502.

**Turbulence Theory and Functional Integration**, by Gerald Rosen, *Phys. of Fluids*, vol. 3, no. 4, July-Aug. 1960, pp. 519-528.

**Energy Transfer in a Turbulent Fluid**, by B. Samuel Tanenbaum and David Mintzer, *Phys. of Fluids*, vol. 3, no. 4, July-Aug. 1960, pp. 529-538.

**Influence of Pressure History on Momentum Transfer in Rarefied Gas Flows**, by F. C. Hurlbut, *Phys. of Fluids*, vol. 3, no. 4, July-Aug. 1960, pp. 541-544.

**Blunt Body Viscous Layer With and Without a Magnetic Field**, by Hakuro Oguchi, *Phys. of Fluids*, vol. 3, no. 4, July-Aug. 1960, pp. 567-580.

**Plasma Viscosity in a Magnetic Field**, by Allan N. Kaufman, *Phys. of Fluids*, vol. 3, no. 4, July-Aug. 1960, pp. 610-616.

**Experiments of Plasmoid Motion Along Magnetic Fields**, by David M. Wetstone, Melvin P. Ehrlich and David Finkelstein,



*Phys. of Fluids*, vol. 3, no. 4, July-Aug. 1960, pp. 617-630.

**On Certain Properties of Hydromagnetic Shocks**, by W. B. Ericson and J. Bazer, *Phys. of Fluids*, vol. 3, no. 4, July-Aug. 1960, pp. 631-640.

**On the Newtonian Theory of Hypersonic Flow for a Blunt Body**, by N. C. Freeman, *Princeton Univ., Dept. Aeron. Engng., Rep. no. 467*, May 1959, 13 pp.

**Flow Properties of An Unyawed 10-Deg. Cone for  $\gamma = 1.28$  to 1.40 At Mach Numbers of 1.5 to 8**, by W. T. Strike Jr. and B. B. Norton Jr., *Arnold Engng. Dev. Center, ARO, Inc., TN no. 60-178*, Oct. 1960, 85 pp.

**Distribution of Time-Averaged Pressure Fluctuations Along the Boundary of a Round Subsonic Jet**, by Walton L. Howes, *NASA TN no. D-530*, Nov. 1960, 20 pp.

**A Visual Technique for Determining Qualitative Aerodynamic Heating Rates on Complex Configurations**, by P. Calvin Stainback, *NASA TN D-385*, Oct. 1960, 25 pp.

**Effect of Surface Roughness on Characteristics of Spherical Shock Waves**, by Paul W. Huber and Donald R. McFarland, *NASA TR no. R-23*, 1959, 25 pp.

**Heat Transfer to Sharp and Blunt Yawed Plates in Hypersonic Air-Flow**, by J. G. Hall and T. C. Golian, *Cornell Aeron. Lab. Rep. no. AD-1052-A-11*, Sept. 1960, 4 pp. (*AFOSR TN no. 60-938*.)

**Variational Procedure for Minimizing Heating Effects During the Re-Entry of a Lifting Vehicle**, by Ely S. Levinsky, *Wright Air Dev. Div., TR no. 60-369*, July 1960, 81 pp.

**A Generalized Ohm's Law of Plasma**, by Ching-Sheng Wu, *Calif. Inst. Tech., Jet Propulsion Lab., TR no. 32-23*, May 1960, 23 pp.

**Boundary-Layer Transition on Blunt Bodies With Highly Cooled Boundary Layers**, by Kenneth F. Stetson, *Avco-Everett Res. Lab., Res. Rep. 41*, Jan. 1959, 11 pp.

**Shock-Wave Laminar-Boundary-Layer Interaction on a Convex Wall**, by Isaac Greber, *NASA TN D-338*, Oct. 1960, 77 pp.

**Flight Measurement of Wall-Pressure Fluctuations and Boundary-Layer Turbulence**, by Harold R. Mull and Joseph S. Algranti, *NASA TN D-280*, Oct. 1960, 26 pp.

**Numerical Solutions of Shock-Induced Unsteady Boundary Layers**, by S. H. Lam, *Princeton Univ., Dept. Aeron. Engng., Rep. 480*, Aug. 1959, 37 pp. (*AFOSR TN 59-926*.)

**Turbulent Skin Friction at High Mach Numbers and Reynolds Numbers in Air and Helium**, by Fred W. Matting, Dean R. Chapman, Jack R. Nyholm and Andrew G. Thomas, *NASA TR R-82*, 1960, 85 pp.

**Three-Dimensional Boundary Layer Equations of an Ionized Gas in the Presence of a Strong Magnetic Field**, by Ching-Sheng Wu, *Calif. Inst. Tech., Jet Propulsion Lab., TR 32-17*, March 1960, 24 pp.

**Transient Characteristics of a Rotating Plasma**, by Ching-Sheng Wu, *Calif. Inst. Tech., Jet Propulsion Lab., Tech. Release 34-122*, Oct. 1960, 19 pp.

**Nearly Free Molecular Flow Through an Orifice**, by Roddam Narasimha, *Calif. Inst. Tech., Guggenheim Aeron. Lab., Oct. 1960*, 19 pp.

**Moment Equations and Boundary**

**Conditions for Magneto-Gas Dynamics**, by Hsun-Tiao Yang, *Univ. Southern Calif., Engng. Center, USCEC Rep. 56-216*, July 1960, 51 pp.

**Low-Speed Plane Couette Flow of a Rarefied Conducting Gas in a Uniform Transverse Magnetic Field**, by Hsun-Tiao Yang, *Univ. Southern Calif., Engng. Center, USCEC Rep. 56-218*, Aug. 1960, 24 pp. (*AFOSR TN 60-1002*.)

**The Structure of an Electromagnetically Driven Shock**, by Vernal Josephson and Richard W. Hales, *Space Tech. Labs., Inc., Phys. Res. Lab., TR 60-0000-19313*, Sept. 1960, 30 pp.

**On the Distribution Function and Mean Energy of Electrons in a Slightly Ionized Gas in the Presence of Magnetic and Electric Fields**, by Ching-Sheng Wu, *Calif. Inst. Tech., Jet Propulsion Lab., TR 32-14*, July 1960, 23 pp.

**The Magnetic Field of a Finite Solenoid**, by Edmund E. Callaghan and Stephen H. Maslen, *NASA TN D-6465*, Oct. 1960, 23 pp.

**Hypersonics**, by Richard D. Linnell, *ASTRONAUTICS*, vol. 5, Nov. 1960, p. 36.

**Magnetohydrodynamics**, by Ali Bulent Cambel, *ASTRONAUTICS*, vol. 5, Nov. 1960, p. 39.

**Measurement of Convective Heat Transfer by Means of the Reynolds Analogy**, by R. A. Granville and G. Boxall, *Brit. J. Appl. Phys.*, vol. 11, Oct. 1960, pp. 471-474.

**Determination of Streaming Velocity and the Flow of Heat and Mass in High Current Arcs**, by T. B. Reed, *J. Appl. Phys.*, vol. 31, Nov. 1960, pp. 2048-2051.

**An Experimental Investigation of Turbulent Spots and Breakdown to Turbulence**, by J. W. Elder, *J. Fluid Mech.*, vol. 9, Oct. 1960, pp. 235-246.

**On Unsteady Laminar Boundary Layers**, by H. A. Hassan, *J. Fluid Mech.*, vol. 9, Oct. 1960, pp. 300-304.

**Transient Temperatures and Thermal Stresses in Hollow Cylinders Due to Heat Generation**, by John E. Schmidt and George Sonnemann, *J. Heat Transfer (ASME Trans.)*, vol. 82C, Nov. 1960, pp. 273-278.

**Mass Transfer, Flow and Heat Transfer About a Rotating Disk**, by E. M. Sparrow and J. L. Gregg, *J. Heat Transfer (ASME Trans.)*, vol. 82C, Nov. 1960, pp. 294-302.

**Heat Transfer and Effectiveness for a Turbulent Boundary Layer With Tangential Fluid Injection**, by R. A. Seban, *J. Heat Transfer (ASME Trans.)*, vol. 82C, Nov. 1960, pp. 303-312.

**Laminar Skin Friction and Heat Transfer on Flat Plates With Wedge-Shaped Grooves in Flow Direction**, by T. F. Irvine Jr., and E. R. G. Eckert, *J. Heat Transfer (ASME Trans.)*, vol. 82C, Nov. 1960, pp. 325-332.

**Heat Transfer to Liquid Metals With Variable Properties**, by R. Viskanta and Y. S. Touloukian, *J. Heat Transfer (ASME Trans.)*, vol. 82C, Nov. 1960, pp. 333-340.

**An Experimental Study of the Effects of Nonuniform Wall Temperature on Heat Transfer in Laminar and Turbulent Axisymmetric Flow Along a Cylinder**, by R. Eichhorn, E. R. G. Eckert and A. D. Anderson, *J. Heat Transfer (ASME Trans.)*, vol. 82C, Nov. 1960, pp. 349-359.

**Geometric Factors for Radiative Heat Transfer Through an Absorbing Medium in Cartesian Coordinates**, by A. K.

Oppenheim and J. T. Bevans, *J. Heat Transfer (ASME Trans.)*, vol. 82C, Nov. 1960, pp. 360-368.

**Thermal Radiation From a Cylindrical Enclosure With Specified Wall Heat Flux**, by C. M. Usiskin and R. Siegel, *J. Heat Transfer (ASME Trans.)*, vol. 82C, Nov. 1960, pp. 369-374.

**Application of Variational Methods to Radiation Heat Transfer Calculations**, by E. M. Sparrow, *J. Heat Transfer (ASME Trans.)*, vol. 82C, Nov. 1960, pp. 375-380.

**Heat Transfer to Boiling Mercury**, by F. E. Romie, S. W. Brovarney and W. H. Giedt, *J. Heat Transfer (ASME Trans.)*, vol. 82C, Nov. 1960, pp. 387-388.

## Flight Mechanics

**Physics and Medicine of the Atmosphere and Space**, *International Symposium on the Physics and Medicine of the Atmosphere and Space*, 2d, San Antonio, Texas, Nov. 10-12, 1959, ed. by Otis O. Benson Jr. and Hubertus Strughold, John Wiley & Sons, New York, 1960, 645 pp.

**Deceleration During Entry into Planetary Atmospheres**, by Dean R. Chapman, pp. 339-351.

**A Flight Study of a Power-off Landing Technique Applicable to Re-entry Vehicles**, by Richard S. Bray, Fred J. Drinkwater III and Maurice D. White, *NASA TN D-323*, July 1960, 27 pp.

## Vehicle Design, Testing and Performance

**Measurement of the Maximum Altitude Attained by the X-15 Airplane Powered With Interim Rocket Engines**, by W. H. Stillwell and T. J. Larson, *NASA TN no. D-623*, Oct. 1960, 12 pp.

**Measurement of the Maximum Speed Attained by the X-15 Airplane Powered With the Interim Rocket Engines**, by W. H. Stillwell and T. J. Larson, *NASA TN no. D-615*, Sept. 1960, 14 pp.

**Analytical and Computational Aspects of Dynamic Programming Processes of High Dimension**, by R. E. Beckwith, *Calif. Inst. Tech., Jet Propulsion Lab., Mem. no. 30-11*, 1960.

*NASA-Industry Program Plans Conference, 1st, July 28-19, 1960, Proceedings.*

**Introduction to Launch Vehicle Programs**, by D. R. Ostrander, pp. 34-38.

**The NASA Current Launch Vehicle Program**, by Abraham Hyatt, pp. 39-45.

**The Saturn Space Vehicle Program**, by O. H. Lange, pp. 46-49.

**Introduction to the Space Flight Programs**, by Abe Silverstein, pp. 58-60.

**Space Science Experiments With Sounding Rockets and Satellites**, by M. J. Stoller, pp. 61-64.

**Satellite Applications**, by N. D. Sanders, pp. 74-78.

**Funding the Space Program**, by Maurice H. Stans, *ASTRONAUTICS*, vol. 5, Nov. 1960, p. 22.

**Progress in Space Flight**, by Abe Silverstein, *ASTRONAUTICS*, vol. 5, Nov. 1960, p. 24.

**What Is An Optimum Program?** by Werner von Braun, *ASTRONAUTICS*, vol. 5, Nov. 1960, p. 26.

"Big Sticks" of the Space Age, by



O. J. Ritland, *ASTRONAUTICS*, vol. 5, Nov. 1960, p. 28.

Missiles and Space Vehicles, by Maxwell W. Hunter, *ASTRONAUTICS*, vol. 5, Nov. 1960, p. 40.

Test, Operations, and Support, by Richard A. Schmidt, *ASTRONAUTICS*, vol. 5, Nov. 1960, p. 48.

Missiles, *Flight*, vol. 78, Nov. 4, 1960, pp. 711-734.

## Instrumentation and Communications

Transmission of Information in a Channel with Feedback, by R. L. Dobrushin (transl. of *Teoriya Veroyatnosti i ee Primeneniya*, vol. 3, no. 4, 1958, pp. 395-412), *Johns Hopkins Univ., Appl. Phys. Lab.*, TG 230-T 134, June 8, 1960, 23 pp.

On the Optimum Synthesis of Sampled Data Multiple Filters with Random and Non Random Inputs, by H. C. Hsieh and C. T. Leondes, *Calif. Univ., Dept. Engng., (AFOSR TN 60-440)*, Feb. 1960, 42 pp.

Cumulative Probability of Recognizing a Signal on a Radar Set, by N. M. Sediakin (transl. of *Radiotek.*, vol. 14, no. 5, 1959, pp. 44-48), *Johns Hopkins Univ., Appl. Phys. Lab.*, TG 230-T-166, March 1960, 5 pp.

An Analysis of Critical Simultaneous Gas/Liquid Flow Through a Restriction and Its Application to Flowmetering, by N. C. J. Ros, *Appl. Sci. Res.*, sec. A, vol. 9, no. 5, 1960, pp. 374-388.

Characteristics of 488 Megacycles Per Second Radio Signals Reflected from the Moon, by B. C. Blevis and J. H. Chapman, *J. Res. Nat. Bur. Standards*, vol. 64D, (Radio Propagation), no. 4, July-Aug. 1960, pp. 331-334.

Experimental Investigation of the Long Range Tropospheric Propagation of Ultrashort Waves in Double Reception Conditions, by A. V. Prosin, I. P. Levshin and G. I. Slobodnick, *Radio Engng. (transl. of Radiotek.)*, vol. 14, no. 10, 1959, pp. 1-18.

Spectrum Compression of a Multichannel Signal in Communication Systems with Frequency Division of Channels, by A. N. Svenson, *Telecomms. (transl. of Elektrosvyaz')*, no. 9, 1959, pp. 927-939.

Curves of the Field Intensity Distribution of Ultrashort Wave Signals and the Dependence of Number of Errors on the Signal-to-noise Ratio, by E. N. Konopleva, *Telecomms. (transl. of Elektrosvyaz')*, no. 9, 1959, pp. 950-960.

A Method of Calculating Sections of Cosine Equalizers and Their Frequency Characteristics, by O. F. Kosminskii, *Telecomms. (transl. of Elektrosvyaz')*, no. 9, 1959, pp. 996-1009.

Filterless Methods for Analysing Stationary Random Processes, by A. F. Beletskii, *Telecomms. (transl. of Elektrosvyaz')*, no. 9, 1959, pp. 1010-1018.

Which System for Propellant Level Sensing? by G. J. Friedman and Louis DeBottari, *Space/Aeron.*, vol. 34, Aug. 1960, p. 103.

Feasibility of a Radiation Detection System for Space Travel, *Air Force Missile Dev. Center, Holloman AFB, New Mexico, AFMDC-TR-60-15*, July 1960, 48 pp., 17 refs.

Indication Error of an Accelerometer Resulting from Reaction with a Vibrating Surface, by I. I. Kliukin, *Johns Hopkins Univ., Appl. Phys. Lab., Transl. TG 230-T 128 (transl. of Izmeritel'naya Tekh.*,

no. 6, 1958, pp. 30-35), July 6, 1960, 13 pp.

Methods of Indicating a Glide Path by Visual Means, by J. W. Sparke, *Gl. Brit. Aeron. Res. Council, Current Paper 502*, Dec. 1958, 16 pp.

Portable Automatic Data Recording Equipment (Padre), by James M. Kendall, *Naval Ordn. Lab., White Oak, Md., NAVORD Rep. 4207*, Aug. 24, 1959, 17 pp.

Avionics Research: Satellites and Problems of Long Range Detection and Tracking: Papers Presented at the AGARD Avionics Panel Meetings, Copenhagen, Oct. 20-25, 1958, *NATO, AGARD*, ed. by E. V. D. Glazier, E. Rechlin and J. Voge, Pergamon Press, New York, 1960, 257 pp.

A Generalized Theory of Radar Observations, by Roland J. Lees, pp. 1-5.

The Calculus of Radar Observations, by P. M. Woodward, pp. 6-11.

Echoing Area Characteristics, by J. S. Hey, H. Gent and P. G. Smith, pp. 12-28.

Ground Scatter by Ionospheric Radar, by Walter Dieminger, pp. 29-43.

The Sun As a Noise Source in Radar Aerial Investigations, by E. Eastwood, pp. 44-56.

U.H.F. Radar Propagation Research, by B. C. Blevis and J. H. Chapman, pp. 57-67.

Electrohydrodynamic Properties of Satellites, by Lester Kraus, pp. 92-100. Electromagnetic Waves and Echos of the Ionized Tracks of Satellites at High Frequency, by A. Flambar and M. Reyssat, pp. 101-102.

Observation of Re-entry of an IRBM, by David D. Woodbridge, pp. 113-124.

Earth Satellite Observations Made with the Millstone Hill Radar, by Gordon H. Pettengill and Leon G. Kraft Jr., pp. 125-134.

Radio Observations of the Russian Earth Satellites, by J. G. Davies, pp. 135-139.

Radar Echos Obtained from Earth Satellites 1957 Alpha and 1957 Beta, by A. M. Peterson, R. L. Leadebrand, W. E. Jaye et al., pp. 140-155.

Sputnik Modulation Patterns, by Walter E. Brown Jr., pp. 156-173.

Satellite Tracking from Several Coordinated Doppler Receiving Stations, by William S. McDonald, pp. 174-187.

Vehicle Motions as Inferred from

Radio-signal-strength Records, by William C. Pilkington, pp. 188-235.

Forty Megacycle Satellite Images and Beyond-the-horizon Propagation, by H. W. Wells, pp. 236-239.

An Interesting Propagation Effect of Sputnik I, by Edmond Dewan, pp. 240-257.

International Symposium on High Temperature Technology, Asilomar Conference Grounds, Calif., Oct. 5-9, 1959, McGraw-Hill Book Co., New York, 1960, 348 pp.

The Accuracy and Precision of Measuring Temperatures Above 1000°K, by H. J. Kostkowski, pp. 33-44.

Radio Astronomy Observations from Space, by Fred T. Haddock, *ARS JOURNAL*, vol. 30, no. 7, July 1960, pp. 598-602.

Manometer Error Caused by Small Leaks in the Casing of a Satellite, by S. A. Kuchay, *ARS JOURNAL*, vol. 30, no. 7, July 1960, *Russian Supplement*, pp. 658-660.

Radio-frequency Mass Spectrometer for the Investigation of the Ionic Composition of the Upper Atmosphere, by V. G. Istomin, *ARS JOURNAL*, vol. 30, no. 7, July 1960, *Russian Supplement*, pp. 676-684.

Space Communications, by J. A. Webb, *Astron. Sci. Rev.*, vol. 2, no. 2, April-June 1960, pp. 17-18, 24.

The Theory and Design of Chirp Radars, by J. R. Klauder, A. C. Price, S. Darlington and W. J. Albersheim, *Bell System Tech. J.*, vol. 39, no. 4, July 1960, pp. 745-808.

The Design of Radar Signals Having Both High Range Resolution and High Velocity Resolution, by J. R. Klauder, *Bell System Tech. J.*, vol. 39, no. 4, July 1960, pp. 809-820.

Measuring Strain to 1000°F, by R. L. Hannah and A. M. Kinan, *Instruments & Control Systems*, vol. 33, no. 7, July 1960, pp. 1166-1167.

Hypervelocity Precision Impact Instrument, by William A. Allen, Gerald E. Meloy and James W. Robers, *Rev. Sci. Instrum.*, vol. 31, July 1960, pp. 726-730.

Evaporation Rate Monitor, by G. R. Giedd and M. H. Perkins, *Rev. Sci. Instrum.*, vol. 31, July 1960, pp. 773-775.

On One Possibility of Increasing the Efficiency of an Ultrashort Wave Meteorburst Communication System, by A. Magazanik, *Telecommunications (transl. of Elektrosvyaz')*, no. 11, 1959, p. 1293.

## CHANGE-OF-ADDRESS NOTICE

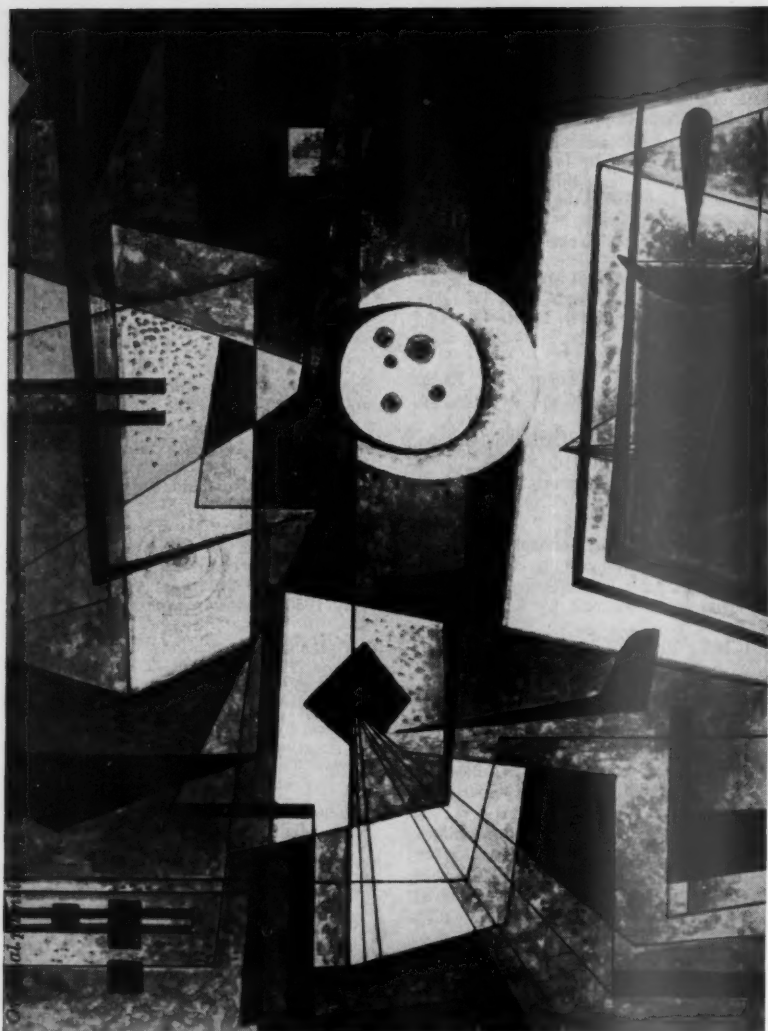
In the event of a change of address, it is necessary to include both your old and new addresses, as well as your membership number and coding, when notifying ARS headquarters in order to insure prompt service. If you are moving or have moved, send the following form to Membership Dept., American Rocket Society, 500 Fifth Ave., New York 36, N. Y.:

Name \_\_\_\_\_

Membership Card No. \_\_\_\_\_ Coding \_\_\_\_\_

Old Address \_\_\_\_\_

New Address \_\_\_\_\_



## Index to Advertisers

AEROJET-GENERAL CORP. . . . . Back cover

*D'Arcy Advertising Co.,  
Los Angeles, Calif.*

AEROJET-GENERAL CORP. . . . . 276

*D'Arcy Advertising Co.,  
Los Angeles, Calif.*

AEROSPACE CORP. . . . . Second cover

*Gaynor & Ducas, Inc.,  
Beverly Hills, Calif.*

COMPUTER ENGINEERING  
ASSOCIATES, INC. . . . . 275

*Guerin, Johnstone, Gage, Inc.,  
Los Angeles, Calif.*

CONVAIR DIV., GENERAL  
DYNAMICS CORP. . . . . Third cover

*D'Arcy Advertising Co.,  
St. Louis 3, Mo.*

FXR, INC. . . . . 277

*Beccher Associates,  
Mineola, N. Y.*

JET PROPULSION LABORATORY 273

*Barton A. Stebbins,  
Los Angeles, Calif.*

LOS ALAMOS SCIENTIFIC  
LABORATORY . . . . . 280

*Ward Hicks Advertising,  
Albuquerque, N. Mex.*

ORIENTATION LECTURES

GRADUATE TRAINING CENTER

FREQUENT SCIENTIFIC COLLOQUIA

ASSOCIATION WITH LEADING SCIENTISTS

GRADUATE THESIS PROGRAM

ADVANCE STUDY PROGRAM

SUMMER GRADUATE STUDENT PROGRAM

... these are some of the Doorways  
to Knowledge at Los Alamos.

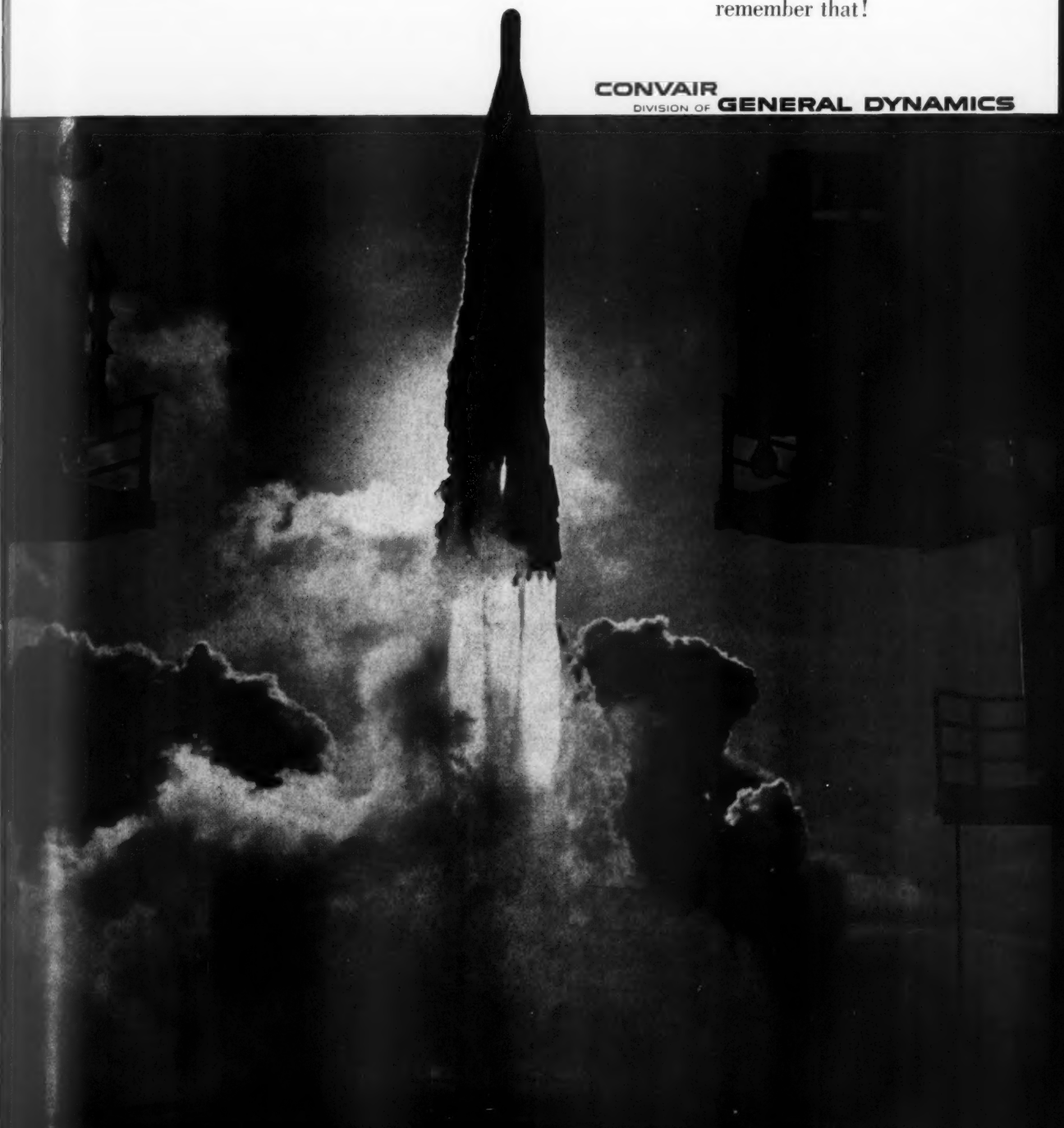
*For employment  
write to  
Personnel Director  
Division 61-11*

**los alamos**  
scientific laboratory  
OF THE UNIVERSITY OF CALIFORNIA  
LOS ALAMOS, NEW MEXICO

# Right Now...

The Air Force's Atlas ICBM  
is standing ready  
at Vandenberg and Warren  
Air Force Bases.  
Let *everyone*  
remember that!

**CONVAIR**  
DIVISION OF **GENERAL DYNAMICS**



Atlas is built by Convair (Astronautics) Division of General Dynamics and over 3000 associate contractors, subcontractors and suppliers in forty-two states. Additional Atlas bases will become operational with the U.S.A.F. Strategic Air Command in the months immediately ahead.

## HIGH ALTIMETRY

Aerojet-General's **AEROBEE/ASTROBEE** series is a complete line of solid and liquid rocket powered vehicles for upper-atmosphere research. There is an **AEROBEE** or **ASTROBEE** for every test requirement, providing a realistic space environment for payloads up to 175 pounds at altitudes up to 3,000 miles.

Over 250 of these reliable vehicles have been launched since 1946—forty during the IGY alone. Typical missions include: studies of atmospheric composition; micrometeorite investigations; ionization, radiation, and magnetic field determinations; aeromedical experiments; high-altitude photography; re-entry problems; communications; and component testing.

Aerojet emphasizes the delivery of complete units ready for payload insertion, followed by overall program management. Included are engineering, field service, logistics, range operation, ground handling equipment, data reduction, and training of customer personnel.

SPACECRAFT DIVISION

**CORPORATION**

Azusa, California

A  
SUBSIDIARY  
OF

THE  
GENERAL  
TIRE

AND  
RUBBER  
COMPANY



Engineers, scientists—investigate outstanding opportunities at Aerojet



